

# Lock Acquisition and Sensitivity Analysis of Advanced LIGO Interferometers

Thesis by  
Denis Martynov

In Partial Fulfillment of the Requirements  
for the Degree of  
Doctor of Philosophy



California Institute of Technology  
Pasadena, California

2015  
(Defended May 29, 2015)

© 2015

Denis Martynov

All Rights Reserved

# Acknowledgments

I am very grateful to my adviser Rana Adhikari for his support in most of my efforts and for his help to find my place in the field. Every day of my graduate schooling was different. I had an opportunity to work at the 40m prototype and LIGO Livingston Observatory as well as participate in various conferences and workshops. This experience and Rana's advice helped me understand how to be part of a big team and contribute to commissioning of LIGO interferometers.

I would like to thank Valera Frolov for his support during our commissioning work at LIGO Livingston Observatory. His deep understanding of the instrument and strong common sense guided our team towards robust lock acquisition and fruitful noise hunting at the Livingston site. Valera helped me, as well as many other students at the site, to believe that we can become successful scientists.

Many thanks to Peter Fritschel, Matt Evans, Lisa Barsotti, Rainer Weiss, and Nergis Mavalvala for many interesting ISC meetings, discussions of current and future LIGO research, and for their support and interest in my work at LIGO.

I would like to thank LIGO Caltech staff and in particular 40m team. I appreciate all the help from Koji Arai, Steve Vass, Aidan Brooks, Jan Harms, Alan Weinstein, Hiro Yamamoto, Gabriele Vajente, Nicolas Smith, Suresh Doravari, Jameson Rollins, Eric Gustafson, and Jenne Driggers.

It was a pleasure for me to work with Livingston local staff, students, operators, installation, detector characterization, and calibration groups. I am thankful for their help, networking and frequent discussions about the instrument. In particular, I would like to thank Adam Mullavey, Shivaraj Kandhasamy, Stuart Aston, Zach Korth, Jan Poeld, Anamaria Effler, Ryan DeRosa, Arnaud Pele, Gary Traylor, Tom Evans, Richard Oram, Brian O'Reily, Joseph Betzwieser, Joe Giaime, Janeen Romie, and Melanie McCandless.

I am grateful to all visiting scientists of LIGO Livingston Observatory: Hartmut Grote, Richard Mittleman, Michael Zucker, Fabrice Matichard, David Shoemaker, and Rich Abbott, who always brought new ideas to the site.

# Abstract

Laser interferometer gravitational wave observatory (LIGO) consists of two complex large-scale laser interferometers designed for direct detection of gravitational waves from distant astrophysical sources in the frequency range 10Hz - 5kHz. Direct detection of space-time ripples will support Einstein's general theory of relativity and provide invaluable information and new insight into physics of the Universe.

The initial phase of LIGO started in 2002, and since then data was collected during the six science runs. Instrument sensitivity improved from run to run due to the effort of commissioning team. Initial LIGO has reached designed sensitivity during the last science run, which ended in October 2010.

In parallel with commissioning and data analysis with the initial detector, LIGO group worked on research and development of the next generation of detectors. Major instrument upgrade from initial to advanced LIGO started in 2010 and lasted until 2014.

This thesis describes results of commissioning work done at the LIGO Livingston site from 2013 until 2015 in parallel with and after the installation of the instrument. This thesis also discusses new techniques and tools developed at the 40m prototype including adaptive filtering, estimation of quantization noise in digital filters and design of isolation kits for ground seismometers.

The first part of this thesis is devoted to the description of methods for bringing the interferometer into linear regime when collection of data becomes possible. States of longitudinal and angular controls of interferometer degrees of freedom during lock acquisition process and in low noise configuration are discussed in details.

Once interferometer is locked and transitioned to low noise regime, instrument produces astrophysics data that should be calibrated to units of meters or strain. The second part of this thesis describes online calibration technique set up in both observatories to monitor the quality of the collected data in real time. Sensitivity analysis was done to understand and eliminate noise sources of the instrument.

The coupling of noise sources to gravitational wave channel can be reduced if robust feedforward and optimal feedback control loops are implemented. Static and adaptive feedforward noise cancellation techniques applied to Advanced LIGO interferometers and tested at the 40m prototype

are described in the last part of this thesis. Applications of optimal time domain feedback control techniques and estimators to aLIGO control loops are also discussed.

Commissioning work is still ongoing at the sites. First science run of advanced LIGO is planned for September 2015 and will last for 3-4 months. This run will be followed by a set of small instrument upgrades that will be installed on a time scale of few months. Second science run will start in spring 2016 and last for about six months. Since current sensitivity of advanced LIGO is already more than a factor of 3 higher compared to initial detectors and keeps improving on a monthly basis, the upcoming science runs have a good chance for the first direct detection of gravitational waves.

# Contents

<b>Acknowledgments</b>	<b>iii</b>
<b>Abstract</b>	<b>iv</b>
<b>1 Introduction</b>	<b>1</b>
1.1 Gravitational waves	2
1.2 Source of gravitational waves	3
1.2.1 Bursts	4
1.2.2 Continuous waves	4
1.2.3 Binary systems	5
1.2.4 Stochastic background	5
1.3 Measurement technique	5
1.4 Structure of this thesis	7
<b>2 Optical detection scheme</b>	<b>9</b>
2.1 Optical measurements	9
2.1.1 Length stabilization	10
2.1.1.1 Homodyne detection	11
2.1.1.2 Heterodyne detection	13
2.1.1.3 Length dithering	15
2.1.1.4 Phase locking	16
2.1.2 Angular stabilization	17
2.1.2.1 DC sensing	18
2.1.2.2 RF sensing	19
2.1.2.3 Angle dithering	21
2.1.3 Mode matching	21
2.2 aLIGO optical design	22
2.2.1 Michelson interferometer	23
2.2.2 Power recycled Michelson interferometer	27

2.2.3	Dual recycled Michelson interferometer . . . . .	28
2.2.4	Dual recycled Fabry Perot Michelson interferometer . . . . .	29
<b>3</b>	<b>Lock acquisition and longitudinal control</b>	<b>31</b>
3.1	Arm length stabilization . . . . .	32
3.2	DRMI locking . . . . .	35
3.3	CARM offset reduction . . . . .	38
3.3.1	CARM control . . . . .	39
3.3.2	DARM control . . . . .	41
3.4	DC readout . . . . .	42
<b>4</b>	<b>Alignment and angular motion stabilization</b>	<b>45</b>
4.1	Interferometer initial alignment . . . . .	46
4.1.1	Alignment sequence . . . . .	46
4.1.2	Alignment precision . . . . .	48
4.2	DRMI angular motion . . . . .	49
4.2.1	ABCDEF model of power recycling cavity . . . . .	49
4.2.2	Angular controls . . . . .	52
4.3	Angular controls during CARM offset reduction . . . . .	53
4.4	Angular motion stabilization in full lock . . . . .	55
<b>5</b>	<b>Suspension control</b>	<b>58</b>
5.1	Longitudinal control . . . . .	59
5.1.1	ALS DIFF loop . . . . .	59
5.1.2	DARM control using L2 stage . . . . .	62
5.1.3	L2/L3 crossover . . . . .	64
5.2	Damping of high-Q modes . . . . .	67
5.2.1	BS bounce and roll damping . . . . .	68
5.2.2	Quad bounce and roll damping . . . . .	70
5.2.3	Quad violin mode damping . . . . .	71
<b>6</b>	<b>Instrument calibration</b>	<b>74</b>
6.1	Front end model . . . . .	74
6.2	Actuator calibration . . . . .	76
6.2.1	Michelson interferometer . . . . .	76
6.2.2	ALS beat notes . . . . .	78
6.2.3	Photon calibrator . . . . .	79
6.3	Error point calibration . . . . .	79

6.4	Total DARM calibration . . . . .	81
<b>7</b>	<b>Data quality</b>	<b>83</b>
7.1	Fundamental noises . . . . .	85
7.1.1	Quantum noise . . . . .	85
7.1.2	Thermal noise . . . . .	87
7.1.3	Seismic noise . . . . .	88
7.2	Charging noise . . . . .	91
7.3	Sensing and actuation . . . . .	95
7.3.1	Electrostatic driver . . . . .	95
7.3.2	Penultimate mass actuators . . . . .	96
7.3.3	Local damping . . . . .	96
7.3.4	OMC electronics . . . . .	96
7.4	Auxiliary loops . . . . .	97
7.4.1	Angular controls . . . . .	97
7.4.2	Laser frequency noise . . . . .	99
7.4.3	DRMI noise . . . . .	99
7.5	Intensity and jitter . . . . .	101
7.5.1	Input amplitude noise . . . . .	101
7.5.2	Input beam jitter noise . . . . .	103
7.6	Residual gas . . . . .	104
7.7	Lines . . . . .	105
7.8	Parametric instability . . . . .	106
7.9	Glitches . . . . .	107
7.9.1	DAC zero crossings . . . . .	107
7.9.2	Frequency and intensity transients . . . . .	108
7.9.3	Data transmission errors . . . . .	109
7.9.4	OMC backscattering . . . . .	109
7.9.5	Optical levers . . . . .	109
7.10	Discussion . . . . .	109
<b>8</b>	<b>Losses and scattering</b>	<b>111</b>
8.1	Arm losses . . . . .	111
8.2	Output losses . . . . .	114
8.3	Noise from scattered light . . . . .	115
8.3.1	Interferometer input . . . . .	117
8.3.2	Arm cavities . . . . .	117

8.3.3	In-air paths and chamber walls	118
8.3.4	Output mode cleaner	121
8.4	Mitigation techniques	122
8.4.1	Feedforward cancellation	123
<b>9</b>	<b>Feedforward noise cancellation</b>	<b>126</b>
9.1	Auxiliary length loops	127
9.2	Angular controls	131
9.3	Seismic noise	132
9.3.1	Static filter	133
9.3.2	Adaptive filters	135
<b>10</b>	<b>Optimal feedback control</b>	<b>140</b>
10.1	Linear quadratic regulator	141
10.1.1	State-space augmentation	141
10.1.2	Applications to LIGO	142
10.2	Kalman filter	143
10.2.1	Test mass curvature estimation	145
10.3	$H_\infty$ control technique	148
10.3.1	Optical lever damping	150
10.3.2	Local damping	151
10.4	$\mu$ -synthesis	153
10.4.1	Robust local damping	154
<b>11</b>	<b>Future work</b>	<b>156</b>
11.1	Short term upgrades	157
11.2	Medium term improvements	159
11.2.1	Interferometer control	159
11.2.2	OMC backscattering	160
11.2.3	Data analysis and detector performance	161
11.3	Variable finesse of the signal recycling cavity	163
	<b>Summary and conclusions</b>	<b>167</b>
<b>A</b>	<b>Acronyms</b>	<b>169</b>
<b>B</b>	<b>Quantization noise</b>	<b>171</b>
B.1	Estimation algorithm	173
B.2	Monitor of the full system	174

C Suspension wire heating	175
D Beam clipping in Michelson interferometer	177
E Seismometer isolation kit	181
Bibliography	186

# List of Figures

1.1	Effect of gravitational wave on Michelson interferometer. . . . .	6
1.2	Structure of this thesis . . . . .	7
2.1	S-polarized laser beam incident on moving interferometer mirror. . . . .	10
2.2	Homodyne detection scheme and error signals in Michelson and Fabry-Perot interferometers. . . . .	12
2.3	Heterodyne detection scheme and error signals in Michelson and Fabry-Perot interferometers. . . . .	15
2.4	Locking Fabry-Perot cavity using auxiliary laser. . . . .	17
2.5	Cavity, input, and central axes of a misaligned Fabry-Perot cavity. . . . .	18
2.6	Sensing of Fabry-Perot cavity axis motion using two QPDs in transmission. . . . .	18
2.7	Fabry-Perot cavity alignment scheme using RF sensors. . . . .	20
2.8	Optical configurations for gravitational wave detection. . . . .	24
2.9	Quantum noise coupling to gravitational wave channel in different optical configurations when interferometer input power is 125W. . . . .	28
3.1	Stabilization of arm cavities using auxiliary lasers. . . . .	33
3.2	Measured ALS COMM noise. Blue trace shows ALS COMM noise measured when X-arm was controlled using PDH signals. Orange trace shows residual longitudinal noise measured by PDH signals when low passed ALS COMM signal is used for IMC length control. . . . .	34
3.3	DRMI control using REFL PDH signals. . . . .	35
3.4	Response of REFL heterodyne signals to PRCL, MICH, and SRCL detuning. . . . .	36
3.5	Signals used to control interferometer during CARM offset reduction. . . . .	38
3.6	TRX and REFL9I signals depending on CARM offset. . . . .	40
3.7	Frequency response of $\sqrt{TRX + TRY}$ and REFL9I to CARM depending on CARM offset. . . . .	40

3.8	DARM transition from ALS DIFF to $AS45Q/\sqrt{TRX}$ is done when CARM offset is 100pm. A slow servo corrects DARM DC offset when CARM offset is between 250pm and 100pm. . . . .	41
3.9	Signals used to control interferometer in full lock. . . . .	42
3.10	Interferometric signals during the process of lock acquisition. Input power of interferometer is 0.75W. . . . .	43
4.1	Steps of interferometer initial alignment. First, arm cavities are aligned using green beam and serve as a reference to power and signal recycling cavity axis, BS and input beam. . . . .	47
4.2	Seismically driven angular motion of input mirrors (IM), small triple suspensions (HSTS), large triple suspensions (HLTS), beam splitter suspension (BSFM) and quadruple suspensions (QUAD). . . . .	49
4.3	Linear coupling of seismic motion to PRC power fluctuations. . . . .	51
4.4	Response of AS A and B WFS to DHARD mode during CARM offset reduction. . . . .	54
4.5	Angular controls of the full interferometer. . . . .	56
4.6	Optical power resonating in the power recycling cavity during 30 hour lock stretch. Interferometer input power is 22 Watts. . . . .	57
5.1	Open loop transfer function of ALS DIFF loop and M0, L1 and L3 stages. Loop is unconditionally stable when it is being engaged and M0 gain is lower than nominal. Then boost is turned on to suppress low frequency motion and M0 gain is increased. . . . .	60
5.2	ALS DIFF loop suppression and control signal to L1 and L3 stages. . . . .	61
5.3	Compensation filter from quad L2 to L3 stage. . . . .	62
5.4	Control signal to L2 stage. . . . .	63
5.5	Wide violin resonance. . . . .	64
5.6	Bringing L2/L3 crossover in full lock. . . . .	65
5.7	DARM control scheme. $P$ represents transfer functions from L3, L2, L1, and M0 stages to DARM, $C$ - correction filters, $G_0$ - DARM control servo, $G$ - crossover filters. . . . .	66
5.8	Control signal to L2 and L3 stages using L2/L3 crossover. . . . .	67
5.9	Phase sectors of open loop transfer function $H$ . . . . .	68
5.10	Open loops transfer function of BS bounce mode damping. . . . .	69
5.11	Comparison of BS longitudinal transfer function. . . . .	70
5.12	Excitation and damping of ITMX violin modes. Top plot shows control signal to suspension L2 actuator. Bottom plot shows amplitude of violin mode. . . . .	73
6.1	Calibration of external disturbance. . . . .	75

6.2	Beam splitter calibration using Michelson interferometer. . . . .	77
6.3	Calibration of L2 stage actuator using ALS DIFF beatnote. . . . .	78
6.4	Measurement of the DARM pole. . . . .	80
6.5	Comparison of DARM open loop transfer functions obtained from the calibration model and loop sweep. . . . .	81
6.6	Check of the final DARM calibration using photon calibrators. . . . .	82
7.1	Interferometer optical configuration in low noise regime. . . . .	84
7.2	DARM sensitivity curve and known noise couplings. . . . .	85
7.3	Coupling of fundamental noises to DARM. . . . .	86
7.4	Seismic noise and motion of isolated optical tables during summer and winter time. . . . .	89
7.5	Transfer function from longitudinal table motion to optic motion. . . . .	90
7.6	Side view of ETM with electrostatic blades, lower and upper ring heaters and metal cage. . . . .	91
7.7	Transfer function from electrostatic blades and TCS ring heater to DARM. . . . .	92
7.8	Potential noise coupling to DARM through static charge on end test masses. . . . .	94
7.9	Sensing and actuation noise coupling to DARM. . . . .	95
7.10	Coupling from auxiliary length and angular loops to DARM. . . . .	97
7.11	Angular motion of test masses in pitch degree of freedom measured by AS45Q WFS. . . . .	98
7.12	Angular motion of test masses in yaw degree of freedom measured by AS45Q WFS. . . . .	98
7.13	MICH noise budget. . . . .	100
7.14	SRCL noise budget. . . . .	100
7.15	PRCL noise budget. . . . .	101
7.16	Coupling of laser amplitude noise and beam jitter to DARM. Orange trace shows DARM spectrum with broken PZT of PMC which created high frequency intensity and jitter noise. . . . .	102
7.17	Input RIN coupling to OMC RIN. . . . .	103
7.18	Coupling of squeezed film damping and noise from residual gas in the arms to DARM. . . . .	104
7.19	Excitation and ringing down of the test mass body mode due to parametric instability. . . . .	106
7.20	Glitches in PRCL error signal due to PRM M3 DAC zero crossing. . . . .	107
7.21	Glitches in frequency and intensity servos depending on IMC VCO control signal calibrated to kHz. . . . .	108
7.22	Improvements in DARM sensitivity from June 2014 up to March 2015. . . . .	110
8.1	Dependence of power recycling gain and interferometer visibility on intracavity losses. . . . .	112
8.2	Round trip loss measurement depending on beam position on ITM. . . . .	113
8.3	Reflected power during ringdown measurement. . . . .	113

8.4	Dependence of optical losses in X- and Y-arm on different beam offsets from the optic center. . . . .	114
8.5	Simulation and measurement of OMC transmitted power in dependence of DARM offset. . . . .	115
8.6	Backscattering from moving objects. Light backscatters from intracavity baffles or chamber walls, output Faraday isolator and mode cleaner. . . . .	116
8.7	Range fluctuations due to alignment drift. . . . .	116
8.8	Scattered light noise at the interferometer input degrades behavior of intensity stabilization servo. . . . .	117
8.9	Comparisons of seismic noise with motion of X- and Y-arm tubes. If tube is insulated then motion in directions perpendicular to the cavity axis is significantly reduced above 20Hz. . . . .	118
8.10	Scattered light noises from in-air beams. . . . .	119
8.11	Scattering from the output port. Orange trace shows scattering shelves seen in DARM if motion of HAM5 ISI is increased by 1 $\mu$ m/sec. Pink trace shows scattered light noise if HAM6 fans are turned on. Fans increase acoustic noise around HAM6 chamber by factor of 3 around 70Hz and factor of 10 at higher frequencies. . . . .	120
8.12	Measurement of output port reflectivity. . . . .	122
8.13	Simulation of scattering noise coupling to DARM. Scattering shelf comes from large low frequency motion. Coherence between DARM and high frequency motion of the scattering object depends on low frequency motion. . . . .	124
8.14	Coherence between accelerometers installed on the same wall on HAM6 chamber. . . . .	125
9.1	Simplified scheme of feedforward subtraction. Noise source couples to gravitational wave channel with transfer function $T$ . Noise is measured by witness instrument with transfer function $S$ , and is conditioned and canceled from DARM using actuator $A$ . . . . .	127
9.2	Coherence between DARM and auxiliary length degrees of freedom. Red trace shows coherence with MICH. Blue trace shows coherence with SRCL. . . . .	128
9.3	Simulated and measured MICH and SRCL coupling to DARM. . . . .	129
9.4	Online feedforward subtraction scheme of MICH and SRCL from DARM. . . . .	130
9.5	DARM spectrum with and without online feedforward subtraction of MICH and SRCL. . . . .	130
9.6	Online feedforward subtraction scheme of angular controls noise. Noise couple through beam offcentering or coil imbalance $x$ and is subtracted with feedforward filter $K$ . Transfer functions $A_{P2P}$ and $A_{L2L}$ denote actuator transfer function for angle and length actuation. . . . .	131
9.7	Fitting of FIR filter with 10000 coefficients using IIR filter with 10 poles and zeros using Vectfit utility. . . . .	134

9.8	Result of static feedforward subtraction using static Wiener filtering technique. Red trace shows initial target signal before subtraction. Green curve is residual signal after applying FIR Wiener filter. Blue trace shows residual motion after applying IIR filter obtained by fitting optimal FIR filter. Black trace shows residual motion after installing IIR filter in the online system. . . . .	135
9.9	Test of LMS adaptive filters at the 40m prototype. Seismometers are located in the corner and end stations. . . . .	136
9.10	Online adaptive seismic noise cancellation scheme using FxLMS algorithm. . . . .	137
9.11	Norm of the filter coefficient vector during convergence process of FxLMS filter. . . . .	138
9.12	Feedforward subtraction of seismic noise from IMC and arms. . . . .	139
10.1	Application of LQR technique to BS optical lever servo. . . . .	143
10.2	Test mass and ring heater. . . . .	146
10.3	Norm of Kalman gain during the process of iterative solution of equations 10.13. . . . .	147
10.4	Estimation of test mass radius of curvature using model and measurement. . . . .	148
10.5	Application of $H_\infty$ technique to LIGO suspension control problems. . . . .	149
10.6	Application of $H_\infty$ technique to BS optical lever damping. Blue trace shows BS pitch to pitch transfer function when loop is open, and orange trace shows the same transfer function when loop is closed. . . . .	150
10.7	Magnitude of control cost functions developed for design of $H_\infty$ controllers. . . . .	151
10.8	Simulation of damping BS suspension modes using $H_\infty$ controller. . . . .	152
10.9	Transfer function of BS top stage in longitudinal degree of freedom. Black trace corresponds to the case when BS is undamped, red trace - damped using $H - \infty$ controller. . . . .	153
10.10	Frequency shape of position and control cost function generated for longitudinal damping of BS suspension. . . . .	154
10.11	Damping of BS longitudinal resonances using robust controller. . . . .	155
10.12	BS longitudinal displacement due to sensor noise. . . . .	155
11.1	Interferometer quantum noise depending SRM transmission $T$ and detuning of signal recycling cavity $a$ . . . . .	162
11.2	Compound SR2 mirror inside the signal recycling cavity. . . . .	163
11.3	Power transmission and reflection phase from compound SR2 mirror based on cavity detuning. . . . .	164
11.4	Interferometer quantum noise with SR2 cavity depending on cavity detuning and mass of the mirrors. . . . .	165
11.5	Comparison of SRCL quantum noise in aLIGO configuration and with compound SR2 cavity. SRC finesse for carrier is the same in both cases. . . . .	166

B.1	Filter forms used in initial and advanced LIGO to compute output of SOS. . . . .	172
B.2	DARM filter bank. Algorithm downloads input signal and computes output using two types of variables to estimate quantization noise of digital filters that are engaged. . .	173
B.3	Quantization noise of HAM ISI vertical damping loop. Noise is lower if "biquad" form is used instead of direct form 2. . . . .	174
C.1	Drift of BS pitch after lock is lost. Blue trace shows intracavity power measured by POP18 signal, red - BS pitch, magenta - BS yaw angle measured by optical lever. POP18 signal is negative when PRC is locked on carrier. This signal goes to zero when lock is lost. When PRC was locked, intracavity power was 60W. . . . .	176
C.2	Frequency shift of PR3 violin modes when input power was increased from 3W up to 10W. This shift confirmed that wires are heated by optical power resonating in the power recycling cavity. . . . .	176
D.1	Power recycling gain, Michelson contrast defect and ring heater power during TCS test. Power on ring heaters was increased in steps to monitor effects in recycling gain and contrast defect. . . . .	178
D.2	Measurement of PRC g-factor during TCS test. . . . .	179
D.3	Power recycling gain, Michelson contrast defect and cavity visibility during CO2 laser test. Power of CO2 beam power was slowly increased from 0 up to 175mW. . . . .	180
E.1	Assembly of the seismometer isolation kit. . . . .	182
E.2	Guralp seismometer installed in the seismic isolation kit with internal cabling. . . . .	182
E.3	Drawing of granite block. . . . .	183
E.4	Drawing of connector plate for Guralp seismometer kit. . . . .	184
E.5	Drawing of connector plate for T-240 and STS-2 seismometer kits. . . . .	185

# List of Tables

3.1	PRMI lock statistics. . . . .	37
3.2	DRMI lock statistics. . . . .	37
3.3	Signals used for DRMI control during CARM offset reduction. Correction gain $\alpha$ is tuned to subtract PRCL from SRCL error point. . . . .	37
3.4	Signals used for CARM control. . . . .	39
3.5	Signals used for DARM control. . . . .	41
4.1	Table shows PRC waist position and tilt motion as well as power build up in the cavity relative to maximum value when each specified optic is misaligned by 1 urad. Last four columns show beam spot shift on each optic. . . . .	51
4.2	Simulation of WFS response to angular motion of the mirrors during CARM offset reduction. Interferometer input power was set to 1W, and sensors get all optical power from interferometer. . . . .	53
4.3	Sensing matrix of angular sensors to test masses, IM4 and PR2 in full lock. Input PSL power during the measurement was 2W. Sensing matrix scales linearly with power up to 25W. . . . .	55
5.1	Possible outcomes of tuning procedure of the servo phase. Initial sector indicates servo phase from figure 5.9 when only $BP_{f_0}$ is used. . . . .	68
5.2	Test mass bounce and roll damping parameters. . . . .	71
5.3	Test mass violin modes damping parameters. . . . .	72
5.4	Damping parameters of second harmonics of test mass violin modes. . . . .	72
7.1	Measured projections of electrostatic forces due to charge on test masses and surrounding metal on longitudinal direction. . . . .	93
8.1	Optical loss from individual components. . . . .	115
8.2	Scattered light noise from arm cavities. . . . .	118
8.3	Interferometer field reflectivity from AS port. . . . .	121

9.1	Measured beam decenting on four test masses using dithering technique. . . . .	131
9.2	Adaptive filter parameters used during the seismic noise subtraction. . . . .	138

# Chapter 1

## Introduction

Einstein's theory of general relativity [1] extends Newton's laws of universal gravitation towards large velocities and big gravitational potentials of interacting objects. General relativity could explain and predict many important physical effects including precession of the perihelion of the orbits of planets, angular deflection of light rays by gravity and gravitational lensing, frequency shift of light, and gravitational time dilation, existence of black holes, and other compact objects and radiation of gravitational waves.

The general theory of relativity provides a description of gravity as a geometric property of space and time. The presence of energy and momentum changes the curvature of space-time according to Einstein equations. Gravitational waves are ripples of space-time curvature that propagate outward from the source. Energy loss of a binary star system due to gravitational radiation was indirectly observed by Hulse and Taylor [2].

The mission of LIGO is to directly detect gravitational waves of cosmic origin and extract information about the source from the wave properties [3, 4]. This discovery will build a new branch of astronomy that will complement electromagnetic telescopes and neutrino observatories.

Advanced LIGO [5] is designed for broadband detection of gravitational waves in the frequency range from 10Hz up to 5kHz. US hosts two interferometers located at Livingston, LA and Hanford, WA. Using data from two sites, it is possible to correlate the gravitational wave signal and reduce the probability of false detection due to instrument glitches and noises. The Livingston and Hanford observatories are located 2998km apart and it takes 10msec for light to travel the distance between the two sites. Separation between the two observatories allows one to estimate the direction in the sky of the gravitational wave source.

Two other interferometers outside of U.S. are now under construction with design and sensitivity similar to aLIGO. The first one is the Italian-French VIRGO [6] instrument located in Pisa, and the second one is the Japanese project KAGRA [7] located in the Kamioka mine. Yet another element of the worldwide network of gravitational wave detectors is proposed to be built in India [8].

Other types of terrestrial based gravitational wave detectors include resonant bars [9, 10], atom

interferometers [11], and torsion bar antennas [12]. These techniques can be used as low frequency gravitational wave detectors and complement large-scale optical interferometers.

Ground motion and available space for building instruments are the most significant challenges in detecting gravitational waves below 1Hz using terrestrial based instruments. For this reason space based detectors such as LISA [13] and DECIGO [14] were proposed in the past and research studies are currently undergoing.

This chapter gives an introduction to the concept of gravitational waves and astrophysical sources. The first section describes treatment of gravitational waves as small ripples in space time. The second section describes types of astrophysical sources of gravitational waves. The third section shows response of the Michelson interferometer to gravitational wave signal.

## 1.1 Gravitational waves

Since all objects move in gravitational fields in the same way independent of the object mass, the equivalence principle states that it is possible to cancel gravitational forces locally by moving to non-inertial reference frame. In this frame interval  $ds$  is determined by the quadratic form

$$ds^2 = g_{ij} dx^i dx^j \quad (1.1)$$

where  $g_{ij}$  is a metric tensor and  $x^i$  are coordinates in four dimensional space-time.

In the absence of gravitational field, metric  $g_{ij} = \eta_{ij} \equiv \text{diag}(1, -1, -1, -1)$  in the inertial reference frame if Cartesian coordinates are used. Space-time is flat in this case. In the presence of gravitational field metric  $g_{ij}$  can not be brought to diagonal form by any coordinate transformation. In this case space-time is curved.

If space-time metric tensor  $g_{ij}$  is known, motion of the object is determined by its geodesics equation [15]:

$$\frac{d^2 x^i}{ds^2} + \Gamma_{kj}^i \frac{dx^k}{ds} \frac{dx^j}{ds} = 0 \quad (1.2)$$

where  $\Gamma_{kj}^i = \frac{1}{2} g^{im} \left( \frac{\partial g_{mk}}{\partial x^j} + \frac{\partial g_{mj}}{\partial x^k} - \frac{\partial g_{kj}}{\partial x^m} \right)$  are Christoffel symbols.

Metric tensor  $g_{ij}$  depends on matter and energy distribution and is determined by Einstein equations. These equations are nonlinear partial differential equations due to the fact that gravitational fields carry energy and momentum themselves. This is in contrast with linear Maxwell's equations since electromagnetic field does not carry charge. Einstein equations can be written as [16]:

$$R_{ik} = -\frac{8\pi G}{c^4} (T_{ik} - \frac{1}{2} g_{ik} T^m{}_m) \quad (1.3)$$

where  $T_{ik}$  is the energy-momentum tensor,  $R_{ik} = (\frac{\partial \Gamma_{jk}^l}{\partial x^l} - \frac{\partial \Gamma_{il}^k}{\partial x^k} + \Gamma_{ik}^l \Gamma_{lm}^m - \Gamma_{il}^m \Gamma_{km}^l)$  is the Ricci tensor, and  $G$  is the gravitational constant.

Einstein equations for space-time metric  $g_{ij}$  are usually solved numerically. Precise solutions are known for limited cases of matter and energy distributions. Kerr metric [17] is a solution for empty space-time around a rotating uncharged axially-symmetric black hole with a spherical event horizon. Schwarzschild metric [18] describes gravitational field outside a spherical mass, on the assumption that the electric charge of the mass, angular momentum of the mass and universal cosmological constant are all zero. Reissner-Nordstrom metric [19] is a static solution which corresponds to the gravitational field of a charged, non-rotating, spherically symmetric body of mass  $M$ . KerrNewman metric [20] describes the space-time geometry in the region surrounding a charged, rotating mass.

In the weak field approximation far away from the source space-time metric is close to the diagonal form  $\eta_{ij} = \text{diag}(1, -1, -1, -1)$ :

$$g_{ij} = \eta_{ij} + h_{ij} \quad (1.4)$$

where  $h_{ij} \ll 1$  is a small perturbation. Using gauge invariance, and up to first order in  $h$ , it is possible to write Ricci tensor as  $R_{ik} = \frac{1}{2}(\nabla^2 - \frac{1}{c^2} \frac{\partial^2}{\partial t^2})h_{ik}$ . Einstein equations in the empty space are reduced to:

$$\left( \nabla^2 - \frac{1}{c^2} \frac{\partial^2}{\partial t^2} \right) h_{ij} = 0 \quad (1.5)$$

Thus, elements of  $h_{ij}$  represent a plane wave propagating with the speed of light  $c$ . In the transverse traceless gauge  $h_{ij}$  is given in the form [21]:

$$h_{ij} = \begin{pmatrix} 0 & 0 & 0 & 0 \\ 0 & -h_+ & h_\times & 0 \\ 0 & h_\times & h_+ & 0 \\ 0 & 0 & 0 & 0 \end{pmatrix} \cos(\omega t - kz) \quad (1.6)$$

where  $h_+$  and  $h_\times$  represent two orthogonal polarizations of the gravitational wave with frequency  $\omega$  and wave vector  $k$ .

## 1.2 Source of gravitational waves

Gravitational waves can be produced by any acceleration of matter if spherical and cylindrical symmetries are broken. In the case when motions within the source are slow compared with the speed of light, the largest contribution to gravitational wave radiation comes from variation of the

quadruple moment  $I$ . Retarded potential solution of Einstein equations can be written as [22]:

$$h_{ij}(t) = \frac{2G}{rc^4} \ddot{I}_{ij}(t - R/c) \quad (1.7)$$

LIGO studies all possible types of sources of gravitational waves that can be detected on Earth. However, since there are ambiguities in the models of gravitational radiation, all estimations of detection rates are considered to be approximate with a precision of one, two or even three orders of magnitude.

### 1.2.1 Bursts

Both electromagnetic and neutrino detectors periodically see short transient signals coming from the sky. Fast catastrophic processes in the Universe should also produce gravitational waves. In the general case, waveform of such events cannot be foreseen. Detection primarily relies on a coincidence of excess power in multiple detectors and synchronizing signal arriving time with electromagnetic and neutrino observatories.

Supernovae are potential sources of gravitational waves [23]. An explosion may be triggered by the re-ignition of nuclear fusion in a degenerate star or the gravitational collapse of a massive star. In the latter case of supernova explosion energy is released in the form of neutrinos, photons and also the gravitational waves.

Gamma ray bursts are associated with distant energetic explosions and can be also accompanied by gravitation wave emission [24]. This and other unforeseen astrophysical events have the potential of revealing new discoveries [25]

### 1.2.2 Continuous waves

Continuous waves are produced by the systems with asymmetry which rotate with constant and well-defined frequency [26]. Searching for these signals is a computationally demanding task due to the frequency modulation produced by Earth motion around the Sun. @EinsteinHome program [27] was started to use spare computational time on computers of registered volunteers.

Pulsars are good candidates to emit monochromatic gravitational waves [28]. These magnetized rotating neutron stars are formed after supernova explosion if the mass of the star was in the range of  $\approx (1.4 - 3)$  solar masses according to Chandrasekhar and Tolman - Oppenheimer - Volkoff limits. Size of the star reduces down to  $10km$  after explosion and since a neutron star retains most of its angular momentum, it is formed with high rotation speed.

### 1.2.3 Binary systems

Two compact objects orbiting around their common center of mass lose energy in the form of gravitational waves [29]. Energy loss makes objects gradually approach each other, and frequency of the orbit increases. At the end-of-life stage gravitational waves from the binary system can be detected in the frequency range of the ground based detectors  $10Hz - 5kHz$ .

Binary systems can consist of two neutron stars, two black holes, or a neutron star and a black hole. Waveforms coming from the merger of black holes are well modeled based on the general theory of relativity [30]. Merger of binary neutron stars is less understood due to tidal effects.

### 1.2.4 Stochastic background

The stochastic signal has an approximately constant amplitude and a broad continuous spectrum. These signals are not periodic and not impulsive. Stochastic background can be detected by cross correlating data from two or more detectors [31, 32].

Cosmic gravitational wave background can arise from a large number of random events that occurred after the Big Bang. In this case waves are stretched as the Universe expands, and information about the early universe can be extracted after detection.

One more interesting source is the superposition of the signals from the vast population of compact binaries. Frequencies of emitted gravitational waves lie in the range from 1Hz up to several kHz depending on the mass distribution and time of formation [33].

## 1.3 Measurement technique

Fluctuations of strain are rather small, and significant effort is required to detect gravitational waves. Current section shows that Michelson interferometers can be used as gravitational wave detectors with high sensitivity. In this optical configuration light from the laser is split on the beam splitter, and travels along perpendicular arms to the end mirrors, bounces back, and recombines on the beam splitter. Figure 1.1 shows the effects on the Michelson interferometer when a gravitational wave of + polarization is incident from the top on the setup.

Disturbance of relative arm length produces a signal to the antisymmetric port of the Michelson interferometer. Differential phase shift due to gravitational wave in + polarization can be computed from geodesic equation for light. Time  $dt$  required for the light to travel distance  $dl$  along X-arm can be written as:

$$\begin{aligned}
 ds^2 &= (\eta_{ij} + h_{ij})dx^i dx^j = dt^2 - (1 + h_+)dl^2 = 0 \\
 dt &= \sqrt{1 + h_+}dl
 \end{aligned}
 \tag{1.8}$$

Similarly, time required for the light to travel distance  $dl$  along Y-arm is  $dt = \sqrt{1 - h_+} dl$ . Total phase difference between X- and Y-arm beams after their reunion on the beam splitter is

$$\Delta\varphi = \varphi_x - \varphi_y = \frac{2\pi c}{\lambda}(\tau_x - \tau_y) = \frac{4\pi}{\lambda} \left( \int_0^L \sqrt{1 + h_+} dl - \int_0^L \sqrt{1 - h_+} dl \right) \quad (1.9)$$

Since space-time metric perturbation  $h_+ \ll 1$ , it is possible to write:

$$\Delta\varphi \approx \frac{4\pi}{\lambda} \int_0^L h_+ dl \quad (1.10)$$

If the length of each interferometer arm is much smaller than gravitational wavelength  $L \ll \lambda_{GW}$ , the instrument will detect arm length shift proportional to perturbation of space-time metric:

$$\Delta L = h_+ L \quad (1.11)$$

Two arms of Michelson interferometer are tuned to have equal macroscopic length  $L$  to reject laser frequency noise at the antisymmetric port. Gravitational waves in the  $\times$  polarization produce phase shifts common to the interferometer arms and do not produce a signal at the antisymmetric port.

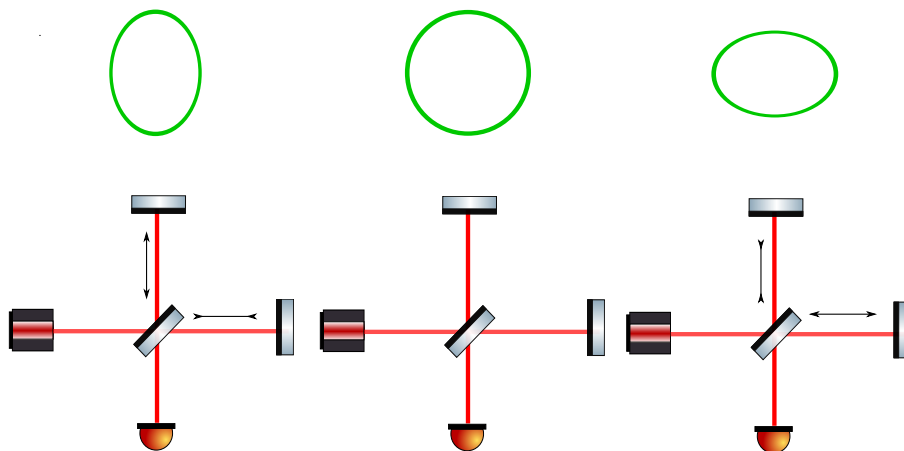


Figure 1.1: Effect of gravitational wave on Michelson interferometer.

Optical configuration of interferometer is optimized for the best sensitivity to gravitational waves in the frequency range 10Hz - 5kHz. For this purpose auxiliary degrees of freedom are introduced in LIGO interferometers, such as arm cavities and power, and signal recycling cavities. Chapter 2 describes the longitudinal and angular control principles of Fabry-Perot cavities and Michelson interferometers, optical readout schemes, and configuration of aLIGO interferometers.

## 1.4 Structure of this thesis

The first part of this thesis describes lock acquisition, alignment and control of advanced LIGO detectors. Chapter 3 and 4 are devoted to the sensing side of control loops and significantly rely on chapter 2 with summarizes interferometric measurement and optical design of advanced LIGO. Chapter 5 is devoted to actuation side of control loops and describes control of multi-stage suspensions and damping of high-Q modes.

The second part of this thesis is devoted to data quality and sensitivity of the instrument. Chapter 6 describes online calibration of advanced LIGO interferometers. Chapter 7 is devoted to broadband sensitivity analysis of the instrument data, narrow band lines and glitches found in data. Chapter 8 describes measurement of optical losses in the arm cavities and noises coming from scattered light. Chapter 9 describes feedforward noise cancellation techniques to reduce coupling of auxiliary loops and seismic noise to gravitational wave channel.

The third part of this thesis describes ideas for future research. Chapter 10 is devoted to simulations and online tests of optimal feedback control loops and state estimation techniques. Chapter 11 describes possible future improvements to advanced LIGO optical and mechanical configurations.

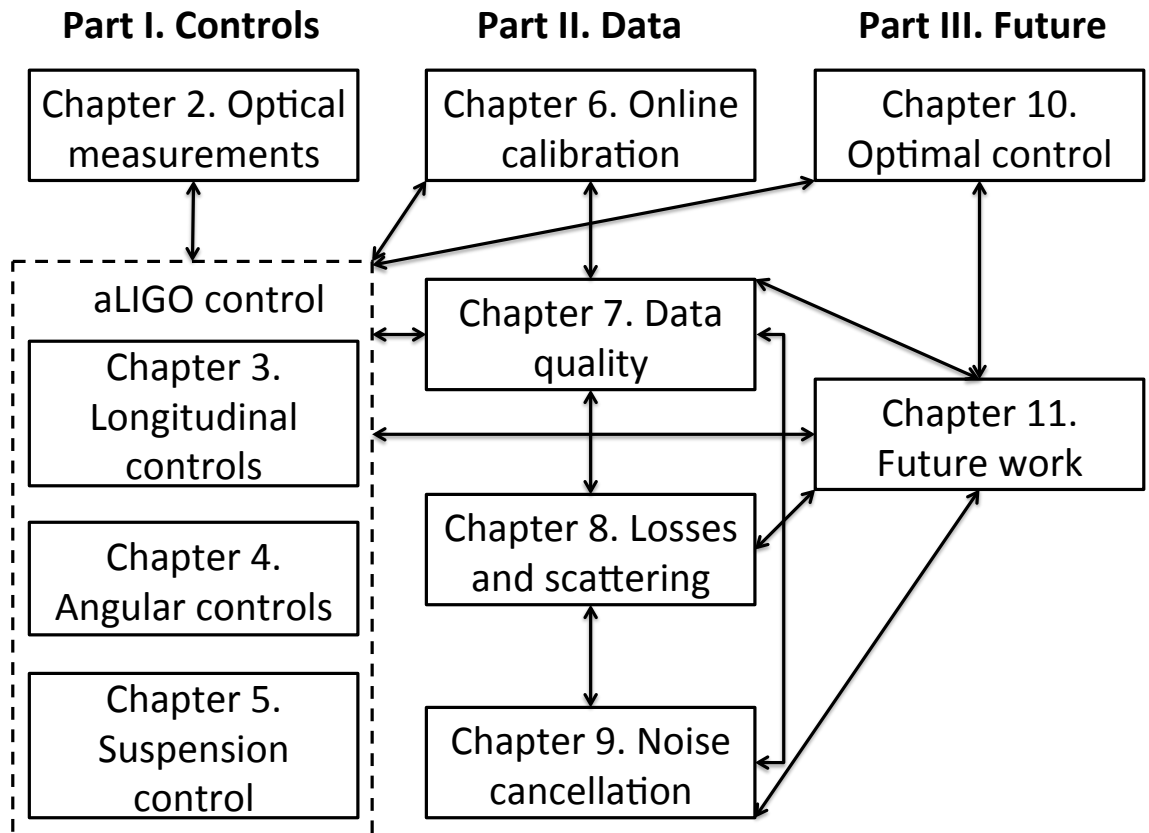


Figure 1.2: Structure of this thesis

Figure 1.2 shows connections between the chapters of this thesis. Columns represent three parts of the thesis devoted to control, data and future ideas. Appendices are devoted to abbreviations frequently used in this thesis, quantization noise due to finite precision of number in digital system, suspension wire heating due to optical power resonating in power recycling cavity. Appendices also discuss effects from the beam clipping inside Michelson interferometer and seismometer isolation kit designed to reduce coupling from environmental noise to seismometer signal and protect the instrument from accidental damage.

## Chapter 2

# Optical detection scheme

This chapter describes how lasers, optical interferometers, and photodetectors can be used as strain meters. The problem of gravitational wave detection is reformulated to the problem of distance measurement between suspended test masses. Stabilized lasers are widely used for precision experiments, and a variety of commercial optical components are available on the market, such as high quality mirrors, low-noise photodetectors, and stable lasers.

The first section of this chapter describes how lasers can be used for precision measurements. Pound-Drever-Hall [34] and DC readout techniques are currently used to control aLIGO optical cavities. In both cases readout signal is achieved by non-linear mixing of phase modulated light coming out from the interferometer with the light of a reference frequency. Optical power measured on the photodetector contains information about motion of interferometer mirrors relative to the laser wavelength.

The second section describes aLIGO optical configuration. Four test masses form two arm resonators, and the gravitational wave signal is derived from the differential length of these two arms. Common arm length is used to stabilize the laser. Beam splitter is used to equally split input laser beam between the arm cavities. The simple Michelson interferometer formed by the beam splitter and input test masses is controlled to keep the interferometer antisymmetric port at dark fringe. Power and signal recycling cavities installed at the input and output ports of interferometer are used to optimize sensing noise in the frequency range 10Hz - 10kHz.

## 2.1 Optical measurements

Longitudinal and angular motion of the mirrors can be measured using properties of light. Test mass is a part of the interferometer, and its motion is measured relative to other mirrors rather than to inertial frame. This limitation is not important for aLIGO since the gravitational wave signal is derived from the distance between test masses.

Optical measurement requires a stable laser, interferometer, and photodetector. The laser pro-

duces a coherent optical wave of known frequency and spatial mode. aLIGO uses Nd:YAG 1064nm laser and TEM00 mode. Electric field is given by equation [35]:

$$E(r, z, t) = E_0 \frac{w_0}{w(z)} \cdot \exp\left(-\frac{r^2}{w(z)^2} - ik \frac{r^2}{2R(z)} + i\xi(z)\right) \cdot \exp(i\omega_0 t - ikz) \quad (2.1)$$

where  $r$  is the radial distance from the beam axis,  $z$  is the axial distance from the waist,  $w_0$  is the beam size at the waist,  $w(z)$  is the beam size at axial distance  $z$  from the waist,  $R(z)$  is the beam's wavefront radius of curvature, and  $\xi(z)$  is the Gouy phase shift.

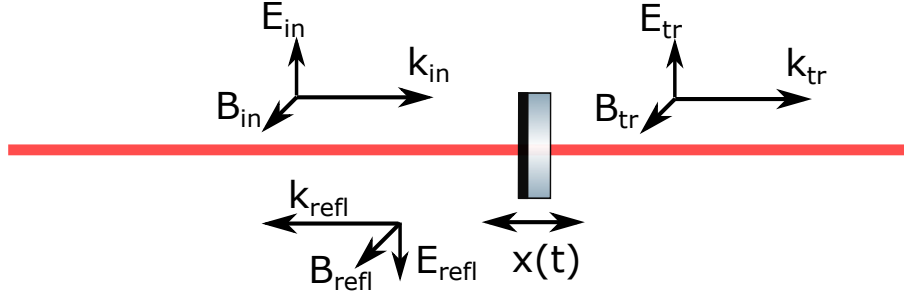


Figure 2.1: S-polarized laser beam incident on moving interferometer mirror.

### 2.1.1 Length stabilization

The interferometer dielectric mirrors split the incident laser beam into transmitted and reflected beams, as shown in figure 2.1. If the mirror moves along the direction of the incident laser beam, then reflected light is modulated in phase. Once interferometer is controlled in linear regime and mirror motion relative to other mirrors is much smaller compared to laser wavelength, reflected light can be expanded into three independent waves – a carrier and two audio sidebands. Frequency of the sidebands is offset from the carrier by the frequency of the mirror oscillations:

$$\begin{aligned} E_{refl}(r, z_{mirror}, t) &= \pm r E_{in}(r, z_{mirror}, t) \cdot \exp\left(i \frac{4\pi x_0}{\lambda} \sin\omega t\right) \\ &\approx \pm r E_{in}(r, z_{mirror}, t) \cdot \left(1 + \frac{2\pi x_0}{\lambda} \exp(i\omega t) - \frac{2\pi x_0}{\lambda} \exp(-i\omega t)\right) \end{aligned} \quad (2.2)$$

where  $x_0 \ll \lambda$  is the amplitude of mirror longitudinal motion,  $\omega$  is the frequency of the oscillation,  $r$  is the field reflectivity of the mirror. Choice of plus or minus sign of reflected wave in equation 2.2 depends on which mirror side the wave is incident.

Audio sidebands generated by moving mirrors propagate through the interferometer in a similar way as carrier field. For mathematical treatment it is convenient to introduce a vector of carrier and sideband electric fields  $(E^0, E^+, E^-)'$  and propagate this vector through the interferometer.

Reflection from mirrors is given by equation 2.2. In the first order approximation propagation through free space, reflection from optics can be written in matrix form as

$$M_{free}(L) = \begin{pmatrix} e^{i\frac{\omega_0}{c}L} & 0 & 0 \\ 0 & e^{i\frac{\omega_0+\omega}{c}L} & 0 \\ 0 & 0 & e^{i\frac{\omega_0-\omega}{c}L} \end{pmatrix} \quad M_{refl}(x_0) = \pm r \begin{pmatrix} 1 & 0 & 0 \\ \frac{2\pi x_0}{\lambda} & 1 & 0 \\ -\frac{2\pi x_0}{\lambda} & 0 & 1 \end{pmatrix} \quad (2.3)$$

Transmission through the optics can be written in matrix form as  $M_{tr} = tI$ , where  $t$  is mirror field transmission and  $I$  is the  $3 \times 3$  identity matrix.

Once input electric fields are set, vector can be computed at any point inside the interferometer and output ports. A number of simulation tools like Optickle [36], Finesse [37], and MIST [38] do these calculations and compute fields generated by moving mirrors.

$$\begin{pmatrix} E^0 \\ E^+ \\ E^- \end{pmatrix}_{out} = \prod M \begin{pmatrix} E^0 \\ E^+ \\ E^- \end{pmatrix}_{in} \quad (2.4)$$

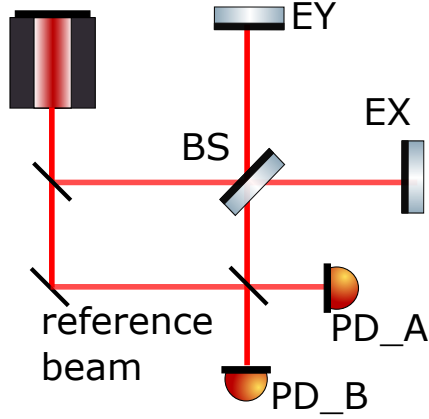
where  $\prod M$  is the product of all propagation matrices from the input to output port.

Audio sidebands from moving mirrors or laser frequency noise propagate through the interferometer and reach the photodetectors. Information about the mirror motion is extracted from measured power using homodyne or heterodyne detection schemes. The major difference between these two techniques is the origin of reference light or local oscillator.

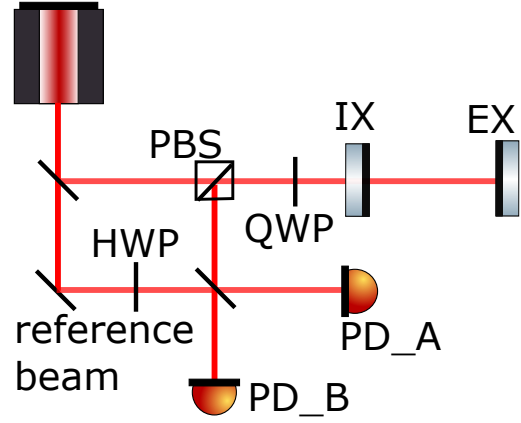
### 2.1.1.1 Homodyne detection

In the homodyne readout scheme signal and reference fields are derived from the same source. The signal field contains audio sidebands from the motion of the interferometer mirrors. The reference field is picked off directly from the interferometer input beam and shifted in phase on the way to the photodetector. Alternatively, the reference field can come out from interferometer together with the signal field if the locking point is offset from the dark fringe in the Michelson configuration or resonance point in the Fabry-Perot configuration.

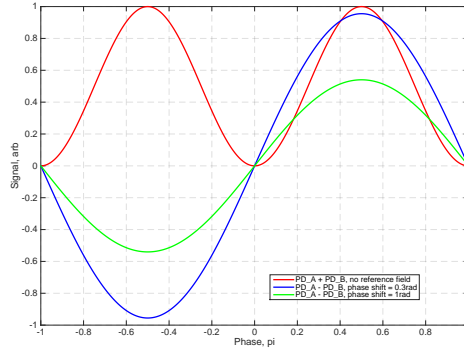
The electric field at the anti-symmetric port of the Michelson interferometer  $E_{as}$  is given by equation 2.5 assuming that beam splitter field reflectivity  $r_{bs}$  and transmissivity  $t_{bs}$  are equal to  $1/\sqrt{2}$ . The end mirrors of two arms have the same reflectivity  $r_{ex} = r_{ey}$ . If there is no reference field present at the anti-symmetric port, then the interferometer cannot be locked on the dark fringe since the error signal is quadratic, as shown in figure 2.2c. In this case the Michelson interferometer can be locked with DC offset from the dark fringe, and carrier light can be considered as local oscillator



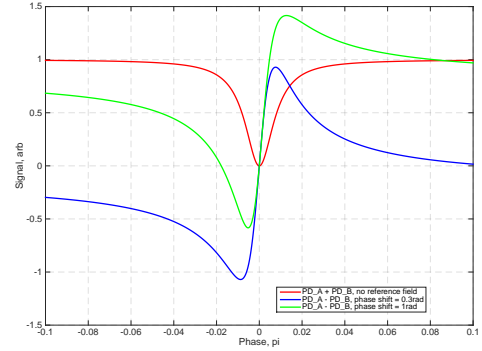
(a) Michelson interferometer.



(b) Fabry-Perot cavity.



(c) Comparison of photodetector signals set up in anti-symmetric port of Michelson interferometer with and without reference field.



(d) Comparison of photodetector signals set up in reflection of Fabry-Perot cavity with and without reference field.

Figure 2.2: Homodyne detection scheme and error signals in Michelson and Fabry-Perot interferometers.

field

$$\begin{aligned}
 E_{as} &= E_{in}^{bs}(r_{ex}r_{bs}t_{bs}e^{2i\varphi_x} - r_{ey}r_{bs}t_{bs}e^{2i\varphi_y}) \\
 &= E_{in}^{bs}r_{ex}ie^{i(\varphi_x+\varphi_y)}\sin(\varphi_x - \varphi_y)
 \end{aligned} \tag{2.5}$$

where  $\varphi_x, \varphi_y$  are phases acquired by laser beam during propagation along X- and Y-arms of the Michelson inteferometer.

When the reference field is present at the anti-symmetric port as shown in figure 2.2a, the power on photodetectors A and B can be written as

$$P_A = (E_{ref} - E_{as})(E_{ref} - E_{as})^*; \quad P_B = (E_{ref} + E_{as})(E_{ref} + E_{as})^* \tag{2.6}$$

Signal  $P_A - P_B$  is linear when the phase difference between the two inteferometer arms is close to zero. Figure 2.2c shows the difference between photodetector readings  $P_A - P_B$  when the phase shift between reference and signal fields is 0.3rad and 1rad.

The homodyne detection scheme can be used to control the Fabry-Perot cavity. Local oscillator can be added to the signal field in the transmission or reflection of the cavity, as shown in figure 2.2b. Assuming field reflectivities of input and output mirrors equal  $r_1$  and  $r_2$ , the reflected field can be written in the form

$$E_{refl} = E_{in} \frac{-r_1 + r_2 e^{2i\varphi}}{1 - r_1 r_2 e^{2i\varphi}} \quad (2.7)$$

This signal is shown in figure 2.2d and is quadratic around the cavity resonance. If phase shift between reference and signal fields is properly set, then linear response can be achieved using the homodyne detection scheme as shown in figure 2.2d.

The homodyne detection scheme uses reference and signal fields from the same origin and makes it more simple compared to the heterodyne scheme. However, an additional control loop should be set to control the phase shift between reference and signal fields. Locking Michelson or Fabry-Perot interferometers with DC offset from the dark fringe or cavity resonance can be achieved without phase control of reference field since in this case both fields follow the same path. However, DC offsets usually add technical problems such as backscattering from Michelson anti-symmetric port, alignment system degradation, and larger intensity noise coupling.

Another drawback of the homodyne detection scheme is the inability to control complex inteferometers with multiple degrees of freedom if only one carrier frequency is used. For this reason the homodyne scheme can only be used for one degree of freedom while others are controlled using heterodyne detection scheme.

### 2.1.1.2 Heterodyne detection

In heterodyne detection scheme, signal and reference fields are shifted in frequency, usually by 0.1MHz-1GHz. Laser beams follow the same path in the interferometer, and relative phase between signal and reference fields, and their magnitude is determined at every point of the optical path by the instrument parameters.

Optical heterodyne detection is achieved by phase modulation at frequency  $\Omega$  of the carrier light on the input to the interferometer. Waves propagate through the instrument and mix on the photodetector. Measured power is demodulated at  $n\Omega, n \in N$  to recover audio sidebands from the motion of the mirrors or frequency noise if  $n$  is odd and sideband power if  $n$  is even.

Electro-optical modulator (EOM) is commonly used to introduce phase modulation. The driver generates the electric field of required frequency  $\Omega$  and refraction index of the crystal changes due

to Pockels effect. Output beam consists of carrier light and sidebands shifted in frequency by  $\Omega$ :

$$E_{out}^{eom} = E_{in}^{eom} e^{i\Gamma \sin \Omega t} = E_{in}^{eom} \left( J_0(\Gamma) + \sum_{k=1}^{k=\infty} J_k(\Gamma) e^{ik\Omega t} + \sum_{k=1}^{k=\infty} (-1)^k J_k(\Gamma) e^{-ik\Omega t} \right) \quad (2.8)$$

Pound-Drever-Hall (PDH) technique uses first order RF sidebands to lock Fabry-Perot interferometer. In this scheme the carrier resonates in the cavity while sidebands are set far from resonance and play the role of local oscillator field on the photodetector:

$$\begin{aligned} E_{refl} &= E_{in} (J_0(\Gamma) r(\omega_0) + J_1(\Gamma) r(\omega_0 + \Omega) e^{i\Omega t} - J_1(\Gamma) r(\omega_0 - \Omega) e^{-i\Omega t} + (2\Omega - \text{terms})) \\ P_{refl} &= P_{refl}^{DC} + 2P_{in} J_0(\Gamma) J_1(\Gamma) (Im[S(\omega_0)] \sin \Omega t + Re[S(\omega_0)] \cos \Omega t) + (2\Omega - \text{terms}) \end{aligned} \quad (2.9)$$

where  $S(\omega_0) = r(\omega_0) r(\omega_0 + \Omega)^* - r(\omega_0)^* r(\omega_0 - \Omega)$ ,  $r(\omega)$  is the field reflectivity of the cavity depending on the frequency  $\omega$ , and  $P_{refl}^{DC}$  is DC power in reflected port.

Measured power  $P_{refl}$  is demodulated at frequency  $\Omega$ . Two quadratures I and Q contain  $Im[S(\Omega)]$  and  $Re[S(\Omega)]$ . For a single cavity the demodulation phase can be rotated to put the signal from mirror motion or laser frequency noise into one quadrature. Near carrier resonance, reflected power has the form:

$$P_{refl}(t) = P_{refl}^{DC} - 16P_{in} J_0(\Gamma) J_1(\Gamma) \frac{F}{\lambda} x(t) \sin \Omega t \quad (2.10)$$

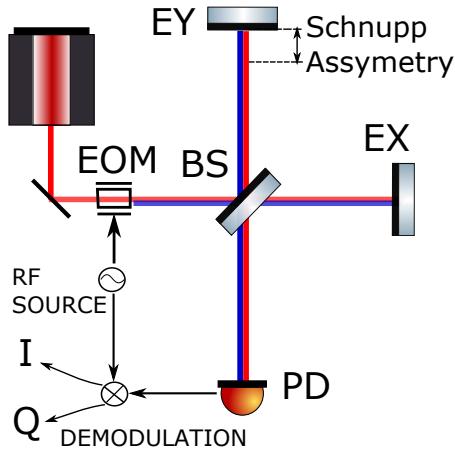
where  $F$  is finesse of the cavity and  $x(t)$  is the time dependent motion of the cavity or input frequency noise in units of cavity length.

After demodulation of  $P_{refl}$  at  $\Omega$ , motion of the cavity mirrors or frequency noise can be recovered. Achieved signal is linear only near carrier resonance. Cavity finesse  $F$  increases the slope of the error signal according to equation 2.10 but reduces the linewidth of the cavity  $\lambda/2F$ .

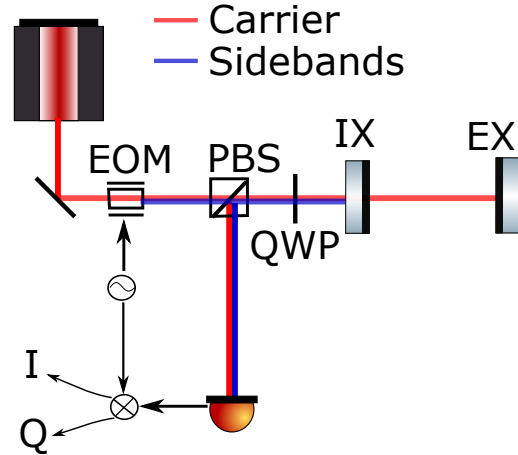
Far from carrier resonance the error signal is non-linear and at particular cavity phase shift sidebands start to resonate in the cavity while the carrier plays the role of local oscillator. Slope of the error signal in this case is the opposite of carrier resonance.

Figure 2.3d shows demodulated reflected power depending on cavity phase shift relative to the carrier. If macroscopic cavity length is set up such that carrier and sideband resonate at the same time, then reflected light will still be phase modulated and PDH signal will be zero. For this reason, cavity macroscopic length is usually set to avoid simultaneous carrier and sideband resonances to achieve conversion from phase to amplitude modulation in the cavity.

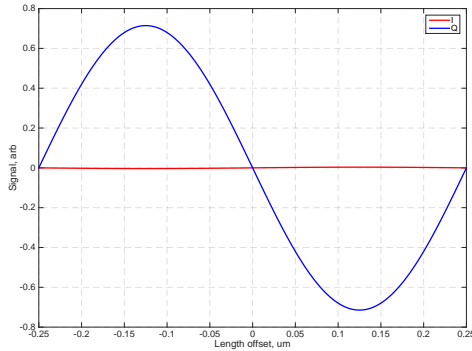
Similar conditions on macroscopic length are applied to Michelson interferometer. Arms should have asymmetry for control using PDH technique. In aLIGO, macroscopic length offset between two Michelson interferometer arms is called Schnupp asymmetry [39]. Using PDH signals the Michelson



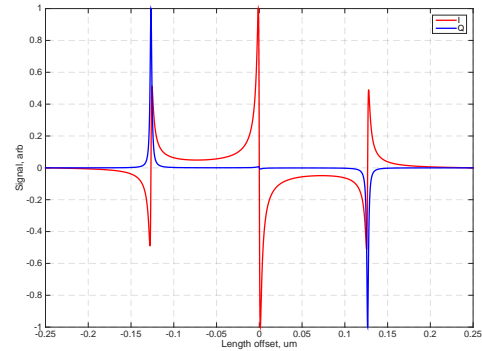
(a) Michelson interferometer.



(b) Fabry-Perot cavity.



(c) Demodulated PDH signal from Michelson anti-symmetric port.



(d) Demodulated PDH signal from Fabry-Perot reflected port.

Figure 2.3: Heterodyne detection scheme and error signals in Michelson and Fabry-Perot interferometers.

interferometer can be locked on the dark fringe without offsets. Sidebands leak to the anti-symmetric port due to Schnupp asymmetry and play the role of local oscillator during wave mixing on the photodetector.

The computation of PDH signals in symmetric or anti-symmetric ports of Michelson interferometer is similar to equation 2.9.  $r(\omega)$  plays a role of Michelson interferometer reflectivity or field leakage to anti-symmetric port. Figure 2.3c shows demodulated PDH signals in anti-symmetric ports of the Michelson interferometer.

### 2.1.1.3 Length dithering

If it is necessary to lock the interferometer without using the RF modulator, cavity length can be dithered at high audio frequency. In this case demodulated and low-passed transmitted power is

used for interferometer control. Near the resonance transmitted power can be written as

$$\begin{aligned} P_{tr} &= E_{tr}E_{tr}^* = P_{in} \left| \frac{t_1 t_2 e^{i\varphi}}{1 - r_1 r_2 e^{2i\varphi}} \right|^2 = P_{tr}^0 \left| \frac{1 + i\varphi - \varphi/2}{1 - 2F\varphi/\pi + 2F\varphi^2/\pi} \right|^2 \\ &= P_{tr}^0 \left( 1 - \left( \frac{2F}{\pi} \varphi \right)^2 \right) \end{aligned} \quad (2.11)$$

where  $P_{tr}^0$  is transmitted power when cavity is on resonance with zero detuning,  $F$  is cavity finesse, and  $\varphi$  is cavity detuning phase.

Cavity motion or laser frequency noise cause one way phase  $\varphi$  to change. If additional modulation is applied, one way trip phase is  $\varphi = \varphi_n + \varphi_{exc}^0 \sin(\omega_{exc}t)$ , where  $\varphi_n$  is one way phase due to mirror motion or frequency noise. Power fluctuations at the cavity transmission port are:

$$\Delta P_{tr} = P_{tr} - P_{tr}^0 = -\left(\frac{2F}{\pi} \varphi\right)^2 = -\frac{8F^2}{\pi^2} \varphi_n \varphi_{exc} \sin \omega_{exc} t + (DC - terms) + (2\omega_{exc} - terms) \quad (2.12)$$

Signal  $\Delta P_{tr}$  is demodulated at  $\omega_{exc}$  and low-passed. Achieved signal is linear in phase shift  $\varphi_n$ . The low-pass filter should have significant attenuation at frequency  $2\omega_{exc}$  and servo unity gain frequency is usually limited to  $(0.1 - 0.3)\omega_{exc}/2\pi$  in the case of dither locking.

#### 2.1.1.4 Phase locking

In complex interferometers with multiple degrees of freedom like aLIGO it is useful to introduce auxiliary lasers to control some of the cavities. The frequency of auxiliary lasers can be significantly shifted or doubled compared to the main laser such that auxiliary laser beams resonate only in particular cavities of the complex interferometer.

Figure 2.4 shows how the Fabry-Perot interferometer can be controlled using the auxiliary laser beam injected from the other side of the cavity relative to the main laser. The auxiliary laser is locked to the cavity using the PDH technique. The transmitted beam is mixed with the beam from the main laser and the relative phase between two beams is measured.

Error signal contains information about the difference in main laser frequency and cavity round trip phase. This signal can be used to actuate on the main laser frequency or cavity mirrors. Error signal is linear in cavity motion:

$$\begin{aligned} E_{beat} &= E_l + E_{cav} = E_l^0 e^{i\omega_0 t - \varphi_0} + E_{cav}^0 e^{i\omega_{cav} t - \varphi_{cav}} \\ P_{beat} &= 2E_l^0 E_{cav}^0 \cos((\omega_0 - \omega_{cav})t - (\varphi_0 - \varphi_{cav})) + (DC - term) \end{aligned} \quad (2.13)$$

where  $E_l$  - field from the main laser of frequency  $\omega_0$ ,  $E_{cav}$  - field coming out from the cavity with



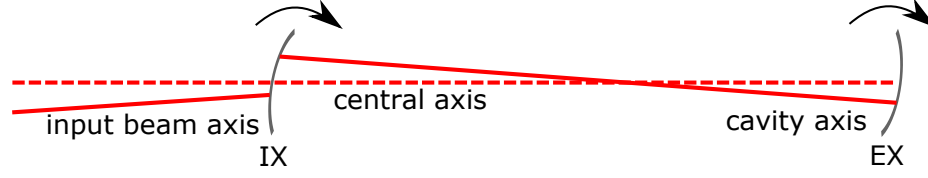


Figure 2.5: Cavity, input, and central axes of a misaligned Fabry-Perot cavity.

sidebands from a moving mirror. Any jitter, displacement, or tilt of the laser beam can be treated in first order as a pair of audio sidebands. The misaligned mirror couples fundamental TEM00 mode with TEM01 mode according to the matrix  $M_{refl}$ . These modes travel together through the interferometer according to the free space propagator [40, 41]

$$M_{refl}(\Theta) = \begin{pmatrix} 1 & -2i\Theta \\ -2i\Theta & 1 \end{pmatrix} \quad M_{free}(L) = \begin{pmatrix} e^{i\omega_0 L/c} & 0 \\ 0 & e^{i\omega_0 L/c+i\xi} \end{pmatrix} \quad (2.15)$$

where  $\Theta = \frac{\pi w(x)}{\lambda} \theta$ ,  $\theta$  is the mirror misalignment angle,  $w(z)$  is the beam size on the mirror,  $\xi$  is additional Gouy phase acquired by TEM01 mode while propagating through distance  $L$ .

#### 2.1.2.1 DC sensing

Two QPD sensors set in transmission of the Fabry-Perot cavities can measure angular motion of the cavity axis in angle and position as shown in figure 2.6. If the Gouy telescope is properly set and the round trip Gouy phase of the cavity is non-zero, then there exists a non-degenerate matrix that converts tilt and translation of the cavity axis to the beam position on QPDs:

$$\begin{pmatrix} y_1 \\ y_2 \end{pmatrix} = A \begin{pmatrix} x_2 \\ \alpha \end{pmatrix}, \det(A) \neq 0 \quad (2.16)$$

where  $y_1$  and  $y_2$  are beam positions on QPDs,  $\alpha$  is the angle between cavity axis and central axis,  $x_1$  and  $x_2$  is the beam positions on cavity mirrors.



Figure 2.6: Sensing of Fabry-Perot cavity axis motion using two QPDs in transmission.

The detection scheme that diagonalizes matrix  $A$  is known as near and far field sensing. Cavity

transmission beam is split in two, and the first beam goes directly into QPD. The second beam passes through the positive lens with focal length  $f$  and is sensed by the second QPD located at the focus of the lens. If the distance between ETM and the first QPD and positive lens can be neglected, then first QPD senses the position of the beam, and second one senses angle:

$$A = \begin{pmatrix} 1 & 0 \\ 0 & f \end{pmatrix} \quad (2.17)$$

This scheme has a disadvantage of the small beam size on the second QPD. Instead, telescope is set to separate Gouy phases at two QPDs by  $90^\circ$  and achieve beam sizes of  $\sim 1mm$  on both detectors. Each of two QPDs sense position and angle of the cavity axis but with different coefficients. Matrix  $A$  is non-diagonal but also non-degenerate and can be inverted to reconstruct beam position and angle on ETM.

Beam positions  $x_1$  and  $x_2$  on cavity mirrors ITM and ETMS as well as tilt of the cavity axis  $\alpha$  depend on misalignment of ITM  $\alpha_1$  and ETM  $\alpha_2$  according to equations:

$$\begin{pmatrix} \alpha \\ x_1/R_1 \\ x_2/R_2 \end{pmatrix} = \frac{1}{R_1 + R_2 - L} \begin{pmatrix} R_1 & R_2 \\ R_2 - L & R_2 \\ R_1 & R_1 - L \end{pmatrix} \begin{pmatrix} \alpha_1 \\ \alpha_2 \end{pmatrix} \quad (2.18)$$

Using equations 2.16, 2.18 it is possible to convert QPD signal to the basis of mirror angles  $\alpha_1$ ,  $\alpha_2$  or cavity axis tilt and beam displacement  $\alpha$  and  $x_2$ . QPD servos suppress fluctuations of the cavity axis but input and cavity axis might not be coalined since QPDs set in arm transmission are not sensitive to the input beam. An alternative scheme involves RF sidebands and measured relative input and cavity axes motion.

### 2.1.2.2 RF sensing

RF sidebands with frequency offset from carrier equal to  $\Omega$  are generated using EOM and propagate together with carrier through the input beam axis and reflect back without resonating in the cavity. The carrier field resonates and the reflected beam propagates along the cavity axis as shown in figure 2.7. According to equations 2.15, the carrier field reflected from the cavity can be written as sum of the TEM00 and TEM01 modes propagating along the input beam axis together with the sideband TEM00 mode. Relative alignment of input beam and cavity axis is derived from the beat of sidebands against carrier on the QPD:

$$S \sim \int_0^{x_0} \int_0^{y_0} |E_{00}^+ + E_{00}^- + E_{00}^0 + E_{01}^0|^2 dx dy \quad (2.19)$$

where  $S$  is signal from one quadrant integrated over the quadrant area  $(0, x_0) \times (0, y_0)$ ,  $E_{00}^+$  and

$E_{00}^-$  are TEM00 modes of sidebands, and  $E_{00}^0$  and  $E_{01}^0$  are TEM00 and TEM01 modes of carrier.

Since the integral involving TEM00 modes of carrier and sidebands is suppressed by longitudinal servo, total integral from sidebands and carrier TEM00 modes gives zero. For this reason, in the first order approximation alignment signals are not sensitive to DC centering of the beam on QPD.

After integrating terms involving sideband TEM00 modes and carrier TEM01 and combining four QPD signals  $S_j, j = 1, 2, 3, 4$  in pitch and yaw degrees of freedom, signals detected by wave front sensors can be written as [42]:

$$S_i^{wfs} = \sum_{j=1,2} A_{ij} \theta_j \cos(\eta_i - \eta_{ij}) \cos(\Omega t - \psi_{ij}) \quad (2.20)$$

where  $S_i^{wfs}, i = 1, 2$  are the signal from first and second WFS,  $\theta_j, j = 1, 2$  are misalignment angles of cavity axis relative to input beam,  $A_{ij}$  is optical transfer matrix from misaligned mirrors to WFS,  $\eta_i$  is Gouy phase shift between the detection port and WFS,  $\eta_{ij}$  is the intrinsic Gouy phase shift of the signal,  $\psi_{ij}$  is the intrinsic rf phase shift of the signal.

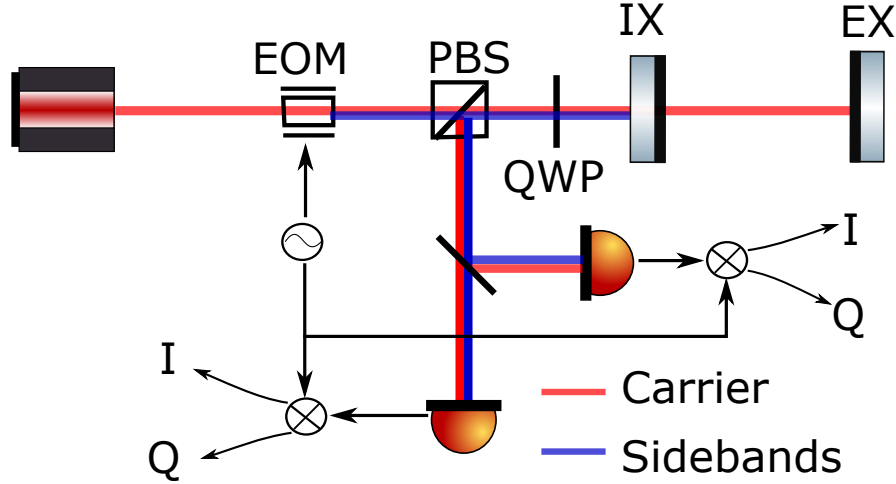


Figure 2.7: Fabry-Perot cavity alignment scheme using RF sensors.

WFS signals 2.20 are demodulated using the RF local oscillator with frequency  $\Omega$  and misalignment angles  $\theta_j$  can be recovered. Input beam or cavity axis are controlled to reduce TEM01 of the carrier light at the reflection port.

If the cavity is locked on sidebands, then the carrier is used as a local oscillator and sidebands contain information about the cavity axis. Equations 2.19 and 2.20 can be rewritten for this case and misalignment angles derived from WFS signals.

### 2.1.2.3 Angle dithering

This alignment technique does not require RF sidebands and can align the input beam axis relative to the cavity axis. Two mirrors with Gouy phase separation are dithered in angle to recover relative axis position and angle:

$$\frac{\Delta P}{P_{tr}^0} \approx -\frac{\theta^2}{\theta_0} = -2\frac{\theta_w}{\theta_0}\frac{\theta_{exc}}{\theta_0}\sin\omega_{exc}t + \frac{\theta_w^2}{\theta_0^2} + \frac{\theta_{exc}^2}{\theta_0^2}\frac{1 - \cos 2\omega_{exc}t}{2} \quad (2.21)$$

where  $\theta_0$  is cavity divergence angle,  $\theta_w$  is waist tilt due to angular fluctuation, and  $\theta_{exc}$  is waist tilt due to excitation.

Cavity transmitted power is demodulated at frequency  $\omega_{exc}$  and low-passed to remove  $2\omega_{exc}$  components. The resultant signal is proportional to  $\frac{\theta_w}{\theta_0}\frac{\theta_{exc}}{\theta_0}$  and is used as an error signal to the alignment servos.

### 2.1.3 Mode matching

TEM00 mode of the input beam should be matched to the cavity eigen mode to achieve maximum power build up and reduce higher order Laguerre-Gaussian modes in the reflection port. For mode matching calculations it is convenient to use  $q$ -parameter determined by the beam radius of curvature  $R$  and size  $w$ :

$$\frac{1}{q} = \frac{1}{R} - \frac{i\lambda}{\pi w^2} \quad (2.22)$$

$q$ -parameter is convenient to use in calculations because it propagates according to ABCD matrices [35]:

$$q_2 = \frac{Aq_1 + B}{Cq_1 + D} \quad (2.23)$$

During free space propagation over distance  $l$   $q$ -parameter evolves as  $q_2 = q_1 + l$ . In the case of beam reflection from the mirror with radius of curvature  $R_m$  changes  $q$ -parameter according to equation  $q_2 = (\frac{-2}{R_m}q_1 + 1)^{-1}$ .

For a Fabry-Perot cavity of length  $L$  and mirrors of radii of curvature  $R_1$  and  $R_2$  waist location and size  $w_0$  is determined by setting beam and mirror radii of curvature equal at the location of the mirror. Beam sizes  $w_1$  and  $w_2$  on the mirrors are derived from imaginary part of the  $q$ -parameters:

$$\begin{aligned} \operatorname{Re} \left[ \frac{1}{iz_0 + l_1} \right] &= \frac{1}{R_1} & \operatorname{Im} \left[ \frac{1}{iz_0 + l_1} \right] &= \frac{\lambda}{\pi w_1^2} \\ \operatorname{Re} \left[ \frac{1}{iz_0 + l_2} \right] &= \frac{1}{R_2} & \operatorname{Im} \left[ \frac{1}{iz_0 + l_2} \right] &= \frac{\lambda}{\pi w_2^2} \end{aligned} \quad (2.24)$$

where  $l_1$  and  $l_2$  are distances from the cavity mirrors to the waist location,  $l_1 + l_2 = L$ ,  $z_0 = \frac{\pi w_0^2}{\lambda}$  is the Rayleigh range.

Equations 2.24 are solved relative to the waist size  $w_0$  and location  $l_1, l_2$ . Beam sizes  $w_1$  and  $w_2$  on the mirrors can also be found:

$$\begin{aligned} l_1 &= L \frac{L - R_2}{2L - R_1 - R_2} & l_2 &= L \frac{L - R_1}{2L - R_1 - R_2} \\ w_0 &= \left( \frac{\lambda}{\pi} ((R - l_1)l_1)^{1/2} \right)^{1/2} = \left( \frac{\lambda}{\pi} ((R - l_2)l_2)^{1/2} \right)^{1/2} \\ w_1 &= \left( \frac{\lambda}{\pi} \left( 1 + \frac{l_1^2 \lambda}{\pi w_0^2} \right) \right)^{1/2} & w_2 &= \left( \frac{\lambda}{\pi} \left( 1 + \frac{l_2^2 \lambda}{\pi w_0^2} \right) \right)^{1/2} \end{aligned} \quad (2.25)$$

Waist size and location of the input beam should be matched to waist size and location of the intracavity beam for perfect mode matching. In general case mode matching  $0 \leq K \leq 1$  between two beams with  $q$ -parameters  $q_1$  and  $q_2$  can be written as:

$$K = \frac{4Im[q_1]Im[q_2]}{|q_1^* - q_2|^2} \quad (2.26)$$

Cavity input beam passes through the optical telescope in order to achieve perfect mode matching  $K = 1$ . Adjustment of position and focal length of lenses is usually an iterative procedure. Various computer programs are available, such as Alamode [43], for mode matching solutions. In complex interferometers all cavities should be matched between each other and the input beam.

## 2.2 aLIGO optical design

aLIGO interferometers were designed to achieve optimal sensitivity and minimize noise couplings to the gravitational wave channel. Compared to initial LIGO a number of mechanical upgrades were developed to improve displacement noises [44], including:

- The active seismic isolation system replaced passive stacks to reduce seismic motion in the frequency band above 0.1 Hz as discussed in section 7.1.3.
- Multiple-stage suspensions are used instead of single stage suspensions to improve passive seismic isolation at frequencies above 1Hz. Four isolation stages of test masses made it possible to increase the gravitational wave band from 40Hz-5kHz up to 10Hz-5kHz.
- Suspension thermal noise was improved by more than two orders of magnitude. Test masses are suspended using fused silica fibers instead of metal wires as discussed in section 7.1.2.

- Optical coatings and mirror substrates were manufactured with smaller surface roughness and optical losses.
- Masses of the mirrors increased up to 40kg to reduce quantum radiation pressure noise and suspension thermal noise.

Optical configuration of advanced interferometers was optimized to reduce coating Brownian noise and quantum noises:

- Beam size on the test masses was increased by a factor of 1.5 to reduce coating Brownian noise, as discussed in section 7.1.2.
- Maximum input power of Nd:YAG 1064nm laser was increased from 25W up to 125W to reduce shot noise level.
- Signal recycling cavity was introduced to increase DARM pole up to 400Hz and have an ability to shape quantum noise by detuning the cavity.

This section describes the optical design of aLIGO and shows quantum noise in various configurations to justify the choice of the dual recycled Fabry-Perot Michelson interferometer as a gravitational wave detector.

### 2.2.1 Michelson interferometer

A simple Michelson interferometer consists of a beam splitter and two end mirrors, as shown in figure 2.8a. Differential distance between two arms is derived from the phase measurement at the antisymmetric port.

Quantum radiation pressure and shot noises can be computed by propagating creation and annihilation operators of the input fields to the interferometer shoulders and output port [45]. The interferometer input state is pure:

$$|\psi\rangle = D_1(\alpha) |0\rangle_1 |0\rangle_2 = e^{\alpha a_1^\dagger / 2} e^{\alpha a_1^\dagger} e^{-\alpha^* a_1} |0\rangle_1 |0\rangle_2 \quad (2.27)$$

where subscript 1 denotes symmetric port, subscript 2 denotes antisymmetric port. The state of the input field from the symmetric port is coherent and generated using displacement operator  $D(\alpha)$ . Parameter  $\alpha$  is determined by the laser port, and mean value of the number operator  $a_1^\dagger a_1$  is  $\alpha\alpha^*$ . Since no laser light is injected from interferometer antisymmetric port, the electromagnetic field is in vacuum state and mean value of the number operator  $a_2^\dagger a_2$  is zero.

The beam splitter creates correlations between the states of electromagnetic radiation from symmetric and antisymmetric ports. It is convenient to consider the problem in the Heisenberg picture

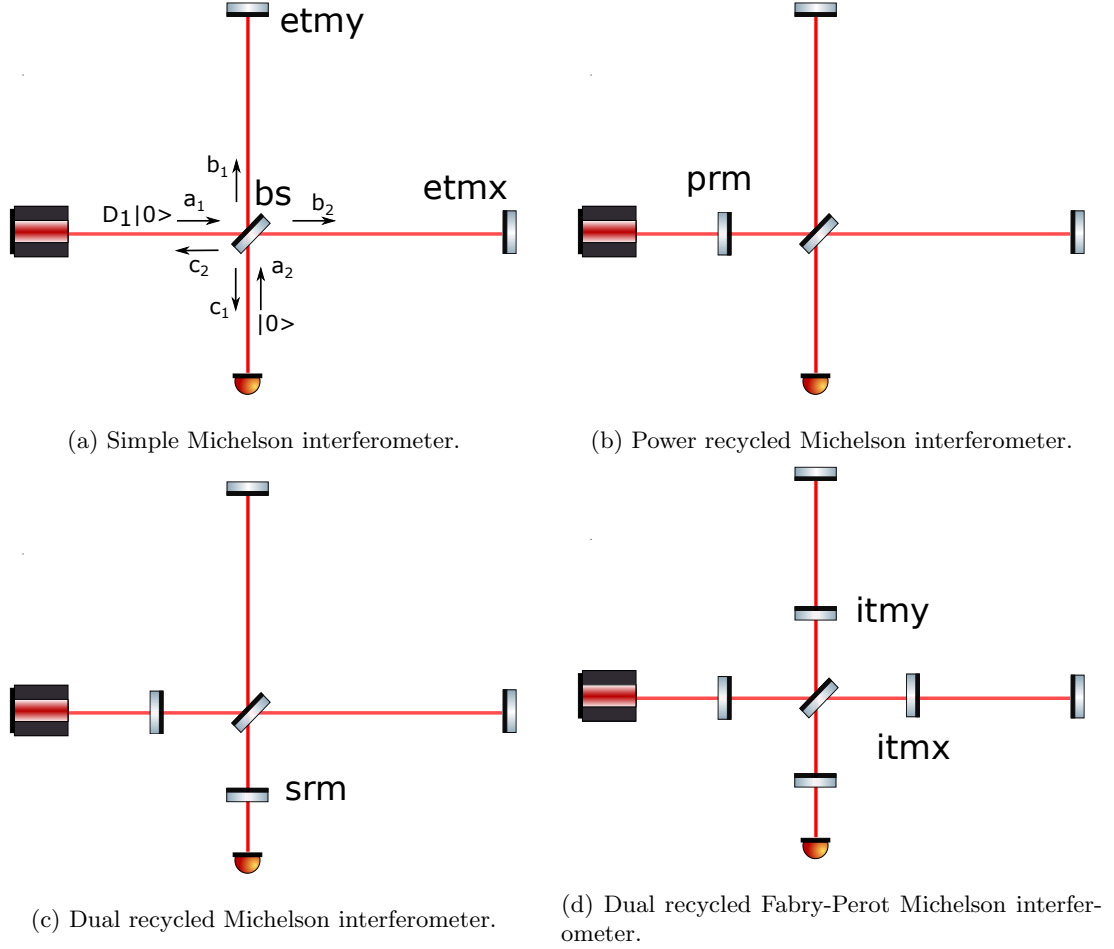


Figure 2.8: Optical configurations for gravitational wave detection.

and propagate operators rather than states of electromagnetic radiation. Annihilation operators propagate similarly to electric fields and in case of very thin beam splitter can be written as

$$b_1 = \frac{1}{\sqrt{2}}(a_1 + a_2) \quad b_2 = \frac{1}{\sqrt{2}}(a_1 - a_2) \quad (2.28)$$

Differential momentum  $p_q$  acquired by the end mirrors due to quantum radiation pressure is determined by the difference in the number of photons in the two arms of the Michelson interferometer:

$$p_q = \frac{2h\nu}{c}(b_1^\dagger b_1 - b_2^\dagger b_2) = \frac{2h\nu}{c}(a_1^\dagger a_2 + a_2^\dagger a_1) \quad (2.29)$$

$$p_q^2 = \left(\frac{2h\nu}{c}\right)^2 (a_1^\dagger a_2 a_1^\dagger a_2 + a_1^\dagger a_2 a_2^\dagger a_1 + a_2^\dagger a_1 a_1^\dagger a_2 + a_2^\dagger a_1 a_2^\dagger a_1)$$

Since  $a_1$  and  $a_2$  commute and  $\langle 0|a_2|0\rangle = 0$  and  $\langle 0|a_2^\dagger|0\rangle = 0$ , then the mean value of operator  $p_q$  is zero. First, third, and fourth components in the sum  $p_q^2$  are also zeros since  $\langle 0|a_2 a_2|0\rangle =$

0,  $\langle 0|a_2^+a_2|0\rangle = 0$ ,  $\langle 0|a_2^+a_2^+|0\rangle = 0$ . At the same time second component is non-zero since  $\langle 0|a_2a_2^+|0\rangle = 1$ . This component leads to quantum radiation pressure noise of variance:

$$\langle p_q^2 \rangle = \left( \frac{2h\nu}{c} \right)^2 \langle 0|D_1^*(\alpha)a_1^+a_1D_1(\alpha)|0\rangle = \left( \frac{2h\nu}{c} \right)^2 \alpha^* \alpha \quad (2.30)$$

The number of input photons obeys Poissonian statistics and the power spectrum of differential impulse  $p_q$  is white. Power spectrum density of differential force  $S[F]$  applied to end mirrors can be computed according to Parseval theorem:

$$\frac{\langle p_q^2 \rangle}{\Delta t^2} = \int_0^{f_s/2} S[F](f)df = S[F](f) \frac{f_s}{2} \quad (2.31)$$

where  $f_s = 1/\Delta t$  - sampling frequency of the measurement.

Since  $\alpha^* \alpha$  is the mean number of photons in the input laser beam of power  $P_0[W]$  then

$$\alpha^* \alpha = \frac{P_0 \Delta t}{h\nu} = \frac{P}{h\nu f_s} \quad (2.32)$$

Power spectral density of differential force on end mirrors and differential displacement are given by equations:

$$\begin{aligned} S[F] &= \frac{8h\nu P}{c^2} \\ l_{qrp}(f) &= \sqrt{\frac{8h\nu}{Mc^2}} \frac{1}{(2\pi f)^2} \left[ \frac{m}{\sqrt{Hz}} \right] \end{aligned} \quad (2.33)$$

where  $M$  is mass of the end mirrors. The second equation assumes that mirrors are free masses and that the equation of motion is  $M\ddot{x}(t) = F(t)$ . This leads to the condition  $f \gg f_0$ , where  $f_0$  is eigen frequency of suspension. The equation for differential displacement  $l_{qrp}(f)$  also assumes that the mass of the beam splitter is much larger compared to the mass of the end mirrors and quantum radiation pressure noise does not couple through the beam splitter. For  $M = 40kg$  quantum radiation pressure noise is

$$l_{qrp}(f) = 2.88 \cdot 10^{-20} \sqrt{\frac{P_0}{125W}} \frac{1}{f^2} \left[ \frac{m}{\sqrt{Hz}} \right] \quad (2.34)$$

Sensing noise comes from fluctuations of the number of photons at antisymmetric port of Michelson interferometer. Assuming full reflectivity of end mirrors, annihilation operator  $c_1$  is determined by equation:

$$c_2 = (i\sin\varphi a_1 + \cos\varphi a_2) e^{i(\varphi_x + \varphi_y)} \quad (2.35)$$

where  $\varphi_x$  and  $\varphi_y$  are phases acquired by the laser beam during one way propagation along the  $x$  and  $y$  shoulders,  $\varphi = \varphi_y - \varphi_x$ .

Mean number and variance of photons arriving to antisymmetric port are computed using the number operator:

$$\begin{aligned}
c_2^+ c_2 &= \sin^2 \varphi a_1^+ a_1 + \cos^2 \varphi a_2^+ a_2 + i \sin \varphi \cos \varphi (a_2^+ a_1 - a_1^+ a_2) \\
\langle (c_2^+ c_2)^2 \rangle &= \sin^4 \varphi a_1^+ a_1 a_1^+ a_1 + \sin^2 \varphi \cos^2 \varphi a_1^+ a_1 a_2^+ a_2 + \\
&\quad \cos^4 \varphi a_2^+ a_2 a_2^+ a_2 + \sin^2 \varphi \cos^2 \varphi a_2^+ a_2 a_1^+ a_1 + \\
&\quad i \sin \varphi \cos^3 \varphi (a_1^+ a_1 + a_2^+ a_2) (a_2^+ a_1 - a_1^+ a_2) + i \sin^3 \varphi \cos \varphi (a_2^+ a_1 - a_1^+ a_2) a_1^+ a_1 + \\
&\quad i \sin \varphi \cos^3 \varphi (a_2^+ a_1 - a_1^+ a_2) a_2^+ a_2 - \sin^2 \varphi \cos^2 \varphi (a_2^+ a_1 - a_1^+ a_2)^2
\end{aligned} \tag{2.36}$$

Computations of mean values of  $c_2^+ c_2$  and  $(c_2^+ c_2)^2$  are similar to the ones done to evaluate mean value of  $p_q^2$ :

$$\begin{aligned}
\langle c_2^+ c_2 \rangle &= \sin^2 \varphi \langle 0 | D_1^*(\alpha) a_1^+ a_1 D_1(\alpha) | 0 \rangle = \sin^2 \varphi \alpha^* \alpha \\
\langle (c_2^+ c_2)^2 \rangle &= \sin^4 \varphi \langle 0 | D_1^*(\alpha) a_1^+ a_1 a_1^+ a_1 D_1(\alpha) | 0 \rangle + \sin^2 \varphi \cos^2 \varphi \langle 0 | D_1^*(\alpha) a_1^+ a_1 D_1(\alpha) | 0 \rangle = \\
&\quad \sin^4 \varphi \alpha^* \alpha (1 + \alpha^* \alpha) + \sin^2 \varphi \cos^2 \varphi \alpha^* \alpha = \\
&\quad \sin^4 \varphi (\alpha^* \alpha)^2 + \sin^2 \varphi (\sin^2 \varphi + \cos^2 \varphi) \alpha^* \alpha
\end{aligned} \tag{2.37}$$

The last equation uses commutation rule:  $a_1 a_1^+ = 1 + a_1^+ a_1$ . The variance of number of photon at interferometer antisymmetric port equals  $\sin^2 \varphi (\sin^2 \varphi + \cos^2 \varphi) \alpha^* \alpha$ . The first component comes from the laser and the second one from correlations of electromagnetic fields from symmetric and antisymmetric input ports.

The number of photons measured at antisymmetric port obeys Poisson distribution and the shot noise is white. The power spectrum density of relative power fluctuation  $S[P]$  at antisymmetric port can be computed using the Parseval theorem:

$$\frac{\langle (c_2^+ c_2)^2 \rangle - \langle c_2^+ c_2 \rangle^2}{\langle c_2^+ c_2 \rangle^2} = \frac{1}{\sin^2 \varphi \alpha^* \alpha} = \int_0^{f_s/2} S[P](f) df = S[P] \frac{f_s}{2} \tag{2.38}$$

Using equation 2.32 for mean number of photons  $\alpha^* \alpha$ , the power spectral density of relative intensity fluctuation at antisymmetric port is

$$S[P] = \frac{2h\nu}{P_0 \sin^2 \varphi} = \frac{2h\nu}{P_{as}} \tag{2.39}$$

where  $P_{as} = P_{in} \sin^2 \varphi$  is DC power at antisymmetric port. Since fluctuations in power  $P_{as}$

are related to fluctuation of differential phase  $\varphi$  according to equation  $\delta P_{as} = 2P_0 \sin\varphi \cos\varphi \delta\varphi$ , longitudinal noise can be written as

$$l_{shot} = \lambda \frac{\varphi_{shot}}{2\pi} = \frac{\lambda}{2\pi \cos\varphi} \sqrt{\frac{h\nu}{2P_0}} \quad (2.40)$$

If the Michelson interferometer operates with small DC fringe offset, then shot noise level computed in units of  $m/\sqrt{Hz}$  is

$$l_{shot} = 4.34 \cdot 10^{-18} \sqrt{\frac{125W}{P_0}} \left[ \frac{m}{\sqrt{Hz}} \right] \quad (2.41)$$

Equations 2.34 and 2.41 show that shot noise level is several orders of magnitude above quantum radiation pressure noise in the frequency range 10Hz - 5kHz. In the Michelson interferometer with small DC fringe offset most power goes to the symmetric port and the amount of power lost in the interferometer equals

$$P_{loss} = 2L_a P_0 \ll P_0 \quad (2.42)$$

where  $L_a$  is loss inside each interferometer arm. Power in the arm cavities can be increased to improve shot noise level. Maximum power that can be accumulated inside interferometer arms is determined by the law of energy conservation:

$$P_{arm} \approx \frac{P_0}{2L_a} \quad (2.43)$$

Power in the interferometer arms can be increased by introducing an additional mirror at the symmetric port and/or Fabry-Perot cavities in each interferometer shoulder [46].

### 2.2.2 Power recycled Michelson interferometer

The additional mirror in the reflected port together with the simple Michelson interferometer shown in figure 2.8b forms a power recycling cavity. Intracavity power is maximized by choosing transmission of the power recycling mirror to minimize reflected power. Optimal transmission of power recycling mirror should be equal to the total loss in the arm cavities

$$T = L_{total} \quad (2.44)$$

Transmission of the end mirrors is also considered as optical loss and should also be set to zero in order to optimize power in the interferometer arms. Assuming loss per optic surface  $L_0 = 37.5ppm$ , optimal PRM transmission should be  $T_{prm} = 150ppm$ . If input power is 125W then optical power incident on BS is 0.4MW and large thermal lens is created in the optic substrate.

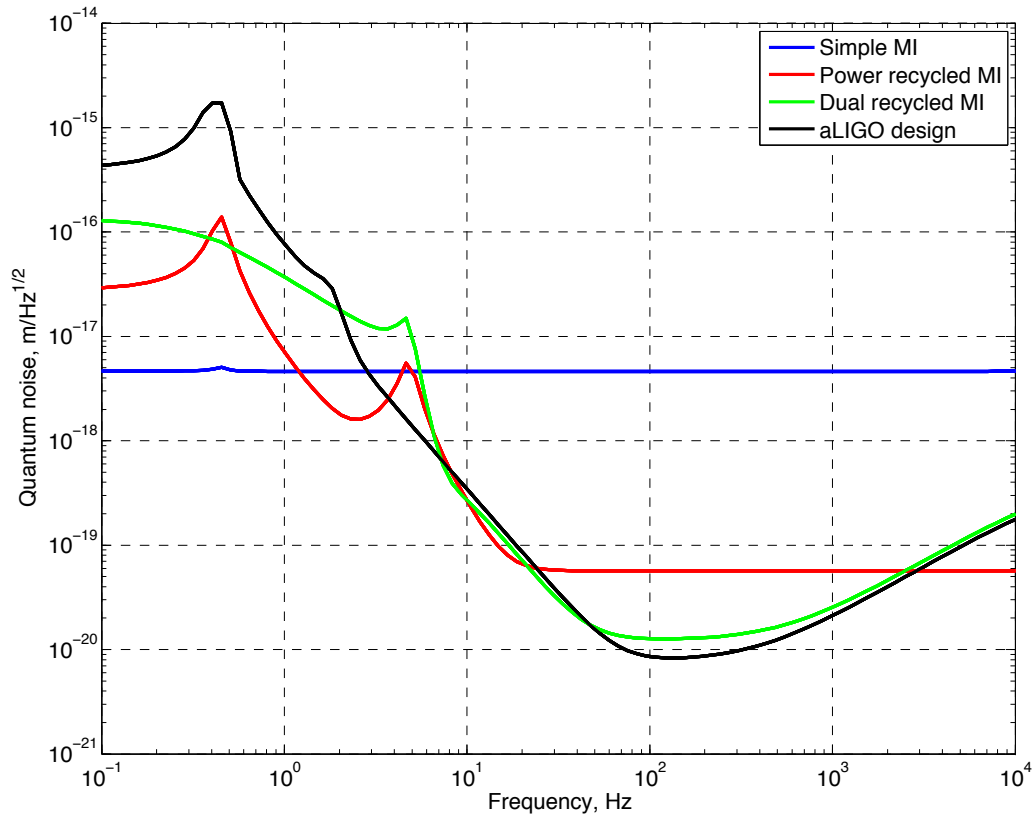


Figure 2.9: Quantum noise coupling to gravitational wave channel in different optical configurations when interferometer input power is 125W.

For power recycled Michelson interferometer quantum noise is computed using Optickle software [36] and shown in figure 2.9. This design outperforms the simple Michelson interferometer by 2 orders of magnitude at frequencies above 10Hz.

The differential arm pole in this configuration is still 37.5kHz for 4km interferometer arms. An additional mirror in the antisymmetric port can reduce DARM pole and improve sensitivity in the frequency band 10-5000Hz.

### 2.2.3 Dual recycled Michelson interferometer

Signal recycling mirror together with the end test mirrors forms a signal recycling cavity, shown in figure 2.8c. Once carrier resonates in the cavity, DARM pole is reduced proportional to the cavity finesse. In order to optimize interferometer response to gravitational waves in the frequency range 10Hz - 5kHz, the DARM pole should be reduced to a few hundred Hertz. If SRM transmission is set to  $T_{sr} = 0.17$ , then DARM coupled-cavity pole is reduced from 37.5kHz down to 400Hz. Figure 2.9 shows quantum noise coupling to DARM in DRMI configuration.

DRMI quantum noise is lower by factor of 5 in the frequency range 50Hz-500Hz compared to

PRMI configuration. Major disadvantages of these configurations are:

- High optical power on BS causes significant thermal lens and thermo refractive noise. If input power is 125W than power on BS is 0.4MW. Half of this power is transmitted through the beam splitter and heats the substrate due to absorption, creating a large thermal lens.
- The power recycling cavity is critically coupled if PRM transmission equals the loss in the cavity. This implies that total interferometer loss is doubled due to PRM transmission. Power in the arms is a factor of 2 less than optimal, determined by equation 2.43.
- Since BS is set  $45^\circ$  relative to the beam, the effective cross section is  $\sqrt{2}$  less than optic size. This means that BS should be manufactured bigger than other optics to avoid large geometrical losses.

These problems can be solved by introducing Fabry-Perot cavities in the arms. These cavities help to significantly reduce power on BS, avoid large optical power passing through mirror substrate and increase power in the arm cavities by factor of 2.

#### 2.2.4 Dual recycled Fabry Perot Michelson interferometer

This configuration is shown in figure 2.8d and used by advanced LIGO for gravitational wave detection. It takes advantage of couple cavities and consists of five major segments:

- Simple Michelson interferometer splits light between two arms
- Two Fabry-Perot arm cavities are set to measure differential motion of test masses
- Power recycling cavity increases power circulating inside interferometer to improve sensing noise
- Signal recycling cavity is anti-resonant to carrier and shifts DARM pole from 40Hz up to 400Hz to improve broadband sensitivity to gravitational waves.

Product of power build ups in the arm cavities  $G_{arm}$  and power recycling cavity  $G_{prc}$  is determined by the total loss in the arm cavities:

$$G_{arm} \cdot G_{prc} = 1/2L_a \quad (2.45)$$

This equation sets first condition on transmission of ITMs and PRM. Second condition comes from noise considerations. Higher arm finesse filters more MICH noise as discussed in chapter 9, reduces power on BS, and makes optical losses in power recycling cavity less significant for carrier

build-up in the arms. Higher power recycling gain  $G_{prc}$  improves filtering of input beam jitter, laser intensity, and frequency noises and reduces sensing noises for PRCL, SRCL, and MICH control.

In aLIGO configuration round trip optical losses in the arm cavities are predicted to be 50ppm according to coating quality of the test masses. Power transmission of PRM and ITM mirrors are set to 0.03 and 0.0148. Resultant power recycling gain is 60 and total power on BS is 7.5kW when input power to interferometer is 125W. Power build-up in the arm cavities is  $G_{arm} = 260$ . Total optical power resonating in the arms is 0.8MW when interferometer input power is 125W.

Since the arm cavity pole in this configuration equals to 40Hz, signal recycling cavity is set antiresonant for carrier light. This configuration increases DARM pole up to 400Hz. SRM transmission is set to  $T_{srms} = 0.3688$ . Figure 2.9 shows coupling of quantum noise to gravitational wave channel in aLIGO configuration. Sensitivity has improved compared to optical configurations considered in this section in the frequency range 30Hz-3kHz.

aLIGO optical configuration has 4 auxiliary degrees of freedom and the process of lock acquisition becomes complicated. Chapter 3 describes the sequence of transitioning aLIGO interferometers from the uncontrolled free swinging state to the linear regime.

## Chapter 3

# Lock acquisition and longitudinal control

Interferometer mirrors swing longitudinally by  $\sim 1\mu\text{m}$  due to seismic motion. In these conditions light can not stably resonate in the optical cavities since their linewidth is much smaller compared to the ground motion. Instead, cavities randomly flash when resonance conditions are satisfied. The task of the longitudinal control system is to transition the interferometer from the free swinging state to the linear regime when light resonates in the optical cavities and search for gravitational waves becomes possible.

One possible way to acquire interferometer lock is to enable the longitudinal control system when light flashes in the optical cavities and error signals are linear during this short period of time. This approach was successfully used in initial LIGO [47, 48]. First, power recycling cavity and Michelson interferometer were locked on sidebands and then each arm was brought on resonance in series.

The main advantage of iLIGO locking scheme is short lock acquisition time. It took less than a minute to wait for a proper flash and bring the interferometer into the linear regime. One possible drawback of this technique came from the fact that 1f PDH signals were used for PRC control. When the second arm is brought on resonance, carrier field reflectivity from the arms changes sign. At that time sidebands and carrier start to resonate simultaneously in the PRC, and the sensing matrix gets a singularity. The sensing matrix of interferometer control was inverted on the fly, and for a short period of time power recycling cavity was not controlled due to singularity.

Application of iLIGO locking scheme to aLIGO configuration becomes more complicated since aLIGO interferometers have signal recycling cavity, and singularity in the sensing matrix would occur for PRC and SRC control when carrier power builds up in the arm cavities. For this reason, DRMI is controlled using 3f PDH signals [49] during lock acquisition. These signals are much less sensitive to carrier build-up in the arm cavities, and singularity in the sensing matrix does not occur.

After being tested in TAMA [50], the 3f PDH technique was also used in the Virgo to control the power recycling cavity during lock acquisition sequence [51]. It was also found difficult to catch the

lock of the arm cavities using iLIGO scheme since it was not possible to measure the optical sensing matrix before lock was acquired, and 0.6Hz pendulum resonance of Virgo multi-stage suspension got easily excited during locking transients. For this reason, variable finesse technique was developed to bring the interferometer into full lock adiabatically and to avoid locking transients [52].

In case of aLIGO configuration it would also be difficult to catch arm resonances using iLIGO technique since bottom and penultimate actuators of aLIGO quadruple suspensions have a range of only  $\sim 400nm$  at DC. Actuator range was optimized to reduce electronics and magnetic noise injections to gravitational wave in the frequency range 10-100Hz. Application of the variable finesse technique to aLIGO interferometers becomes more difficult compared to the initial VIRGO since light leaving the interferometer through the antisymmetric port will be partially reflected back by the signal recycling mirror. For this reason, the auxiliary length control technique was developed and tested [53, 54, 55] to bring arm cavities on resonance without transients.

Even though lock acquisition sequence for advanced LIGO was well planned and simulated in case of perfect mode matching, contrast defect, mirrors and photodiodes, it was not clear how this sequence will work out on practice in the presence of imperfections in the instrument, noise level of ALS system, angular motion of the test masses and finite range of actuators. These problems are discussed in the first part of the thesis devoted to control of the instrument.

This chapter describes performance of longitudinal control system set in LIGO observatories for lock acquisition. Section 1 describes control of arm cavities using ALS and noise level of this system. Section 2 is devoted to DRMI locking using 1f PDH technique and transition to 3f signals. Section 3 describes interferometer control during CARM offset reduction. Section 4 gives an overview of longitudinal control to keep the interferometer in its operating point.

### 3.1 Arm length stabilization

During the first step of the lock acquisition sequence, longitudinal motion of arm cavities relative to the laser wavelength is stabilized using ALS system. Two laser beams are injected into the arm cavities from the X- and Y- end stations, resonate in the cavities, and beat against each other and the main laser beam, as shown in figure 3.1. Error signals for common and differential arm control are derived from demodulated beat note signals.

In more details, ALS system consists of the following parts:

- 1064 nm Nd:YAG auxiliary lasers are set in the X- and Y- end stations. The frequencies of these lasers are stabilized using phase locked loops. Light from the main laser is shifted by plus and minus 80MHz for X- and Y-arms and transmitted to the end stations via optical fibers. Light coming out of the fibers at the end stations beats against laser beams from auxiliary

lasers. Photodetector signals go to phase frequency discriminators. Output signals are used to control phase of auxiliary lasers with bandwidth of 40kHz.

- Second harmonic generators double frequencies of auxiliary laser beams at the end stations and pick-off beam from the main laser beam. 1064nm IR light is upconverted to 532 green light. This process is done to achieve a different transmission of test masses and power recycling cavity mirrors for the main IR beam and upconverted auxiliary green beams.
- PDH servos at both end stations are used to lock auxiliary lasers to free swinging arm cavities by actuating at the error point of PLL loops with bandwidth of 10kHz. Frequency of the transmitted green light is determined by the longitudinal motion of the arm cavities.

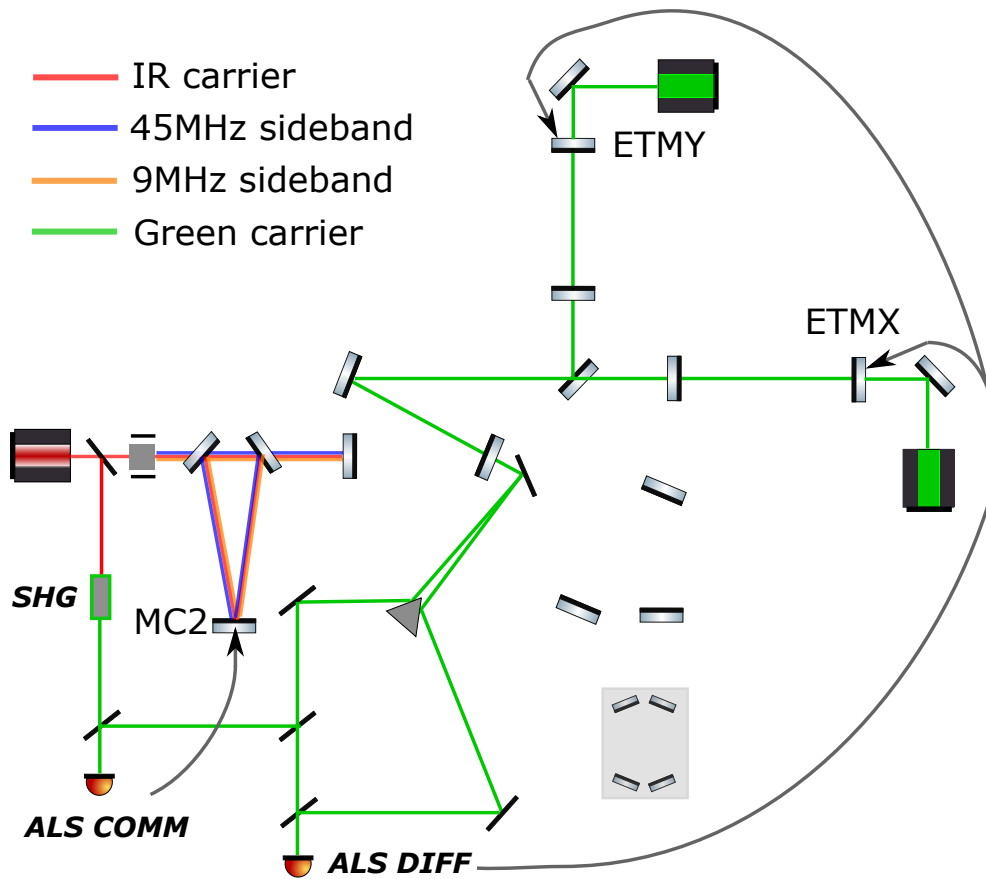


Figure 3.1: Stabilization of arm cavities using auxiliary lasers.

- Beat notes at the corner station measure frequency difference between green beams transmitted through X- and Y-arms for DARM control and between upconverted main laser beam and X-arm beam for CARM control. RF signal from ALS DIFF and ALS COMM PDs are demodulated at 160MHz and 80MHz using phase frequency discriminators and voltage controlled oscillators for DIFF and COMM paths. VCO output signals are locked to RF beat

note signals, and control signals to VCOs are used as error signals for ALS DIFF and COMM paths as shown in figure 3.1

- ALS COMM servo is used to stabilize main laser frequency to the common arm length by actuating on MC2 with bandwidth of 100Hz. ALS DIFF servo stabilized differential arm cavity length by actuating on ETMs with bandwidth of 10Hz.
- ALS COMM and DIFF servo offsets are swept to find IR resonances in the arm cavities. First, a coarse sweep is done around expected offsets and then power in the arm cavities is optimized by fine tuning. After IR resonances are found, CARM offset of 10nm is introduced for DRMI locking.

Spectrum of ALS COMM noise is shown in figure 3.2. RMS of residual arm cavity motion relative to laser wavelength is  $\approx 100pm$ . Low frequency noise is dominated by angular motion of arm cavities since PDH signal from higher order modes gives offset to pdh signal from 00 mode. This problem is caused by low-finesse of arm cavities for green light (10-20) due to ETM transmission of 40 – 50%.

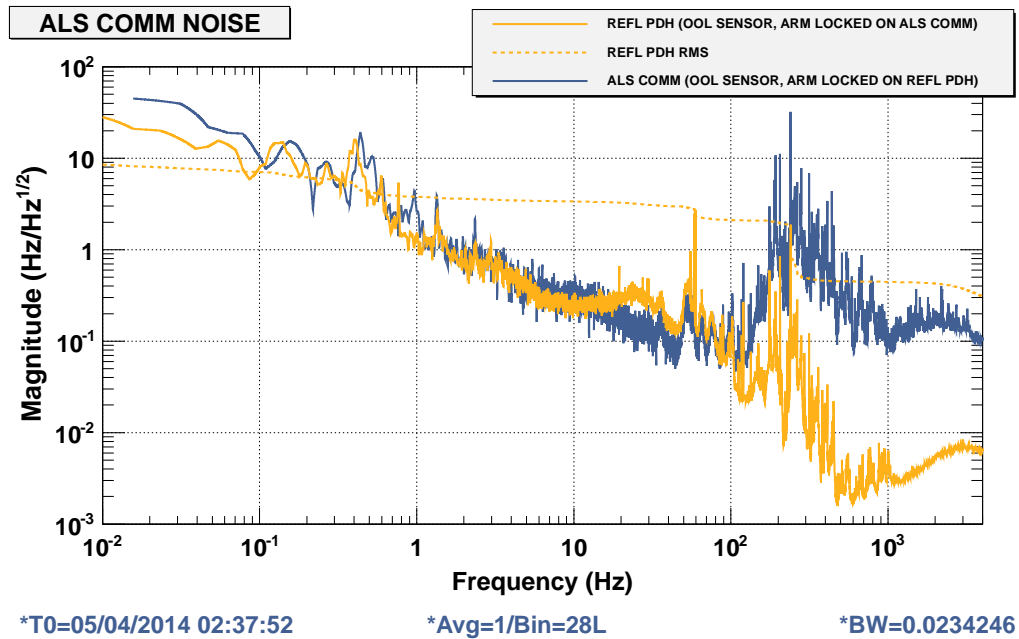


Figure 3.2: Measured ALS COMM noise. Blue trace shows ALS COMM noise measured when X-arm was controlled using PDH signals. Orange trace shows residual longitudinal noise measured by PDH signals when low passed ALS COMM signal is used for IMC length control.

Time required to engage ALS system and find IR resonances in the arm cavities is  $\approx 3min$ . CARM offset of 10nm is introduced to prevent arm cavities from resonating carrier light during lock acquisition of the corner station cavities.

### 3.2 DRMI locking

Dual recycled Michelson interferometer consists of power recycling cavity, simple Michelson interferometer, and signal recycling cavity, as shown in figure 3.3. Schnupp asymmetry of 8cm is introduced to control MICH using PDH signals. Macroscopic length of PRC is tuned to simultaneously resonate 9MHz and 45MHz sidebands while the carrier is perfectly anti-resonant. Length of SRC is tuned to resonate 45MHz sidebands and carrier while 9MHz sidebands is anti-resonant.

$$\begin{aligned} L_{prc} &= \frac{7}{2} \frac{c}{2\Omega_1} = 57.658m \\ L_{src} &= 17 \frac{c}{2\Omega_2} = 56.011m \end{aligned} \quad (3.1)$$

where  $\Omega_1 = 9099055Hz$  is exact frequency of 9MHz sideband,  $\Omega_2 = 5\Omega_1$  is frequency of 45MHz sideband.

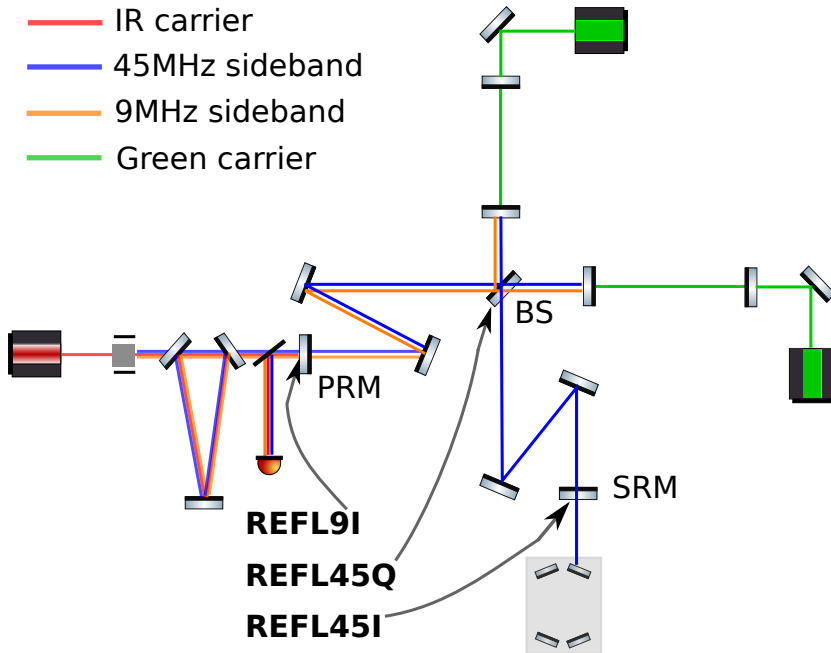


Figure 3.3: DRMI control using REFL PDH signals.

PDH signals derived from REFL port are used for DRMI lock acquisition. Responses of these signals to PRCL, MICH, and SRCL sweeps are shown in figure 3.4. When arms are kept off resonance, PRCL linewidth is 1nm, MICH is 13nm, and SRCL is 40nm. Photodetector phases are tuned such that all PRCL and SRCL are sensed by I-quadrature and MICH is sensed by Q-quadrature. Since

the 45MHz sideband resonates in the signal recycling cavity, REFL 9 I signal is used for PRCL and REFL 45 I for SRCL control. MICH signal is controlled using REFL 45 Q.

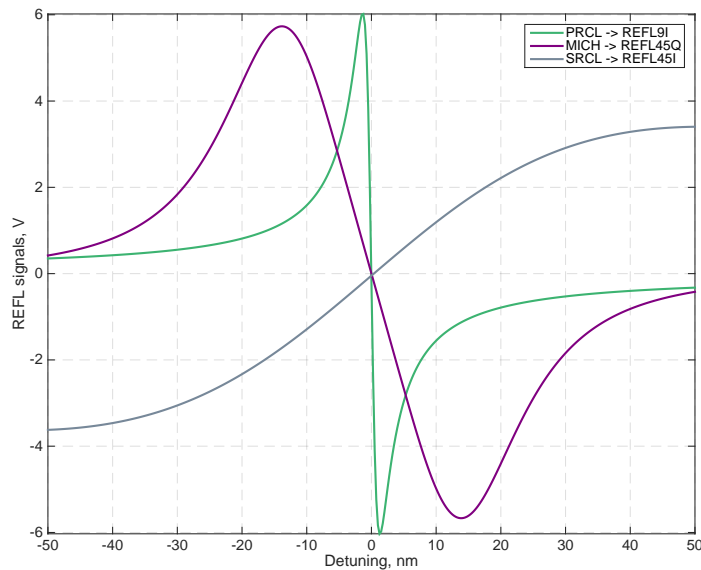


Figure 3.4: Response of REFL heterodyne signals to PRCL, MICH, and SRCL detuning.

Servo outputs are engaged when sideband flashed in the power recycling cavity. POP18 signal should go above the threshold level for the control signal to engage. Sideband flash in the power recycling cavities guarantees that MICH and PRCL error signals are close to or in linear regime. In the general case SRCL can be in an arbitrary position, but the servo is still engaged to push cavity on resonance. Locking threshold level is optimized to minimize lock acquisition time.

Tables 3.1 and 3.2 show statistics of lock acquisition time for PRMI and DRMI optical configurations depending on power threshold level. Each power threshold was tested for 150sec in PRMI and 300 sec in DRMI configuration.

When triggering threshold is high in PRMI configuration, longitudinal servos grab lock every fringe but the number of fringes is small since MICH and PRCL should be very close to zero detuning. When threshold is low, cavity fringes more often but lock is not achieved every time since PDH signal is non-linear at the moment of triggering. Maximum number of locks was achieved at triggering threshold of 1/3 of maximum power build up. During this test PRMI was locked using REFL9I and AS45Q signals. Triggering threshold was the same for PRCL and MICH. Average time for lock acquisition with thresholds 1/3 of maximum power is 15 sec.

In case of DRMI lock acquisition, control signal to suspensions is triggered when PRC is on resonance, and fringes are not counted in this measurement since SRC might be off resonance. The average time for lock acquisition with thresholds 1/6 of maximum power is 30 sec.

Triggering threshold	Number of fringes	Number of locks
3/4	5	5
1/2	6	6
1/3	15	11
1/4	12	8
1/6	18	8
1/8	18	4
1/10	18	3

Table 3.1: PRMI lock statistics.

Triggering threshold			Number of locks
PRCL	MICH	SRCL	
1/4	1/2	1/2	6
1/6	1/3	1/3	10
1/8	1/4	1/4	7
1/10	1/6	1/6	9
1/15	1/10	1/10	11

Table 3.2: DRMI lock statistics.

Servo actuates on PRM and PR2 for PRCL control, BS for MICH control, SRM and SR2 for SRCL control. Small triple suspensions have actuators on the bottom stage. This makes it possible to have PRCL and SRCL bandwidth of 100Hz and 70Hz.

Since BS suspension does not have actuators on the bottom stage and frequencies of bounce and roll modes are at 16.8Hz and 24.7Hz, bandwidth of MICH loop is limited to 10Hz. Control filter grows as  $f^3$  from 1Hz up to 25Hz and then is quickly rolled off to avoid actuator saturation. Control filter is split into two pieces. First part is set before the trigger and second part is after the trigger.

Once DRMI is stably locked using 1f PDH signals, error signals for PRCL, MICH and SRCL are replaced with 3f signals according to the table 3.3. SRCL and PRCL are diagonalized by correcting REFL\_135\_I signal with REFL\_27\_I.

DoF	Error signal	Actuation
PRCL	REFL_27_I	PRM, PR2
MICH	REFL_135_Q	BS
SRCL	REFL_135_I - $\alpha$ REFL_27_I	SRM, SR2

Table 3.3: Signals used for DRMI control during CARM offset reduction. Correction gain  $\alpha$  is tuned to subtract PRCL from SRCL error point.

3f signals are proportional to the cube of modulation index  $\Gamma$  and have lower signal to noise ratio compared to 1f signals. At the same time 3f signals weakly depend on carrier build-up in the arm cavities, and DRMI control during CARM offset reduction is stable. While carrier builds up in the arm cavities, optical gain of 3f signals was measured to change by less than 30%.

### 3.3 CARM offset reduction

In this state DRMI is stably locked using 3f signals and arm cavities are controlled using ALS signals. CARM offset of 10nm was introduced for DRMI lock acquisition and should be removed to complete locking of the full interferometer. CARM and DARM control should be transitioned to PDH signals in the reflected and antisymmetric ports of interferometer.

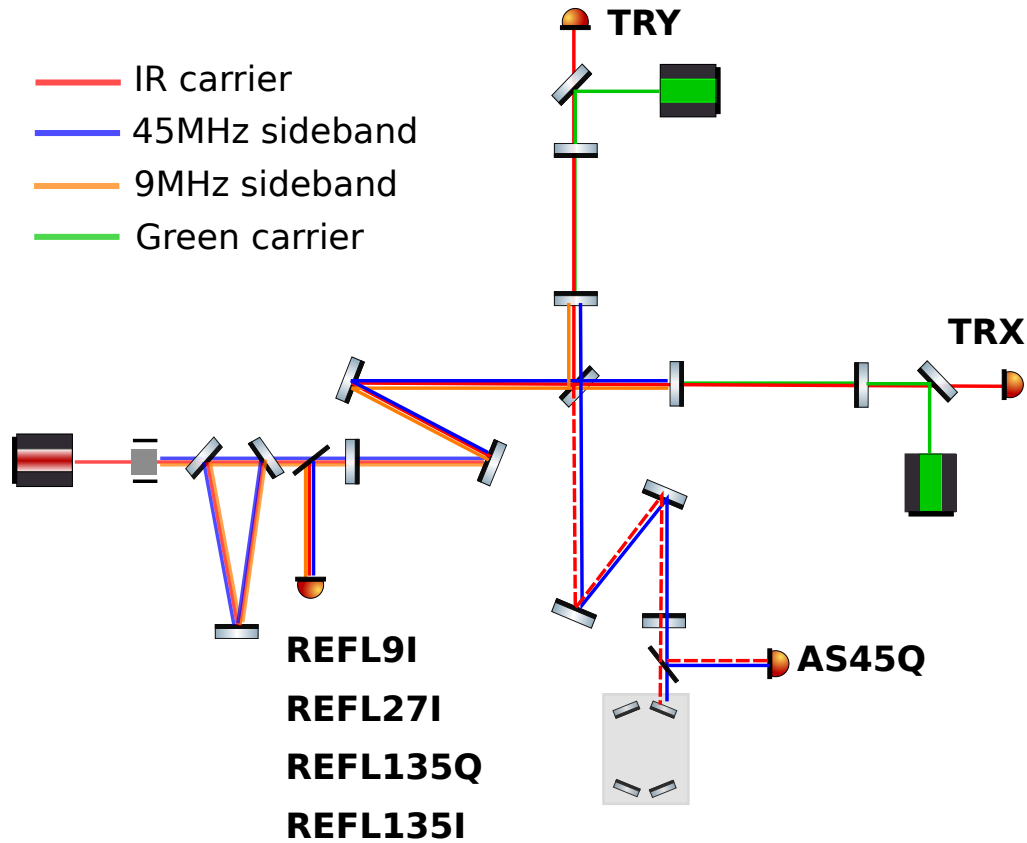


Figure 3.5: Signals used to control interferometer during CARM offset reduction.

Since RMS of ALS noise is 100pm, it is not possible to remove CARM offset and transition CARM and DARM control from ALS COMM and DIFF to PDH signals. Linewidth of REFL9I signal is 7pm and is much smaller compared to ALS COMM noise. Linewidth of AS45Q signal is 200pm, but the response of this signal to DARM depends on CARM offset.

In order to achieve smooth CARM offset reduction, CARM control is transitioned from ALS COMM to arm transmission signals  $\sqrt{TRX + TRY}$  and then to REFL9I. DARM control is transitioned from ALS DIFF to AS45Q when CARM offset is small enough such that AS45Q response to DARM has the same sign as in full lock. Figure 3.5 shows the optical sensors used to control DRMI and arm cavities during CARM offset reduction.

### 3.3.1 CARM control

Table 3.4 shows signals used for CARM control during CARM offset reduction, transition points between these signals and points of actuation:

CARM offset	Error signal	Actuation
10nm - 400pm	ALS COMM	IMC length
400pm - 10pm	$\sqrt{TRX + TRY}$	IMC length
10pm - 0pm	$REFL9I/\sqrt{TRY}$	IMC length
0pm	REFL9I	IMC length + AO

Table 3.4: Signals used for CARM control.

This choice was made with the following factors under consideration:

- ALS noise is  $\sim 100pm$ . Additional step of CARM control using arm transmission signals is required. Attached plot 3.6a shows arm transmitted power during the sweep of CARM offset. Blue section shows ALS length noise. In order to avoid large power fluctuation in the arm cavities, CARM control should be transitioned from ALS COMM to  $\sqrt{TRX + TRY}$  at CARM offsets larger than 300pm.
- Frequency response of  $\sqrt{TRX + TRY}$  signal to CARM is shown in figure 3.7a. Frequency of the optical resonance due to cavity detuning increases with CARM offset. Since the loop is digital during the process of offset reduction, CARM UGF is set to 200Hz and optical resonance should be below this frequency. CARM control should be transitioned from ALS COMM to  $\sqrt{TRX + TRY}$  signal at CARM offsets smaller than 800pm.
- Frequency response of REFL9I to CARM is shown in figure 3.7b. DC sweep is shown in figure 3.6b. REFL9I is linear only when CARM offset is smaller than 5pm. Normalization by arm transmission power helps to increase linear range. However, when CARM offset is more than 30pm, asymptotic 1/f behavior of REFL9I to CARM is lost. In order to prevent servo modifications, CARM control should be transitioned from  $\sqrt{TRX + TRY}$  to REFL9I at CARM offsets smaller than 30pm.

- CARM bandwidth of 200Hz is enough during CARM offset reduction. Switching control to REFL DC signal and introducing additive offset path for higher CARM bandwidth during CARM offset reduction is not necessary

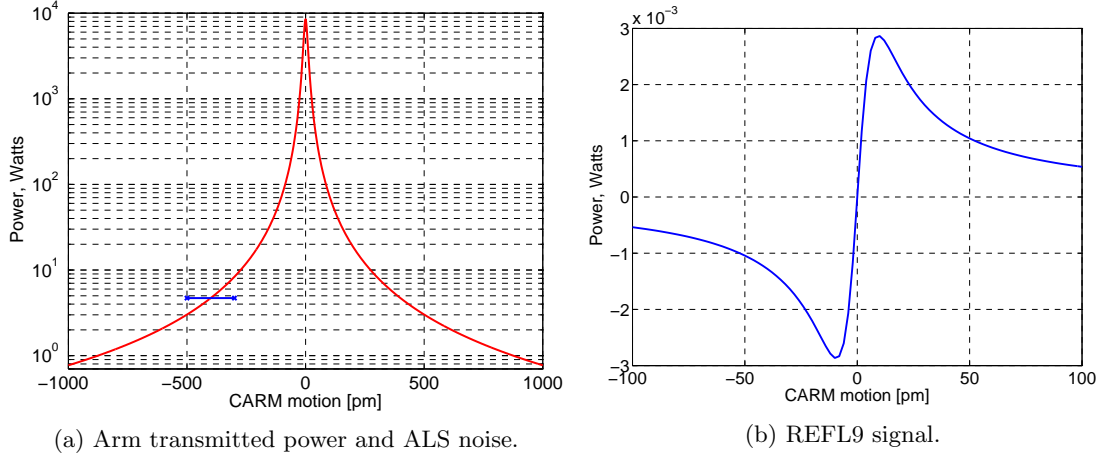
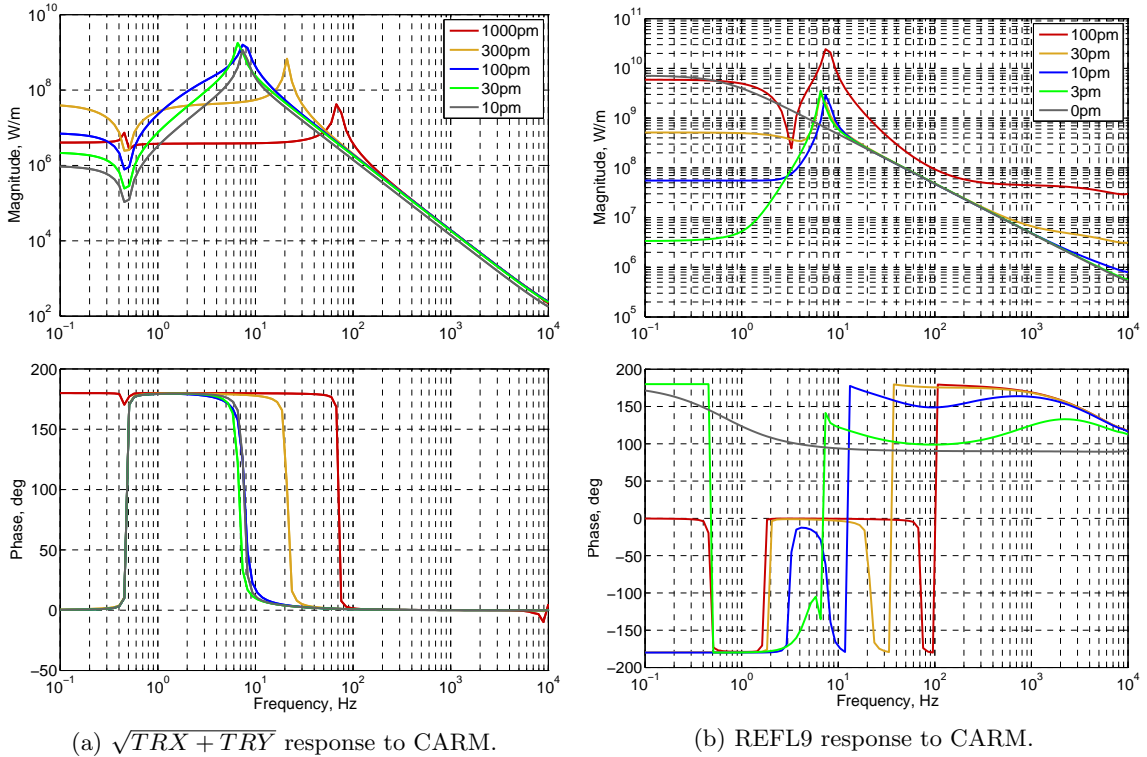


Figure 3.6: TRX and REFL9I signals depending on CARM offset.

Figure 3.7: Frequency response of  $\sqrt{TRX + TRY}$  and REFL9I to CARM depending on CARM offset.

### 3.3.2 DARM control

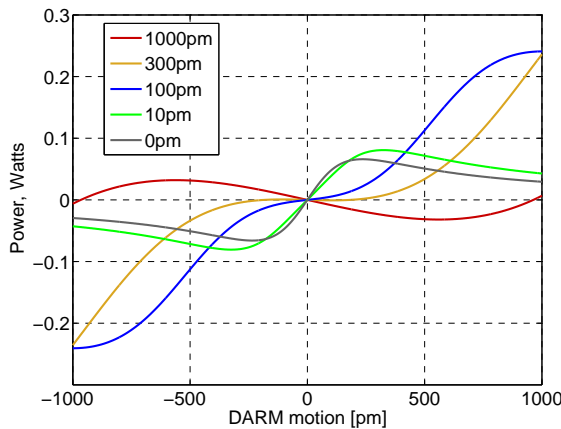
Table 3.5 shows sensing signals used for DARM control during CARM offset reduction and transition points between these signals:

CARM offset	Error signal	Actuation
10nm - 250pm	ALS DIFF	ETMX-ETMY
250pm - 100pm	ALS DIFF; AS45Q	ETMX-ETMY; ALS DIFF offset
100pm - 0pm	$AS45Q/\sqrt{TRX}$	ETMX-ETMY
0pm	OMC DC	ETMX-ETMY

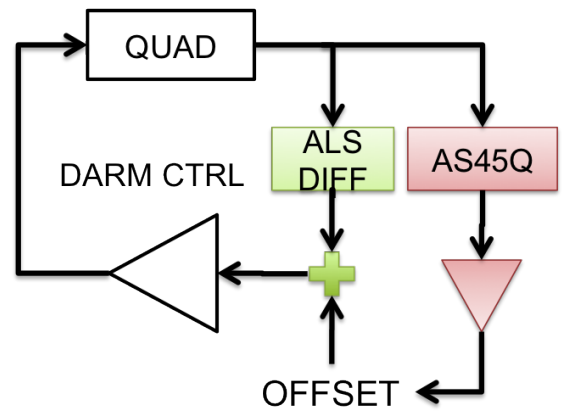
Table 3.5: Signals used for DARM control.

Figure 3.8a shows response of the signal  $AS45Q/\sqrt{TRX}$  to DARM during different CARM offsets. When CARM offset is 300pm,  $AS45Q$  response to DARM changes sign and  $AS45Q/\sqrt{TRX}$  can be used as DARM error signal at lower offsets. In practice, it is hard to control DARM using  $AS45Q$  signal close to the point when response changes sign. For this reason, full transition is done when CARM offset is 100pm.  $AS45Q$  is still used to correct for static DARM offset that comes from angular misalignment of arm cavities (1 nm/urad of waist motion) in the range of CARM offsets 250pm - 100pm. Slow servo actuates on ALS DIFF offset as shown in figure 3.8b.

DC response of  $AS45Q/\sqrt{TRX}$  to DARM increases by the factor of 6 during CARM offset reduction from 100pm to 0pm. DARM UGF increases from 12Hz up to 70Hz. Low UGF of ALS DIFF loop is due to the broadband noise of ALS DIFF signal and small range of electrostatic actuators as discussed in the section 5.1.1



(a)  $AS45Q/\sqrt{TRX}$  response to DARM.



(b) Slow servo corrects for DC DARM offset.

Figure 3.8: DARM transition from ALS DIFF to  $AS45Q/\sqrt{TRX}$  is done when CARM offset is 100pm. A slow servo corrects DARM DC offset when CARM offset is between 250pm and 100pm.

### 3.4 DC readout

When CARM offset is reduced, the interferometer is fully locked but DRMI is still controlled using 3f signals, CARM is controlled using  $REFL\_9\_I/TRY$  and DARM is controlled using  $AS\_45\_Q/\sqrt{TRX}$ . A number of steps are done to transition the instrument to the low noise regime.

First, frequency loop bandwidth is increased by introducing additive offset path. REFL9I signal is plugged into the common board and is used as an error signal for fast CARM loop with bandwidth of 30kHz. Crossover between AO and the digital path that actuates on input mode cleaner length is set to 100Hz.

Once AO is engaged and laser frequency noise is suppressed, DRMI control is transitioned to 1f POP signals from 3f REFL PDH signals. POP9I is used for PRCL control, POP45Q is used for MICH, and linear combination of POP45I and POP9I is used for SRCL. POP9I correction for SRCL is used to decouple PRCL and SRCL signals.

The last step in bringing interferometer to low noise regime is to transition DARM control from heterodyne signal to DC readout. DARM offset of 11pm is introduced and small fraction of carrier light leaves interferometer through antisymmetric port. This light is filtered from higher order modes and sidebands using narrow-band output mode cleaner. Then DARM control is transitioned from AS45Q signal to OMC PD signals.

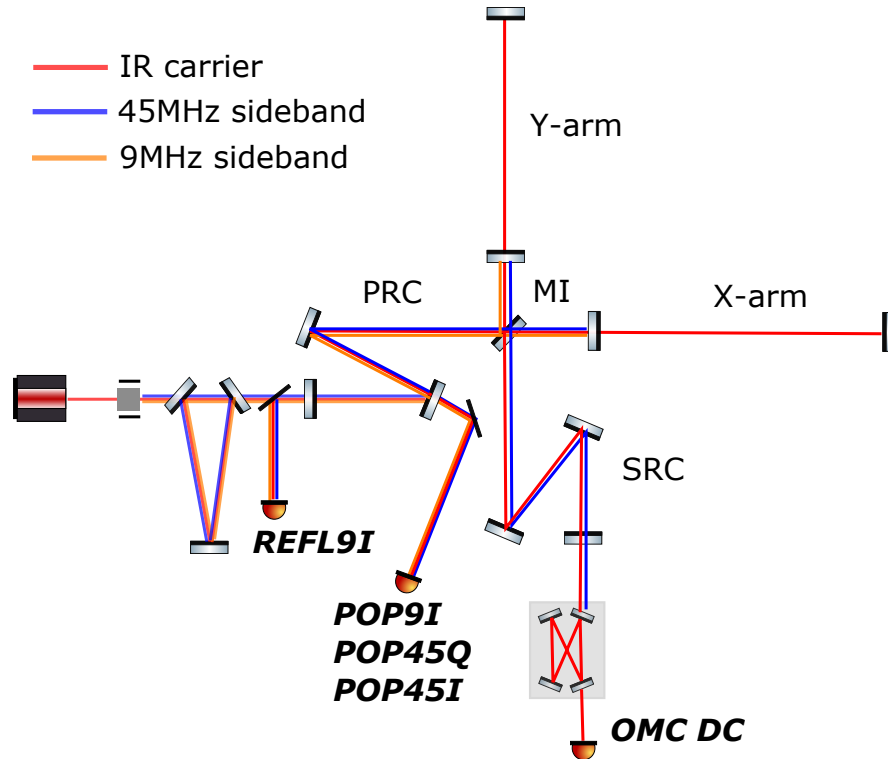


Figure 3.9: Signals used to control interferometer in full lock.

Figure 3.9 shows signals used for interferometer longitudinal control in low noise configuration when DARM is controlled using DC readout. In full lock carrier light is resonant in power recycling cavity and antiresonant in the signal recycling cavity.

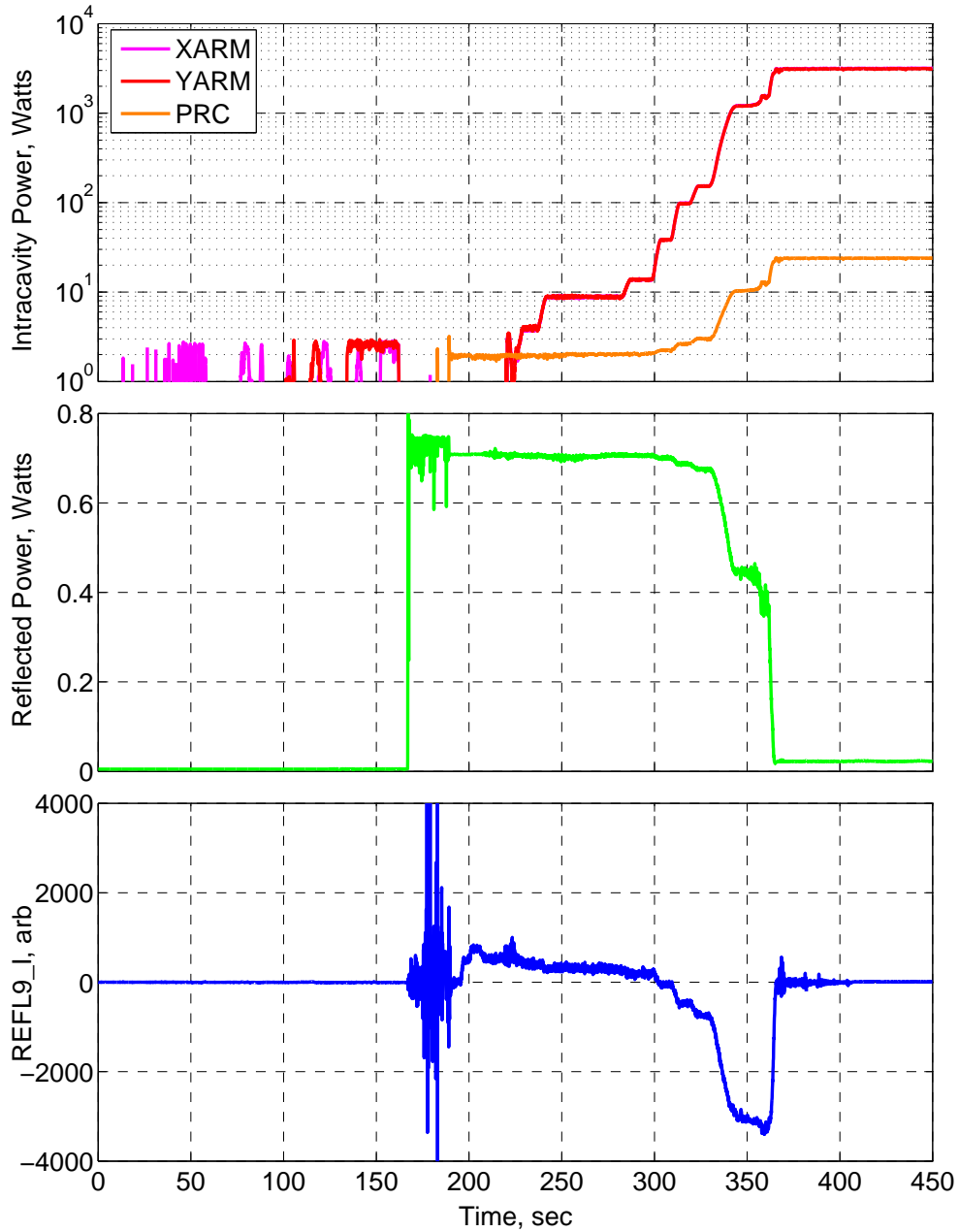


Figure 3.10: Interferometric signals during the process of lock acquisition. Input power of interferometer is 0.75W.

Figure 3.10 summarizes sequence of steps described in this chapter and shows DC power resonating in power recycling and arm cavities, interferometer reflected power and REFL9I signals

during the process of lock acquisition. During time period 0-170sec ALS COMM and DIFF loops are engaged and servo offsets are tuned to find IR resonances in the arm cavities. Both arm cavities resonate IR light during time period 150-170 seconds. Then CARM offset of 10nm is introduced for DRMI lock acquisition.

During time period 170-220 seconds DRMI is locked and aligned, longitudinal control is transitioned to 3f signals and CARM offset is reduced down to 400pm. At this point carrier light starts to build up in the arm cavities but fluctuates due to longitudinal noise of ALS system.

Intracavity power is stabilized after CARM control is transitioned to arm transmission PDs. CARM offset is reduced down to 100pm and DARM control is transitioned to AS45Q signal. After that CARM offset is reduced to 10nm and CARM control is transitioned to REFL9I signal with an offset. Offset is removed at time moment 360sec and interferometer is fully locked. Reflected power is significantly reduced, and total interferometer visibility is more than 98% in full lock.

## Chapter 4

# Alignment and angular motion stabilization

Angular motion of LIGO mirrors is caused by seismic noise, suspension longitudinal control and thermal drifts. Pitch motion is dominated by longitudinal motion of ISI tables. Yaw motion comes from ISI motion in yaw and is usually a factor of 3-5 less compared to pitch. Both pitch and yaw are driven by longitudinal suspensions control through non-diagonal cross couplings in the actuation chain. Thermal drifts are slow but can significantly misalign interferometer on a time scale of few hours.

Angular control of aLIGO optical cavities and input beam relative to each other is set up to maximize optical power and keep it stable inside interferometer [56]. This is important for robust lock acquisition and control of the instrument, since optical transfer functions and sensing matrices depend on the power circulating inside the instrument. Stable alignment is also necessary for interferometer stability and precise calibration of gravitational wave and auxiliary channels.

Alignment criteria for a simple Fabry-Perot cavity are formulated in section 2.1.2: input beam axis should be coincident to the cavity axis to maximize the build-up, and cavity axis should be set close to the central axis to minimize geometric losses. These criteria can be generalized for the full interferometer: power and signal recycling cavity axes are aligned to arm cavities while interferometer input beam is aligned to the power recycling axis. Centering of the beams on test masses is crucial due to geometrical losses. Small beam offcentering (few mm) leads to larger scattering noise, reduction of power recycling gain, and lower interferometer sensitivity.

This chapter is devoted to automated alignment system of aLIGO interferometers. The first section describes the process of initial alignment when interferometer internal cavities are coaligned with the input beam. The second section discusses angular motion stabilization in DRMI configuration when arms are misaligned or held out of resonance. The third section is devoted to alignment servos engaged during CARM offset reduction when optical transfer functions significantly change due to carrier build-up in the arm cavities. The fourth section describes angular motion stabilization

in full lock configuration.

## 4.1 Interferometer initial alignment

The interferometer should be properly aligned before it can be brought to the linear regime and used as a gravitational wave detector. This section describes the automatic procedure designed to align the full interferometer and input beam accurate enough for the locking algorithm to work properly. In order to achieve these goals, there is a set of requirements for the alignment sequence:

- **Robustness.** After initial alignment sequence is complete, the interferometer should be able to lock using automated script.
- **Automatization.** Initial alignment should be done by a script with minimum help of operators. This implies that alignment should be done using only single bounce beams and cavities with one degree of freedom.
- **Alignment time.** The procedure should not take more than 10 minutes in order to reduce time required for the lock acquisition process.

### 4.1.1 Alignment sequence

Arm cavities are aligned using green beams and serve as references for interferometer input beam, power, and signal recycling cavity axis. A detailed overview of the procedure is given below:

- Alignment of X- and Y-arm cavity axes is done using ALS green beams that are injected from the end stations. Straight beam shot is used for TMS and ITM alignment, as shown in figure [4.1a](#). ETMs are misaligned to avoid interference patterns on the mirrors.  
TMS is steered to ITM center using camera image processing or baffle PDs installed around the test mass. ITM is aligned using ETM baffle PDs 1 and 4. This is possible since the diameter of baffle PDs is significantly smaller compared to the beam size. TMS suspensions are dithered and ITM angles are adjusted to maximize readout signal from baffle PDs. The optic center is assumed to be in the middle between PD 1 and PD4.
- BS is aligned relative to ITMs in simple Michelson configuration as shown in figure [4.1e](#). MICH is locked using AS45Q PDH signal. Once BS is perfectly aligned, AS port should be dark for carrier light. BS is dithered in pitch and yaw, and alignment error signal is derived by demodulating power at the antisymmetric port.
- ETMs are aligned using green beams as shown in figure [4.1b](#). Alignment consists of coarse and fine tuning. First, ETMs are servoed to ITM geometrical center using camera signals. Then, ETM angle is swept to maximize transmitted power.

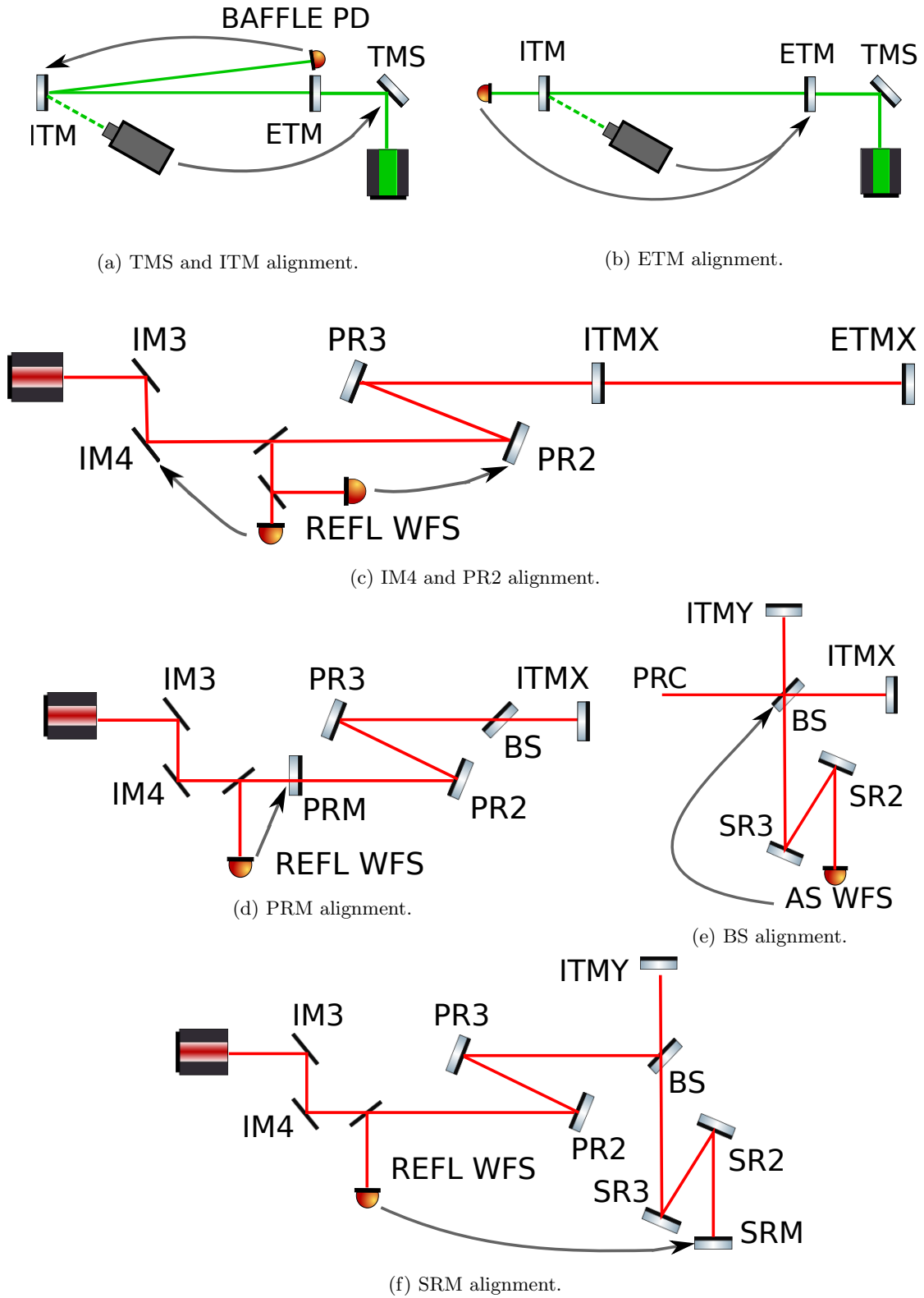


Figure 4.1: Steps of interferometer initial alignment. First, arm cavities are aligned using green beam and serve as a reference to power and signal recycling cavity axis, BS and input beam.

- PR3 is aligned to maximize amplitude of the beat note between two green beams transmitted through X- and Y-arms. This step helps to minimize clipping on the D-mirror, which separates the green beams from two arm cavities.
- PR2 and IM4 are aligned relative to X-arm axis. First, IR laser is locked to XARM by actuating on IMC length. Once IR light resonates in the cavity, reflected light contains information about input beam misalignment relative to the arm axis. This signal is extracted using two REFL WFS and servoed to IM4 and PR2, as shown in figure 4.1c.
- SR2 is aligned to center the beam on AS C QPD. This reference is also used in full lock. SRM is aligned relative to the ITMY - SR3 - SR2 axis as shown in figure 4.1f. Low-finesse SRY cavity is locked using REFL9I PDH signal. SRM is aligned using REFL WFS.
- PRM is aligned relative to the IM4 - PR2 - ITMX axis, as shown in figure 4.1d. Low-finesse PRX cavity is locked using REFL9I PDH signal. PRM angle is servoed using one REFL WFS. Signal in the second sensor should also be zero if IM4 and PR2 alignment is done correctly in the previous step.

#### 4.1.2 Alignment precision

The procedure of beam centering on the test masses using baffle PDs and camera signals has tolerance of  $\approx 4mm$ . Precision of images is limited by the slow drift of the camera and additional beams coming from optical lever beams and shadow sensors. Tolerance of baffle PDs is determined by the uncertainty in their position relative to the optic.

Relative alignment of the arm cavities is not directly controlled by the initial alignment procedure since aLIGO interferometers do not have PDH sensors in reflection of ITMs. Each arm is aligned separately and residual tilt between two axes is estimated to be less than  $2\mu rad$ . This number corresponds to misalignment of test masses by  $\approx 0.2\mu rad$  and was estimated based on precision of beam centering on the test masses and then measured during CARM offset reduction when carrier starts to resonate in the arm cavities.

Precision of BS alignment is  $0.1\mu rad$  and limited by BS angular motion due to length to angle coupling. Even though during the process of IM4 and PR2 alignment input beam passes PRM twice before being sensed by REFL WFS, SNR is good enough for precise alignment of the XARM input beam if PSL power is more than 10W.

Alignment signals from REFL WFS for PRM and SRM in low finesse PRX and SRY cavities have good SNR. After initial alignment procedure is implemented, DRMI can be locked without the operator's help. Power build-up in PRC and SRC is usually higher than 0.8 of maximum. Once locked, DRMI alignment loops are engaged and bring power in optical cavities to the maximum level.

## 4.2 DRMI angular motion

Alignment fluctuations driven by seismic noise cause power fluctuation in DRMI cavities of up to 5% in summer time and 50% in winter. Figure 4.2 shows angular motion of the mirrors estimated using ISI inertial sensors. Pitch comes from longitudinal motion of the table while yaw motion is caused by the table rotation around vertical axis.

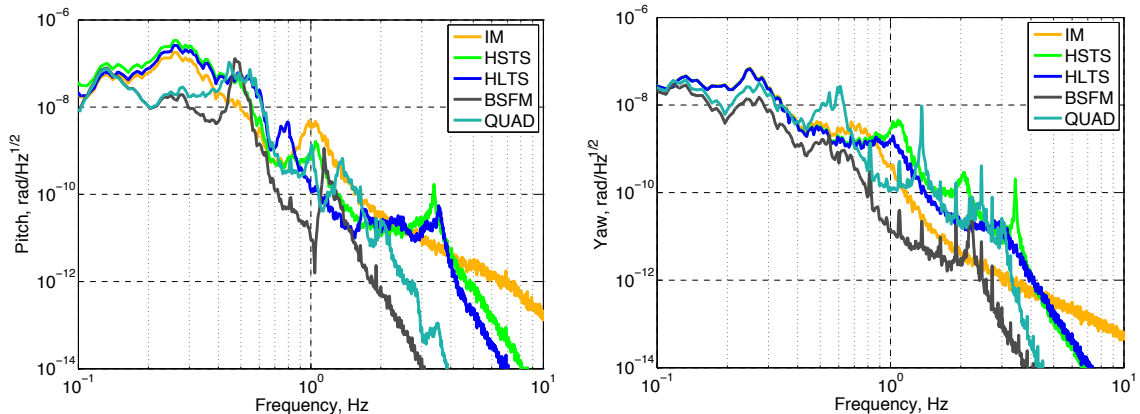


Figure 4.2: Seismically driven angular motion of input mirrors (IM), small triple suspensions (HSTS), large triple suspensions (HLTS), beam splitter suspension (BSFM) and quadruple suspensions (QUAD).

In order to estimate how angular motion of particular mirror couples to the cavity waist motion and intracavity power fluctuations, an ABCDEF model was developed for the power recycling cavity. This model computes beam offcentering from the mirror center, tilt of the cavity axis, and shift of the waist position in response to angular motion of PRM, PR2, PR3, and ITM.

### 4.2.1 ABCDEF model of power recycling cavity

For simplicity, the Michelson interferometer is replaced with a single mirror in the ABCDEF model of the power recycling cavity. The geometrical path of the beam is computed in the basis of angle and position. Model considers only tilt of cavity mirrors and ignores horizontal and vertical translations perpendicular to the cavity axis since this is the case for aLIGO suspensions.

ABCDEF matrix for free space propagation and reflection from optics can be represented as:

$$V_{basis} = \begin{pmatrix} b \\ \alpha \\ 1 \end{pmatrix} \quad P_{free} = \begin{pmatrix} 1 & L & 0 \\ 0 & 1 & 0 \\ 0 & 0 & 1 \end{pmatrix} \quad M_{mirror} = \begin{pmatrix} 1 & 0 & 0 \\ -2/R & 1 & 2/\theta \\ 0 & 0 & 1 \end{pmatrix} \quad (4.1)$$

where  $b$  is position and  $\alpha$  is beam angle,  $L$  is distance of free space propagation,  $R$  is optic radius of curvature,  $\theta$  is misalignment angle.

Basis vector is propagated through the cavity, and a  $3 \times 3$  round trip matrix is computed. Eigen vector that corresponds to the eigen value of 1 represents the solution for the cavity axis tilt and position shift.

$$V_{axis} = K \cdot V_{axis}$$

$$K = M_{PRM} \cdot P_{PRM-PR2} \cdot M_{PR2} \cdot P_{PR2-PR3} \cdot M_{PR3} \cdot P_{PR3-ITM} \cdot M_{ITM} \cdot P_{PR3-ITM} \cdot M_{PR3} \cdot P_{PR2-PR3} \cdot M_{PR2} \cdot P_{PRM-PR2} \quad (4.2)$$

where  $K$  is the round trip ABCDEF matrix of the power recycling cavity.

The following parameters were used in the model:

- Virtual waist position is 6 m before the power recycling cavity, waist size equals to 1.01 mm, cavity divergence angle is 318 urad
- Optics radii of curvature: (PRM, PR2, PR3, ITM) = (-11, -4.544, 36.01, -1934 / nSiO2), nSiO2 = 1.45
- Distance between optics PRM-PR2 = 16.604m, PR2-PR3 = 16.156m, PR3-ITM = 24.899m
- Focal lens of PRM substrate is 24.5 m (used to propagate beam parameters to the waist)

If there is no optic misalignment  $\theta = 0$  then the cavity axis is assumed to coincide with the central axis and is coaligned with the input beam path. In this case intracavity power build up is maximized and round trip matrix equals to

$$K = \begin{pmatrix} -0.33 & 12.76 & 0 \\ -0.13 & 1.99 & 0 \\ 0 & 0 & 1 \end{pmatrix} \quad (4.3)$$

Half trace of the round trip ABCD matrix equals to 0.83 and is a strong function of optics radii of curvature and distance between the mirrors since beam size increases from 1 mm up to 5.3 cm through the PRC telescope. This number represents a g-factor of the folded cavity and gives an idea of the mirror angular motion amplification to cavity waist motion.

If one or several optics are misaligned, then cavity axis shifts relative to the input beam. In this case intracavity power build-up drops according to equation:

$$\frac{\delta P}{P_0} \approx \frac{1}{2} \left( \frac{\delta \alpha}{\alpha_0} \right)^2 + \frac{1}{2} \left( \frac{\delta x}{x_0} \right)^2 \quad (4.4)$$

where  $P_0$  is maximum intracavity power,  $\delta \alpha$  is tilt of the waist,  $\alpha_0 = 335 \text{ urad}$  is cavity divergence angle,  $\delta x$  is translation of the waist and  $x_0 = 1.01 \text{ mm}$  is waist size.

Table 4.1 shows waist motion in position and tilt as well as power build up in the cavity relative to maximum value when each optic was misaligned by 1 urad:

Optic	Waist, mm	Waist, urad	Build up	PRM, mm	PR2, mm	PR3, mm	ITM, mm
PRM	0.01	-11	0.998	0.08	0.21	1.81	1.78
PR2	0.09	-54.75	0.962	0.42	1.04	9.10	8.94
PR3	0.76	-477.83	0	3.63	9.10	79.16	77.71
ITM	0.37	-234.54	0.32	1.78	4.47	38.85	38.12

Table 4.1: Table shows PRC waist position and tilt motion as well as power build up in the cavity relative to maximum value when each specified optic is misaligned by 1 urad. Last four columns show beam spot shift on each optic.

ABCDEF model shows that PR3 angular motion causes the largest power fluctuations in power recycling cavity. It is enough to misalign PR3 by 0.8urad to reduce intracavity power from maximum down to zero. PR2 gives larger power fluctuations when tilted by the same amount as PRM. Table 4.1 shows that PRM should be used for low frequency longitudinal control to minimize angular fluctuations caused by the length to angle couplings in suspensions.

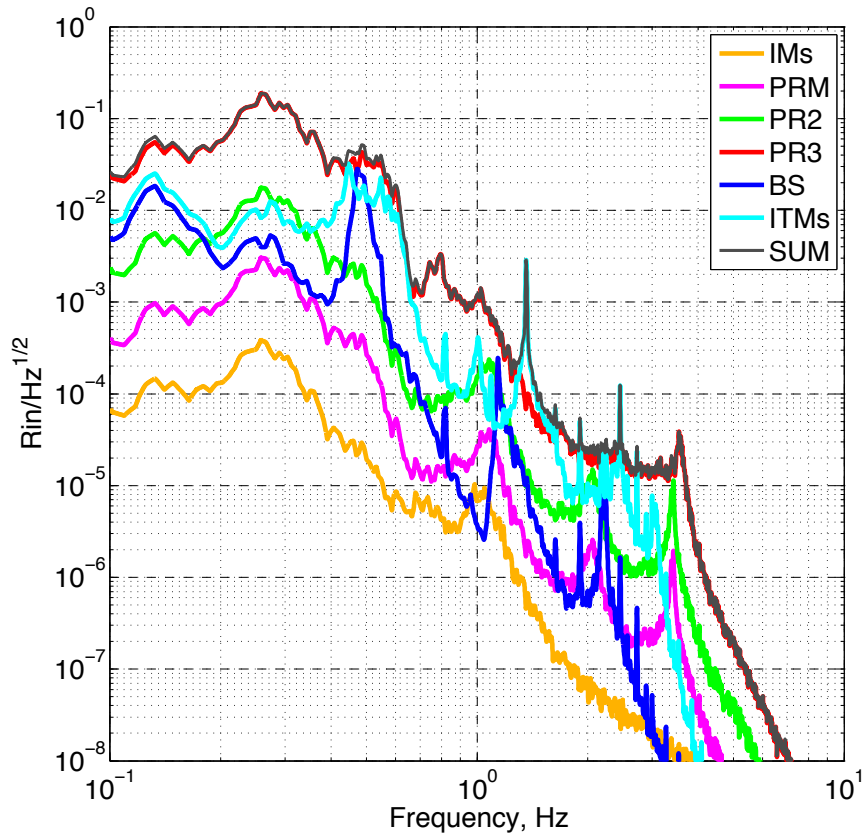


Figure 4.3: Linear coupling of seismic motion to PRC power fluctuations.

Given the angular motion of each optics shown in figure 4.2, ABCDEF model can estimate power fluctuations in the cavity. Figure 4.3 shows power recycling cavity relative intensity noise assuming DC misalignment of the cavity axis relative to the input beam equals to  $\delta\alpha/\alpha_0 = 0.1, \delta x/x_0 = 0.1$ . These numbers are related to the RMS of the power fluctuations in the cavity when angular controls are not engaged.

Figure 4.3 shows that RMS of intracavity power fluctuations comes from PR3 motion at microseismic frequencies. Power fluctuations coming from Michelson interferometer are significantly smaller since BSC ISI stage two platforms move less compared to HAM ISI tables by more than factor of 5 in the frequency range 0.1-0.5 Hz due to low noise T-240 seismometers.

Angular control system has been set to suppress power fluctuations in power and signal recycling cavities down to the level of 0.1%. Control system also removed residual misalignments left after running initial alignment procedure.

### 4.2.2 Angular controls

Once DRMI is locked on sidebands, alignment loops are engaged. Four WFS angular loops keep maximum power build up in power and signal recycling cavities, and two DC loops keep the beams on the center of PR2 and SRM. Similar loops are set in pitch and yaw degrees of freedom:

- IM4 and PR2 are controlled using linear combinations of REFL9I A and B WFS with bandwidth of 1.5Hz. These loops suppress relative motion of input beam and power recycling cavity axes at microseismic frequencies and maximize power build up in power recycling cavity.
- PRM is controlled using POP QPD with bandwidth of 0.1 Hz to keep beam position on BS.
- BS is controlled using AS36Q WFS with bandwidth of 1.5Hz. Michelson angular motion is dominated by the main BS and quad resonances around 0.5Hz. Loop has enough gain at this frequency and is rolled off at 4 Hz to reduce sensor noise injection at the interferometer sensitivity band.
- SR2 is controlled using AS C QPD with bandwidth of 2 Hz. This loop holds the beam on the center of SRM and suppresses angular motion of the cavity below 1Hz.
- SRM is controlled using AS36 I WFS with bandwidth of 0.1 Hz. The function of this loop is to keep alignment of signal recycling cavity axis.
- Beam centering servos are engaged to keep beam position on REFL and AS WFS with bandwidth of 0.1Hz. Servos actuate on RM1,2 and OM1,2,3 tip-tilts.

After DRMI is aligned, longitudinal control of PRCL, MICH, and SRCL is transitioned to 3f signals, and locking guardian moves to the next step of CARM offset reduction as discussed in section 3.3.

### 4.3 Angular controls during CARM offset reduction

During the process of CARM offset reduction carrier builds up in the power recycling and arm cavities and becomes anti-resonant in the signal recycling cavity. Since carrier reflectivity from arm cavities changes sign, response of 1f WFS to angular motion also depends on CARM offset. At the same time sidebands do not resonate in the arm cavities and are insensitive to CARM offset. The response of WFS signals, derived from the beat between 9MHz and 45MHz sidebands, to angular motion of power and signal recycling cavities and Michelson interferometer does not depend on CARM offset as shown in table 4.2.

DRMI angular loops that use 1f WFS signals are turned off when CARM offset is 80pm. Alignment servos of signal recycling cavity continue to run since they use AS36 signals. This scheme suggests to use POP36 signals for alignment of the power recycling cavity. These sensors are not currently installed but simulations show that optical response of POP36 to power recycling cavity does not depend on CARM offset and has a factor of 50 better signal to noise ratio compared to REFL WFS in full lock.

offset, pm	$\frac{AS\_B\_45Q}{ETMX-ETMY} \frac{W}{rad}$	$\frac{REFL9I}{ETMX+ETMY} \frac{W}{rad}$	$\frac{REFL9I}{PR3} \frac{W}{rad}$	$\frac{AS36Q}{BS} \frac{W}{rad}$	$\frac{AS36I}{SR3} \frac{W}{rad}$
3000	-14	-7	2446	-111	-3.13
300	-133	-14	2426	-111	-3.11
30	-1056	-17	1977	-111	-3.10
15	-1400	90	1338	-111	-3.10
5	-307	502	90	-111	-3.10
3	472	643	-129	-111	-3.10
0	1893	802	-112	-111	-3.10

Table 4.2: Simulation of WFS response to angular motion of the mirrors during CARM offset reduction. Interferometer input power was set to 1W, and sensors get all optical power from interferometer.

During aLIGO commissioning it was noticed that in order to achieve robust interferometer control during CARM offset reduction, it is necessary to avoid power leakage to AS port due to relative misalignment of arm cavity axes. This misalignment is left from initial alignment procedure and is also caused by radiation pressure torque on test masses due to beam offcentering on the mirrors. As discussed in section 2.1.2.1, tilt of arm cavity  $\alpha$  axis and beam positions on test masses  $x_{itm}, x_{etm}$

are related to misalignment angles  $\theta_{itm}, \theta_{etm}$  according to equation:

$$\begin{pmatrix} \alpha[urad] \\ x_{itm}[mm] \\ x_{etm}[mm] \end{pmatrix} = \begin{pmatrix} 10.6 & 12.2 \\ -18.5 & 23.7 \\ 23.7 & -25.1 \end{pmatrix} \begin{pmatrix} \theta_{itm}[urad] \\ \theta_{etm}[urad] \end{pmatrix} \quad (4.5)$$

Table 4.2 shows that response of AS A 45Q WFS to differential arm angular motion changes sign at CARM offset of  $\approx 4pm$ . This happens because round trip phase of carrier TEM00 and TEM01 modes changes, and beat signal flows to another Gouy phase plane, as given by equations in section 2.1.2.2. Differential alignment of the arm cavity axes can be sensed by the AS A WFS in orthogonal Gouy phase plane. Figure 4.4 shows measured response of AS A and B WFS from differential ETM motion. AS B WFS is used to control differential arm cavity alignment starting from CARM offset of 80pm. Alignment control is switched to AS A WFS when CARM offset reaches 10pm.

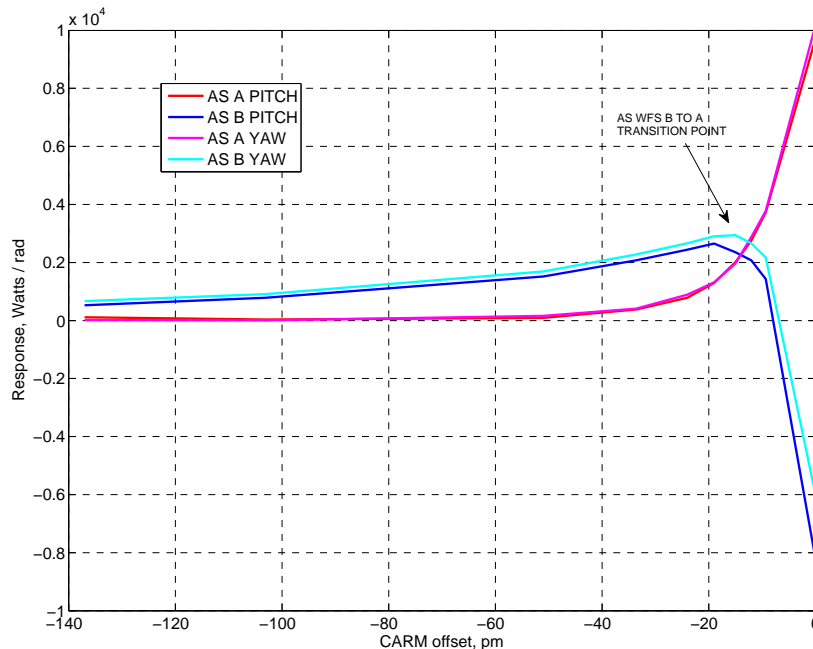


Figure 4.4: Response of AS A and B WFS to DHARD mode during CARM offset reduction.

Alignment of power recycling axis relative to the input beam and arm cavities is engaged after CARM offset is reduced and frequency noise is suppressed using 30kHz CARM loop, and DRMI is transitioned to POP 1f signals.

## 4.4 Angular motion stabilization in full lock

At the end of CARM offset reduction four pairs of alignment loops are running: relative alignment of arm cavities is controlled using AS A 45Q WFS, signal recycling cavity alignment is controlled using AS C QPD and AS36I, and alignment of the Michelson interferometer is controlled using AS36Q signal.

Sensing matrix from power recycling cavity alignment, relative to arm cavities and input beam, was measured in full lock and shown in the table 4.3. This matrix is inverted to complete interferometer alignment in full lock.

Sensor	ITMX	ITMY	ETMX	ETMY	IM4	PR2
REFL A 9I, W/rad	-207	-182	253	253	-18.8	-6.2
REFL B 9I, W/rad	-187	-184	230	253	26.1	-17.5
REFL A 45I, W/rad	-173	-166	180	173	-11.4	24.5
REFL B 45I, W/rad	-101	-99	101	106	10.5	13.3
AS A 45Q, W/rad	-8570	8386	9676	-9906		
POP DC, dx/x/rad	23375	19750	-23938	-20875		

Table 4.3: Sensing matrix of angular sensors to test masses, IM4 and PR2 in full lock. Input PSL power during the measurement was 2W. Sensing matrix scales linearly with power up to 25W.

Table 4.3 shows that differential motion of ITMs and ETMs is not sensed at reflected port of interferometer. At the same time the antisymmetric port is not sensitive to common motion of ITMs and ETMs. This was not the case before the  $CO_2$  laser was engaged to correct the sideband contrast defect caused by difference in ITM radius or curvature.

Sensing matrix also significantly depends on the mode matching between arm cavities and power and signal recycling cavities. When ITMX and ITMY  $CO_2$  lasers were engaged in common to improve mode matching between OMC and signal recycling cavity, optical transfer functions from PR2 to REFL WFS and SRM to AS36I have changed. These transfer functions were found to be least stable in the long run and to significantly depend on beam spot positions on the ITMs, visibility, and contrast defect.

Beam positions on ITMs are currently not controlled and are manually tuned by dithering the angle of test masses and optimizing beam positions in the arm cavities and power build up as discussed in section 9.2. Amount of losses in the arm cavities is crucial for robust work of alignment system since total losses are 85-90ppm and interferometer visibility is close to 1. Small fluctuations of arm losses can change sign of carrier reflectivity from the interferometer and sensing matrix will significantly change. Once losses in the arm cavities are improved up to 50-60ppm and 10% of carrier light is reflected from interferometer as discussed in section 8.1, sensing matrix will be more stable

and alignment system more robust.

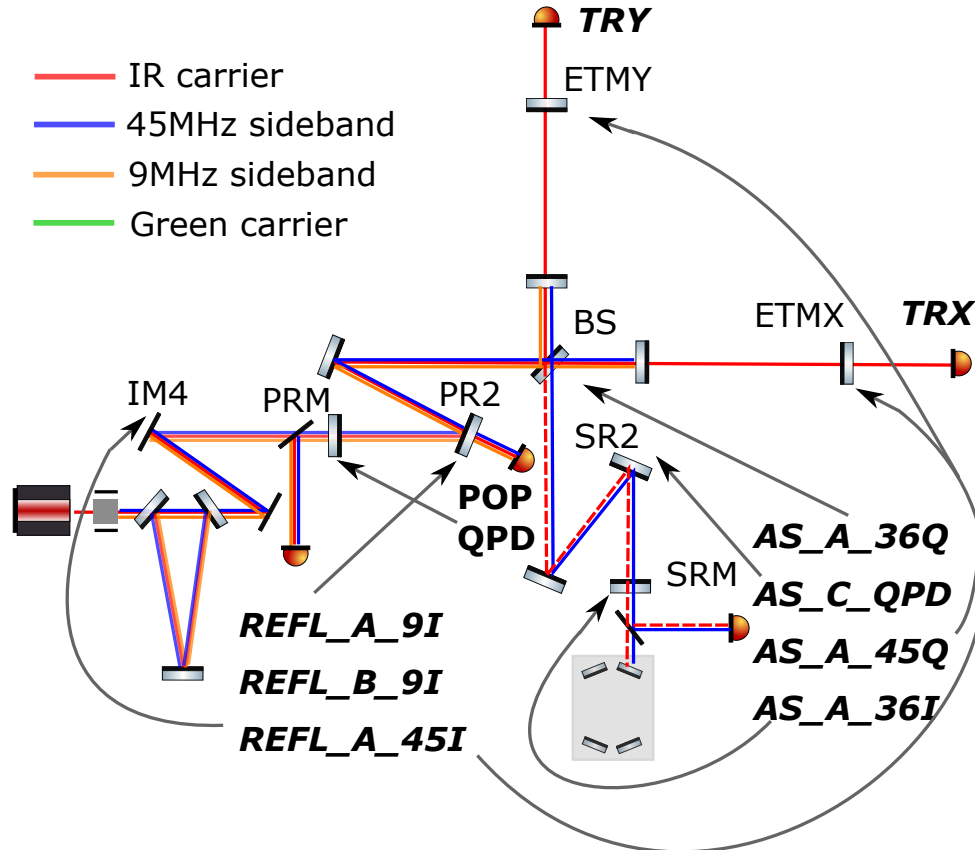


Figure 4.5: Angular controls of the full interferometer.

Figure 4.5 shows six WFS and two DC servos being engaged in the full lock to stabilize angular motion of the interferometer pitch and yaw degrees of freedom:

- Differential hard mode is controlled with AS45Q signal with bandwidth of 3Hz by actuating on ETMs
- Common soft mode is controlled using combination of REFL WFS signals with bandwidth of 1Hz by actuating on ETMs
- Two more combinations of REFL WFS are used to control PRC axis and input beam alignment by actuating on PR2 and IM4
- Beam position on PR2 is kept using POP B QPD signal and actuating on PRM with bandwidth of 0.1Hz
- Michelson alignment is controlled using AS36Q signal with bandwidth of 1.5 Hz and actuating of BS

- SRM is servoed using AS36I signal with bandwidth of 0.1Hz
- Beam position on SRM is maintained using AS C QPD and actuating on SR2 with bandwidth of 1Hz

Once angular controls are engaged, interferometer power fluctuations are stabilized on the level of 0.2% RMS. Alignment system was proven to be robust during multi-hour lock stretches. Figure 4.6 shows carrier power resonating in the power recycling cavity during 30 hour lock in low noise regime. For the first half an hour power increases due to heating of ITM substrates. This effect is caused by small size of BS optic and is discussed in appendix D.

Residual power fluctuations are caused by angular drift ITMs since these degrees of freedom are not actively controlled. Beam positions on the test masses depend on ITM alignment according to equation 4.5. Intracavity losses change when beams shift since distribution of dust is not uniform on the mirror surface.

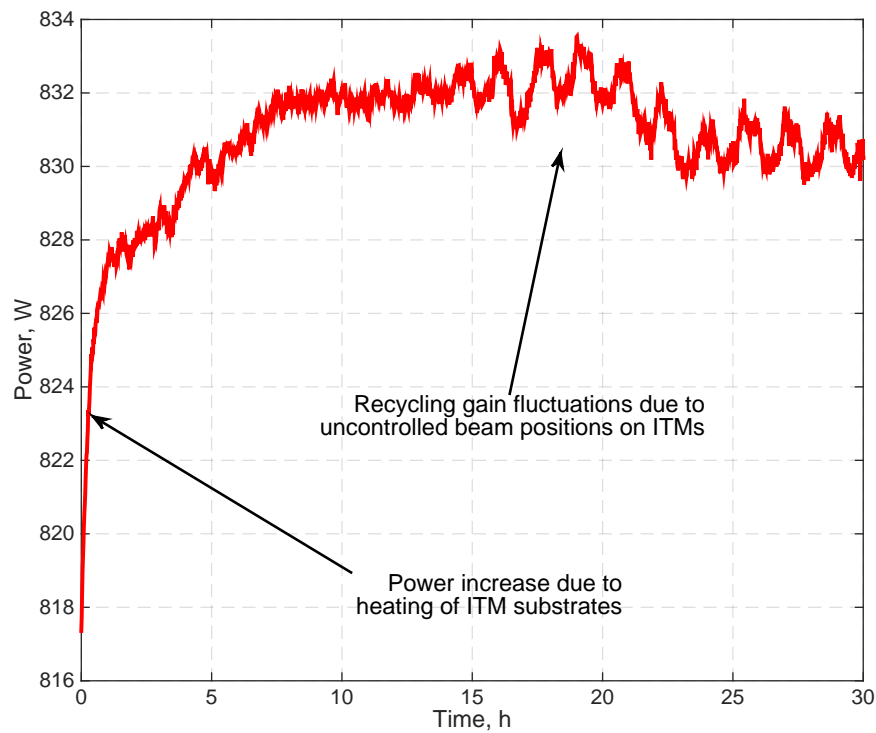


Figure 4.6: Optical power resonating in the power recycling cavity during 30 hour lock stretch. Interferometer input power is 22 Watts.

Once interferometer is stably locked and angular motion is stabilized, damping of high-Q bounce, roll, and violin modes is required before interferometer can be transitioned to low noise state. This topic is discussed in chapter 5.

## Chapter 5

# Suspension control

Design of advanced LIGO mechanical suspensions underwent a significant upgrade compared to initial LIGO design. Single stage suspensions were replaced with multi-stage ones for better seismic isolation. Test masses are located at the bottom stage of quadruple suspension. Triple suspensions are used for DRMI optics.

Actuation has also significantly changed. Initial LIGO current drivers had to produce enough force at low frequencies to acquire lock and at the same time have low electronics noise at high frequencies above 40Hz to avoid noise injections to gravitational wave channel. Coil-magnet pairs were used to actuate on the test mass, and strong low-frequency force produced Barkhausen noise [57]. This noise was filtered only by a single stage suspension and was close to sensitivity curve.

Advanced LIGO test mass suspensions have strong coil-magnet actuators on the top stages for low frequency control and weak electrostatic actuators on the bottom stage for high frequency control. This approach guarantees that Barkhausen noise is filtered by multi-stage suspension and does not limit aLIGO sensitivity in the frequency range 10Hz-10kHz.

Longitudinal range of top stage actuator M0 on quadruple suspension is 300um, on L1 stage is 25um, on penultimate mass L2 is 0.5um, and range of bottom stage ESD is 0.5um on ETMs when maximum bias of 400V is engaged. ESD range on ITMs was measured to be 20 times less compared to ETMs due to a larger gap between test masses and capacitor plates. Actuator ranges suggest that control design of aLIGO suspensions should be hierarchical with stable crossovers between different stages.

Another significant difference between initial and advanced LIGO suspension is high Q-factors of suspension fibers. Fused silica suspension fibers are used instead of metal wires and designed to minimize thermal noise contribution to gravitational wave channel. However, low loss fibers increase ring down time of violin modes to up to 1 week. Bounce and roll ring down time is a few hours. Longitudinal and angular servos are tuned to avoid excitation of suspension modes but they still get excited during lock losses and ISI trips. For this reason, suspension violin, bounce, and roll modes are damped every lock before interferometer is transitioned to low noise state.

This chapter is devoted to aLIGO suspension control developed during commissioning of LIGO Livingston interferometer. Feedback loops are designed and analyzed using frequency domain approach [58]. Section 1 describes longitudinal control of quadruple suspensions in different optical configurations. Section 2 gives procedure on damping of high-Q bounce, roll and violin modes.

## 5.1 Longitudinal control

DARM feedback control loop actuates on test masses. During the process of lock acquisition and transition of interferometer to low noise regime, three signals are used as an error signal: ALS DIFF, AS45Q, and OMC DC. These sensors have different signal to noise ratios and suppression requirements of the error point. For this reason, DARM control loop, as well as crossover filters between suspension stages, depends on particular interferometer configuration. Initial design is set for ALS DIFF loop and then updated during the process of lock acquisition.

### 5.1.1 ALS DIFF loop

Broadband sensing noise level of ALS DIFF signal in the frequency range 5Hz-1kHz is  $10^{-13} - 10^{-12} m/\sqrt{Hz}$  and sets the limit for DARM loop bandwidth of 15Hz. ETM electrostatic drivers with bias of 400V are used in this state for high frequency DARM control, and RMS control signal is dominated by sensing noise in the frequency range 10-100Hz.

L2 stage actuators are not used in this configuration since its maximum actuation range at DC below suspension resonances decreases as  $1/f^4 \cdot T_w$ , where  $T_w$  is actuator whitening transfer function. Small range of L2 actuators makes it very difficult to use this actuator in DARM control using ALS DIFF signal.

DARM motion in the frequency range from 40mHz to 1Hz depends on seismic noise and varies from 1 to 10um RMS. L1 actuator is used to compensate for this motion. L1/L3 crossover is determined by the following arguments:

- L1/L3 crossover gain should be more than 30dB at 0.1Hz to avoid ESD saturation due to low frequency seismic motion
- L1/L3 crossover should be low enough to avoid saturation of L1 actuator due to high frequency ALS DIFF sensing noise

L1/L3 crossover was set to 1.5Hz with phase margin of 30 degrees. Since suspension has resonances in the frequency range 0.4-5Hz, L1/L3 crossover filter was tuned in iterations starting from initial guess based on simulation of suspension dynamics.

M0 stage has maximum actuation range and is used for DARM control below 40mHz. Control signal is dominated by tidal motion of the ground with period of 6 hours.

ALS DIFF loop is engaged with ramp time of approximately 30 seconds to avoid saturation of actuators due to transients and angular motion caused by cross couplings in the suspensions. For this reason, crossover and DARM control filters are set in such way that loop is unconditionally stable when it is being turned on. L1 and L3 stages are engaged from beginning of DARM control and M0 stage is turned on when DARM UGF is higher than 0.3Hz to keep stability of the loop. Then low frequency boosts are engaged to suppress low frequency DARM motion. Figure 5.1 shows DARM open loop transfer function and control loops for three suspension stages.

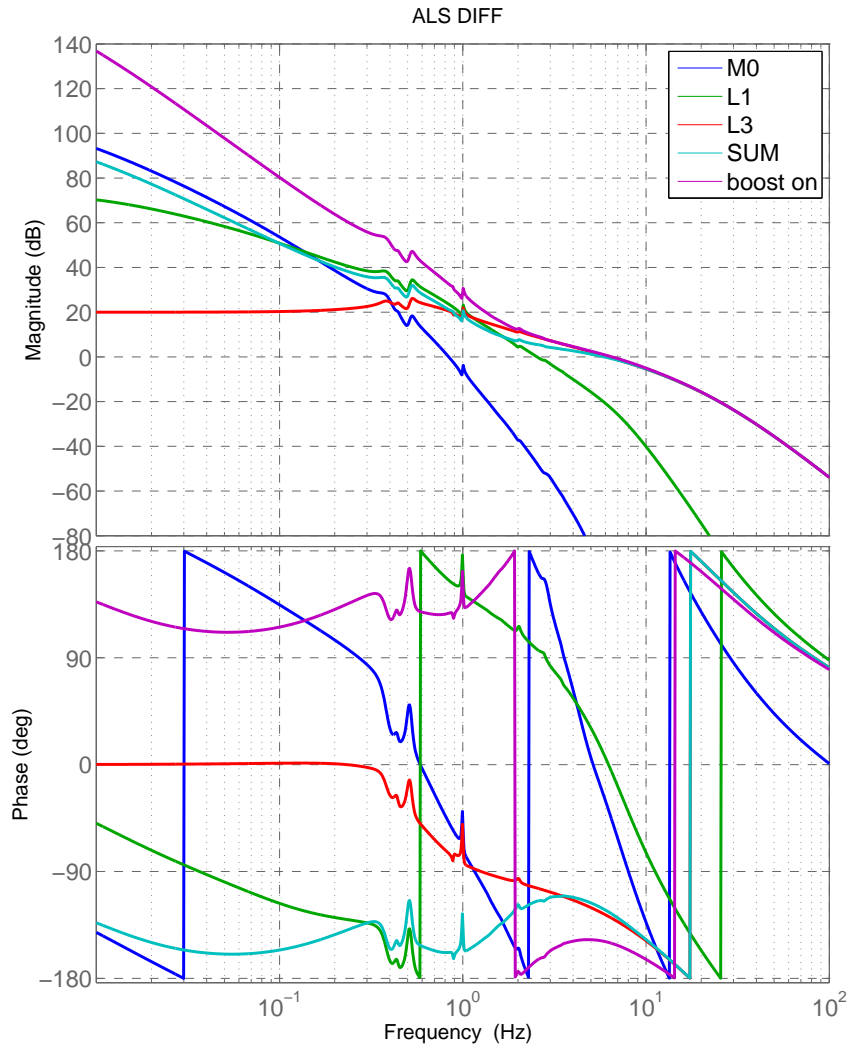


Figure 5.1: Open loop transfer function of ALS DIFF loop and M0, L1 and L3 stages. Loop is unconditionally stable when it is being engaged and M0 gain is lower than nominal. Then boost is turned on to suppress low frequency motion and M0 gain is increased.

Amplitude of control signals to L1 and L3 stages is  $\approx 20000\text{cnts}$  and is 15% of actuator range

as shown in figure 5.2. During winter times when seismic noise is high at microseism frequencies, control signal to L1 stage increases up to 30 – 40%. Figure 5.2 also shows suppression of ALS DIFF signal using loop with 15Hz bandwidth. RMS of residual motion is 5Hz and is less than ALS DIFF noise.

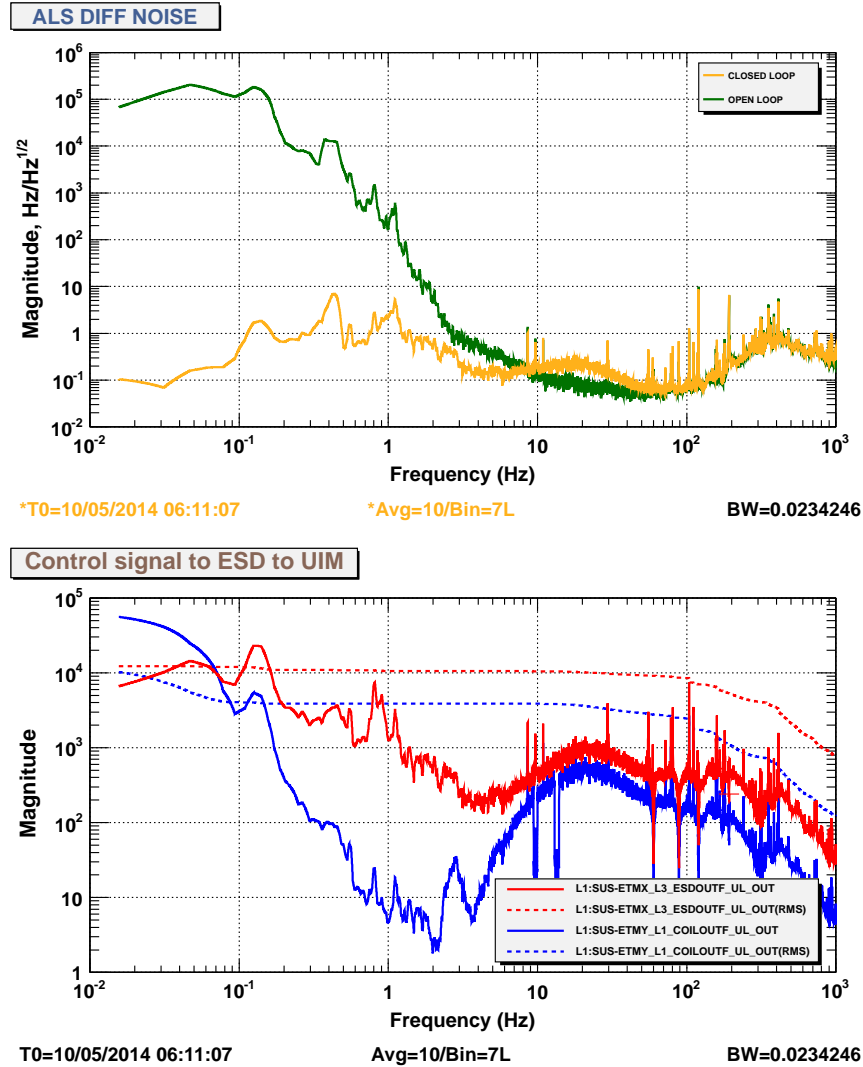


Figure 5.2: ALS DIFF loop suppression and control signal to L1 and L3 stages.

DARM is controlled using ALS DIFF loop during DRMI lock acquisition, and then error point is transitioned to AS45Q signal. During CARM offset reduction DARM bandwidth increases up to 70Hz and broadband sensing noise reduces down to  $10^{-16}m/\sqrt{Hz}$ . At this point high frequency control signal to electrostatic drivers is negligible and becomes even smaller when interferometer is transitioned to low noise state and DARM is controlled using DC readout scheme. However, ETM

ESD electronics noise limits DARM sensitivity in the frequency range 10-100Hz as discussed in section 7.3. For this reason, DARM control scheme is modified to switch off noisy ETM electrostatic drivers in low noise regime.

### 5.1.2 DARM control using L2 stage

One possible solution to eliminate ETM ESD noise is to transition high frequency DARM control to L2 stage and turn off electrostatic drivers. DARM noise is less than  $10^{-19}m/\sqrt{Hz}$  in the frequency range 40Hz-1kHz and L2 saturation can be avoided.

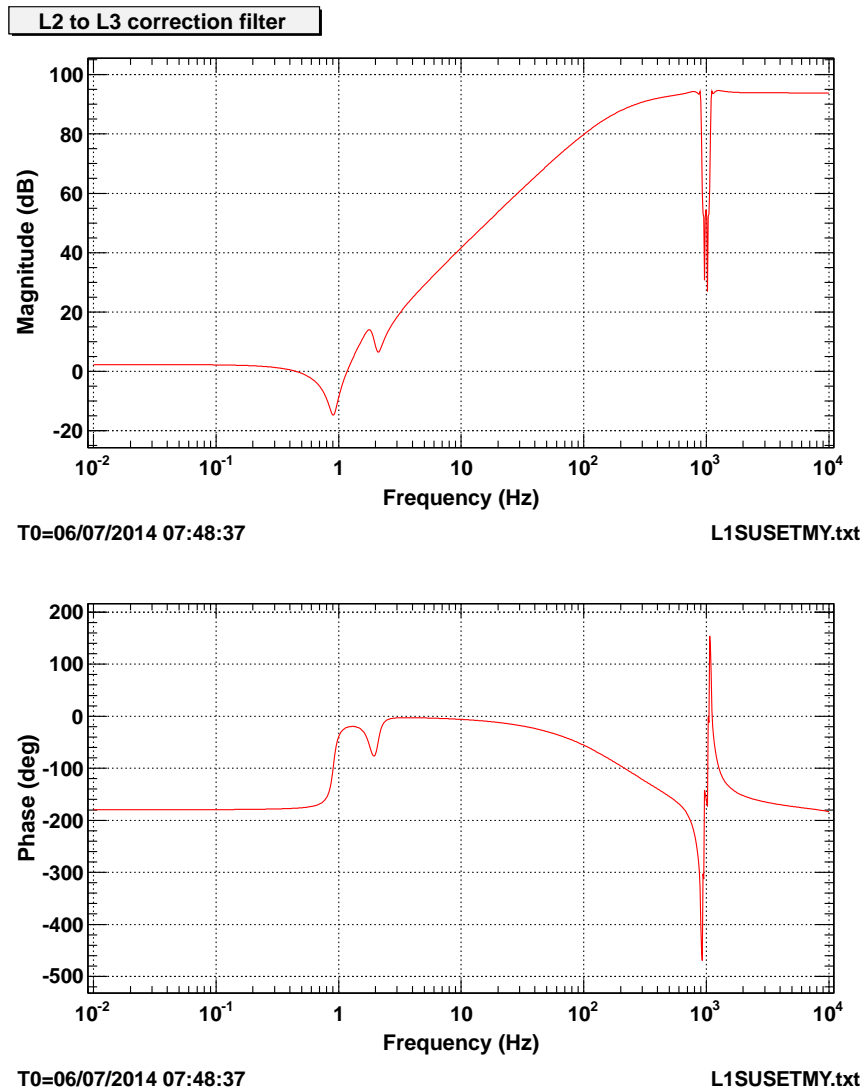


Figure 5.3: Compensation filter from quad L2 to L3 stage.

In order to keep L1/L2 crossover similar to L1/L3 and leave L1 control filter same during transi-

tion, compensation filter was introduced into L2 actuation path to make L2 to L3 suspension transfer function look the same as L3 to L3 transfer function below 100Hz. Figure 5.3 shows Bode plot of correction filter.

Control signal to L2 stage is 100-1000 times higher compared to L3 stage above 10Hz due to additional  $1/f^2$  isolation compensated by filter 5.3. Spectrum of control signal to L2 in the low noise regime is shown in figure 5.4. RMS is dominated by high frequency control signal and is 4% of actuator range when seismic noise is low.

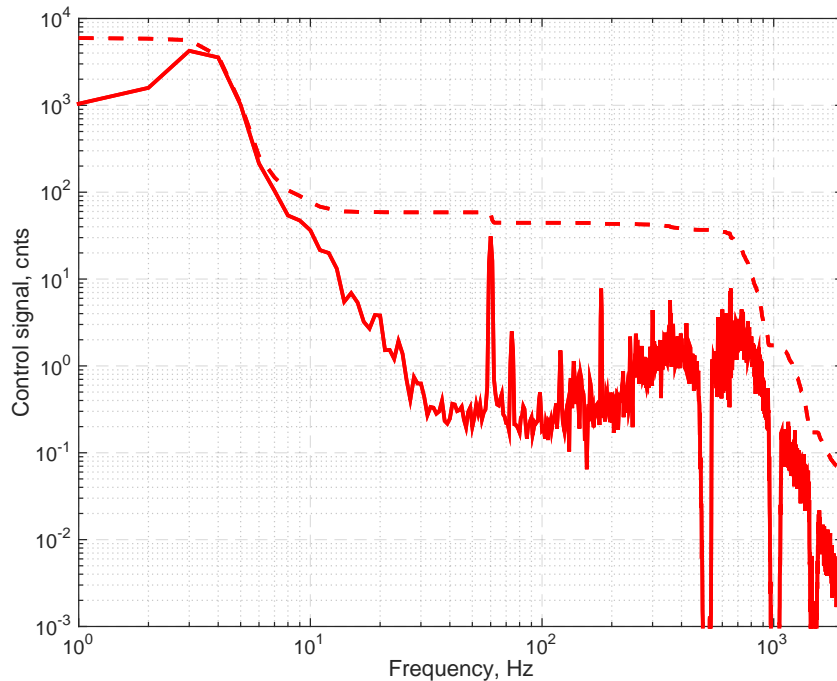


Figure 5.4: Control signal to L2 stage.

The process of controlling DARM at high frequencies using L2 actuator is more complex compared to L3 stage since violin modes and five harmonics should be well notched as well as other modes above 1kHz. Also bounce and roll modes are in loop and can get excited by the length servo depending on the phase of the open loop transfer function around 10Hz.

Most significant disadvantage of controlling DARM using L2 stage without L3 is wide violin resonance around 500Hz in longitudinal transfer function from L2 to L3. Figure 5.5 shows comparison of L3 to L3 transfer function with L2 to L3 transfer function multiplied by  $f^2$ . Narrow violin resonances are notched in the frequency range 450-550Hz but wide resonance becomes significant above 100Hz and limits DARM bandwidth to 50Hz with phase margin of 10 degrees.

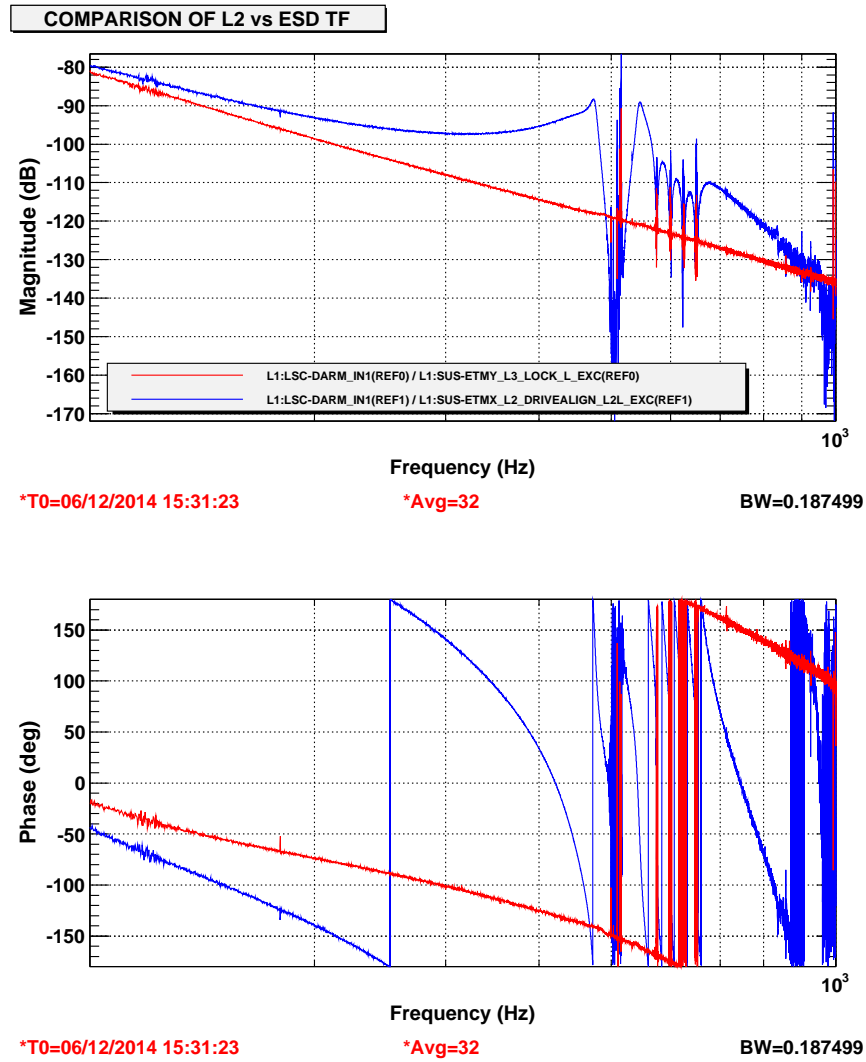


Figure 5.5: Wide violin resonance.

High frequency DARM control using L2 stage was proven to be robust. This configuration was used during engineering run ER6. However, due to wide violin resonance around 500Hz, control scheme was modified to include low range and low noise ITM ESD actuator and use L2/L3 crossover to avoid ITM ESD saturation.

### 5.1.3 L2/L3 crossover

Longitudinal range of ITM ESD was measured to be  $5nm$  with bias voltage of 100V. In this configuration noise from electrostatic actuator is far below instrument sensitivity curve as discussed in the section 7.3. At the same time open loop transfer function of L2/L3 crossover should have more

than 80dB of gain at microseismic frequencies. For this reason, ITM ESD is used for DARM control only at frequencies higher than 10Hz. Figure 5.6 shows measured crossover between L3 and upper suspension stages.

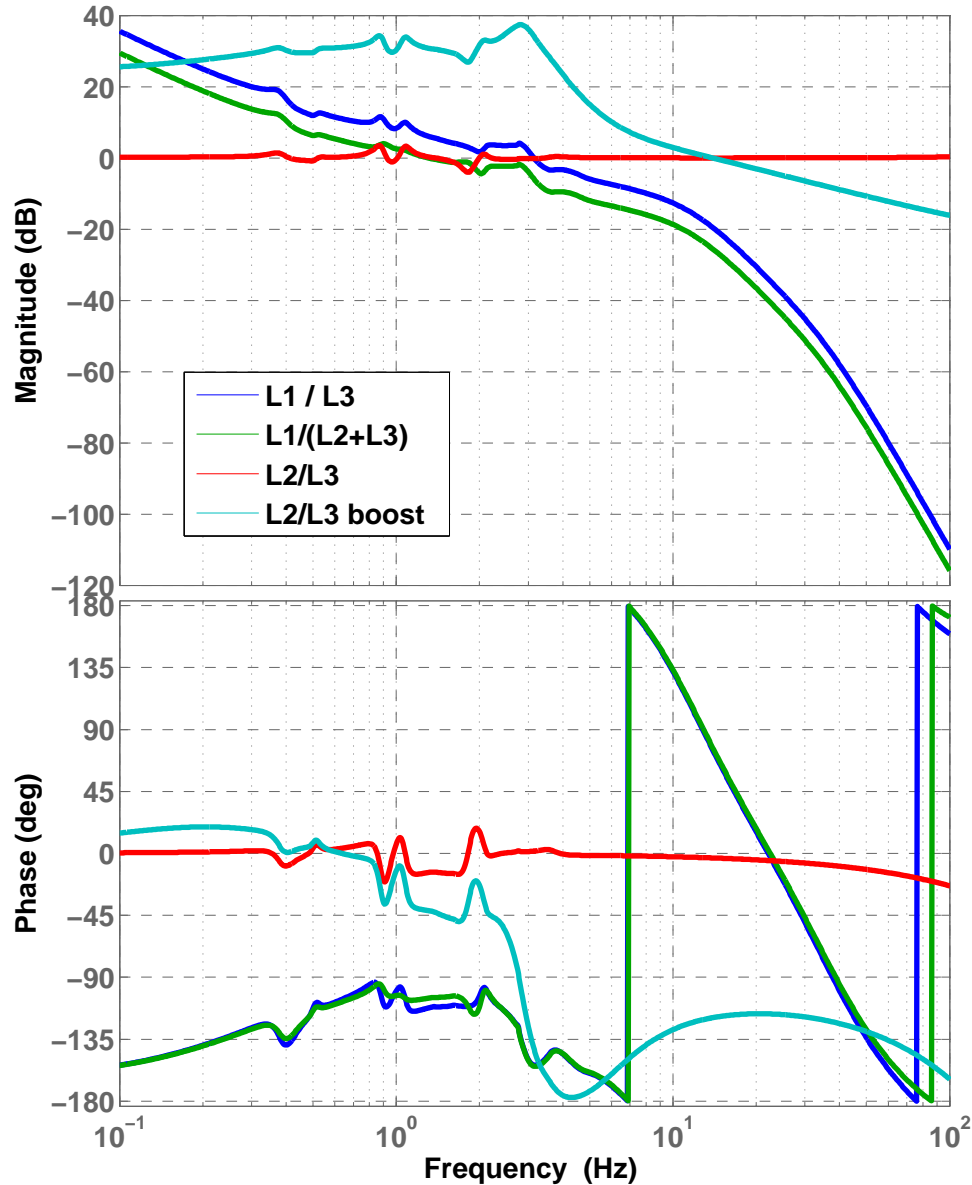


Figure 5.6: Bringing L2/L3 crossover in full lock.

L2/L3 crossover is not used during the process of lock acquisition due to arguments listed in section 5.1.1. Control signal to L2 is introduced already in full lock using the following procedure:

- L2 correction filter 5.3 is turned on to make L2 to L3 transfer function look the same as L3 to L3. This step makes it possible to introduce L2/L3 crossover without changing L1 crossover filters.

- L2 control path is engaged with ramp of 10secs. During this period of time DARM UGF increases with the speed of  $0.6dB/sec$ , and crossover frequency between L1 and low stages decreases with the same speed.
- After 7 secs L2 crossover filter is engaged and DARM UGF moves back to its initial value, and L1/L2 crossover frequency increases by 3dB compared to initial L1/L3 value. When L2 path is fully engaged, L1/L2 crossover frequency returns to 3Hz.
- Low frequency boost filters are moved from DARM servo to L2 control filter to further suppress control signal to electrostatic actuator. Figure 5.8 shows control signals to L2 and L3 stages. RMS of control signal to L3 stage is 2 cnts.
- High frequency DARM control is moved from ETM to ITM and electrostatic actuators at the end stations are turned off.

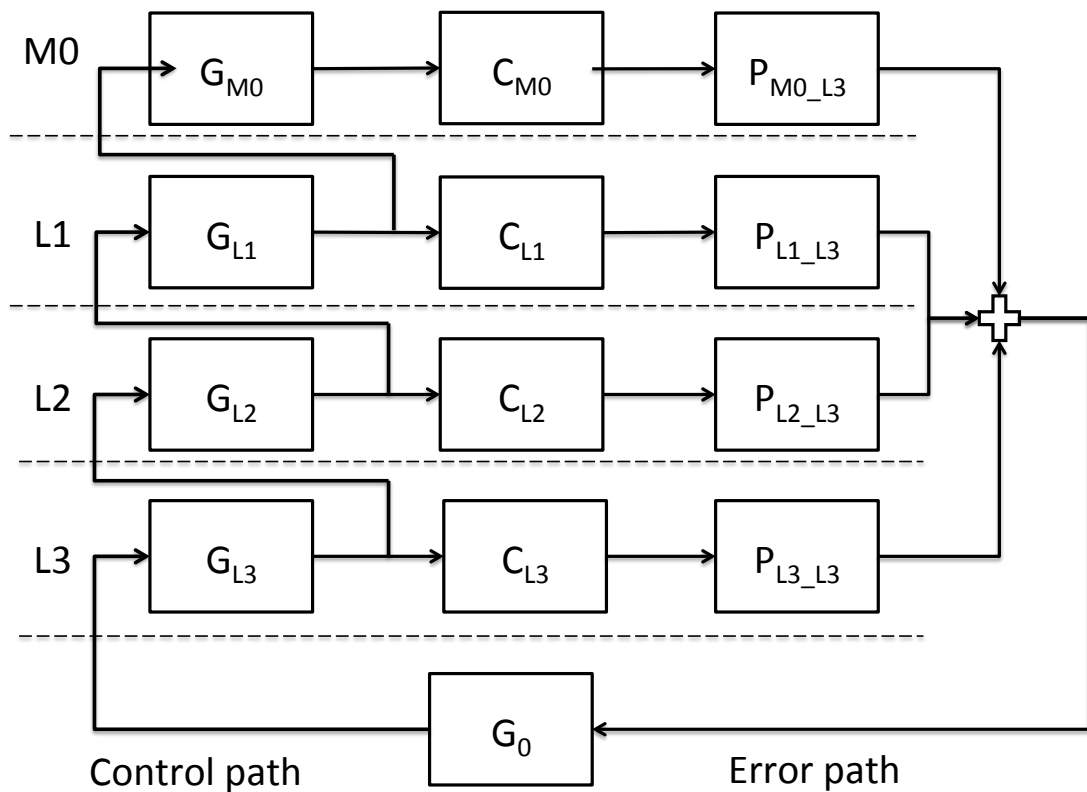


Figure 5.7: DARM control scheme.  $P$  represents transfer functions from L3, L2, L1, and M0 stages to DARM,  $C$  - correction filters,  $G_0$  - DARM control servo,  $G$  - crossover filters.

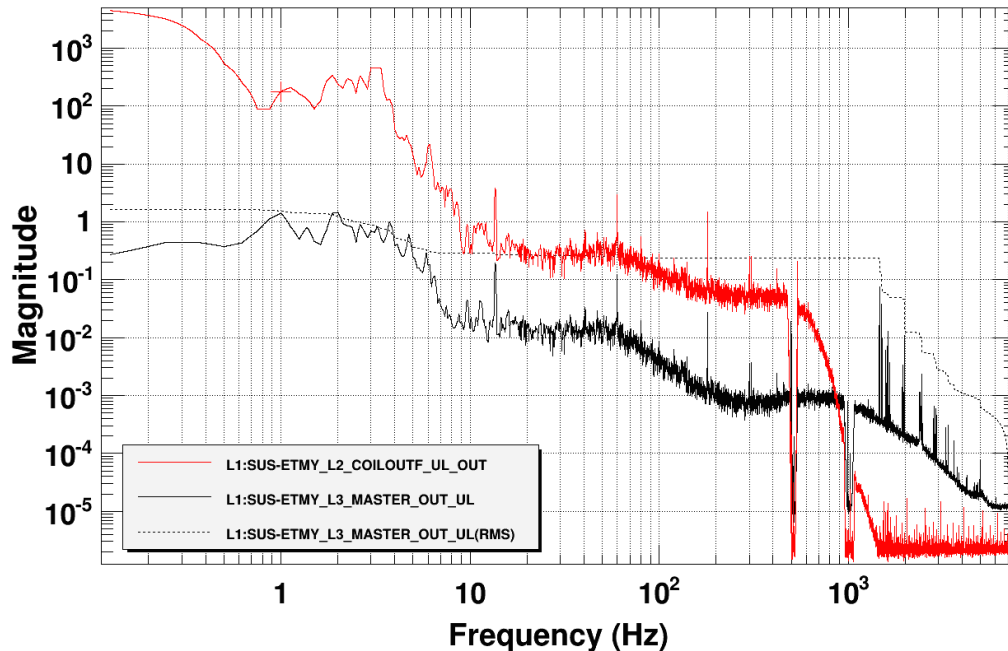


Figure 5.8: Control signal to L2 and L3 stages using L2/L3 crossover.

## 5.2 Damping of high-Q modes

Active feedback systems are used to damp bounce and roll modes of beam splitter suspension. Modes get excited during longitudinal control transients and can significantly increase lock acquisition time. Active damping is also applied to bounce, roll, and violin modes of quadrupole suspension. In low noise regime these modes dominate RMS of DARM error point, and upconversion around modes limit gravitational wave sensitivity.

Damping feedback loop should be stable and have  $60^\circ$  of phase margin for fast damping rate. Feedback controller is designed using the following procedure:

- Forth order Butterworth filter  $BP_{f_0}$  is designed with bandpass frequencies around the mode frequency  $(f_0 - \Delta f, f_0 + \Delta f)$ , where  $f_0$  is frequency of the mode, and  $\Delta f \sim 0.1Hz$  determines uncertainty in the mode position. This value should be small enough to avoid actuator saturation but significantly larger than thermal drift of the mode frequency.
- Sign of the servo gain is chosen randomly in the first iteration. Magnitude is increased before mode gets excited or damped with rate of  $3\%/min$ . If mode gets excited, the sign of the controller is changed. Phase of the open loop transfer function gets in the stable region including sectors 1-3 shown in figure 5.9.
- Servo phase is optimized by engaging filters  $G_{+60^\circ}$  and  $G_{-60^\circ}$ , which add or subtract  $60^\circ$  from the servo phase without changing magnitude. Table 5.1 summarizes possible outcomes of the

test. Design of the final controller guarantees that phase of the open loop transfer function is in the sector 2 shown in figure 5.9.

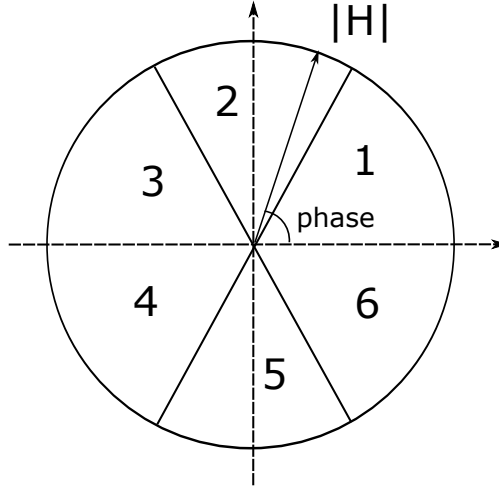


Figure 5.9: Phase sectors of open loop transfer function  $H$ .

Stability test	Initial sector	Servo design
$BP_{f_0} \cdot G_{+60^\circ}$ and $BP_{f_0} \cdot G_{-60^\circ}$ are stable	2	$BP_{f_0}$
$BP_{f_0} \cdot G_{+60^\circ}$ stable, $BP_{f_0} \cdot G_{-60^\circ}$ unstable	1	$BP_{f_0} \cdot G_{+60^\circ}$
$BP_{f_0} \cdot G_{+60^\circ}$ unstable, $BP_{f_0} \cdot G_{-60^\circ}$ stable	3	$BP_{f_0} \cdot G_{-60^\circ}$

Table 5.1: Possible outcomes of tuning procedure of the servo phase. Initial sector indicates servo phase from figure 5.9 when only  $BP_{f_0}$  is used.

### 5.2.1 BS bounce and roll damping

Active damping technique was applied to BS suspension for bounce and roll modes. Servos are engaged during the process of lock acquisition and then turned off in the low noise regime when notch filters are engaged in MICH loop.

M1 vertical shadow sensors are used for bounce and roll sensing with noise floor of  $2 \cdot 10^{-11} m / \sqrt{Hz}$ . Servo actuates on M2 in pitch and yaw degrees of freedom from bounce and roll damping. Active damping relies on cross couplings in the suspension between vertical and angular degrees of freedom.

Figure 5.10 shows open loop transfer function of active damping controller of BS bounce mode. Tests of the servos have shown that amplitude of bounce and roll modes decrease by a factor of 10 in 10 seconds. Energy of the modes is reduced since, when servo is turned off, the height of the mode is still below noise floor in the error signal.

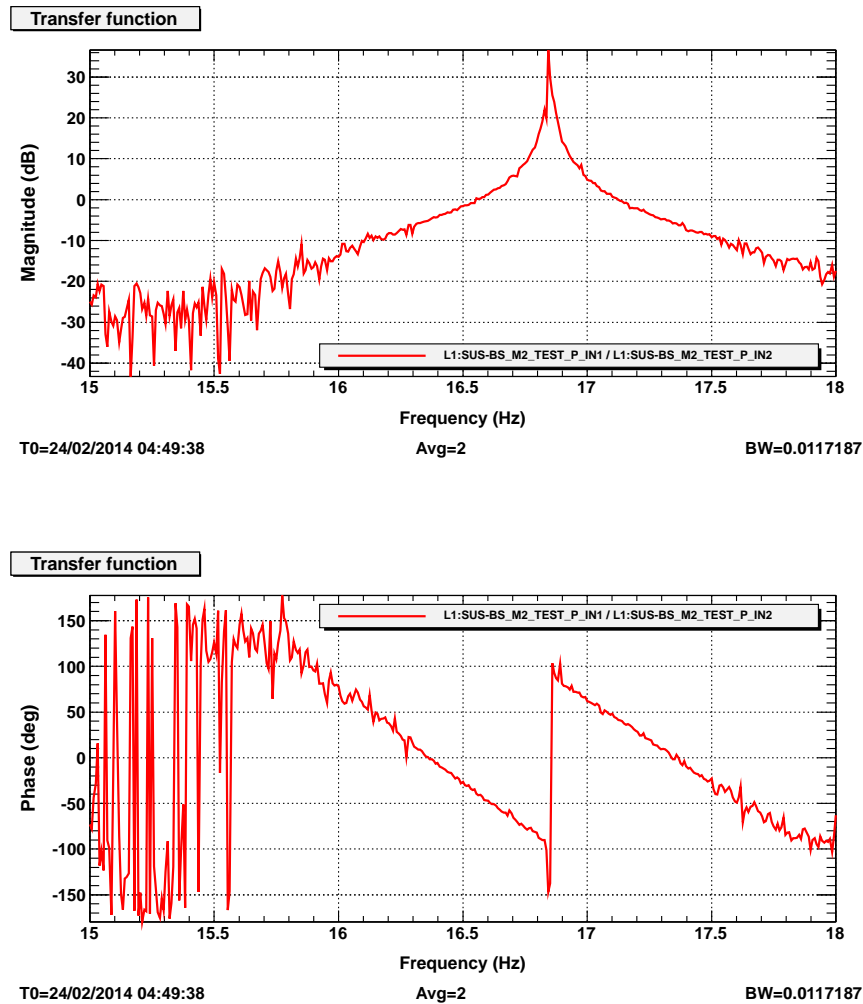


Figure 5.10: Open loops transfer function of BS bounce mode damping.

Damping servo modifies BS longitudinal M2 to M3 transfer function as shown in figure 5.11. When servo is off, MICH loop with bandwidth of 10Hz rings up BS bounce mode due to vertical to longitudinal cross coupling. When servo is engaged, coupling is modified and mode is not excited by the loop.

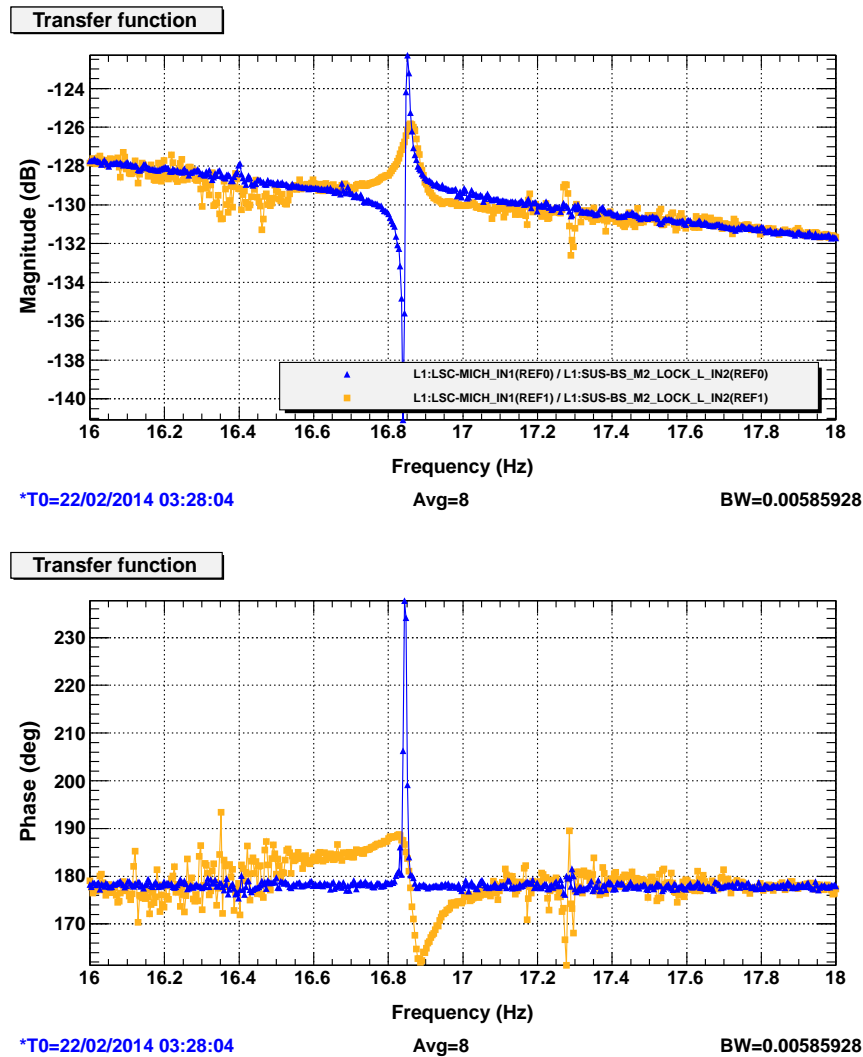


Figure 5.11: Comparison of BS longitudinal transfer function.

### 5.2.2 Quad bounce and roll damping

Local sensors can not be used for bounce and roll damping on test masses since broadband noise level of shadow sensors is much higher than DARM sensitivity. Required level of bounce and roll damping on test masses is  $10^{-15}m$  and  $10^{-18}m$  measured by longitudinal sensor. For this reason, interferometric signals are used for bounce and roll damping.

Table 5.2 shows frequencies of bounce and roll modes for all four test masses. The table also shows error signal, actuator, and servo parameters used for damping of the modes. Controllers are engaged after full lock is acquired and run for 3-5 minutes before modes are damped into the noise

floor. Then interferometer is transitioned to low noise regime, and modes are damped again since noise floor improves by a few orders of magnitude. After modes are damped to required amplitudes, servos are turned off.

Mode	Test mass	$f_0$ , Hz	Error signal	Servo	Actuator
bounce	ETMX	9.59	DARM ERR	$+BP_{f_0} \cdot G_{+60^\circ}$	M0 VERT
bounce	ETMY	9.71	DARM ERR	$-BP_{f_0} \cdot G_{+60^\circ}$	M0 VERT
bounce	ITMX	9.62	DARM ERR	$+BP_{f_0}$	M0 VERT
bounce	ITMY	9.68	DARM ERR	$-BP_{f_0} \cdot G_{+60^\circ}$	M0 VERT
roll	ETMX	13.59	WFS AS45Q PIT	$-BP_{f_0} \cdot G_{-60^\circ}$	L2 PIT
roll	ETMY	13.78	WFS AS45Q PIT	$+BP_{f_0} \cdot G_{+60^\circ}$	L2 PIT
roll	ITMX	13.65	DARM ERR	$+BP_{f_0}$	M0 ROLL
roll	ITMY	13.75	DARM ERR	$-BP_{f_0}$	M0 ROLL

Table 5.2: Test mass bounce and roll damping parameters.

Active damping servo phase shown in the table 5.2 depends on sensing and actuation parameters. Since vertical sensors are not available and height of modes is monitored using longitudinal and angular sensors through suspension cross coupling, servo phase has to be adjusted depending on beam position on the test masses.

### 5.2.3 Quad violin mode damping

Violin modes and harmonics are notched in DARM servo but they get excited during lock losses. Due to high-Q of the modes  $Q \sim 10^9$ , height of the modes decreases by factor of 2-3 in one week. If not actively damped, violin modes seen in DARM have RMS of  $10^{-14}m$  and saturate OMC photodetectors.

Table 5.3 shows frequencies of 16 violin modes and their damping parameters. Controllers are engaged in full lock for 1-2 mins and get turned off when the height of modes seen in DARM spectrum is less than  $10^{-17}m$ . Servos are kept off since they significantly run up violin modes if lock is lost during damping procedure.

Each violin mode listed in the table 5.3 has two orthogonal polarizations separated in frequency by  $\approx 7mHz$ . Since both polarizations are in loop, servo design should be stable for both of them. In some cases  $\Delta f$  is increased from 0.1Hz to 0.3Hz to reduce phase difference between two modes.

In rare cases one of polarizations is not damped when DARM is used as an error signal since mode vibrates in orthogonal direction to the cavity axis. Violin mode seen in DARM is damped by active feedback and, when servo is turned off, rings up again by taking energy from orthogonal polarization. Two polarizations get into equilibrium in  $\sim 30mins$  and damping process is repeated.

Total time required to damp such modes is 4-5 hours. However, excitement of these modes rarely happens after major earthquakes and damping procedure using energy exchange is used once in a few months.

Test mass	$f_0$ , Hz	Servo	Actuator
ETMX	513.15	$+BP_{f_0} \cdot G_{+60^\circ}$	L2 PIT
ETMX	513.27	$+BP_{f_0} \cdot G_{+60^\circ}$	L2 PIT
ETMX	515.55	$BP_{f_0}$	L2 LONG
ETMX	516.9	$+BP_{f_0} \cdot G_{+60^\circ}$	L2 PIT
ETMY	499.6	$-BP_{f_0} \cdot G_{+60^\circ}$	L2 PIT
ETMY	503.1	$+BP_{f_0} \cdot G_{+60^\circ}$	L2 PIT
ETMY	515.34	$BP_{f_0}$	L2 LONG
ETMY	515.37	$BP_{f_0}$	L2 LONG
ITMX	509.0	$+BP_{f_0} \cdot G_{+60^\circ}$	L2 PIT
ITMX	510.9	$+BP_{f_0} \cdot G_{+60^\circ}$	L2 PIT
ITMX	515.8	$BP_{f_0}$	L2 LONG
ITMX	516.0	$BP_{f_0}$	L2 LONG
ITMY	508.4	$-BP_{f_0} \cdot G_{+60^\circ}$	L2 PIT
ITMY	509.4	$-BP_{f_0} \cdot G_{+60^\circ}$	L2 PIT
ITMY	510.2	$-BP_{f_0} \cdot G_{+60^\circ}$	L2 PIT
ITMY	511.5	$-BP_{f_0} \cdot G_{+60^\circ}$	L2 PIT

Table 5.3: Test mass violin modes damping parameters.

Table 5.4 shows frequencies of second harmonics of test mass violin modes that got frequently excited during lock losses or ISI trips. Modes are damped down to the level of  $10^{-17}m$  and then servos are turned off.

Test mass	$f_0$ , Hz	Servo	Actuator
ETMX	1018.25	$+BP_{f_0} \cdot G_{-60^\circ}$	L2 PIT
ETMX	1020.6	$+BP_{f_0} \cdot G_{-60^\circ}$	L2 PIT
ETMX	1023.05	$-BP_{f_0} \cdot G_{-60^\circ}$	L2 PIT
ETMX	1025.2	$+BP_{f_0} \cdot G_{+60^\circ}$	L2 PIT
ETMY	1022.8	$-BP_{f_0}$	L2 PIT
ITMY	1010.95	$-BP_{f_0} \cdot G_{-60^\circ}$	L2 PIT

Table 5.4: Damping parameters of second harmonics of test mass violin modes.

Figure 5.12 shows time series of control signal and ITMX violin mode height during the process

of excitation and damping. Mode excitation is achieved when servo sign is flipped. It took  $\approx 2mins$  to damp the mode by factor of 10-20.

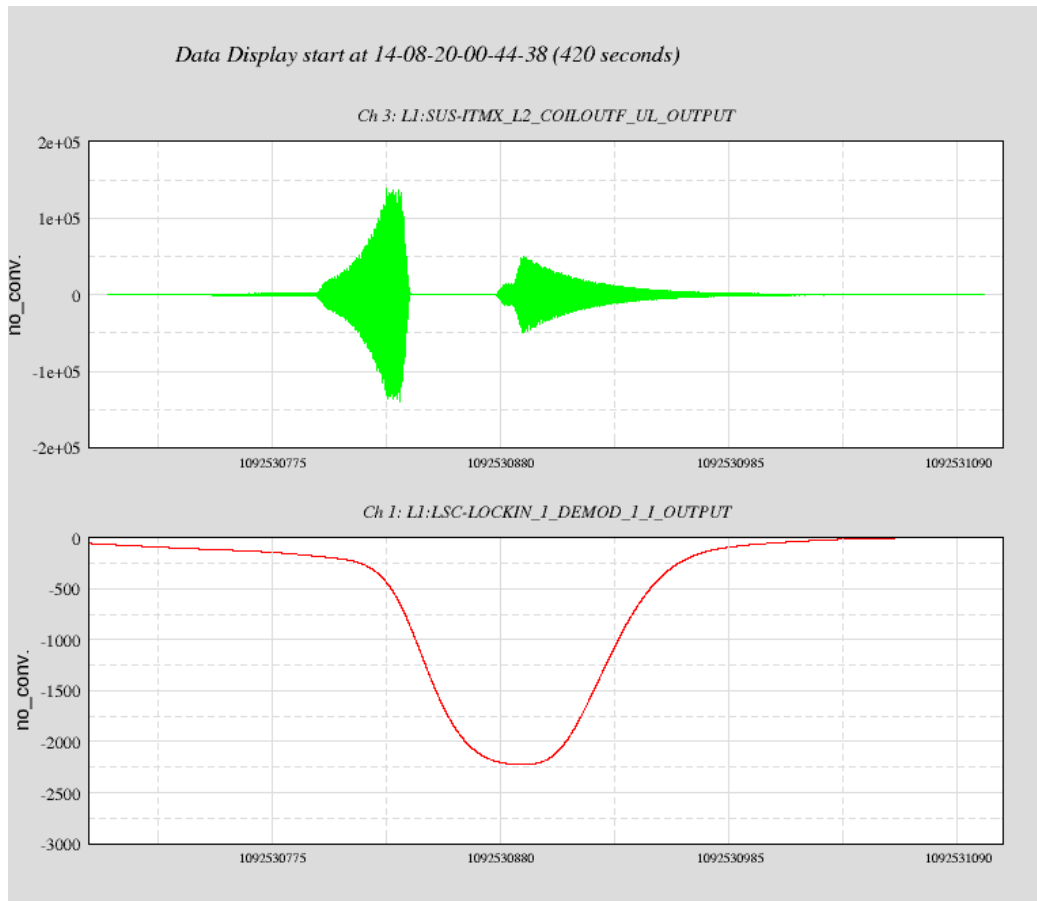


Figure 5.12: Excitation and damping of ITMX violin modes. Top plot shows control signal to suspension L2 actuator. Bottom plot shows amplitude of violin mode.

Damping of suspension modes completes process of lock acquisition and transition of the instrument to low noise regime. Next part of this thesis describes online calibration of data and sensitivity analysis of interferometer.

## Chapter 6

# Instrument calibration

During the process of calibration photodetector output signals in units of Amperes or Volts are converted to meters or units of strain [59]. Calibration in physical units is important for parameter estimation of astrophysical objects.

Process of noise hunting is also more robust when the instrument is properly calibrated. For this reason, online calibration of gravitational wave and auxiliary channels was developed to monitor noise level in real time.

This chapter describes online calibration of aLIGO interferometers. The first section gives overview of front end model and mathematical principles of calibration. The second chapter is devoted to actuator calibration using simple Michelson interferometer, ALS beat notes signals, and photon calibrators. The third section of this paper describes the measurement of DARM cavity pole.

### 6.1 Front end model

Figure 6.1 shows the model of differential arm feedback loop and the process of online calibration. External disturbances  $x$  include gravitational wave signals and instrument noises and are estimated based on feedback loop algebra:

$$x(t) = s'(t) + e'(t) \tag{6.1}$$

where  $s'$  is optic motion due to control signal,  $e'$  is residual unsuppressed motion. These signals are calibrated to units of meters.

Signals  $s'$  and  $e'$  are estimated using signals  $e$  and  $s$  are feedback error and control signals measured in the digital system. These signals have dimensions of counts and even though they are related to each other by equation  $s(t) = G * e(t)$ , it is convenient to use both of them since in this

case any modification to servo  $G$  will not affect the calibration:

$$\begin{aligned} e(t) &= C \cdot PD \cdot AA_{analog} \cdot ADC \cdot AA_{iop} D_{error} * e'(t) \equiv C \cdot Q \cdot D_{error} * e'(t) \\ s'(t) &= D_{ctrl} \cdot AI_{iop} \cdot DAC \cdot AI_{analog} \cdot SUS * s(t) \equiv D_{ctrl} \cdot P * s(t) \end{aligned} \quad (6.2)$$

where  $C$  is optical transfer function in units of Watts / meters;  $PD$  is transfer function of the photodiode in units of Volts / Watts that includes quantum efficiency (0.86) and internal electronics that converts Watts to Amps and then Amps to Volts;  $ADC$  and  $DAC$  converts Volts to digital counts and vice versa;  $AA_{analog}$ ,  $AI_{analog}$  [Volts/Volts] and  $AA_{IOP}$ ,  $AI_{IOP}$  [cnts/cnts] are low-pass filters used to prevent data corruption;  $SUS$  is suspension transfer function in units of meters / Volts.

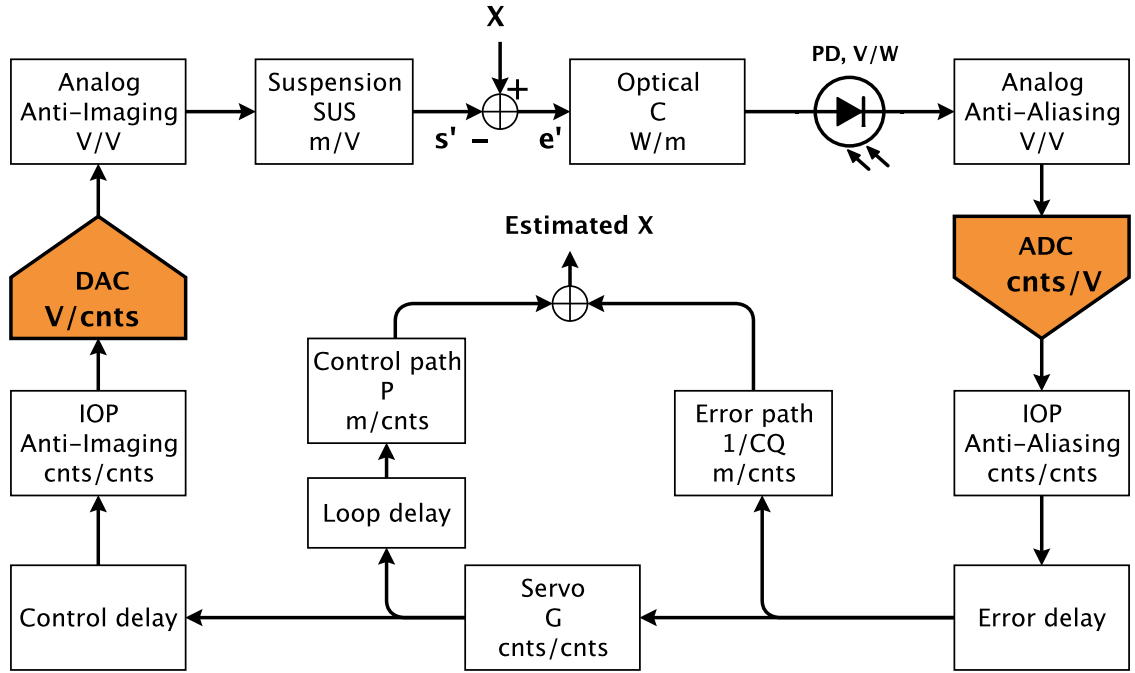


Figure 6.1: Calibration of external disturbance.

Sets of transfer functions in error and control paths are combined into groups  $Q$  and  $P$  since these elements are invertible and time independent. Once measured, these transfer functions are changed in the calibration model only after major hardware update.

Delays in the error and control paths  $D_{error}$  and  $D_{ctrl}$  arise from transmission path between the models and DAC hold. Since delays are not invertible, online calibrated disturbance is delayed:

$$x(t - t_{error}) = P * s(t - t_{loop}) + \frac{1}{C \cdot Q} * e(t) \quad (6.3)$$

where  $t_{error}$  is time delay in the error path,  $t_{loop} = t_{error} + t_{ctrl}$  - full loop delay equal to 230usec.

If signal recycling cavity is not detuned then frequency shape of optical transfer function  $C$  is determined by a single pole. This pole depends on finesse of the arm and signal recycling cavities. Optical transfer function depends on power build-up in the cavities, and amplitude at DC is tuned in such way that calibrated control signal crosses calibrated error signal exactly at unity gain frequency. Power level in optical cavities depend on alignment, losses, and input power. Set of calibration lines is used to keep track of optical transfer function  $C$  as well as total calibration of the instrument.

Suspension transfer function in units of  $m/cnts$  is simulated using a dynamical model. A result is compared to the measurement in different frequency points.

## 6.2 Actuator calibration

Three independent techniques are used to measure aLIGO suspension transfer functions: Michelson interferometer, ALS DIFF beat note and photon calibrator.

### 6.2.1 Michelson interferometer

First of all, beam splitter transfer function is measured and then calibration is propagated to ITMs and further to ETMs by locking laser to the arm cavities.

In this calibration technique Michelson interferometer is formed with BS and ITMs and left in free swinging state. Heterodyne readout signal  $S$  from photodetector installed at the output port depends on the interferometer detuning  $x[m]$ :

$$\begin{aligned} S(x) &= S_0 \sin\left(4\pi \frac{x}{\lambda}\right) \\ \frac{dS}{dx}(x=0) &= 4\pi \frac{S_0}{\lambda} \end{aligned} \tag{6.4}$$

where  $S_0[cnts]$  is amplitude of the photodiode signal measured when Michelson interferometer is in free swinging state.

Once PD calibration is known, Michelson interferometer is locked on dark fringe  $x = 0$  actuating on beam splitter. Transfer function  $T = P_{BS} \cdot \frac{dS}{dx}[cnts/cnts]$  from BS actuation signal (feedback control plus excitation signals) to PD output is measured. BS transfer function  $P_{BS}$  in units of  $[m/cnts]$  is derived from the measurement  $T$ :

$$P_{BS} = T \frac{dx}{dS} = T \frac{\lambda}{4\pi S_0} [m/cnts] \tag{6.5}$$

Equation 6.5 implies that measured transfer function  $T$  should be multiplied by a single number  $\frac{\lambda}{4\pi S_0}$  and feedback control loop does not introduce errors in the measurement.

Figure 6.2 shows comparison of BS M2 stage model and measured transfer functions. Model fits the measurement with precision of 5% in the frequency range  $2 - 80\text{Hz}$ . At low frequencies transfer functions are different due to local angular control servos that are not included in the model. Above suspension resonances transfer function can be approximated as  $2 \cdot 10^{-11} f^{-4} [m/cnts]$ . This approximation is valid below  $100\text{Hz}$  since at higher frequencies violin modes corrupt actuation due to broadband resonances.

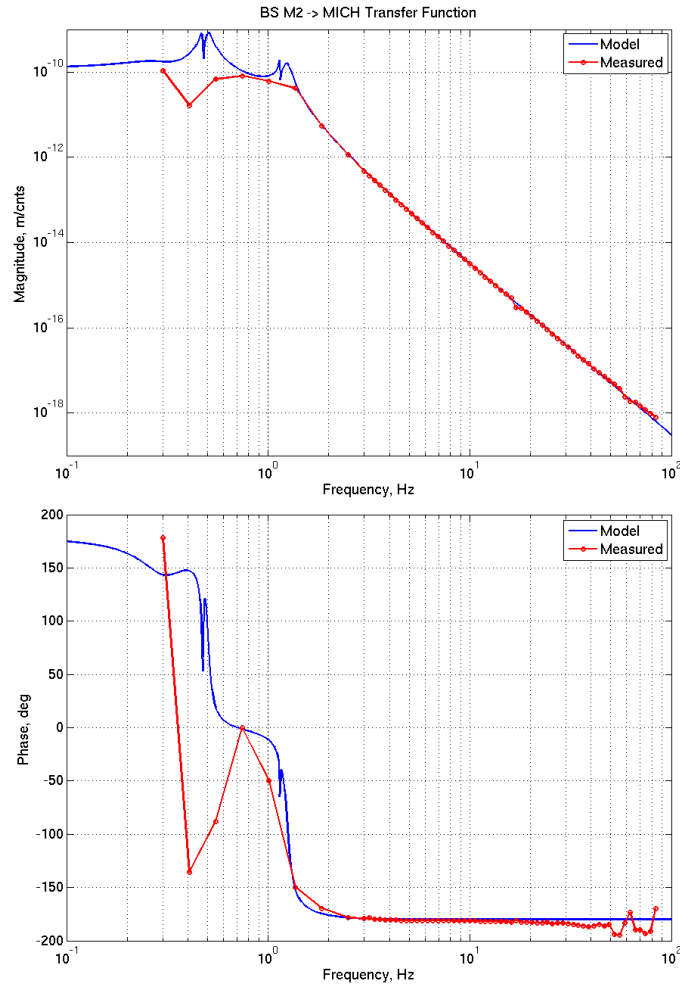


Figure 6.2: Beam splitter calibration using Michelson interferometer.

Errors in the actuator calibration using simple Michelson interferometer come from frequency dependence of photodetector and actuator electronics. Analog whitening and dewhitening filters are compensated with the digital ones. Imbalances between digital and analog filters cause errors in the calibration.

### 6.2.2 ALS beat notes

In this optical configuration both X- and Y-arms resonate green light coming out from auxiliary lasers. ALS DIFF beat note in the corner station measures frequency difference between green beams coming out from the two arms. Photodiode signal is compared to VCO output using phase frequency discriminator (PFD). Control loop with bandwidth of 30kHz is running to lock VCO to PD signal using PFD output.

VCO calibration transfer function  $B, [Hz/V]$  is a reference in this technique. Differential motion of the cavities  $L_-[m]$  is extracted from VCO control signal  $K[V]$  according to equation:

$$L_- = K \cdot B \cdot \frac{L_0}{f_0} \quad (6.6)$$

where  $L_0 = 3994[m]$ ,  $f_0 = 5.64 \cdot 10^{14} Hz$  - frequency of green light.

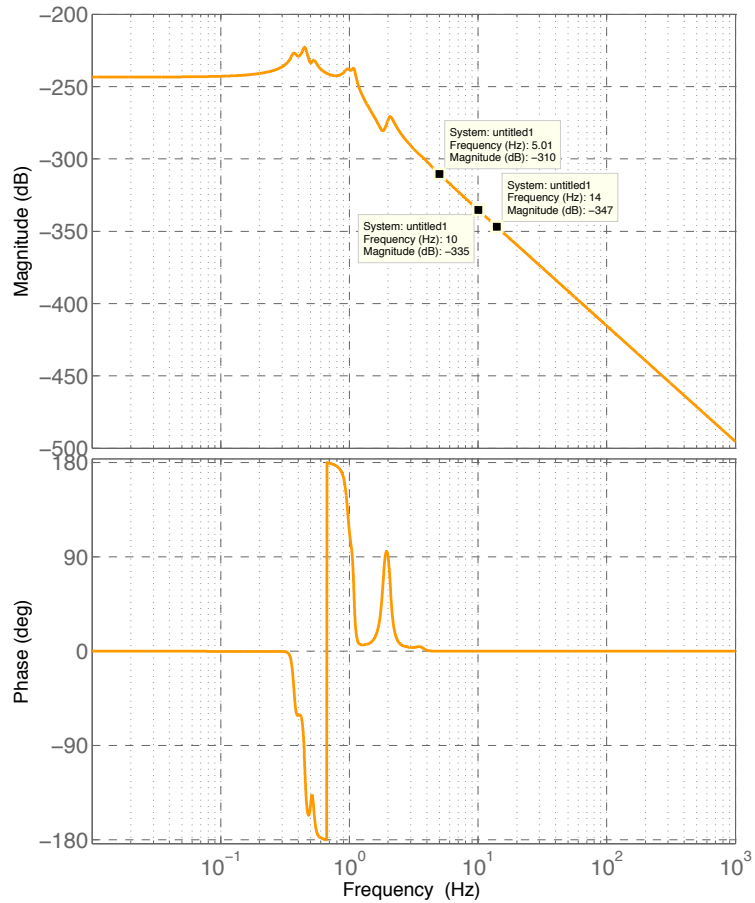


Figure 6.3: Calibration of L2 stage actuator using ALS DIFF beatnote.

Figure 6.3 shows comparison between measured test mass L2 actuation transfer function and fit based on the model. During the calibration procedure test masses were excited at different frequencies in the range 5-15Hz and response in VCO control signal was measured. Calibration

at higher frequencies is limited by the actuator strength and noise level of ALS DIFF beat note. Above suspension resonances transfer function can be approximated as  $1.7 \cdot 10^{-13} f^{-4} [m/cnts]$ . This approximation is valid below 100Hz since at higher frequencies violin modes corrupt actuation due to broadband resonances.

### 6.2.3 Photon calibrator

Auxiliary  $Nd^{3+}$  : *YLF* lasers operating at a wavelength of 1047 nm are installed at both end stations and direct laser beams to ETMs [60]. Intensity of the laser beam is modulated using AOM, and actuation on the test mass is produced by radiation pressure force. Intensity of the reflected beam is measured using integrating sphere. Calibration of this photodetector is a reference in this calibration technique. Once optical power  $P$  on the test mass is measured in units of Watts, optic motion  $x$  in units of meters is given by equation:

$$\frac{x}{P}(f) = -\frac{\cos(\theta)}{Mc2\pi^2} \frac{1}{f^2} \quad (6.7)$$

where  $M$  is mass of the optic,  $\theta$  - angle of incidence of laser beam on the test mass,  $f$  - frequency of intensity modulation. Since equation 6.7 assumes that test mass is free, the equation is correct only if frequency of actuation  $f$  is above suspension resonances  $f \geq 5Hz$

Most significant calibration errors and uncertainties of this technique come from calibration of the photodetector and optical losses between input and output of the laser beam. Mass of the optics  $M$  and angle of laser beam incidence on the test mass  $\theta$  introduce less uncertainties. A lot of attention is paid to calibration of the integrating spheres. These detectors are compared to the one calibrated at NIST with precision of 1%. Optical power lost between input and output ports was measured to be 1.5%. Total calibration error of this technique is computed to be less then 3 – 4%.

## 6.3 Error point calibration

Optical transfer function  $C$  is frequency dependent due to DARM pole at 385Hz according to theoretical computations. This number was verified by measuring transfer function from ETMX L3 actuation signal to OMC PD signal in full lock. High frequency DARM control was sent to ETMX L3 stage and measured transfer function  $E = P_{L3}C[W/cnts]$  was used to derive optical transfer function  $C$ . Since  $P_{L3}[m/cnts]$  is measured using techniques described in the previous section, the equation for  $C[W/m]$  can be written as:

$$C = \frac{E}{P_{L3}} [W/m] \quad (6.8)$$

Figure 6.4 shows measured optical DARM transfer function. Double cavity pole is 390Hz with

precision of 10%. Loop delay  $D_{loop}$  is derived from the phase of the transfer function  $C$ .

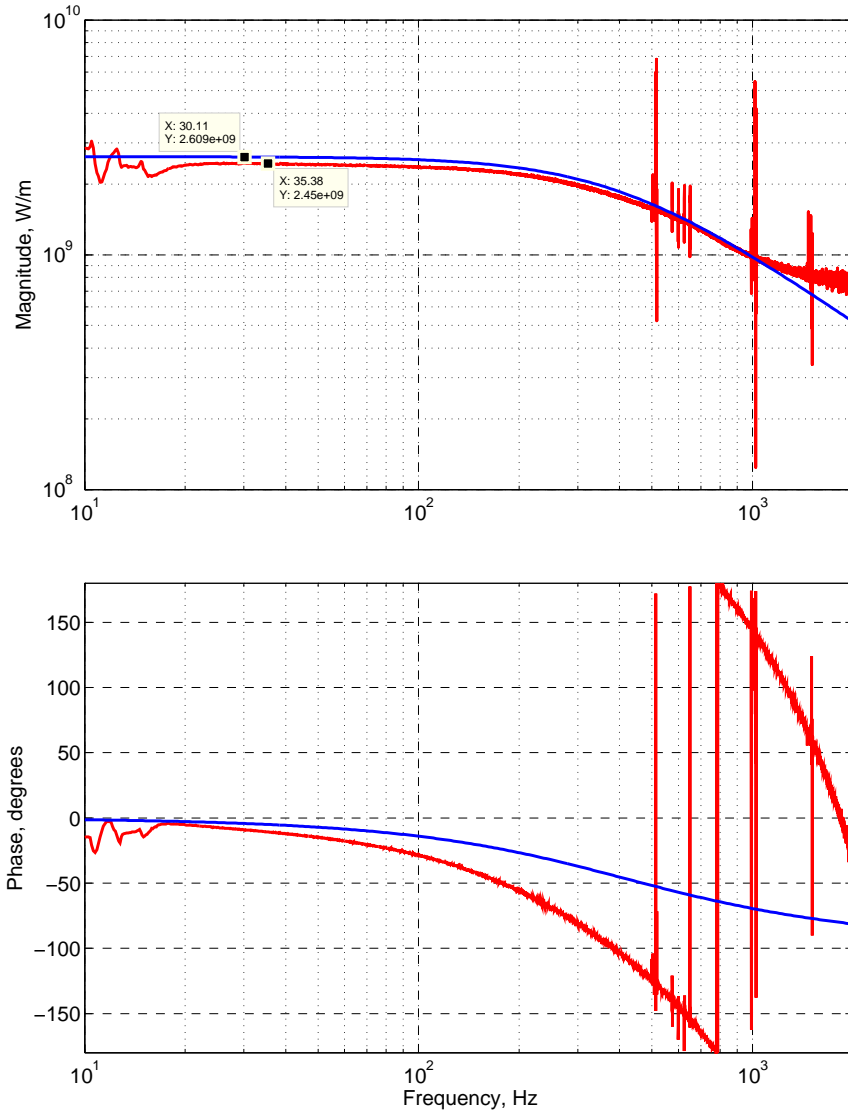


Figure 6.4: Measurement of the DARM pole.

DC gain of optical transfer function  $C$  is corrected relative to the actuator strength. Open loop  $H$  is measured in full lock and compared with ratio of DARM control and error signals. Since  $H(f) = s'(f)/e'(f)$  in the frequency domain, DC gain of  $C$  is adjusted to fit measured open loop transfer function as shown in figure 6.5.

Once DC gain of  $C$  is measured, it can be compared with simulated value. Figure 6.4 shows that simulated and measured DC gains of DARM optical transfer function agree within 10%. This measurement is used to derive optical losses at the output port as described in section 8.2.

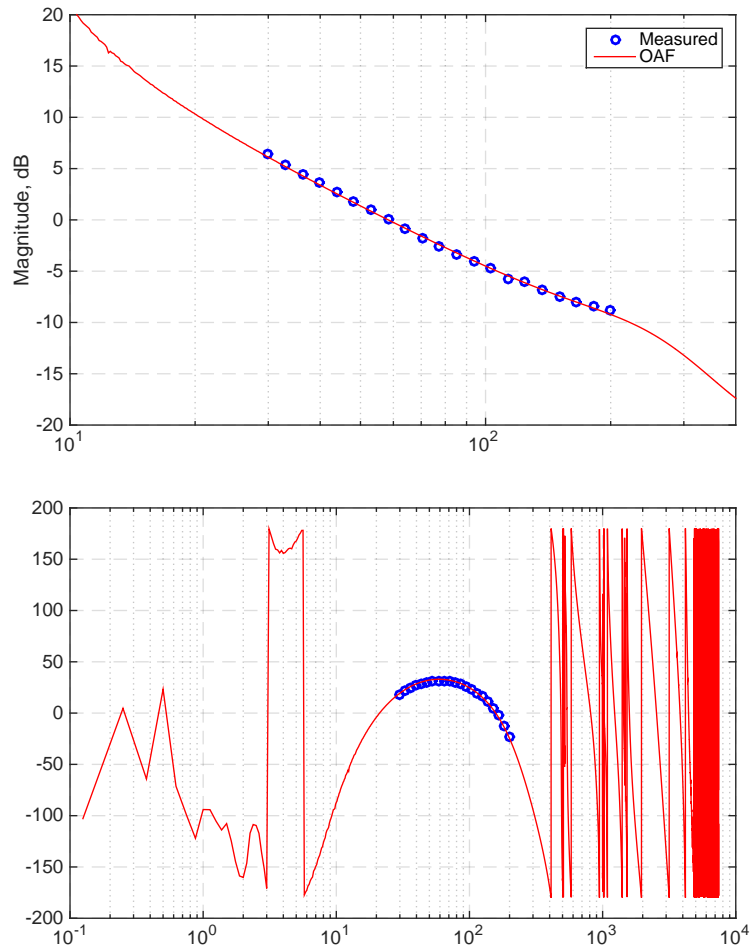


Figure 6.5: Comparison of DARM open loop transfer functions obtained from the calibration model and loop sweep.

## 6.4 Total DARM calibration

Calibrated DARM control and error signals are summed to produce online estimation of gravitational wave signal. Since each calibration step introduces errors, final DARM calibration is verified using photon calibrator. Figure 6.6 shows transfer function from calibrated radiation pressure signal to DARM. These transfer functions match with precision of 5% in the frequency range 10Hz - 1kHz. Actuation strength of photon calibrator is currently not large enough to measure DARM optical response above 1kHz.

When aLIGO interferometer collects data, several calibration lines are constantly running to maintain precision of the calibration. Lines are produced using photon calibrator and suspension

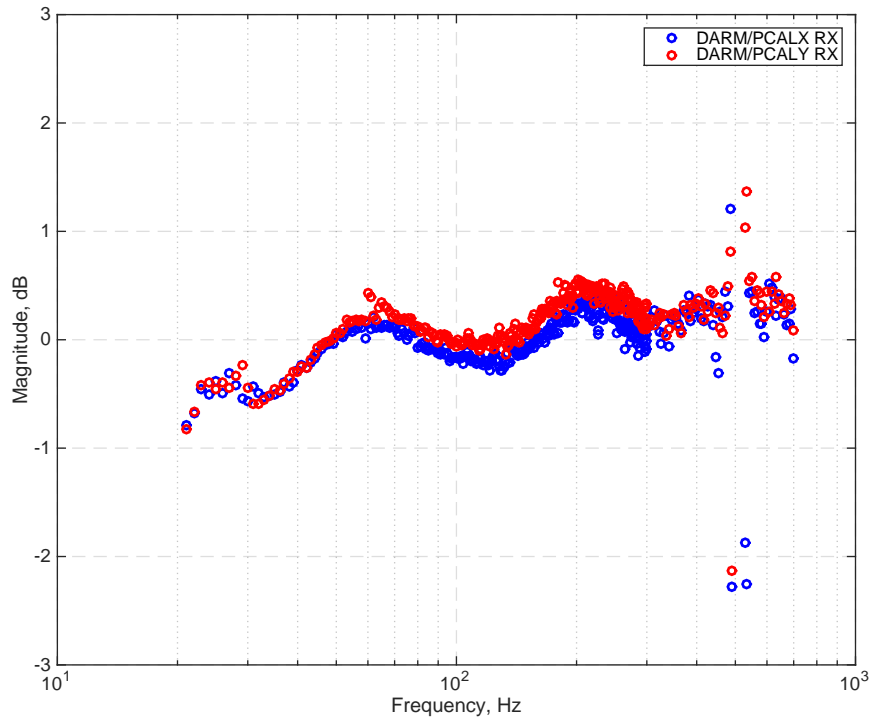


Figure 6.6: Check of the final DARM calibration using photon calibrators.

actuators. Heights of calibration lines in the DARM spectrum change by 3 – 4% RMS when ground velocity is  $1\text{um}/\text{sec}$ . During winter time when ground motion is on the level of  $2\text{um}/\text{sec}$ , height of calibration lines fluctuated by 7% RMS.

Frequency shaping in the calibration of gravitational wave channel seen in figure 6.6 and modulation of DARM optical response come from the following aspects:

- Analog whitening filters of the actuators are not perfectly compensated in the digital domain.
- Frequency of the DARM pole depends on alignment of the signal recycling cavity, and calibration above 300Hz is sensitive to angular fluctuations of SRC mirrors.
- DC optical gain of DARM loop depends on OMC low frequency jitter and residual longitudinal motion of Michelson interferometer. DARM offset is modulated to suppress power fluctuations at OMC PDs, and optical gain follows DARM offset.
- Compensation for the loop delay in the online system is possible to set up with precision of 61usec. This number equals to one cycle of the calibration model running at 16kHz.
- Analog whitening filters of the OMC photodetectors are compensated with precision of 1% using digital filters.

## Chapter 7

# Data quality

Interferometer output signal is the sum of gravitational wave signal and instrument noises. The goal of aLIGO commissioning team is to reduce stationary noises and rate of glitches in gravitational wave channel and improve signal to noise ratio for precise characterization of astrophysical sources.

Initial LIGO noises were described in [61]. Designed instrument sensitivity was achieved in 2009 during the last science run of initial LIGO. Best BNS range achieved during S6 run was 22Mpc, and many interesting results were obtained but no gravitational wave sources were detected.

Designed advanced LIGO sensitivity is an order of magnitude higher compared to initial detectors in the frequency band 40Hz - 5kHz, and several orders of magnitude in the frequency range 10Hz-40Hz due to improvements in seismic isolation system. Some noises limiting aLIGO sensitivity, like laser amplitude noise, BOSEM noise, and shot noise, were studied in initial LIGO. Other noises, like squeezed film damping, charging noise, and ESD noise, are new to LIGO interferometers.

Stationary noises can be divided in categories by different parameters. One such division can be made based on the coupling mechanism: displacement and sensing noises. The first type of noises, like seismic noise, thermal noise and actuator noise, move test masses and create signal to gravitational wave channel. The second type, like PD dark noise, shot noise and frequency noise, do not move the mirrors but couples to gravitational wave channel on the detection side. Some noises, like laser amplitude noise, can be assigned to both categories.

Another possible division of noises into categories can be done based on the nature of noises: fundamental and technical noises. First category of noises, like coating Brownian noise, suspension thermal noise, or quantum noise, can not be eliminated from the instrument sensitivity curve before a major instrument upgrade that involves cryogenics, increasing input laser power and size of the beams on test masses. Second category, like noises from angular controls or auxiliary length loops and scattered light, can be reduced by minimizing coupling or magnitude of these noises in such way that their residual level is smaller compared to irreducible fundamental noises.

Non-stationary noise sources and glitches are also harmful to the instrument sensitivity to gravitational waves. Glitches in gravitational wave channel can originate from the processes, like DAC

zero crossings, IPC errors, or cross talk of RF electronics, and are hardly distinguishable from bursts of astrophysical origin [62]. Non-stationary noises, like input beam jitter and scattering noise, also add power to interferometer sensitivity curve and generate triggers as potential signals from gravitational waves.

This chapter describes current aLIGO sensitivity curve and noise couplings measured and modeled during commissioning period. Best BNS range achieved at the time of this writing is 67Mpc. Optical configuration in low noise regime is shown in figure 7.1. Input PSL power is 25W, interferometer visibility is 98.5%, power recycling gain is 38, darm offset is 12pm, and round trip losses in the arm cavities are 90ppm.

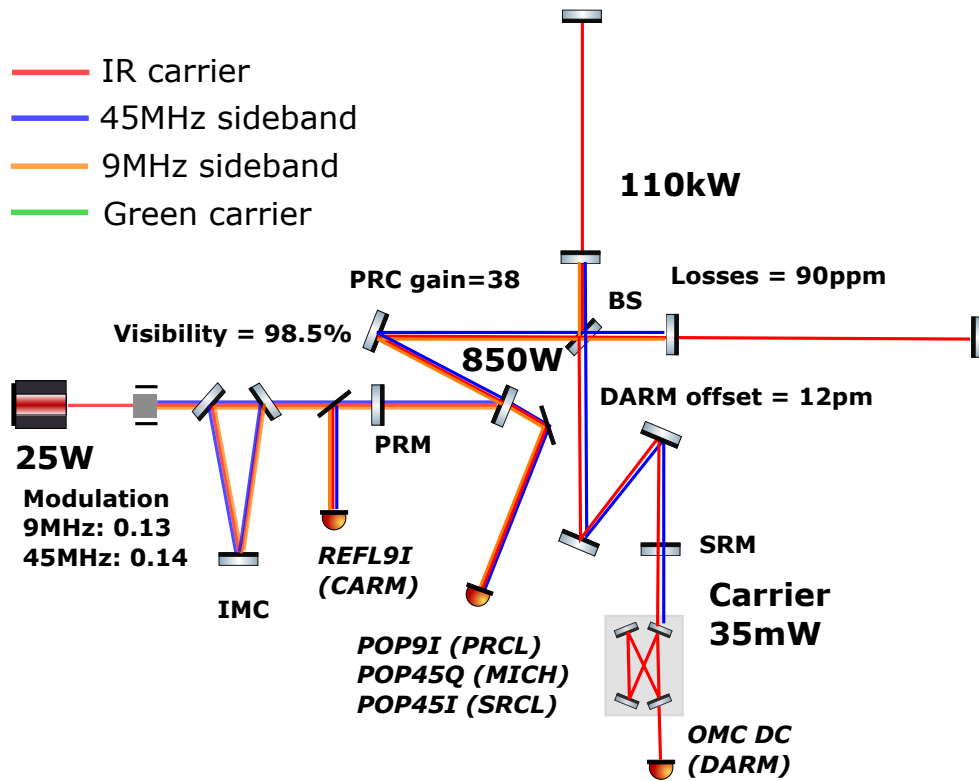


Figure 7.1: Interferometer optical configuration in low noise regime.

Figure 7.2 shows DARM spectrum calibrated to units of  $m/\sqrt{Hz}$  and couplings from known noises. These couplings are discussed in detail in this chapter. Sections 1-6 discuss fundamental noises, coupling of potential fluctuations of metal around end test masses to DARM through surface charge on the test mass, actuation and sensing noises, coupling of auxiliary length and angular loops, intensity and jitter noise, and noise coming from residual gas. Section 7 describes origin and frequencies of narrow lines present in the DARM spectrum. Section 8 describes sources of glitches found during aLIGO commissioning.

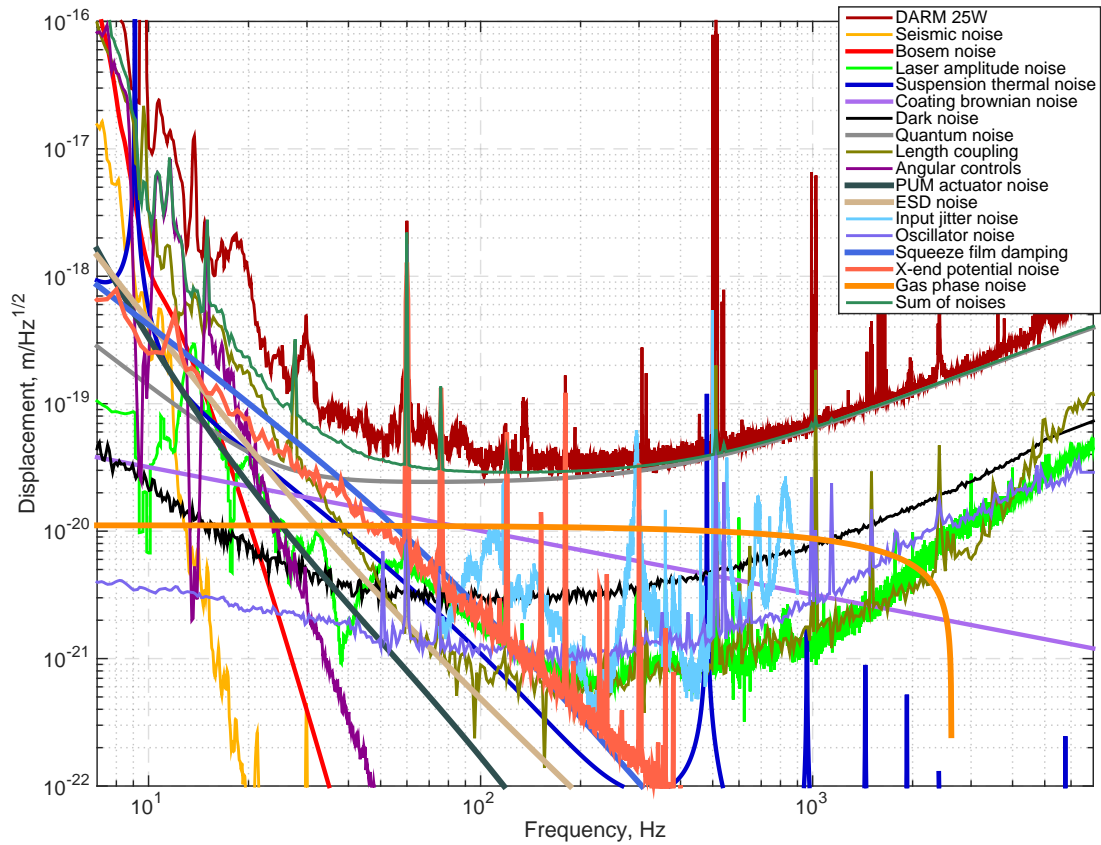


Figure 7.2: DARM sensitivity curve and known noise couplings.

## 7.1 Fundamental noises

Figure 7.3 shows coupling of suspension, substrate and coating thermal noises, seismic noise, quantum noises, and gravity gradient noises [63] to gravitational wave channel. These noises cannot be reduced or subtracted from gravitational wave channel under current interferometer configuration shown in figure 7.1.

### 7.1.1 Quantum noise

Zero vacuum fluctuations that enter interferometer through the antisymmetric port couple to interferometer sensitivity through quantum radiation pressure noise and shot noise [64]. Quantum radiation pressure noise is displacement noise and actuates on test masses due to quantum power fluctuations  $\delta P$  in the arm cavities [65]:

$$x(f) = \frac{\delta P}{2Mc\pi^2} \cdot \frac{1}{f^2} [m] \quad (7.1)$$

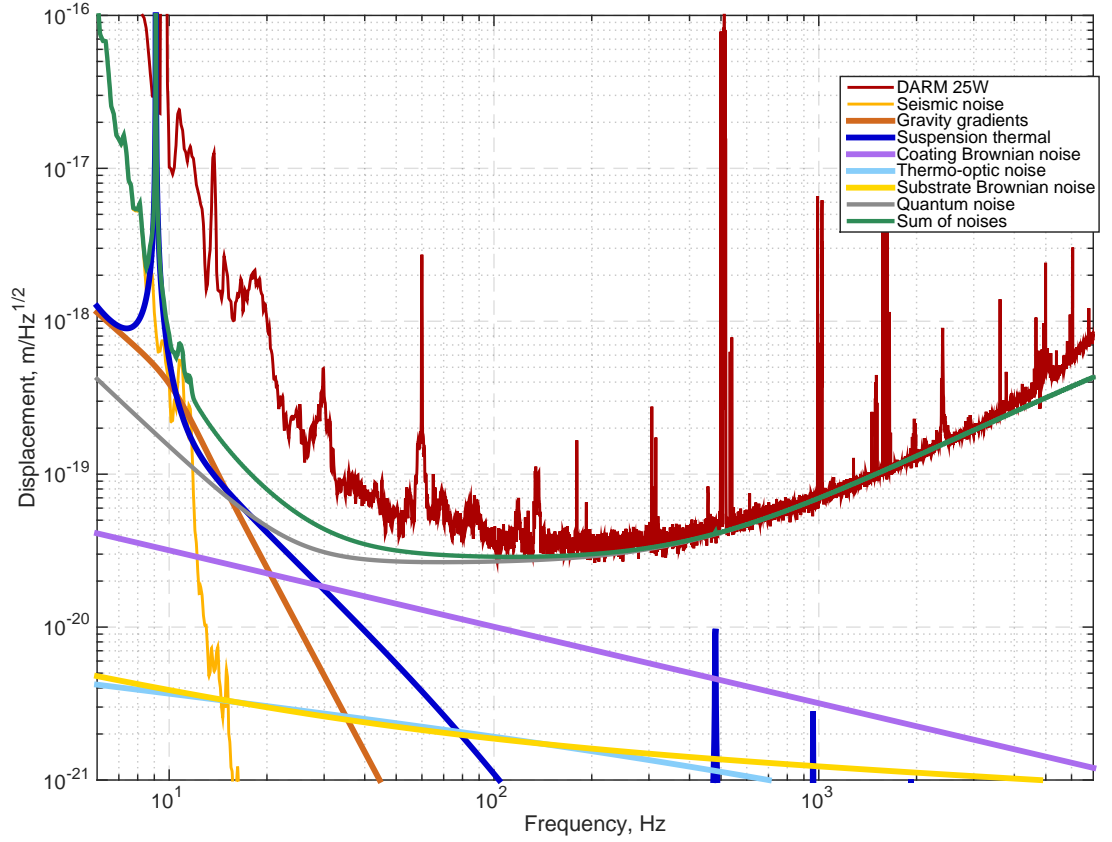


Figure 7.3: Coupling of fundamental noises to DARM.

where  $x(f)$  is motion of the mirror with mass  $M$ .

Shot noise couples on the sensing side and originates from finite amount of photons incident on the photodetector. If carrier laser beam of power  $P$  leaves interferometer through antisymmetric port, relative intensity noise on the OMC photodetectors due to shot noise is given by equation:

$$\delta RIN(f) = \sqrt{\frac{2h\nu}{P}} \quad (7.2)$$

where  $h = 6.62 \cdot 10^{-34} m^2 kg/s$  is Planck constant,  $\nu = 2.82 \cdot 10^{14} Hz$  is frequency of light.

Computation of quantum noise in aLIGO interferometers with detuning of signal recycling cavity is based on [66]. In case of zero detuning and under optical configuration shown in figure 7.1 quantum radiation pressure and shot noise can be estimated as:

$$\begin{aligned} \delta DARM_{rad} &= 1.4 \cdot 10^{-19} \sqrt{\frac{P_{in}}{25W}} \left(\frac{10Hz}{f}\right)^2 |C(f)| \frac{m}{\sqrt{Hz}} \\ \delta DARM_{shot} &= 2.0 \cdot 10^{-20} \sqrt{\frac{25W}{P_{in}}} \frac{1}{|C(f)|} \frac{m}{\sqrt{Hz}} \end{aligned} \quad (7.3)$$

### 7.1.2 Thermal noise

Random thermal motion of particles in suspension, mirror substrate and surface produces displacement noise to gravitational wave channel. Power spectral density of DARM coupling can be computed using fluctuation-dissipation theorem [67]:

$$DARM(f) = \sqrt{\frac{2k_B T}{\pi f} \text{Im}[H(f)]} \quad (7.4)$$

where  $k_B = 1.38 \cdot 10^{-23} \text{ m}^2 \text{ kg/s}^2 / \text{K}$  is Boltzmann constant,  $T \approx 295 \text{ K}$  is temperature of material,  $H(f) = x/F$  is linear response of the system,  $x$  is longitudinal coordinate,  $F$  is applied force.

Dissipation mechanism can be classified as following [68]:

- Viscous damping is caused by the force that is proportional to velocity. Examples of viscous damping are forces due to air resistance, eddy currents, and electrostatic drive impedance. Coupling to DARM above suspension resonance  $f_0$  is given by

$$DARM(f) = \sqrt{\frac{k_B T f_0}{2\pi^3 M Q} \frac{1}{f^2}}, f \gg f_0 \quad (7.5)$$

Thermal noise due to air resistance depends on residual gas pressure and is considered in section 7.6. Damping caused by capacity change, when reaction and test mass move relative to each other, depends on ESD circuit parameters and equals to  $Q = 4.5 \cdot 10^9$  [69] if ESD bias is  $V_0 = 400 \text{ V}$ . Thermal noise level according to equation 7.5 is

$$DARM(f) = 1.5 \cdot 10^{-19} \left( \frac{10 \text{ Hz}}{f} \right)^2 \frac{m}{\sqrt{\text{Hz}}} \quad (7.6)$$

DARM noise determined by equation 7.6 is computed for the gap between test mass and reaction mass of 5mm. Thermal noise is also proportional to bias voltage  $V_0$ . In full lock control is switched to ITMs with larger gap between test mass and reaction mass. Bias voltage is also reduced down to  $V_0 = 100 \text{ V}$ , and coupling of thermal noise due to ESD impedance becomes negligible.

- Structure damping is caused by internal loss, and loss angle is frequency independent. Suspension thermal above suspension resonance frequency  $f_0$  for one test mass is estimated as:

$$x_m(f) = \sqrt{\frac{k_B T f_0^2}{2\pi^3 M Q} \frac{1}{f^{5/2}}}, f \gg f_0 \quad (7.7)$$

$Q$ -factor can be estimated from ring down time of violin modes. Due to long ring down time and excitation of violin modes during lock losses,  $Q$ -factor was not yet measured precisely.

However, estimations from 30 hour lock give ring down time of approximately 7 days and  $Q_v \sim 10^9$ . Since  $Q \approx Q_v/2$ , total contribution to DARM from all four test masses is:

$$DARM(f) \approx 3 \cdot 10^{-19} \left( \frac{10Hz}{f} \right)^{5/2} \frac{m}{\sqrt{Hz}} \quad (7.8)$$

Coating thermal noise directly changes arm cavity length and is a weak function of frequency since it is not filtered by suspension as ESD impedance damping or suspension thermal noise. aLIGO HR coatings consist of alternate  $SiO_2$  and  $Ti_2O_5$  dielectric layers. Applying fluctuation dissipation theorem, the position of the coated mirror yields [70, 71]

$$x_m(f) = \sqrt{\frac{2kTd}{\pi^2 f w^2 Y} \left( \frac{Y'}{Y} \phi_{\parallel} + \frac{Y}{Y'} \phi_{\perp} \right)} \quad (7.9)$$

where  $w$  is beam size on the optic,  $d$  is coating thickness,  $\phi_{\parallel}$  and  $\phi_{\perp}$  is loss angles of coating,  $Y$  is Young's modulus of mirror substrate,  $Y'$  is Young's modulus of coating. The equation implies that coating thermal noise decreases proportionally to the beam size.

According to equation 7.9, coating Brownian thermal noise depends on frequency as  $1/f^{1/2}$ . This slope makes it one of the major aLIGO noise sources in the frequency range 10Hz-1kHz, as shown in figure 7.3. Upper limit on coating thermal noise was set by cross correlating two OMC photodiodes. Since coating thermal noise, unlike sensing noises, is coherent between two PDs, it was possible to set an upper limit for the noise at 300Hz. Upper limit is consistent with GWINC prediction [72]:

$$DARM(f) = 3.2 \cdot 10^{-20} \left( \frac{10Hz}{f} \right)^{1/2} \frac{m}{\sqrt{Hz}} \quad (7.10)$$

Coating Brownian noise dominates thermal noise of the mirror. Other thermal noises arise from thermoelastic and thermorefractive fluctuations in the mirror substrate and dielectric coatings and mechanical loss in the mirror substrate [73, 74]. As shown in figure 7.3, these noises are significantly smaller compared to coating Brownian noise in the frequency range 10Hz-1kHz. Mirror thermal noises are computed using GWINC software.

### 7.1.3 Seismic noise

Ground motion on Earth is caused by ocean waves, winds, human activity, earthquakes, and other sources. By design aLIGO optics should be isolated from the ground motion by more than 9 orders of magnitude in the observation band at frequencies higher than 10Hz. It is also important to reduce seismic noise coupling at lower frequencies for robust lock acquisition and to minimize optics angular motion.

Three levels of seismic isolation are used in advanced LIGO:

- Hydraulic External Pre-Isolators (HEPIs) [75] support each payload using four piers. System was successfully applied in initial LIGO for active isolation of optical tables using inductive position sensors, inertial L4C geophones, and STS-2 seismometers. In aLIGO HEPIs are used to damp high frequency structure resonances and angular and longitudinal control as low frequencies. Each actuator-sensor pair can move optical table by  $\pm 1$  mm. At the time of this writing active isolation using HEPI systems is not used because actuators tilt optical tables and degrade performance of ISI isolation loops.

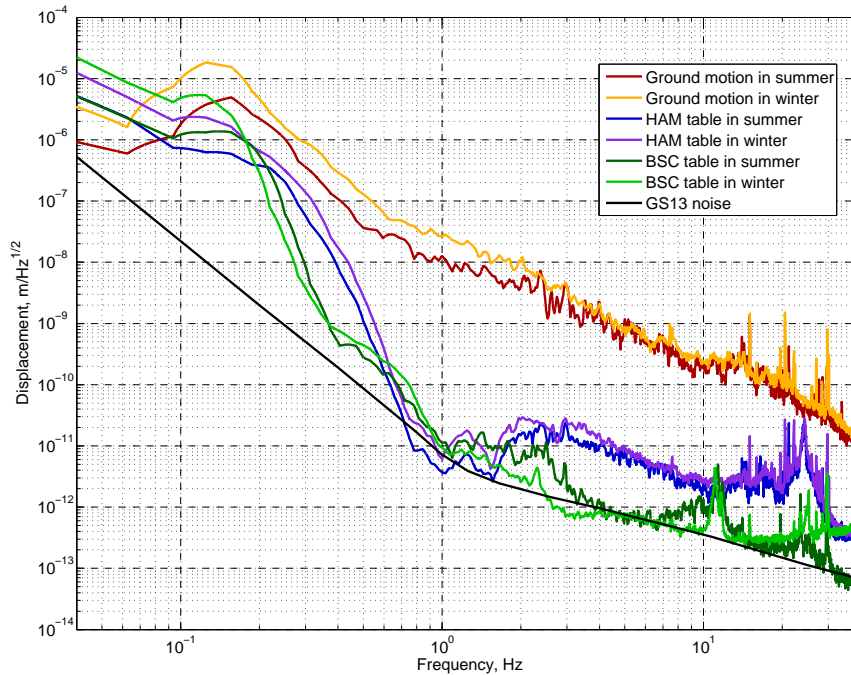


Figure 7.4: Seismic noise and motion of isolated optical tables during summer and winter time.

- Internal Seismic Isolation (ISI) [76] tables are designed for Horizontal Axis Modules (HAM) and Basic Symmetric Chambers (BSC). Major difference between these two systems is that HAM ISI has one stage while BSC ISI has two stages of active and passive isolation. The first type of ISIs is used for input, output, power and signal recycling optics. Tables of the second type provide more isolation and host beam splitter and test masses. Optical tables are suspended for actuation with coil-magnet pairs and for passive seismic isolation below suspension resonance of 1Hz. Table motion is sensed using inertial sensors GS13, T-240, L4C, and capacitive position sensors.

Active control loop bandwidth and blending frequencies between the sensors are determined by the noise floor of the sensors and mechanical resonances of the structures. Position and inertial

sensors are blended with crossover frequency varying from 45mHz to 700mHz depending on the chamber and degree of freedom. Feedforward from ground STS-2 seismometers is applied to position sensor signals to improve seismic isolation below 1Hz. Full bandwidth of isolation loops is set to 20-40Hz.

ISI tables provide excellent active isolation in the frequency range 0.1 - 10Hz. At higher frequencies ground motion is attenuated by passive suspension isolation. At lower frequencies ground motion is amplified by control system, and inertial sensor noise is injected causing the table to move by factor of 2-3 more compared to the ground. Figure 7.4 shows ground motion during summertime in Livingston, ISI platform motion, and optic motion.

Seismic isolation system reduces common mode rejection for short cavities like aLIGO input mode cleaner, power and signal recycling cavities, and simple Michelson interferometer. At microseismic frequencies, two points on the ground separated by  $\sim 10$  meters move together due to large wavelength of ground motion. The ratio between the relative motion of these two points and motion of each point can be as low as  $10^{-2}$ . However, seismic isolation system pushes the ratio up to 0.2 – 0.3 and increases the velocity of the short cavity fringe.

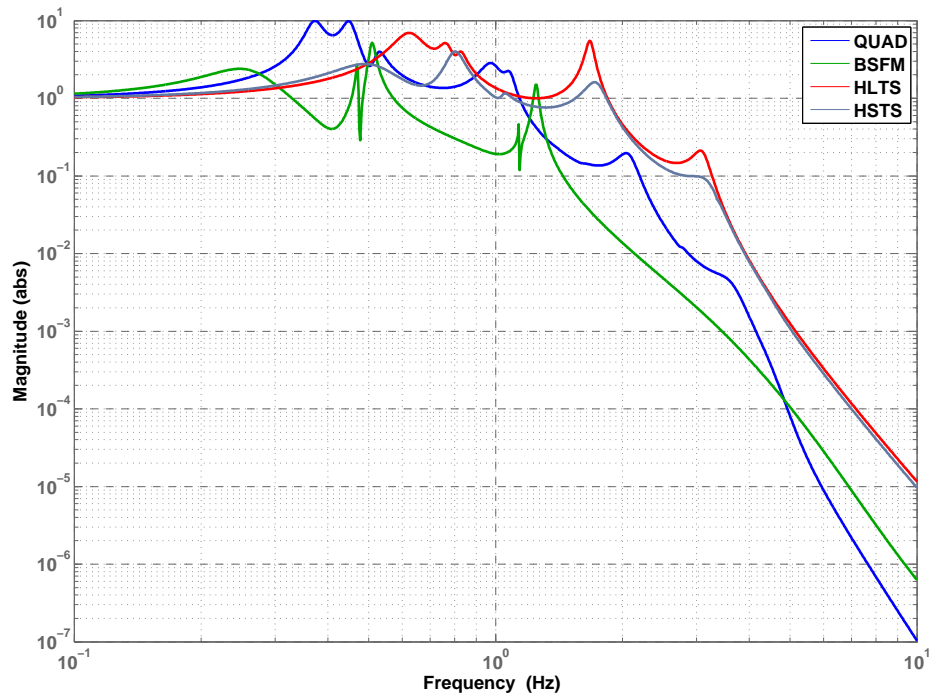


Figure 7.5: Transfer function from longitudinal table motion to optic motion.

- Suspensions [77] provide passive multistage isolation from optical bench to optic motion at frequencies below 0.5 Hz. Figure 7.5 shows transfer function from optical bench longitudinal motion to the optic motion. Quadruple suspension passively isolate optic from the table motion by 7 orders of magnitude at 10Hz.

Seismic noise coupling to gravitational wave channel shown in figure 7.3 is estimated by measuring optical bench motion using inertial sensors and propagating this motion through suspension transfer function 7.5.

## 7.2 Charging noise

During aLIGO commissioning phase it was found that front and back surfaces of end test masses are charged with density of  $\sim 10^{-11} C/cm^2$ . Front surface was losing electrons due to high energy photons from ion pumps located above the test mass. Back surface was charged while removing first contact from the mirror. Since the gap between compensation plate and test mass is only 5mm, discharging procedure was not efficient enough to remove all residual charges from the back surface of the test mass.

Charge from the front surface can be efficiently removed using ion guns [78, 79]. Positive and negative ions are introduced into the chamber, when pressure inside is 10-20 Torr, and annihilate surface charges on the front surface of the test mass. At the same time ions cannot reach back surface due to small gap between test mass and compensation plate.

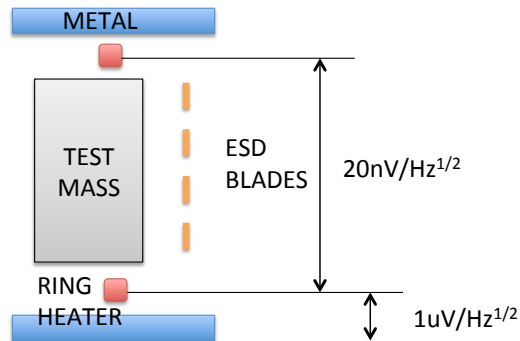


Figure 7.6: Side view of ETM with electrostatic blades, lower and upper ring heaters and metal cage.

The existence of charge on the back surface was confirmed by measuring transfer function from potential on electrostatic blades and ring heaters to DARM as shown in figure 7.7. Upper and lower ring heaters and electrostatic blades are behind front surface but on the different sides relative to the back surface, as shown in figure 7.6. Since signs of the transfer functions are different, measurement shows existence of charge on the back surface of the test mass.

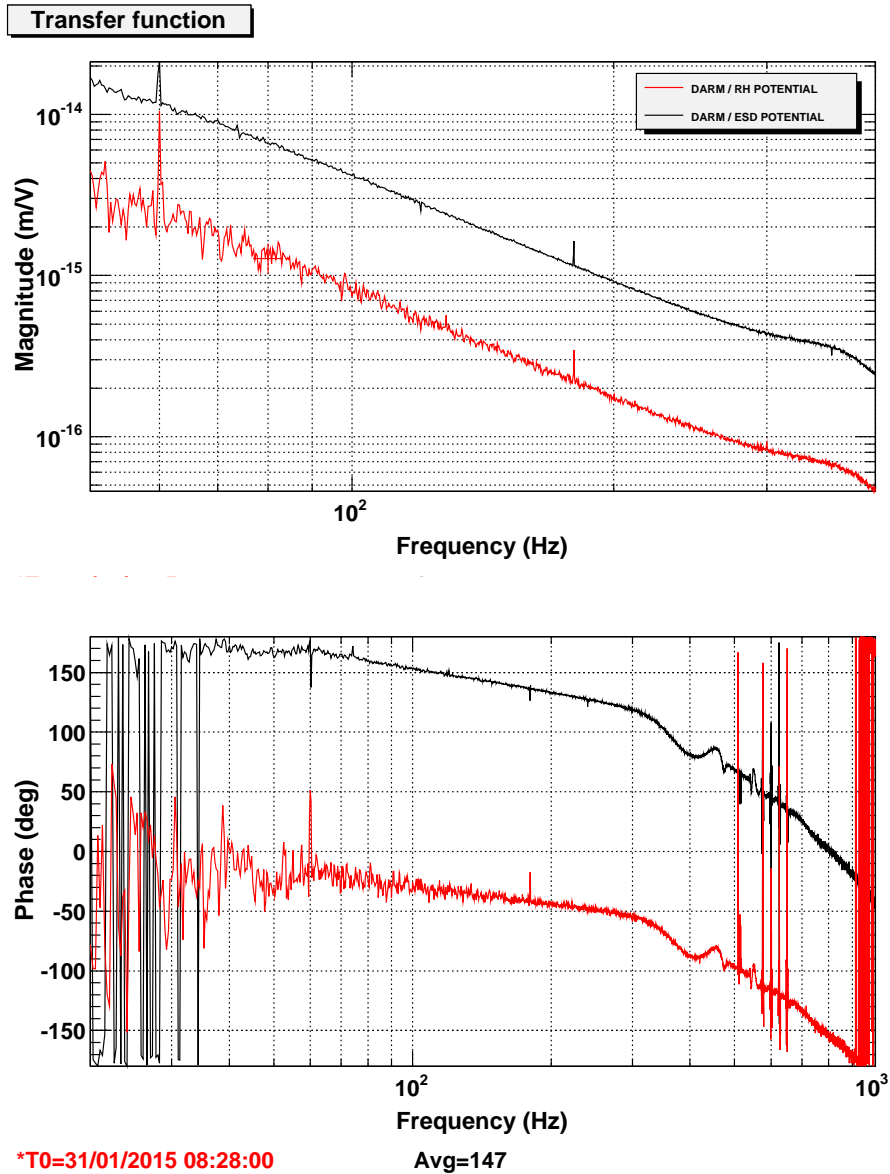


Figure 7.7: Transfer function from electrostatic blades and TCS ring heater to DARM.

By design, lines of electric field should originate and terminate on electrostatic blades with opposite polarity. Voltage between the blades is controlled by electrostatic driver, and test mass is attracted to the blades as dielectric slab to capacitor [80]. Direction of this force coincides with the cavity axis, and actuation from each electrode is longitudinal.

However, due to grounded metal around the test mass, lines of electric field terminate not only on electrostatic blades but also on suspension cage, test mass baffle, and ring heater shield. Metal around test mass creates another third capacitor blade and another force component. This force is also attractive but its direction does not coincide with cavity axis but is determined by geometry of

metal around the test mass.

Lines of electric field that leave electrostatic blades and terminate on surrounding metal go through the charge accumulated on the surface of the test mass. This force is linear in electric field and its direction is determined by the sign of the charge. Total electrostatic force on the test mass from the driver consists of three components:

$$\mathbf{F} = \alpha(V_0 - V_e)^2\mathbf{i} + \beta(V_0 + V_e)\mathbf{j} + \gamma(V_0 + V_e)^2\mathbf{k} \quad (7.11)$$

where  $V_0$  and  $V_e$  are voltages applied to electrostatic blades,  $V_0$  is known as bias voltage and is common to all four electrodes,  $V_e$  is called electrode voltage, while direction of unity vector  $\mathbf{i}$  coincides with arm cavity axis, and direction of unity vectors  $\mathbf{j}$  and  $\mathbf{k}$  is determined by metal around the test mass.

Force coefficient  $\beta$  due to charge on the test mass was estimated by setting DC values of bias and electrode voltages to zero and exciting electrode potential at 5Hz. According to equation 7.11, there is no linear component of the first and third components of electrostatic force. Excitation signal with zero DC voltage on the blades couples only through the charge on the test mass.

Force coefficient  $\gamma$  was estimated by applying the same DC voltage on the bias and electrode  $V_0 = V_e = V_{DC}$  and exciting electrode potential at 5Hz. First component of the force 7.11 is zero, second component is linear with excitation signal but does not depend on  $V_{DC}$ , and third component is linear with electrode excitation and scales with  $V_{DC}$ .

Table 7.1 shows measured projections of second and third force components from equation 7.11 on longitudinal direction.

$(\mathbf{i}, \mathbf{j})\beta/(\alpha \cdot 400V)$	-1.106	-1.018	-1.173	-1.048
$(\mathbf{i}, \mathbf{k})\gamma \alpha$	0.342	0.333	0.359	0.341

Table 7.1: Measured projections of electrostatic forces due to charge on test masses and surrounding metal on longitudinal direction.

Test masses are controlled by applying constant voltage to bias blades in the range  $V_0 = (-400V, 400V)$ . Equation 7.11 shows that larger bias voltage corresponds to larger actuation range. Control signal goes to electrode and changes voltage  $V_e$ . Electrostatic force due to metal around test mass reduces ESD range by a factor of  $(1 - (\mathbf{i}, \mathbf{k})\gamma \alpha)^{-1} \approx 1.5$ .

Coefficient  $\beta$  is proportional to charge and couples noise from potential fluctuation of the metal around the test mass and electrostatic driver noise even when bias voltage is set to zero. Unlike driver noise, potential fluctuations on the metal can not be eliminated unless test mass is discharged. Potential fluctuation on the test mass is estimated by measuring voltage between grounded chamber

wall and floating ring heater. This number is compared to voltage between two floating ring heaters:

$$\begin{aligned}\varphi_g - \varphi_{rh}^u &= \varphi_g - \varphi_{rh}^l = 1\mu V/\sqrt{Hz} \\ \varphi_{rh}^u - \varphi_{rh}^l &= 20nV/\sqrt{Hz}\end{aligned}\tag{7.12}$$

where  $\varphi_g$  is potential of the ground,  $\varphi_{rh}^u$  is potential of upper ring heater, and  $\varphi_{rh}^l$  is potential of lower ring heater.

These measurements suggest that potential fluctuations on the ground  $\varphi_g$  are much larger compared to fluctuations of floating ring heaters  $\varphi_{rh}^u$  and  $\varphi_{rh}^l$ . Ground potential fluctuations are likely caused by currents sunked to the ground from suspension and ISI electronics.

Since test mass is also floating, potential fluctuations on the test mass from grounded metal is assumed to be  $\sim 1\mu V/\sqrt{Hz}$ . Transfer function from potential fluctuations to gravitational channel is estimated using measured transfer function from ring heater potential and electrostatic blades to DARM shown in figure 7.7.

Figure 7.8 shows coupling of potential noise to DARM before test masses were discharged. Estimation of noise is confirmed by lines at 60Hz, 74Hz, and 180Hz that come from potential fluctuation of metal around the test mass.

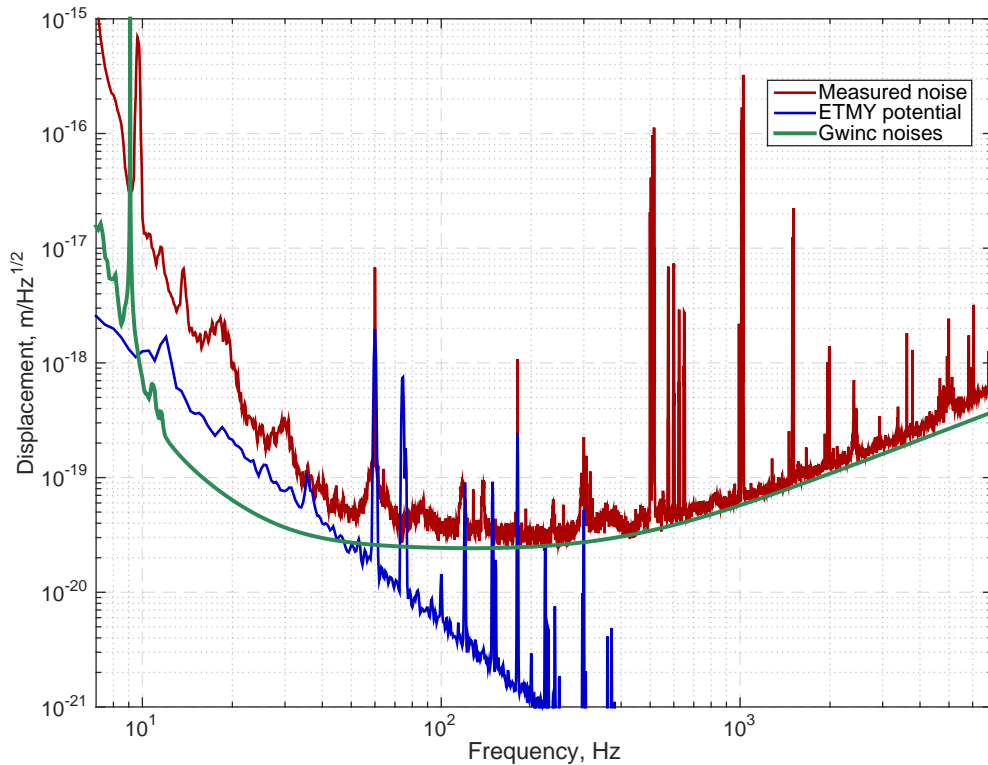


Figure 7.8: Potential noise coupling to DARM through static charge on end test masses.

Back surface of end test masses was discharged by opening the chambers, pulling reaction mass back and shooting ions directly on the back surface. Residual charge was monitored using electrometer. Discharging process was going before electrometer showed small enough values. After discharging process, residual charge on test masses, and the coupling of potential noise was reduced by factor of  $\sim 100$ .

## 7.3 Sensing and actuation

Figure 7.9 shows displacement noises from electrostatic and penultimate actuators, local damping, and electronics noise of OMC photodetectors.

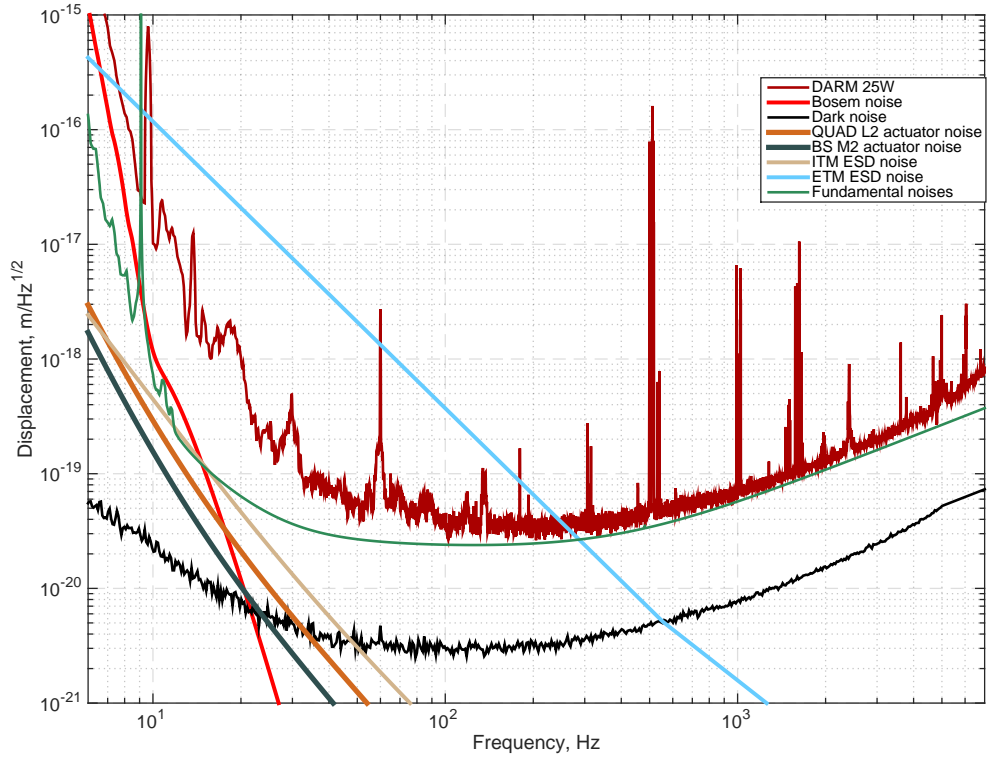


Figure 7.9: Sensing and actuation noise coupling to DARM.

### 7.3.1 Electrostatic driver

Electrostatic actuation noise on test masses is dominated by DAC electronics noise. Figure 7.9 shows that noise from ETM ESD is more than order of magnitude above current DARM spectrum if bias voltage is set to 400V. This is because ETM ESD is used only for acquisition and then turned off in low noise regime, and high frequency control goes to ITM ESD as described in section 5.1.3. DC range of ITM ESD is a factor of 20 less compared to ETM ESD. DAC noise of ITM ESD is also

filtered using a low-pass filter with a pole at 3Hz and zero at 30Hz. Finally, bias voltage of ITM ESD is set to 100V from 400V to reduce electronics noise coupling to gravitational wave channel.

### 7.3.2 Penultimate mass actuators

Four coil-magnet pairs are installed on penultimate masses of all core optic suspensions. Most significant coupling to gravitational wave channel comes from electronics noise in test masses and beam splitter. During the lock acquisition, actuators are in high dynamic range state, and electronics noise of penultimate actuators is seen in DARM with SNR of  $\sim 2$  in the frequency range 30-50Hz. In low noise regime actuators are switched to low range state, and electronics noise is filtered by the driver starting from 1Hz. Total noise from test mass and beam splitter penultimate actuators is below the sum of fundamental noises.

### 7.3.3 Local damping

Mechanical resonances of aLIGO suspensions have high quality factors in order to achieve  $1/f^2$  passive noise filtering per stage. Resonances in all 6 degrees of freedom are actively damped from the top stage to reduce the ring down time after lock loss or other excitation. Feedback loops use shadow sensors that measure distance between the frame or reaction mass and little flags installed on suspension stages [81].

Shadow sensors are shot noise limited above 1Hz. Broadband sensing noise is  $7 \cdot 10^{-11} m/\sqrt{Hz}$ . Control filters are designed to damp multiple resonances from 0.4Hz up to 5Hz. At the same time control signal is aggressively low-passed to reduce shadow sensor noise coupling to gravitational wave channel. Local damping noise shown in figure 7.9 is computed by propagating BOSEM noise through digital control filters and suspension transfer function.

### 7.3.4 OMC electronics

OMC transmitted light is equally split into two beams and sensed using InGaAs photodiodes with quantum efficiency of 0.88 and responsivity of 0.9 A/W. DC transimpedance is switchable between 100Ohms and 400Ohms. First configuration (low-Z) is used when detector input power is more than 25W. Otherwise, interferometer is operated using second option (high-Z). Starting from 6Hz, signal is whitened inside the photodetector. Another set of whitening filters is applied before digitization to avoid coupling of ADC noise.

Maximum DC current through OMC photodiodes with bias voltage of 7V is  $\sim 17mAmps$  in high-Z state and  $\sim 70mAmps$  in low-Z state. Dark noise shown in figure 7.9 was estimated when the current through each OMC photodiode is  $10mAmps$  in high-Z state. This noise level is close to the optimal one under current electronics design and is factor of 7-8 below shot noise. Dark noise

converted to units of meters will degrade by factor of 2-3 once OMC PDs are switched to low-Z state in order to operate with DC currents of 30 – 40mAmps.

## 7.4 Auxiliary loops

Figure 7.10 shows coupling of laser frequency noise, oscillator phase noise, DRMI residual motion, and angular control to gravitational wave channel.

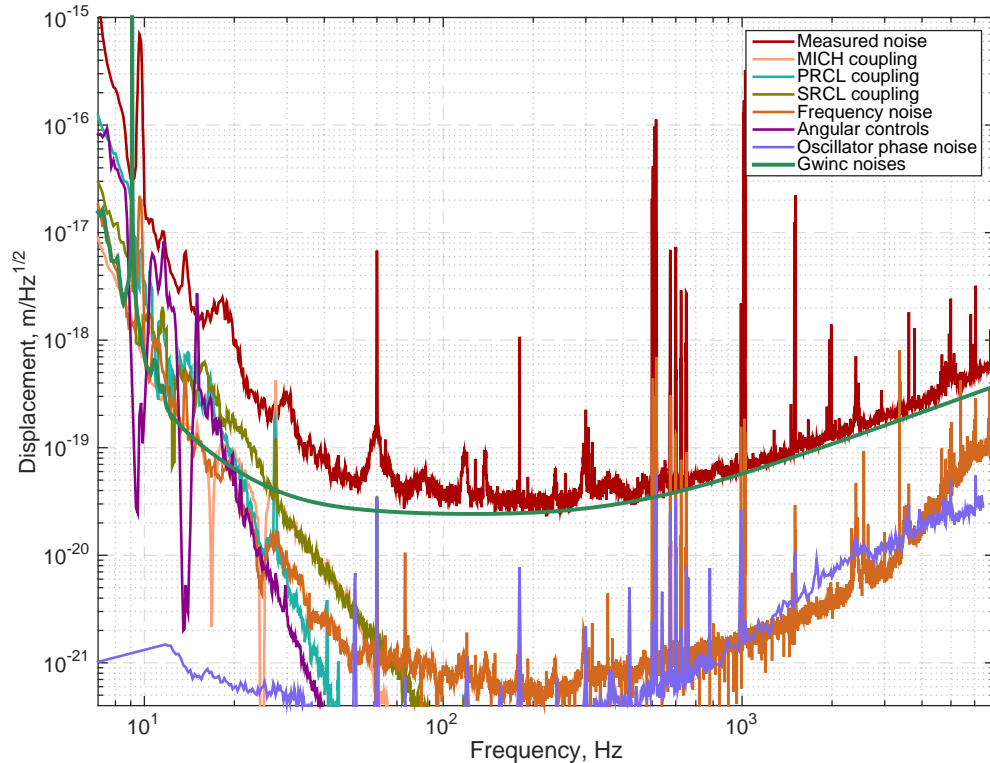


Figure 7.10: Coupling from auxiliary length and angular loops to DARM.

### 7.4.1 Angular controls

Angular feedback loops are used to keep interferometer alignment and suppress angular motion at low frequencies as discussed in section 4.4. At high frequencies angular sensors are limited by electronics and shot noise. Above 5Hz control signal in pitch and yaw degrees of freedom is low passed to reduce coupling to gravitational wave channel as shown in figures 7.11 and 7.12. Feedforward subtraction system is set to reduce noise coupling from angular control to DARM by factor of  $\sim 10 - 30$  as discussed in section 9.2.

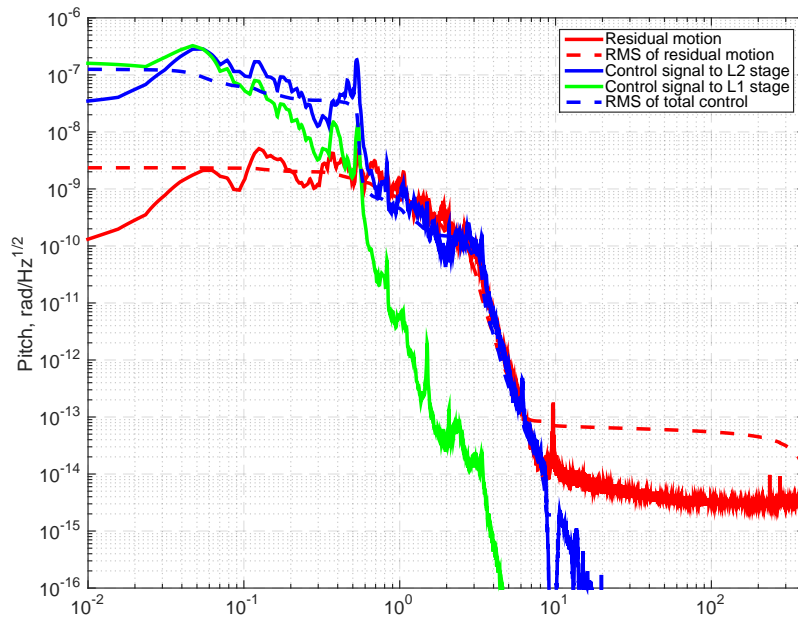


Figure 7.11: Angular motion of test masses in pitch degree of freedom measured by AS45Q WFS.

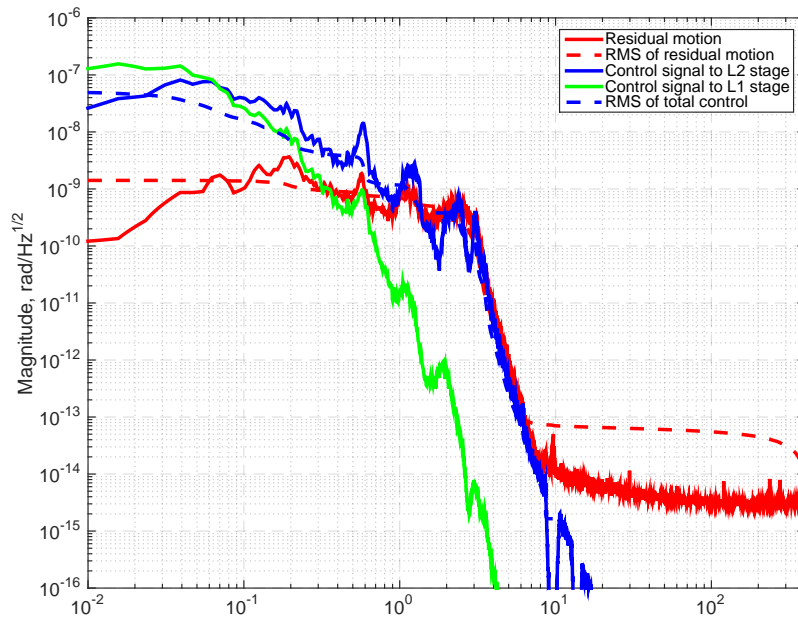


Figure 7.12: Angular motion of test masses in yaw degree of freedom measured by AS45Q WFS.

### 7.4.2 Laser frequency noise

Frequency noise is common to X- and Y-arm and couples to gravitational wave channel only through imbalances in the arm cavities such as difference in pole frequencies and amount of round trip losses. Schnupp asymmetry of  $8\text{cm}$  also gives a small coupling of frequency noise to DARM. Linear coupling was directly measured by modulating error point of the frequency servo and measuring response in DARM.

Three feedback loops are used to suppress frequency noise of the laser. Initially, the laser is locked to reference cavity with bandwidth of  $500\text{kHz}$  using EOM, PZT, and NPRO thermal actuators. Then laser is locked to the input mode cleaner with bandwidth of  $80\text{kHz}$  by shifting frequency of the light going to reference cavity using AOM. Finally, laser is locked to common arm length by actuating on IMC length and error point of IMC loop with bandwidth of  $30\text{kHz}$ .

### 7.4.3 DRMI noise

PRCL, SRCL, and MICH residual motion in the frequency range is unknown since displacement noise is dominated by the sensing noise as shown in figures 7.13, 7.14 and 7.15. However, feedback control loops inject this sensing noise into longitudinal motion. If motion of DRMI degrees of freedom due to seismic, BOSEM, actuator, and other displacement noises is smaller compared to motion due to feedback loop, it is possible to efficiently subtract residual DRMI motion from gravitational channel as discussed in the section 9.1.

MICH length motion couples to OMC transmitted signal the same way as DARM but without amplification by arm cavity build up. Coupling coefficient equals  $1/260$  and weakly depends on DARM offset and alignment unless power build-up in the arm cavities is significantly changed.

SRCL residual motion couples to gravitational wave channel due to DARM offset through radiation pressure. Linear coupling has shape of  $1/f^2$  above optics resonances. Nonlinear component appears due to low frequency beam jitter. DARM servo compensates for the OMC power fluctuations and SRCL coupling coefficient changes. After stabilizing angular fluctuations of interferometer arm cavities and signal recycling axis, nonlinear term in the frequency range  $10\text{Hz}-70\text{Hz}$  was significantly reduced, and linear term dominated by a factor of 10-30 depending on seismic noise level. SRCL coupling above  $70\text{Hz}$  significantly depends on mode matching between signal recycling cavity to arms.

Coupling of PRCL residual motion to gravitational wave channel is less significant compared to MICH and SRCL, and no feedforward subtraction is required to improve DARM noise. PRCL coupling to DARM is mainly due to cross couplings between DRMI degrees of freedom on the sensing and actuation side as discussed in section 9.1.

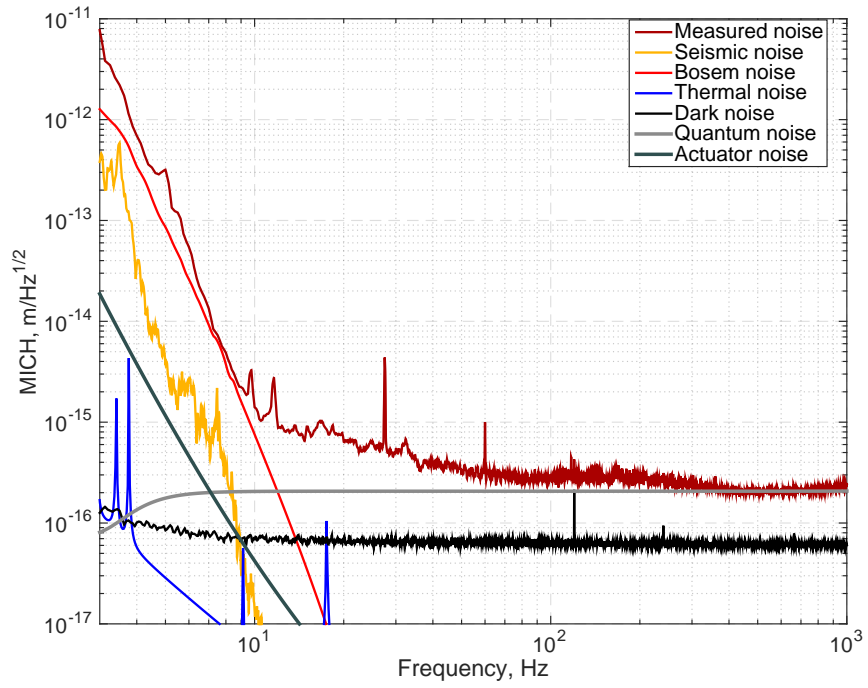


Figure 7.13: MICH noise budget.

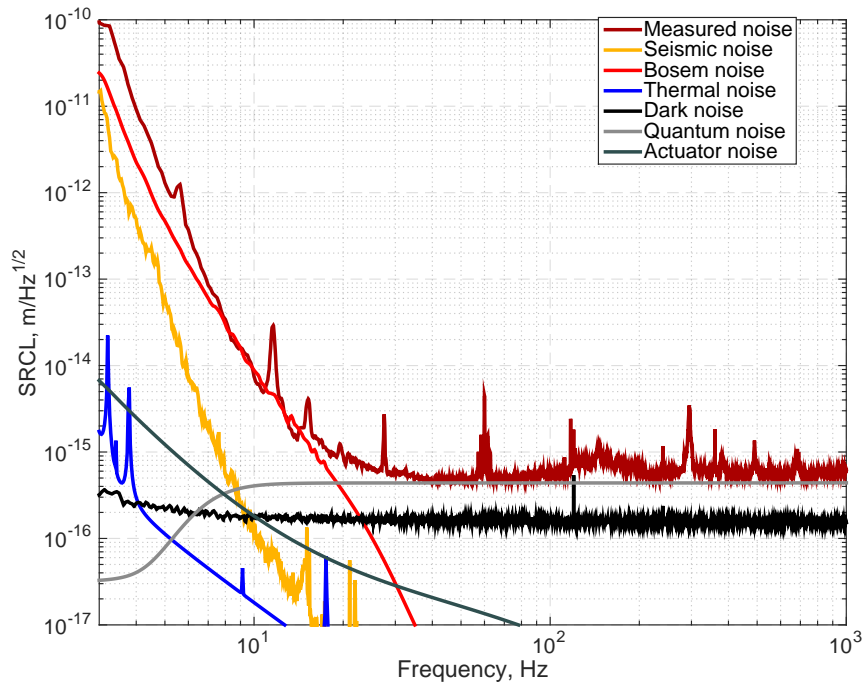


Figure 7.14: SRCL noise budget.

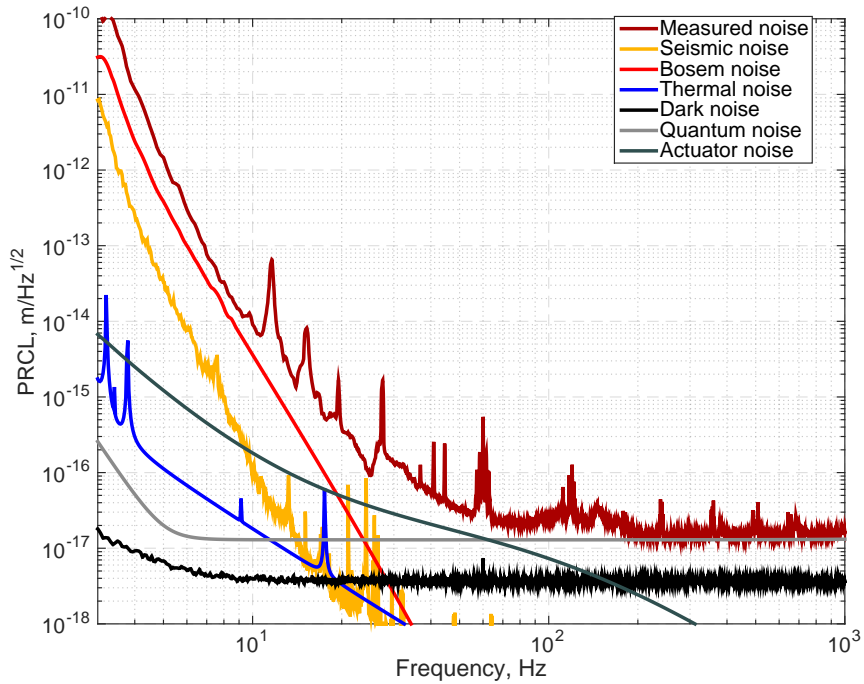


Figure 7.15: PRCL noise budget.

## 7.5 Intensity and jitter

Figure 7.16 shows coupling of laser and RF oscillator amplitude noises and input jitter noise to gravitational wave channel.

### 7.5.1 Input amplitude noise

Interferometer input amplitude fluctuations are filtered by the double cavity pole at  $0.6\text{Hz}$  and directly couple to gravitational wave channel as sensing noise. Power fluctuations also move test masses through radiation pressure force and couple to gravitational wave channel as displacement noise in case of arm imbalances. Coupling of input amplitude noise to gravitational wave channel due to radiation pressure depends on frequency as  $1/f^3$ .

Coupling of input amplitude noise significantly depends on contrast defect of simple Michelson interferometer.  $\text{CO}_2$  laser power is tuned to compensate to ITM curvature mismatch of  $\sim 30m$ . In case of no compensation,  $1/f$  filtering by double cavity pole is lost above  $40\text{Hz}$  and input noise is filtered only by  $30\text{dB}$ . Figure 7.17 shows measured coupling of input amplitude noise to OMC RIN depending on the  $\text{CO}_2$  power.

Laser amplitude noise is stabilized using two ISS loops. The first loop is set on the PSL table and the second one uses sensors in IMC transmission and actuates at the error point of the first loop.

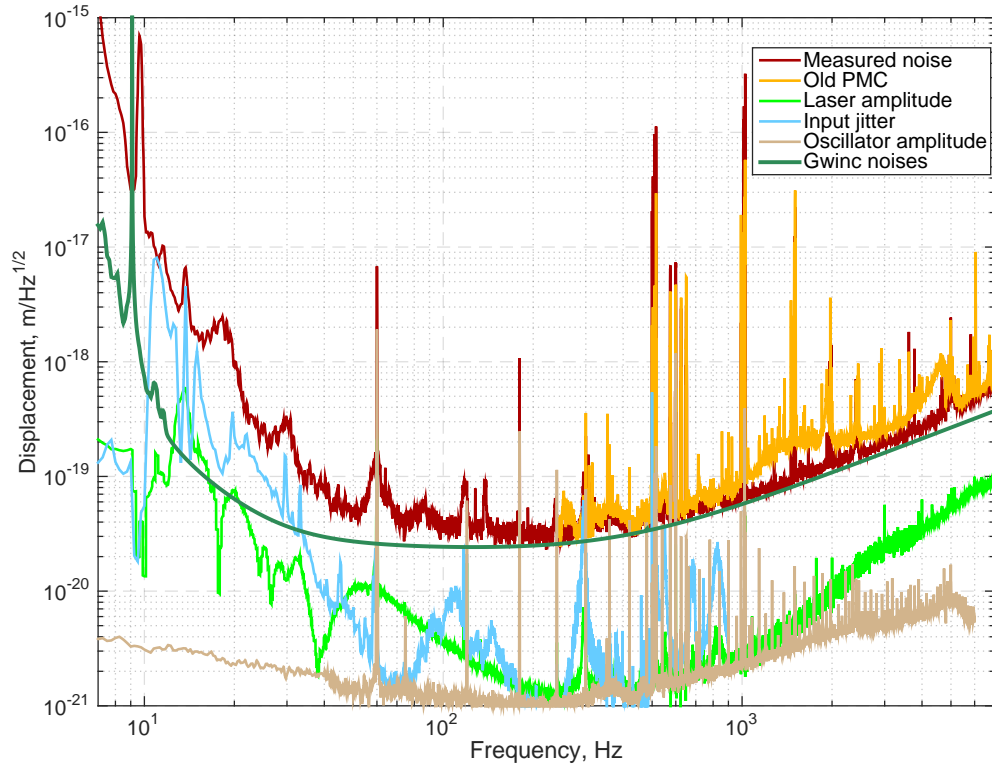


Figure 7.16: Coupling of laser amplitude noise and beam jitter to DARM. Orange trace shows DARM spectrum with broken PZT of PMC which created high frequency intensity and jitter noise.

Residual noise measured by out-of-loop sensor installed in transmission of OM1 is  $\sim 10^{-8} 1/\sqrt{Hz}$  in the frequency range 20-300Hz. Actual intensity noise of interferometer input beam can be higher due to scattering on HAM6 witnessed by IM4 transmission QPD.

Second loop out-of-loop sensor also does not account for RF oscillator amplitude noise since this PD measures sum of sideband and carrier noises. After stabilizing amplitude noise of RF oscillator, DARM spectrum improved by  $\approx 3\%$  in the frequency range 100Hz-1kHz and lines at 120Hz and 240Hz disappeared from the spectrum.

Pre mode cleaner length noise also coupled through input amplitude noise. Due to broken, PZT significant beam jitter was created and was converted to amplitude noise by the input mode cleaner. Figure 7.16 shows that DARM spectrum has improved in the frequency range 1kHz – 5kHz after PMC swap.

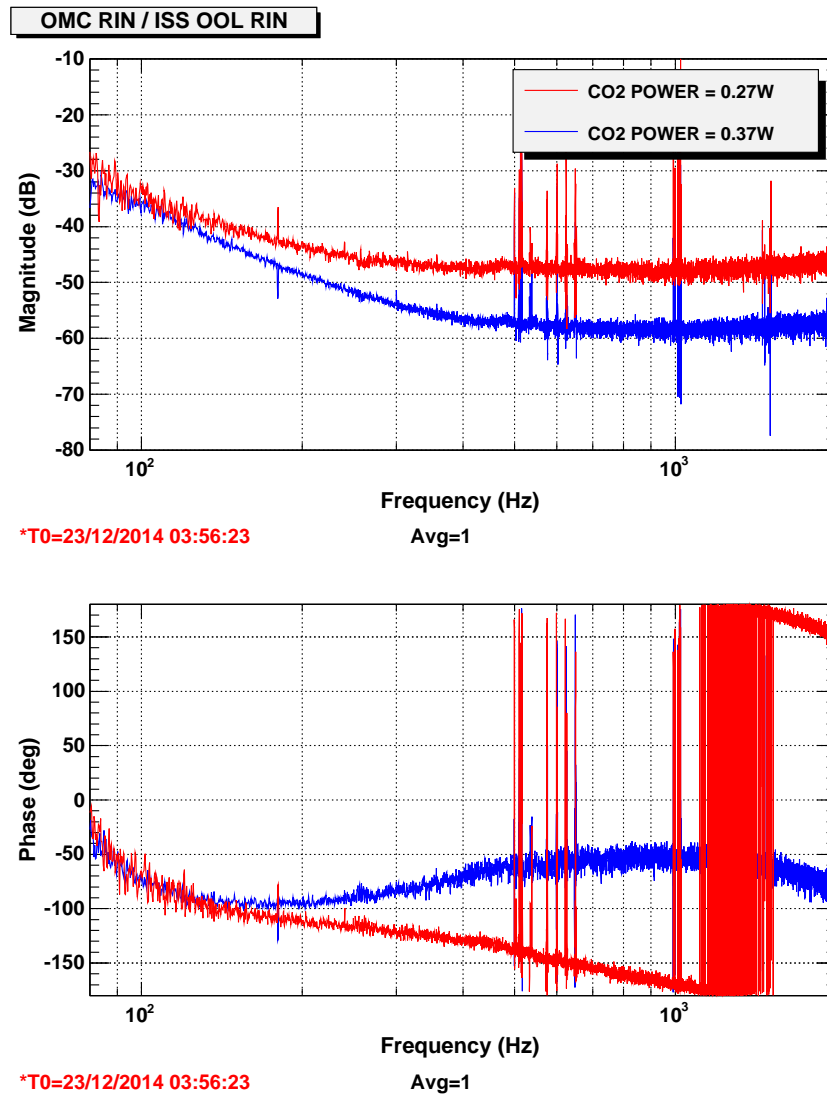


Figure 7.17: Input RIN coupling to OMC RIN.

### 7.5.2 Input beam jitter noise

Interferometer input beam jitter in the frequency range 10Hz-1kHz is dominated by motion of steering mirrors and periscope on the PSL table. This jitter is filtered by the input mode cleaner by factor of  $\approx 180$  and couples to gravitational wave channel through auxiliary length channels and frequency noise. Input jitter is also converted to amplitude modulation in the power recycling cavity and couples to DARM as sensing noise.

Coupling of interferometer input beam jitter to DARM was measured by exciting IM3 in angle and measuring transfer function from IM4 transmitted QPD to OMC RIN. Then, this transfer

function is multiplied by the PSL beam jitter, propagated through IMC. PSL jitter is measured using IMC reflected QPDs when IMC is unlocked.

Coupling of the input beam jitter to DARM depends on interferometer alignment, and height of the peaks in figure 7.16 in the frequency range 100Hz - 1kHz can change with time. For this reason, input jitter noise should be suppressed on the PSL table using additional in-vacuum QPDs. Peak around 300Hz comes from PZT mount and is already being actively suppressed using IMC WFS signals.

## 7.6 Residual gas

Figure 7.18 shows coupling of squeezed film damping and noise due to residual gas in the arm cavities to gravitational wave channel.

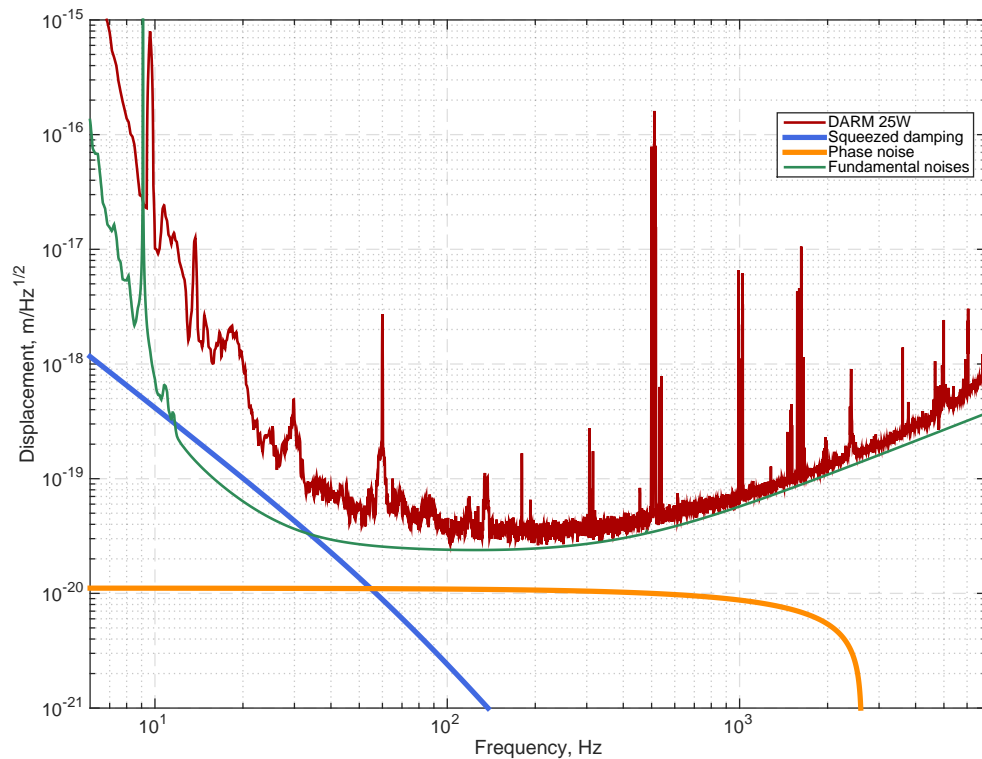


Figure 7.18: Coupling of squeezed film damping and noise from residual gas in the arms to DARM.

Residual gas asserts damping force on test masses due to the moment exchange between molecules and mirror surfaces. As was shown in [82, 83, 84], a small gap of 5mm between end test masses and reaction mass increases damping noise below 100Hz by factor of  $\approx 10$  compared to the unconstrained case [85]. Force coefficient depends on gas pressure and molecular mass and can be estimated using

fluctuation-dissipation theorem or using Monte Carlo simulation:

$$F = 1.5 \cdot 10^{-14} \left( \frac{p}{10^{-8} \text{ Torr}} \right)^{1/2} \left( \frac{m}{m_{H_2}} \right)^{1/4} N \quad (7.13)$$

where  $p[\text{Torr}]$  is pressure of residual gas,  $m[\text{kg}]$  - mass of gas molecule.

Squeeze damping noise in figure 7.18 is the sum of nitrogen and hydrogen noises. Total gas pressure at the end stations at the moment of writing is  $3 \cdot 10^{-8} \text{ Torr}$ . Since damping noise depends on square root of gas pressure, this noise can be reduced by factor of 3-4 by pumping down to the pressure of  $p \approx 10^{-9} \text{ Torr}$ .

Another source of noise from residual gas is due to the passage of molecules through laser beams in the arm cavities. Noise can be modeled by calculating the impulsive disturbance to the laser field phase as a gas molecule moves through the beam [86]. Estimation of phase noise shown in figure 7.18 is computed using gwinc software.

## 7.7 Lines

Most lines in the DARM spectrum in the frequency range 10Hz - 2kHz are well understood and summarized below:

- 30Hz comes from HVAC at Y-end station. This line is seen on all local seismometers on the ground, accelerometers on the ETMY chamber walls, and geophones on ISI table. One HVAC system was fixed, line in the gravitational wave channel disappeared.
- 60Hz, 180Hz lines come from potential fluctuation at end stations and couple through surface charge on the test masses as discussed in section 7.2. Lines are significantly reduced after discharging of test masses.
- 120Hz, 240Hz come from amplitude noise of Marconi RF generator. Lines were eliminated after stabilizing amplitude noise of RF generator and further swapping it to Wenzel oscillator.
- 300Hz comb likely comes from violin modes triple suspensions
- 500Hz comb and harmonics are violin modes of test mass suspension. Precise frequencies are summarized in section 5.2.3
- 845Hz line is downconversion from parametric instability [87]. True mode frequency is 15.5kHz.
- 1600Hz comb comes from OMC dither alignment.

## 7.8 Parametric instability

Exponentially growing line at 15.5kHz was first observed when interferometer input power was 12W [88]. Figure 7.19 shows parametric instability growing in amplitude. At time moment 2500sec power was reduced and body mode was ringing down for the next 1 hour.

The transverse mode spacing in the arm cavities is  $\approx 5.1kHz$ , and  $HOM_{mn}, (m+n) = 3$  excites body mode of one of the test masses. By looking at the arm transmission photodetectors, it is possible to determine in which arm parametric instability is excited. Parametric gain is reduced by changing g-factor of the arm cavities using TCS ring heaters. Shift of the transverse mode  $HOM_{mn}, (m+n) = 3$ , depending on ETM curvature change, is 80Hz/m.

Since frequencies of body modes of four test masses are different by a few hundreds of Hz, it is hard to shift frequencies of  $HOM_{mn}$  to prevent excitation of all body modes and their harmonics if input power is high enough. Parametric gain depends on beam position on the test mass, and instabilities cause lock losses after 10-30 hours after lock acquisition if input power is increased to 25W.

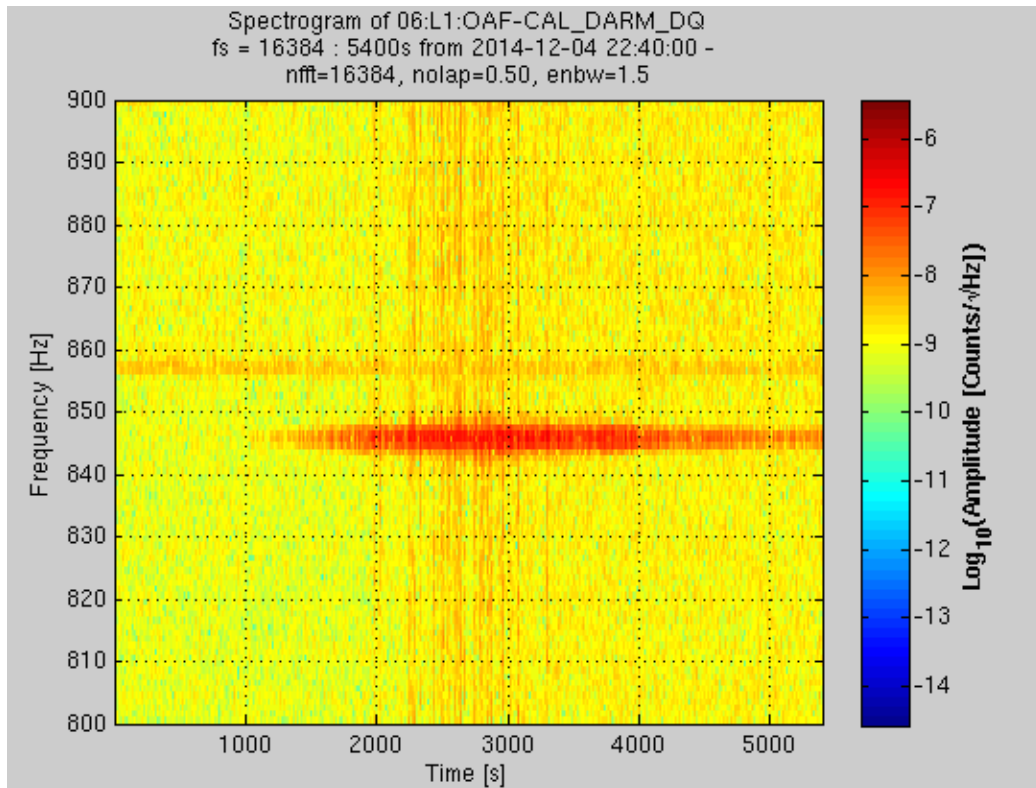


Figure 7.19: Excitation and ringing down of the test mass body mode due to parametric instability.

When input power is increased to 125W, detuning of arm cavity g-factor using TCS ring heaters will not remove parametric instabilities, and damping of the body modes will be necessary using electrostatic actuators.

## 7.9 Glitches

Noise transients can cause interferometer to loose lock, reduce quality of the data and ring up bounce, roll, and violin modes. During aLIGO commissioning a number of glitches has been discovered and eliminated.

### 7.9.1 DAC zero crossings

Significant glitches in DARM and auxiliary channels were observed when control signal to suspensions crossed zero or half range values as shown in figure 7.20. This happened due to design of internal circuits of commercial 18 bit DACs. When signal crossed zero or half range values, DAC output signal was switched between internal 16 bit DACs and glitch in output signal was produced.

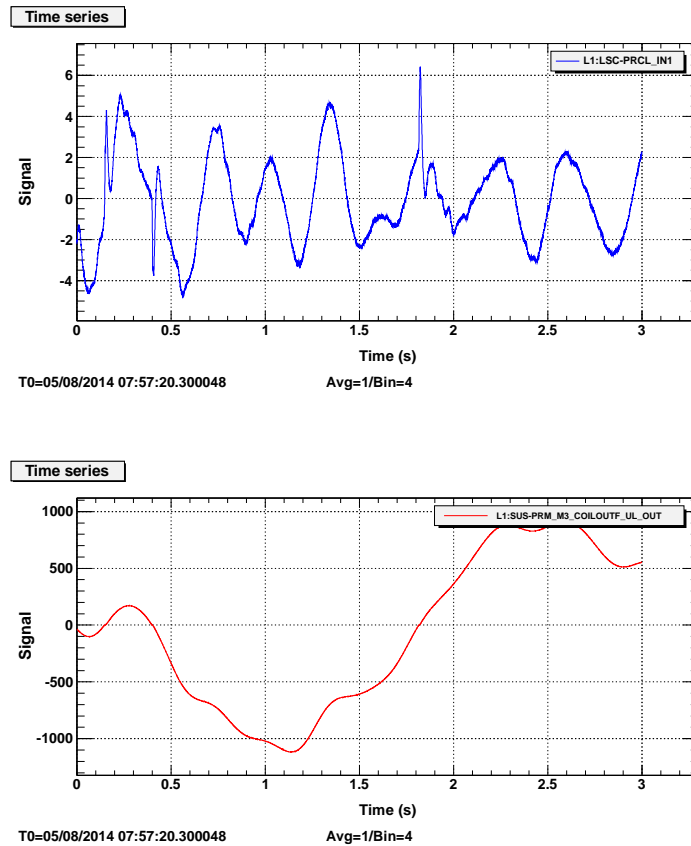


Figure 7.20: Glitches in PRCL error signal due to PRM M3 DAC zero crossing.

DAC auto calibration routing built into the board reduces size of glitches but discontinuities are still present for some DACs. Control signal was offset using other actuators to avoid flips of 2 bit

DAC. Single chip 20 bit DACs with lower noise are now being tested to replace 18 bit DACs.

### 7.9.2 Frequency and intensity transients

When interferometer is locked, common arm length is servoed to the PSL reference cavity with bandwidth of 0.1Hz. Frequency servo suppresses residual seismic motion of the arm cavities, and control signal to FSS AOM fluctuates by  $\sim 100kHz$  around 80MHz.

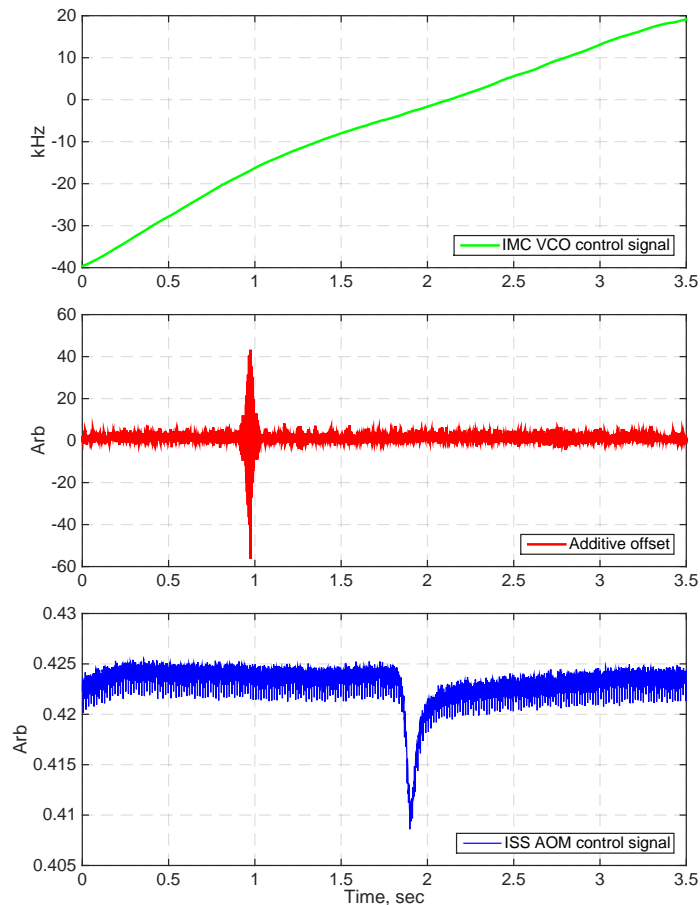


Figure 7.21: Glitches in frequency and intensity servos depending on IMC VCO control signal calibrated to kHz.

Glitches in laser frequency and intensity stabilization servos are observed when control signal to IMC VCO crosses particular voltage levels. Frequency glitches are clearly seen in auxiliary degrees of freedom, such as PRCL and SRCL, in the frequency range 10Hz - 1kHz. MICH and DARM are less sensitive to frequency noise but are still seen above 1kHz. Glitches in the intensity servo are clearly seen in control signal to ISS AOM and REFL DC signals.

Glitches in frequency and intensity servos do not coincide and happen when IMC VCO control

signal crosses different critical voltages as shown in figure 7.21.

### 7.9.3 Data transmission errors

In the beginning of commissioning period data, transmission errors happened every hour due to large processing time of LSC model. Data from OMC photodetectors is digitized in the corner station, conditioned in the DARM control filter bank in the LSC model, and sent to the end stations to suspensions models over 4km fiber. If end station models do not receive signal on time, control signal is replaced with zero and glitch is produced.

Data transmission glitches were eliminated by reducing computational time of the LSC model. This was achieved by splitting LSC model into two and installing faster front-end computers.

### 7.9.4 OMC backscattering

During winter time scattering shelves were observed in DARM spectrum in the frequency range from 10Hz to 40Hz with periodicity from 10 seconds to a few minutes. Shelves are caused by backscattering from the output mode cleaner and modulation of the distance between interferometer and OMC as discussed in section 8.3.4.

### 7.9.5 Optical levers

Optical lever servos are used during lock acquisition to suppress angular motion of the test masses in the microseismic band and around main resonance at 0.5Hz. Glitches in the laser intensity occurred every minute due to mode hopping in the optical lever laser. Rate of the glitches was significantly reduced after stabilizing temperature of the lasers. New type of lasers might be installed in the future.

## 7.10 Discussion

Interferometer sensitivity above 100Hz is dominated by shot noise as shown in figure 7.2. At low frequencies acoustic peaks can be seen in DARM spectrum. Most probably these peaks are originated at the output port on HAM6 table as discussed in the chapter 8. Output mode cleaner will be baffled to reduced backscattering from HAM6 chamber walls and ISI table.

Figure 7.22 shows sensitivity curve of aLIGO Livingston observatory during first the 9 months of commissioning effort. Interferometer sensitivity continues to improve towards its designed value. Commissioning effort is now concentrated on low frequencies.

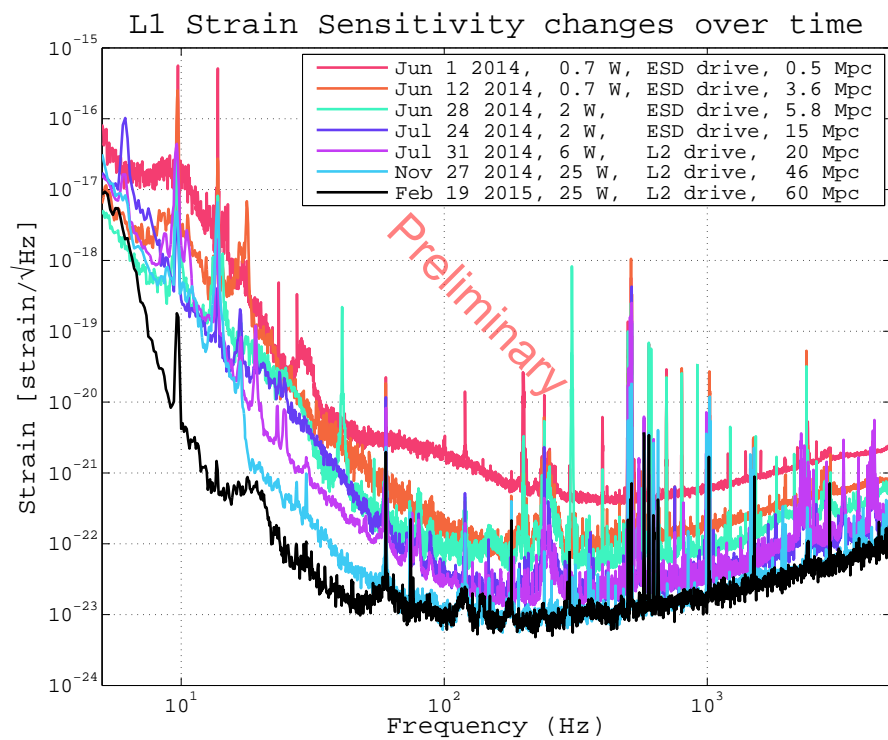


Figure 7.22: Improvements in DARM sensitivity from June 2014 up to March 2015.

## Chapter 8

# Losses and scattering

The problem of optical losses and scattering is one of the most significant problems in interferometric gravitational wave detectors. Losses are caused by absorption in optical coatings and mirror substrates, scattering on the defects, dust particles on the mirror surfaces and coating ripples, beam clipping on the apertures and Faraday isolators.

Optical losses cause two types of problems in advanced LIGO. The first one is related to optical power resonating in the cavities and leaving interferometer through the antisymmetric output port. Round trip losses in the arm cavities determine power build up in the interferometer and instrument sensitivity at high frequencies where it is limited by shot noise. Losses at the output port reduce DARM optical gain and instrument sensitivity to gravitational waves.

The second problem arises if light scattered from the main beam is scattered back from moving chamber walls, and baffles, mirrors, or photodiodes into the main beam. Backscattered light is modulated in phase and amplitude and introduces noise to gravitational wave channel. Phase modulation is directly detected at the antisymmetric port, and amplitude modulation moves test masses by means of radiation pressure.

This chapter describes optical losses and scattered light noises seen in aLIGO. The first section is devoted to losses measured in the arm cavities. The second section gives an estimation of optical losses at the output port. The third section describes scattered light noise from the end stations and output port. Forth section discusses possible techniques to mitigate scattered light noise.

### 8.1 Arm losses

Round trip losses in the arm cavities are expected to be 50ppm. Corresponding power recycling gain is  $58W/W$ . Dust particles on the surface of test masses can increase scattering and reduce power recycling gain. Figure 8.1 shows simulated aLIGO power recycling gain and interferometer visibility depending on optical losses in the arm cavities.

Measured round trip losses are higher compared to design value. On the moment of writing

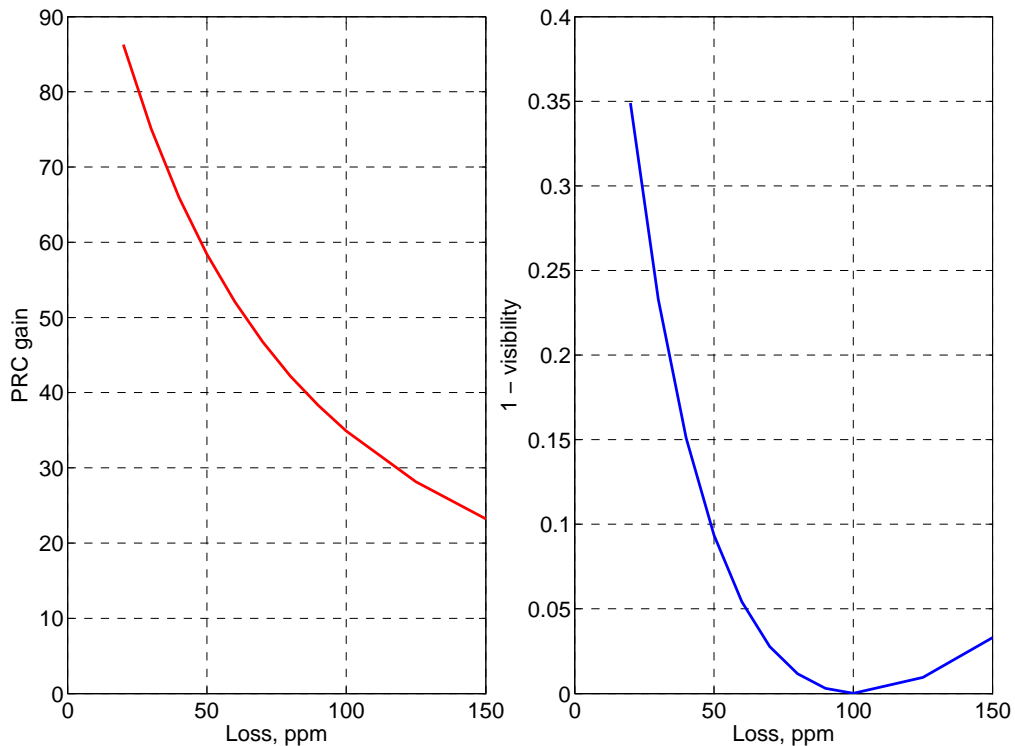


Figure 8.1: Dependence of power recycling gain and interferometer visibility on intracavity losses.

lowest optical losses measured using ringdown measurement [89] are

$$L_x = 85ppm, \quad L_y = 90ppm \quad (8.1)$$

where  $L_x$  is round trip loss in the X-arm cavity and  $L_y$  - in the Y-arm. Figure 8.1 shows that 90ppm of losses correspond to power recycling gain of  $38W/W$ . This number agrees with the measured power recycling gain in full lock.

Intracavity losses strongly depend on beam position on each of the test mass. This geometrical factor comes from the fact that size of the beam on test masses is 5 – 6cm while coating quality degrades further from the center of the optic. Dust particles are also distributed non-uniformly.

Round trip loss dependence on test mass beam position was measured using ringdown technique. Laser is locked to the arm cavity by actuating on the input mode cleaner length. Cavity axis is moved to set the beam position on test masses. Input beam alignment is compensated using IM4 and PR2 mirrors as shown in figure 8.2. Beam position on ITM is measured using camera. Beam position on ETM is kept constant.

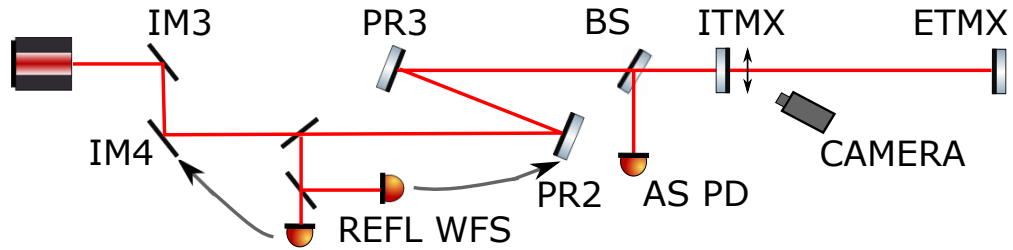


Figure 8.2: Round trip loss measurement depending on beam position on ITM.

In order to get accurate ringdown measurement, input light to the arm cavity should be instantly blocked. This is achieved by unlocking input mode cleaner using fast polarity switch in the servo. Ringdown time of the IMC is much less compared to the arm cavity.

Once arm cavity input beam is blocked, reflected power jumps up and rings down as shown in figure 8.3

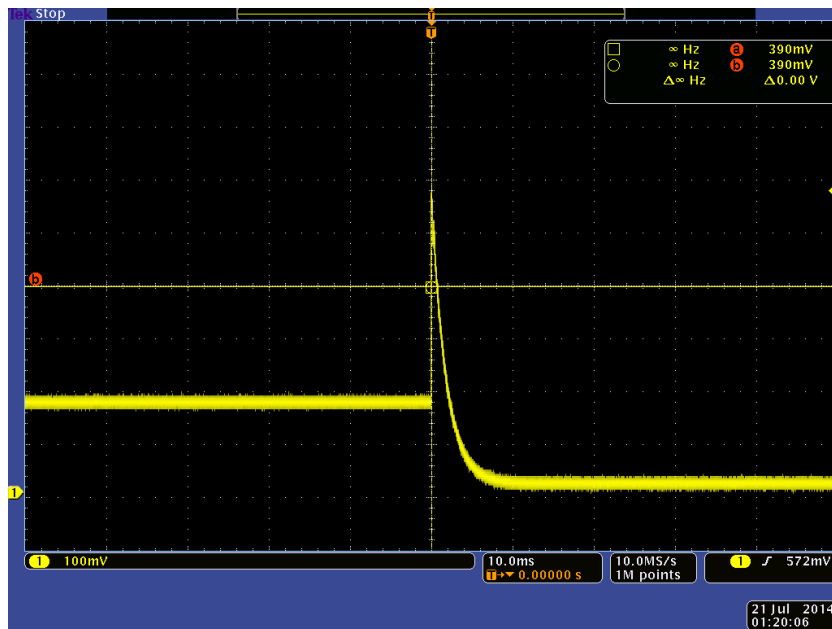


Figure 8.3: Reflected power during ringdown measurement.

Ringdown technique allows to derive cavity finesse, losses, and input mode matching. Dependence of round trip loss on beam position on ITM is shown in figure 8.4. Zero on the x-axis corresponds to geometrical center of ITM based on the camera view. When interferometer is locked, alignment of ITMs is optimized to reduce optical losses in the arm cavities and maximize power recycling gain.

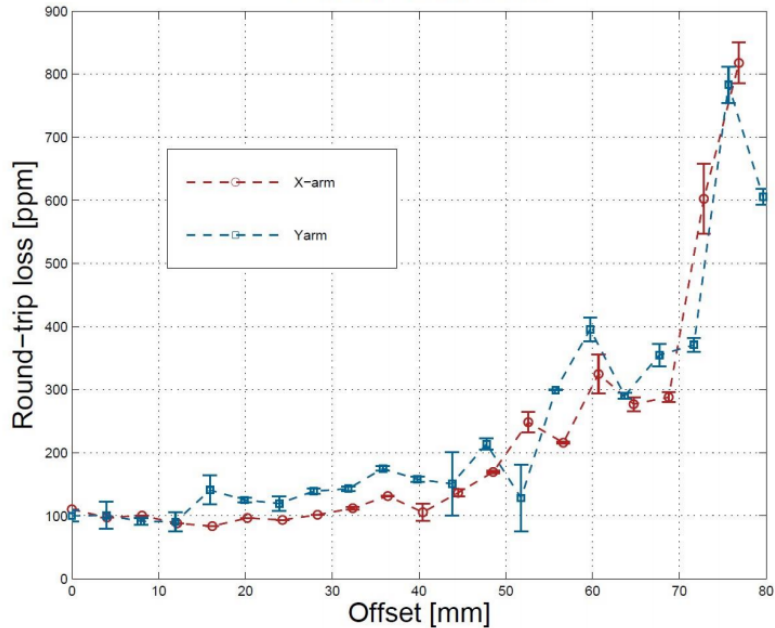


Figure 8.4: Dependence of optical losses in X- and Y-arm on different beam offsets from the optic center.

## 8.2 Output losses

Interferometer sensitivity is reduced if significant amount of light is lost on the output port of interferometer. Magnitude of DARM optical transfer function depends similarly on input and output losses. However, input losses can be compensated by increasing laser power in contrast to output losses since amount of power resonating in the arm cavities is currently limited by parametric instabilities. At the same time output losses are harmful for the squeezing technique [90].

Output losses were estimated by comparing measured OMC transmitted power with the simulated one. DARM offset is computed using calibration of the error signal discussed in chapter 6:

$$\Delta DARM = 2A_0 \frac{\delta l}{\delta A} \quad (8.2)$$

where  $A_0$  is DC current on the OMC photodetectors,  $\frac{\delta l}{\delta A} [m/A]$  is transfer function from OMC PD current in amperes to DARM meters when OMC PD current is  $A_0$ .

When interferometer input power is 22W, power incident on BS is 837W and OMC PD current is 20mAmps, and DARM offset according to equation 8.2 equals 11.8pm. Figure 8.5 shows a comparison of simulated power on OMC PDs assuming no output loss, and measured power assuming quantum efficiency of OMC photodiodes equal to 0.88.

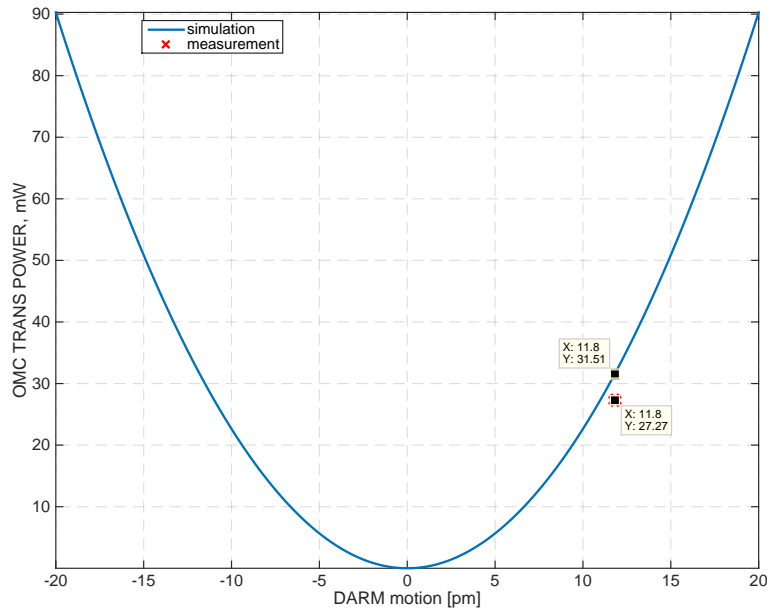


Figure 8.5: Simulation and measurement of OMC transmitted power in dependence of DARM offset.

Measured output optical losses are 14%. The table below summarizes loss from individual optical components when light travels from SRM to OMC PDs.

Output Faraday isolator	4%
OM3 transmission	1%
OMC mode matching	5%
OMC throughput	4%

Table 8.1: Optical loss from individual components.

Table 8.1 shows that output losses are well understood. However, uncertainty in the calibration coefficient  $\frac{\delta I}{\delta A}$  is 3 – 4%, and this introduces uncertainty in the output loss of 6 – 8%.

### 8.3 Noise from scattered light

Light scattered out from the main beam can be scattered back from moving objects like baffles or chamber walls as shown in figure 8.6. Scattered light noise is seen in the DARM spectrum in the frequency range 10-200Hz and is one of the most dominant noise sources on the moment of writing.

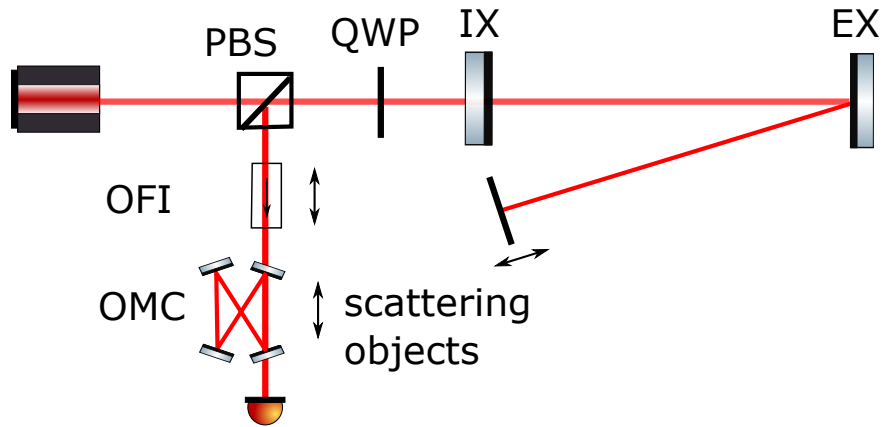


Figure 8.6: Backscattering from moving objects. Light backscatters from intracavity baffles or chamber walls, output Faraday isolator and mode cleaner.

Scattering noise is modulated by alignment of the interferometer. Since PR3 and ITMs are not controlled, alignment of the cavity axes drifts. Power build up in all cavities is maximized but beam positions on the mirrors move due to thermal drifts of PR3 and ITM alignment. Figure 8.7 shows fluctuation of BNS range due to angular fluctuations of uncontrolled mirrors. Drift is mostly caused by PR3 pitch and yaw fluctuations.

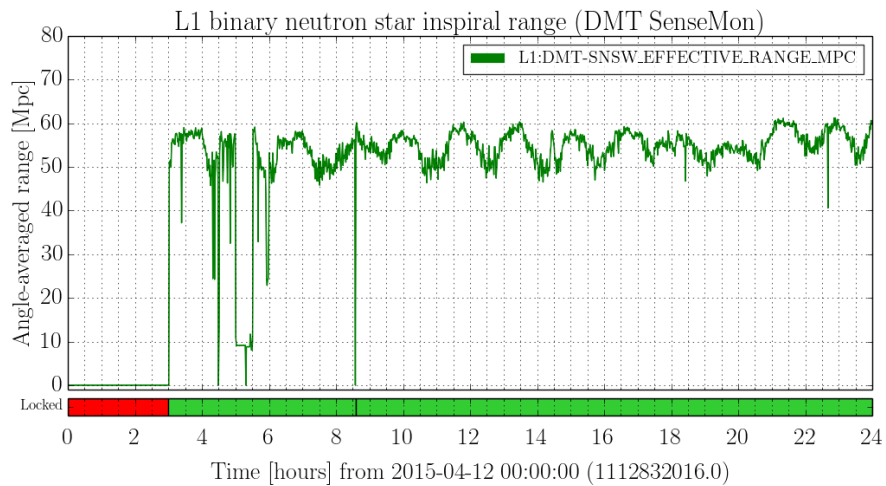


Figure 8.7: Range fluctuations due to alignment drift.

Sources of scattered light noise can be divided into several categories determined by the place of scattering: interferometer input, arm cavities, chamber walls and output mode cleaner.

### 8.3.1 Interferometer input

Scattering at the interferometer input couples to gravitational wave channel through auxiliary degrees of freedom like intensity noise. Scattered light in HAM2 chamber significantly degrades performance of intensity stabilization servo. Figure 8.8 shows relative intensity fluctuations in the power recycling cavity when ISS second loop is turned on and off. ISS out of loop sensors located close to in loop sensors see the same scattered light noise and show reduction in intensity noise. However, intracavity fluctuations increase.

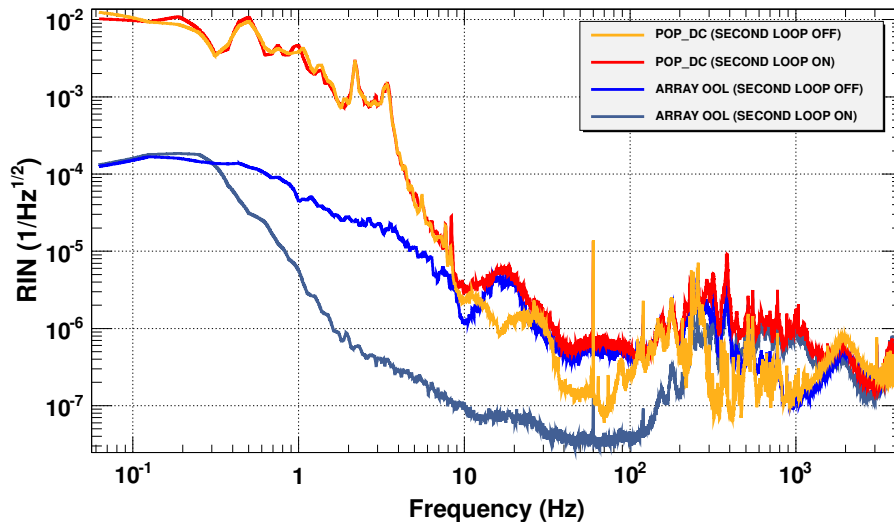


Figure 8.8: Scattered light noise at the interferometer input degrades behavior of intensity stabilization servo.

At the same time direct coupling of scattered light noise to gravitational wave channel was not observed since frequency and intensity noise produced by scattered light are filtered by the double cavity pole.

### 8.3.2 Arm cavities

Scattered light from the LMA coating ripple hits a beam tube baffle near the ITM end of the tube, is scattered back towards the ETM by the baffle material, and then scatters back into the cavity mode on the ETM surface. Noise in gravitational wave channel comes from radiation pressure and phase noise of scattered light. Scattering noise coming from test mass scattering is analyzed in [91] and measured by shaking beam tubes. Estimations of scattered light noise coming from the arm cavities to gravitational wave channel are factor of 50-100 below current interferometer sensitivity in the frequency range 10-100Hz as shown in the table 8.2

	14.38Hz	45Hz	90Hz
Measured noise at 10W, $m/Hz^{1/2}$	$< 1.3 \cdot 10^{-20}$	$< 5.8 \cdot 10^{-22}$	$1.8 \cdot 10^{-22}$
Current sensitivity at 25W, $m/Hz^{1/2}$	$1.5 \cdot 10^{-18}$	$7 \cdot 10^{-20}$	$5 \cdot 10^{-20}$
Designed sensitivity at 125W, $m/Hz^{1/2}$	$2.5 \cdot 10^{-19}$	$2.7 \cdot 10^{-20}$	$1.4 \cdot 10^{-20}$

Table 8.2: Scattered light noise from arm cavities.

Table 8.2 shows that when input power will be increased up to 125W, scattered light can limit sensitivity at 14.38Hz. Ground motion at this frequency is amplified by the tube resonance as shown in figure 8.9.

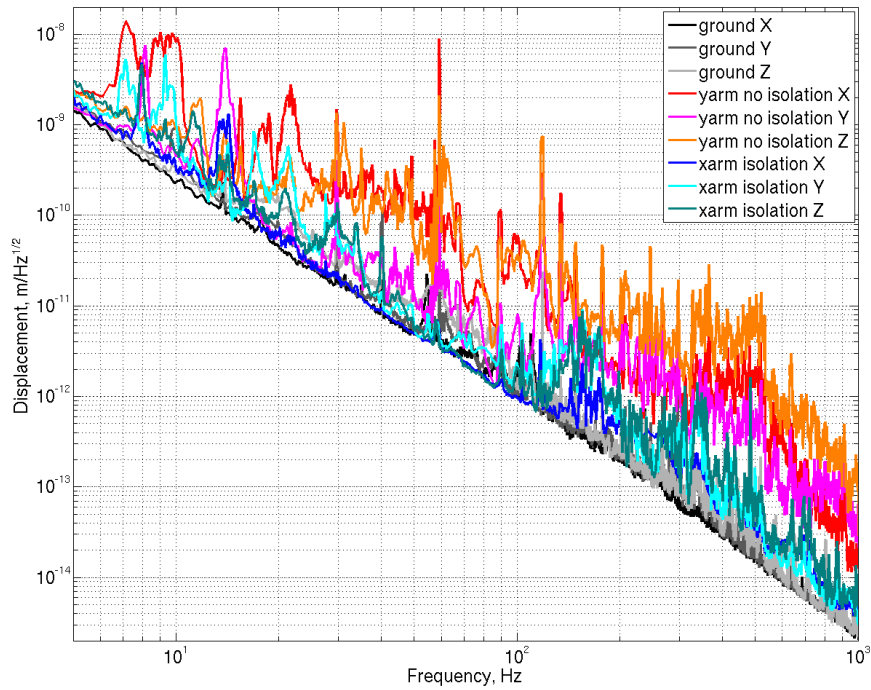
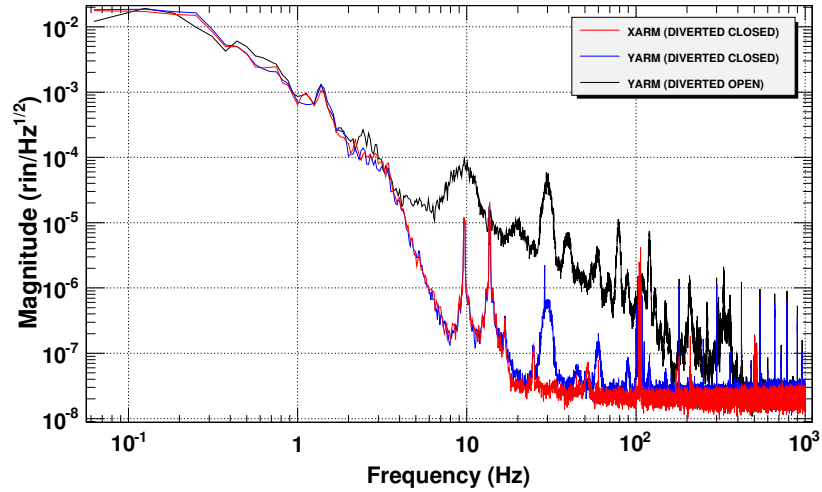


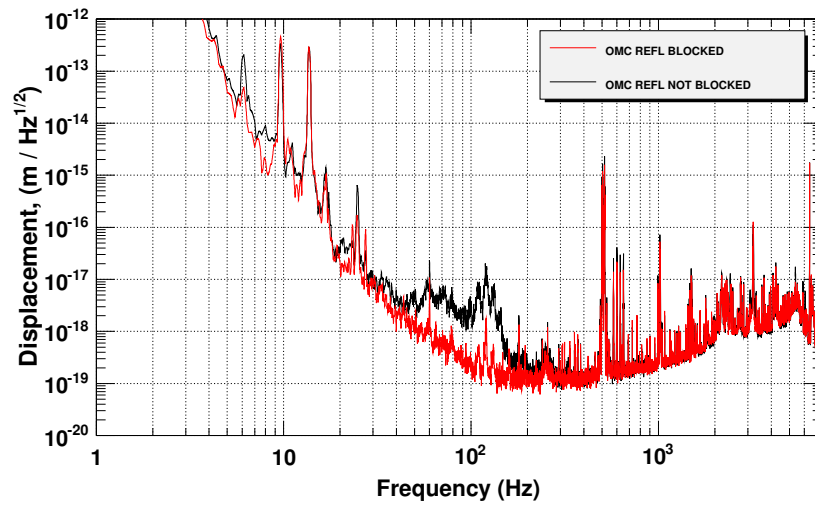
Figure 8.9: Comparisons of seismic noise with motion of X- and Y-arm tubes. If tube is insulated then motion in directions perpendicular to the cavity axis is significantly reduced above 20Hz.

### 8.3.3 In-air paths and chamber walls

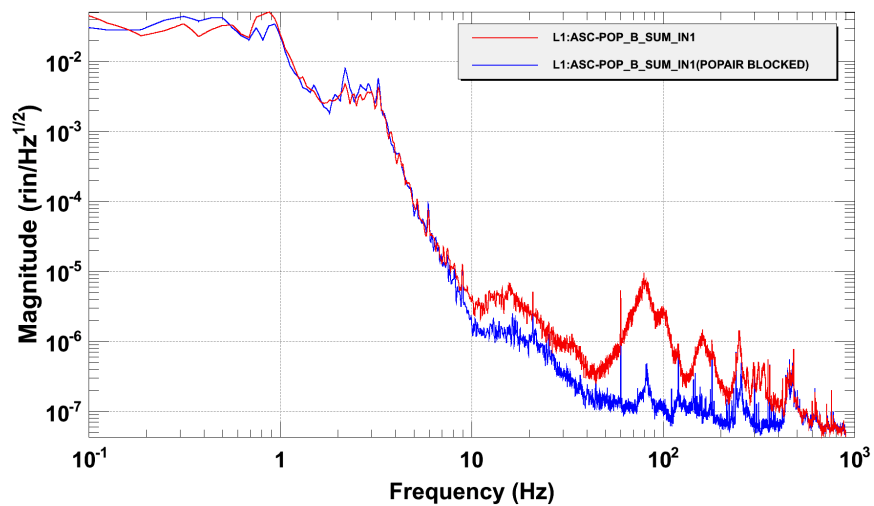
Scattered light noise from in-air paths was witnessed several times during commissioning process. Most significant noises in the frequency range 40Hz - 300Hz comes from in-air paths at end stations and OMC reflected beam. This noise was mitigated by blocking all in-air paths using shutters and beam diverters. Another source of scattered light noise comes from in-air POP beam. In full lock beam diverter is closed to reduce power of in-air beam by factor of 10 but scattered light noise is still seen on POP QPDs. Figures 8.10 show scattered light noises in arm transmission QPDs, DARM and POP QPD coming from in-air beams.



(a) Comparison of arm transmission QPD signals when in-air paths are open and closed using beam diverters.



(b) Comparison of DARM spectrum when OMC reflected in-air path is open and blocked.



(c) Comparison of POP QPD signal when POP beam diverter is open and closed.

Figure 8.10: Scattered light noises from in-air beams.

Scattering from chamber walls is measured by providing acoustic excitation and measuring response in DARM. If clean room fans located above the chambers are turned on, motion of chamber walls increases by factor of 30-100 above 40Hz. Most significant effect from acoustic excitation seen in DARM comes from HAM6 chamber as shown in figure 8.11.

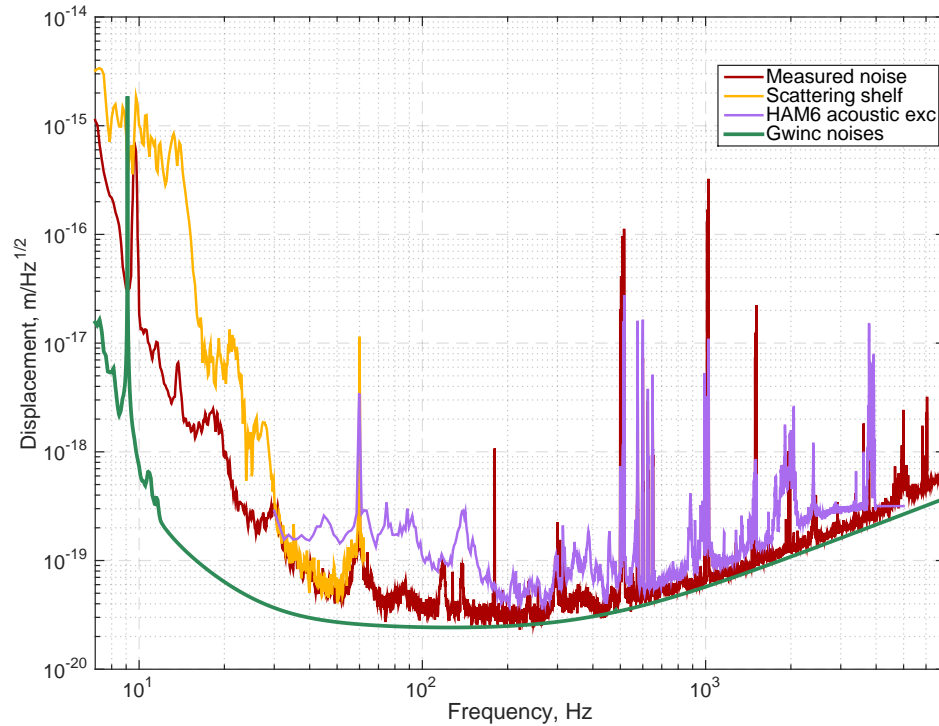


Figure 8.11: Scattering from the output port. Orange trace shows scattering shelves seen in DARM if motion of HAM5 ISI is increased by 1 $\mu$ m/sec. Pink trace shows scattered light noise if HAM6 fans are turned on. Fans increase acoustic noise around HAM6 chamber by factor of 3 around 70Hz and factor of 10 at higher frequencies.

Scattering from the chamber and test mass baffles was observed around 30Hz and came from HVAC system. One of the support beam was sitting on a stone bypassing the effect of the springs. Whole Y-end building was moving at 30Hz and this line was seen in ground seismometers, accelerometers on the chamber walls and ISI inertial sensors. Motion reduced by two orders of magnitude after removing the stone from the support beam.

If interferometer input power is 25W, transmission power through arm cavities is 0.5W and most of this power goes to the beam dumps. However, scattering noise from end stations was witnessed during aLIGO commissioning when loud vacuum pumps were running. Pumps produced acoustic noise factor of 10 stronger compared to background, and interferometer noise increased by 10-20% in the frequency range 80Hz-200Hz.

### 8.3.4 Output mode cleaner

Backscattering from the output mode cleaner produces scattering shelves in the gravitational wave spectrum. Light coming out from interferometer passes through Faraday isolator, mode matching telescope, output mode cleaner and reaches photodiodes. Laser beam is partially scattered back into interferometer due to losses in the output mode cleaner. Scattered light reflects back from interferometer into OMC and is seen as additional noise. Scattering produces relative intensity noise given by equation:

$$\begin{aligned} E_{PD} &\approx E_{out} \cdot (1 + rr_{IFO} e^{4\pi i L(t)/\lambda}) \\ RIN(t) &= 2 \cdot r \cdot r_{IFO} \cdot \cos(4\pi i L(t)/\lambda) \end{aligned} \tag{8.3}$$

where  $r$  is OMC amplitude reflectivity multiplied by OFI isolation factor, and  $r_{IFO}$  is interferometer amplitude reflectivity from AS port. Distance between interferometer and OMC  $L$  is modulated by relative motion between HAM5 and HAM6 optical benches, control signal applied to SRM. Angular motion of the signal recycling cavity axis couples to distance fluctuations quadratically.

Reflectivity of the output port was measured in different optical configurations to reduce possible errors due to carrier jitter, HOMs, and clipping on HAM6 table. Table 8.3 shows interferometer field reflectivity  $r_{IFO}$  from AS port. Since  $r_{IFO}$  is different for carrier and sidebands, a third row of the table specifies the field for which  $r_{IFO}$  is computed:

Configuration	$r_{IFO}$	Field
Single bounce	0.184	carrier, sidebands
SRX sideband lock	0.92	carrier
Full lock	1	carrier
Full lock	0.26	45MHz sidebands
PRX carrier lock	0.36	carrier
PRX sideband lock	0.12	carrier

Table 8.3: Interferometer field reflectivity from AS port.

Output port reflectivity  $r$  is derived from the level of scattering shelf in the frequency domain. Shelf is produced by exciting OMC at 0.2 Hz with velocity of  $20\mu\text{m}/\text{sec}$ . Figure 8.12 shows OMC RIN measured in optical configurations described in the table 8.3 and fit for  $r$  equal to  $1.3 \cdot 10^{-4}$ . Measurements in these configurations show close results (within 50%) for both carrier and sidebands. It was noticed that carrier reflectivity  $r$  depends on the beam path through the Michelson interferometer and can be improved by order of magnitude by proper alignment.

Figure 8.11 shows scattering shelves in DARM when seismic feedforward correction path on

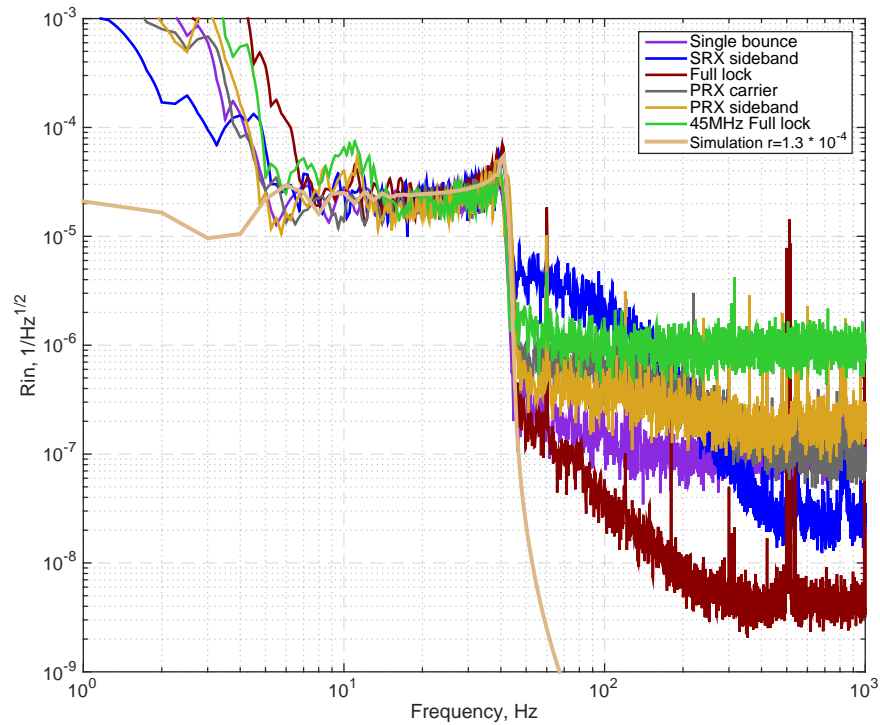


Figure 8.12: Measurement of output port reflectivity.

HAM5 chamber was detuned to increase relative velocity between interferometer and OMC by 5 $\mu$ m/sec. Secondary shelves can also be seen at higher frequencies coming from back reflections from OMC reflected path and output Faraday isolator. Scattering shelves of similar size were seen during winter time when microseismic activity is high.

## 8.4 Mitigation techniques

The problem of reducing scattered light noise to gravitational wave channel is addressed in different ways. There are attempts to reduce motion of the scattering surfaces and coupling transfer functions. Most efforts are currently concentrated around HAM6 chamber since scattered light noise is the dominant one. The list below summarizes current projects and future technique developed to reduce scattered light noise:

- All in-air beams are blocked using shutters and beam diverters. Only in-vacuum photodetectors are used in low noise regime
- OMC shield is currently under construction. It is designed to reduce probability of direct coupling of scattered light to OMC photodetectors

- Amount of scattered light phase modulation can be reduced by installing insulation on HAM6 chamber walls and tubes located near the chamber. Figure 8.2 shows that if insulation is installed then motion of the chamber walls can be significantly reduced above 20Hz
- Scattering shelves from the output mode cleaner can be reduced if balanced homodyne detection scheme is used instead of DC readout
- Feedforward cancellation scheme can be used to subtract scattered light noise from gravitational wave detector if motion of scattering surfaces is measured

### 8.4.1 Feedforward cancellation

Algorithms for static and adaptive feedforward subtraction are discussed in chapter 9. This section is devoted to construction of witness signals coherent with scattered light noise. Phase modulation of light due to moving scattering surfaces causes noise in gravitational wave channel according to equation:

$$E_{pd}(t) = E_{dc} + E_{darm}(t) + E_{scatter}(t)e^{4\pi iL(t)/\lambda} \quad (8.4)$$

where  $E_{pd}(t)$  is electric field on OMC photodetectors,  $E_{darm}(t)$  - audio sidebands from the arm cavities,  $E_{scatter}(t)$  - scattered light field,  $L(t)$  - distance between the main beam and moving scattering surface.

Scattering surfaces move by influence of ground motion and acoustic background, and distance between main beam and surface  $L(t)$  can be written as a sum of low and high frequency components  $L_{lf}(t) \sim \lambda, L_{hf}(t) \ll \lambda$ . First term produces scattering shelves as shown in figure 8.11. Second term is seen in gravitational wave channel at higher frequencies. However, coupling is not linear due to large low-frequency motion. This can be seen from the following equation for DARM signal due to scattered light noise:

$$\begin{aligned} DARM_{scatter}(t) &\sim \sqrt{P_{dc}P_{scatter}} \operatorname{Re} \left[ e^{4\pi i(L_{lf}(t)+L_{hf}(t))/\lambda} \right] \\ &\sim \operatorname{Re} \left[ \sim e^{4\pi iL_{lf}(t)/\lambda} \left( 1 + \frac{4\pi iL_{hf}(t)}{\lambda} \right) \right] \end{aligned} \quad (8.5)$$

where  $P_{dc} = E_{dc}E_{dc}^*$  - DC power on OMC PDs,  $P_{scatter} = E_{scatter}E_{scatter}^*$  - power of scattered light. Equation 8.5 shows that coupling of high frequency motion of scattering surfaces is modulated by the term  $\exp(4\pi iL_{lf}(t)/\lambda)$ . In case of large low frequency motion  $L_{lf}(t) \sim \lambda$  coupling of high frequency motion  $L_{hf}(t)$  to gravitational wave channel becomes non-linear as shown in figure 8.13.

In order to subtract scattered light noise at high frequencies, it is not sufficient to measure motion of the scattering surface using accelerometers installed on the chamber walls. Low frequency

seismometers should also be used to reconstruct low frequency modulation factor. Fortunately, only one seismometer and a few accelerometers are required to subtract scattered light noise coming from one chamber. RMS of ground motion comes from microseismic frequencies and all chamber walls move in common with ground measured by seismometer.

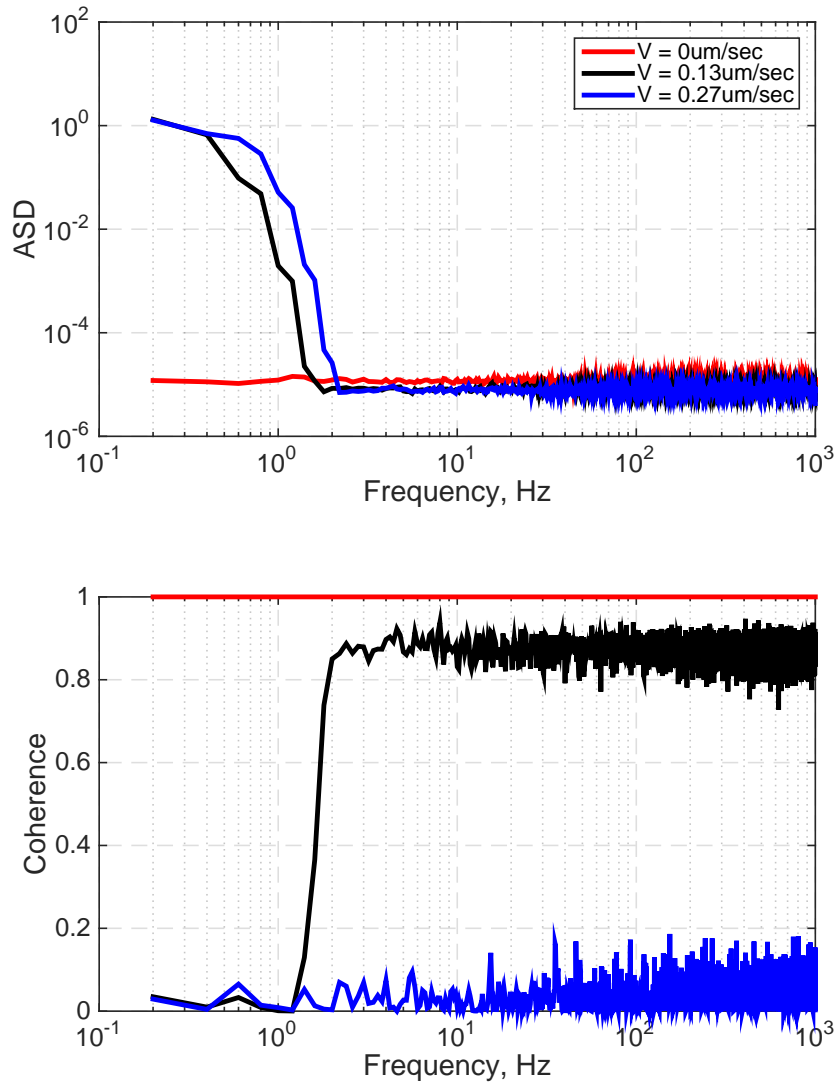


Figure 8.13: Simulation of scattering noise coupling to DARM. Scattering shelf comes from large low frequency motion. Coherence between DARM and high frequency motion of the scattering object depends on low frequency motion.

Amount of accelerometers required for feedforward cancellation depends on the coherence length

of chamber walls motion. A set of measurements was done to determine that coherence length is on the order of  $\sim 1m$ . Several accelerometers were installed on HAM6 chamber with spacing from 10cm to 100cm, and coherence between accelerometer signals was measured as shown in figure 8.14.

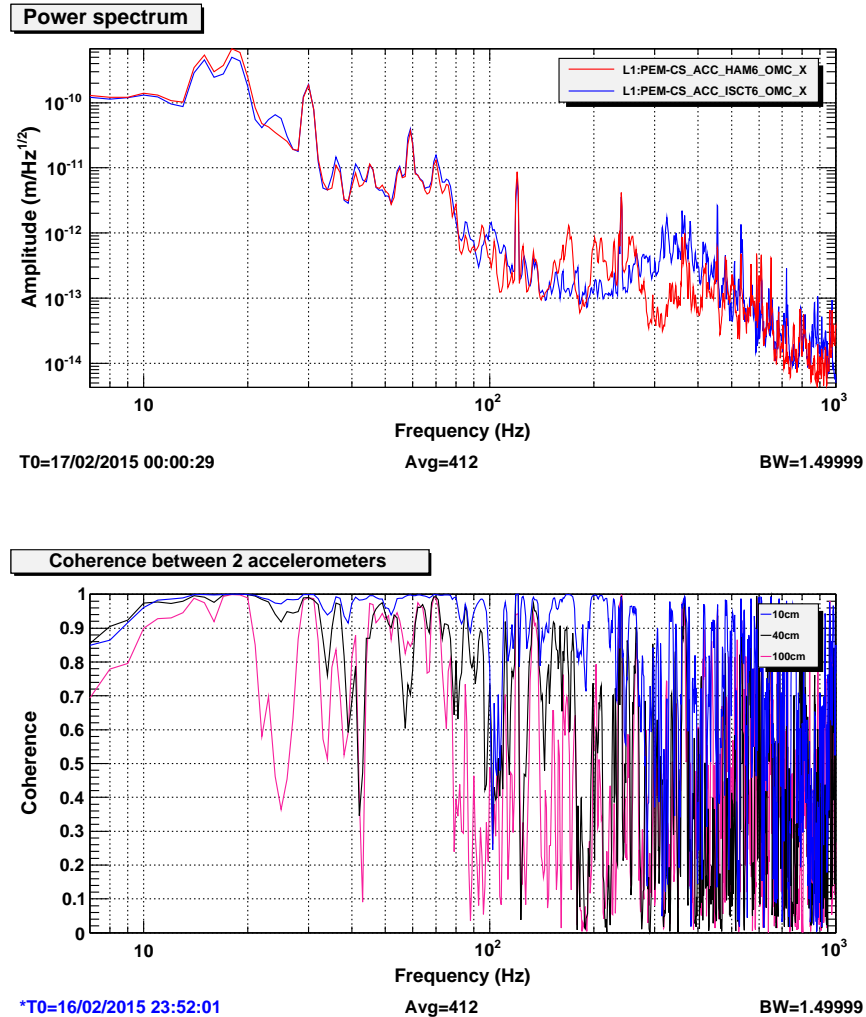


Figure 8.14: Coherence between accelerometers installed on the same wall on HAM6 chamber.

Scattering points are likely to move due to jitter of the main beam. In this case transfer function from scattering surface motion to gravitational wave channel is modulated by angular motion, and adaptive filters should be used for feedforward cancellation.

## Chapter 9

# Feedforward noise cancellation

Noises in the gravitational wave channel limit aLIGO sensitivity to astrophysical sources. It is sometimes possible to eliminate noise source itself, for example, to reduce actuation or sensing electronics noise, improve laser amplitude noise or cool down the test masses. In other cases, it is feasible to reduce coupling coefficient from the noise source to gravitational wave channel, for example, to block scattering beams in order to avoid acoustic noise coupling, set active seismic isolation to reduce seismic noise coupling or eliminate optical losses in X- and Y-arms to reduce frequency noise coupling.

However, many types of noise sources and their coupling to gravitational channel cannot be completely reduced. Feedforward cancellation scheme gives an opportunity to filter DARM signal and subtract noise source measured by another instrument. This instrument can be seismometer, accelerometer, magnetometer, or photodiode which is non sensitive to gravitational waves. Feedforward cancellation scheme actively reduces noise coupling to gravitational wave channel.

Figure 9.1 shows feedforward cancellation scheme of measured noise source from gravitational wave channel. Filtering can be done offline with collected data of DARM and noise witness channels or online using actuator  $A$ . Effective noise coupling is reduced from  $T$  to  $T - SS_{est}^{-1}T_{est}A_{est}^{-1}A$ . If estimations of the noise coupling as well as sensing and actuation transfer functions are properly done  $S = S_{est}, T = T_{est}, A = A_{est}$ , then noise source is completely decoupled from gravitational wave channel.

Transfer functions  $S$  and  $A$  are usually well-known and noise coupling transfer function  $T$  can be measured or simulated. In real experiments noise sources are usually measured using several sensors and witness signals are correlated between themselves. In this case optimal estimation schemes, such as Wiener filtering, are required for optimal feedforward cancellation. If coupling transfer function  $T$  changes with time then adaptive filters are required to compute time dependent transfer function  $T_{est}$ .

Feedforward cancellation schemes were already successfully applied during initial LIGO phase. Offline schemes were applied to subtract magnetic noise measured by magnetometers and MICH noise

measured by optical sensor from gravitational wave channel [92]. Online seismic noise subtraction scheme using static Wiener filter was set up in LIGO Livingston observatory and improved lock acquisition of the instrument [93]. Seismic noise subtraction schemes from the input mode cleaner length signals using adaptive filters were tested at the 40m prototype [94].

Sections 1 and 2 of the current chapter describe feedforward noise cancellation of auxiliary length and angular degrees of freedom from aLIGO gravitational wave channel. Section 3 describes optimal static and adaptive subtraction schemes from input mode cleaner and arm length signals applied at the 40m prototype.

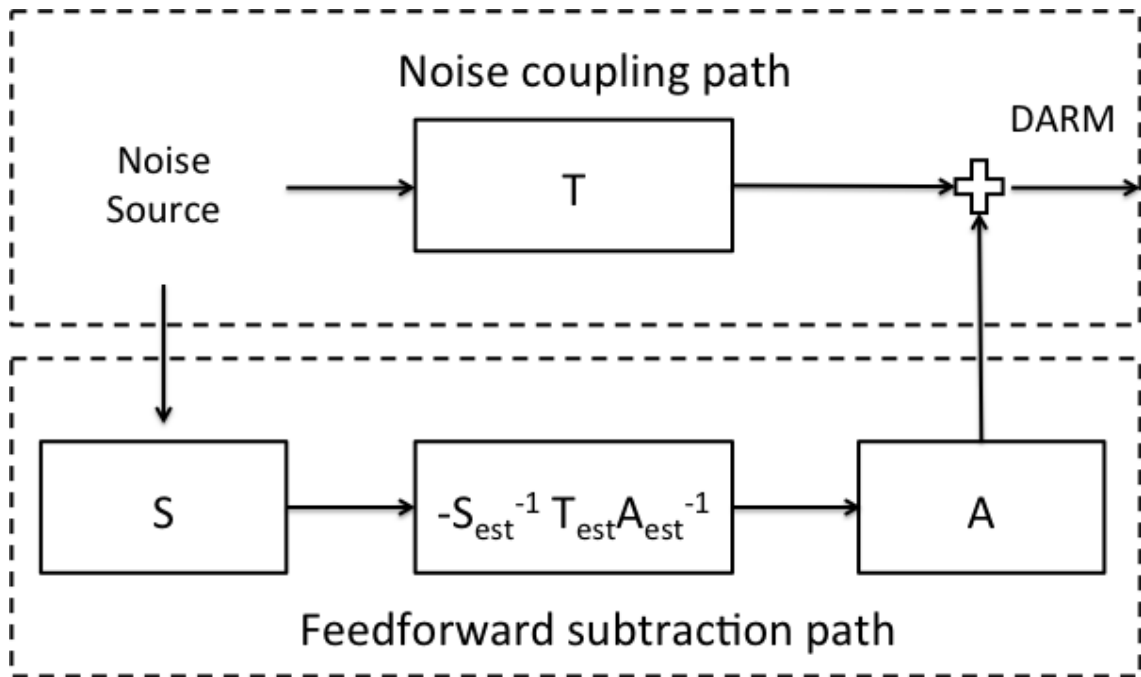


Figure 9.1: Simplified scheme of feedforward subtraction. Noise source couples to gravitational wave channel with transfer function  $T$ . Noise is measured by witness instrument with transfer function  $S$ , and is conditioned and canceled from DARM using actuator  $A$ .

## 9.1 Auxiliary length loops

Frequency noise and DRMI residual motion couples to gravitational wave channel as discussed in chapter 5. Figure 9.2 shows coherence between DARM and auxiliary longitudinal degrees of freedom. Most significant contributions come from MICH and SRCL.

Residual motion of MICH and SRCL is dominated by the sensing noise at frequencies above 10Hz. Feedback control loops inject POP45 I and Q sensing noise back into interferometer. It is therefore reasonable to run feedforward correction from MICH and SRCL control signals to DARM. Transfer functions from MICH and SRCL to DARM are measured and compared to the model as

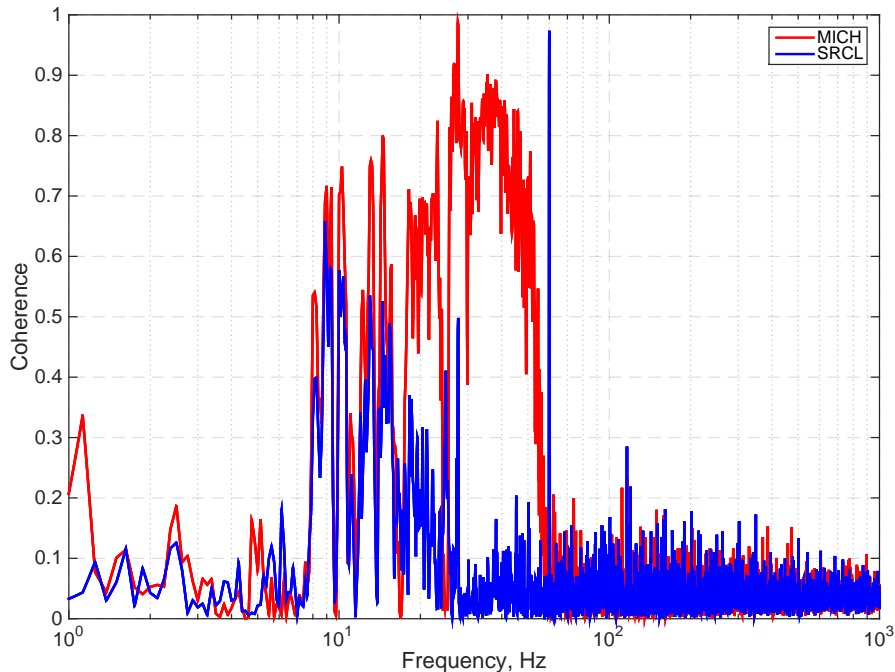


Figure 9.2: Coherence between DARM and auxiliary length degrees of freedom. Red trace shows coherence with MICH. Blue trace shows coherence with SRCL.

shown in figure 9.3.

Online feedforward cancellation scheme assumes that MICH control signal does not disturb other longitudinal degrees of freedom. Since MICH is controlled by the beam splitter, PRCL and SRCL are also disturbed according to the following equations:

$$\delta PRCL = -\delta L_{PRM} - \frac{1}{\sqrt{2}}\delta L_{BS} \quad \delta MICH = \sqrt{2}\delta L_{BS} \quad \delta SRCL = -\delta L_{SRM} + \frac{1}{\sqrt{2}}\delta L_{BS} \quad (9.1)$$

where  $\delta L_M$  is motion of the optic  $M$  in the longitudinal direction.

If MICH motion couples to SRCL, then transfer function from MICH control signal to DARM becomes more complicated since in this case MICH control couples not only through DARM sensing but also through radiation pressure mechanism with coupling coefficient  $\alpha$ :

$$\frac{DARM(f)}{MICH(f)} = \frac{1}{260} + \alpha \frac{1}{f^2} \quad (9.2)$$

and  $\alpha$  is proportional to SRCL coupling to DARM and MICH coupling to SRCL.

In order to avoid cross couplings and diagonalize actuation matrix in DRMI loops, auxiliary feedforward correction loops from BS to SRM and PRM are set up. These loops subtract MICH

control signal from PRCL and SRCL. MICH feedforward signal goes to penultimate mass of PRM and SRM, and correction filter  $K$  depends only on the ratio of the actuator strengths and is assumed to be frequency independent.

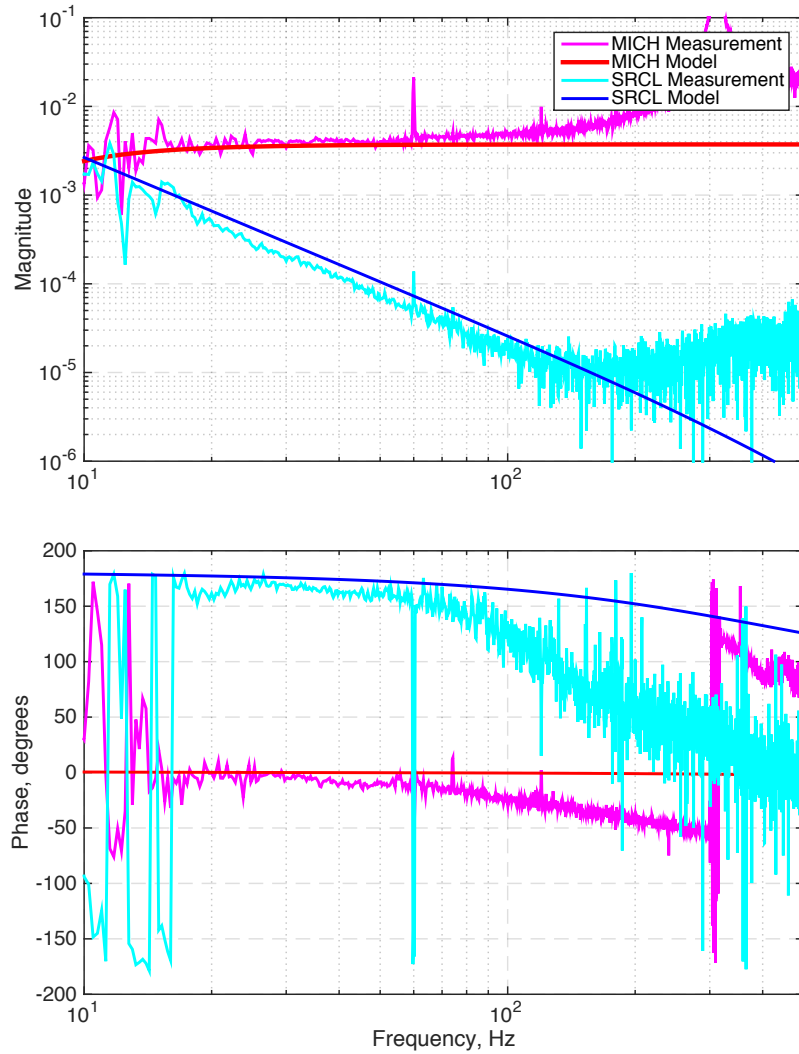


Figure 9.3: Simulated and measured MICH and SRCL coupling to DARM.

Diagram of complete feedforward cancellation scheme of MICH and SRCL from DARM is shown in figure 9.4. Diagonalized MICH and SRCL control signals are used as witnesses in the feedforward cancellation scheme from DARM. MICH feedforward filter is dependent only on the arm finesse, and actuator strength and can be considered to be frequency independent.

Since coupling of SRCL to DARM is due to radiation pressure effects, coupling transfer function has shape of  $1/f^2$  as shown in figure 9.3. SRCL control at high frequencies goes to bottom SRM stage, and feedforward correction signal goes to penultimate state of test masses to compensate for  $1/f^2$  slope. Feedforward correction filter is frequency independent in this case.

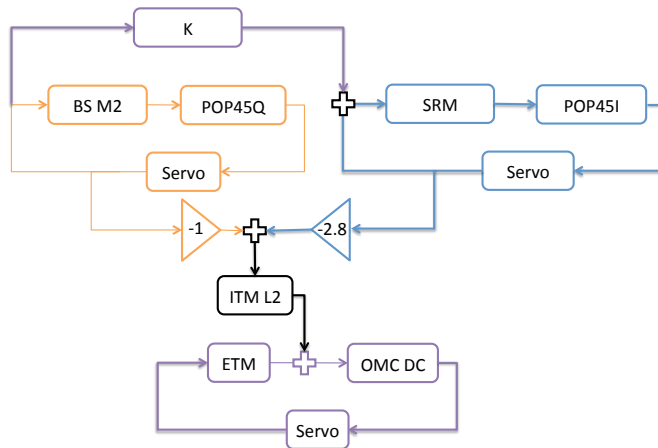


Figure 9.4: Online feedforward subtraction scheme of MICH and SRCL from DARM.

Feedforward cancellation scheme reduces MICH coupling to DARM by factor 30 and SRCL coupling by factor of 10. Efficiency of MICH subtraction is limited by the precision of the actuator compensation. SRCL subtraction is limited by OMC beam jitter. Alignment fluctuations modulate DARM offset and coupling of SRCL to DARM becomes non-linear. Figure 9.5 shows result of online subtraction of MICH and SRCL from gravitational wave channel.

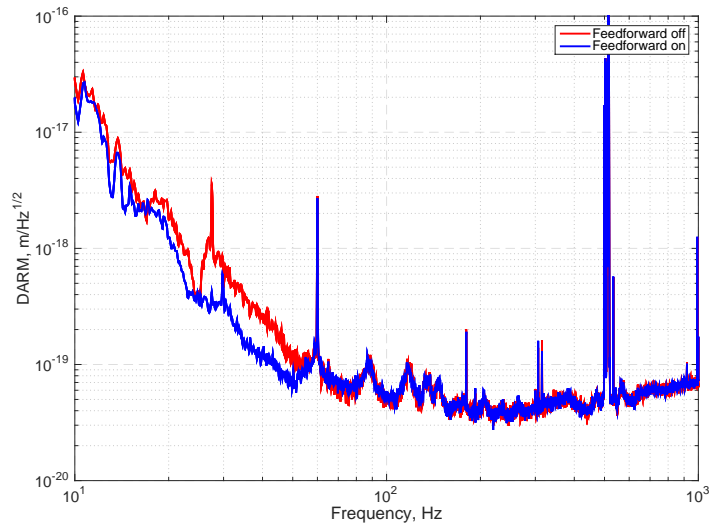


Figure 9.5: DARM spectrum with and without online feedforward subtraction of MICH and SRCL.

## 9.2 Angular controls

Sensing noise from the arm cavities angular degrees of freedom linearly couples to DARM by beam offset from the mirror center and imperfections in the coil balancing of quadruple suspensions. Coupling transfer function is flat in this case and subtraction gains are tuned to compensate for beam position.

Beam position inside the arm cavities is estimated by dithering optics in pitch and yaw and demodulating length signal. Table 9.1 summarizes measured beam positions on four aLIGO test masses. Since DARM signal from coil imbalance is indistinguishable from signal related to beam decentering, results shown in table 9.1 are valid in case if coil imbalance is smaller than  $\frac{\delta F}{F_0} < 10^{-3}$ , where  $F_0$  is signal applied to all four coils and  $\delta F$  is difference in actual force applied to the mirror magnets. Imbalance level of  $10^{-3}$  is achieved by driving optics in pringle mode and minimizing signals in pitch and yaw using optical level sensors.

	ETMX, mm	ETMY, mm	ITMX, mm	ITMY, mm
Pitch	10	2	0	5
Yaw	2	5	17	0

Table 9.1: Measured beam decentering on four test masses using dithering technique.

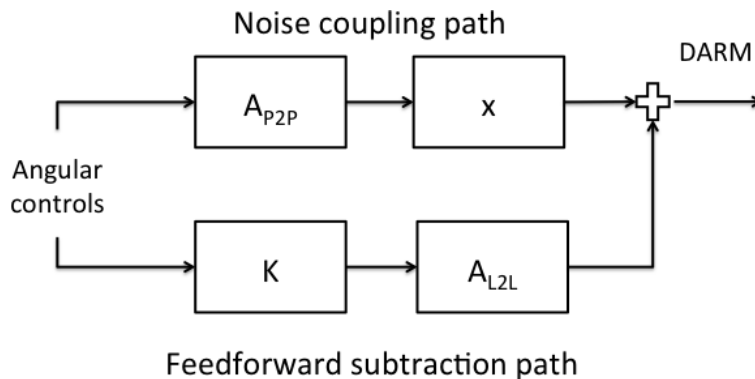


Figure 9.6: Online feedforward subtraction scheme of angular controls noise. Noise couple through beam offcentering or coil imbalance  $x$  and is subtracted with feedforward filter  $K$ . Transfer functions  $A_{P2P}$  and  $A_{L2L}$  denote actuator transfer function for angle and length actuation.

Figure 9.2 shows scheme of feedforward cancellation of angular control noise from gravitational wave channel. Performance of angular feedforward subtraction is limited by two factors:

- RMS of angular motion of the arm cavity axis causes beam spots to move on the mirrors. Static feedforward gain can not account for this motion. This means that linear feedforward

cancellation scheme has the limit of:

$$\delta DARM = l \cdot \alpha_{RMS} \delta \alpha \quad (9.3)$$

where  $l$  in units of [m/rad] determines how much beam moves on a particular arm mirror in response to mirror angular fluctuations of  $\alpha_{RMS}$ ;  $\delta \alpha$  is angular motion above 10Hz.

- Transfer functions are usually known with precision of 0.3 – 1%. This sets the limit on feedforward cancellation given by equation

$$\delta DARM = x \cdot \delta \alpha \frac{\delta A}{A} \quad (9.4)$$

where  $x$  is beam decentering on the optic given in the table 9.1,  $\frac{\delta A}{A} \approx 10^{-2}$  is uncertainty in the transfer function  $A$

Angular control loops are designed to maximize open loop gain at low frequencies to reduce RMS of residual cavity axis motion  $\alpha_{RMS}$ . This approach stabilizes beam motion on the cavity mirrors and feedforward subtraction limit 9.3 becomes softer. At the same time higher bandwidth loops introduce more noise above 10Hz and limit DARM sensitivity since not all angular control noise can be canceled out due to subtraction limit 9.4.

Optimal control loop depends on the level of seismic noise that significantly changes during the year period. During winter time microseismic activity is high and ground velocity is 2 – 3  $\mu\text{m}/\text{sec}$  RMS. In this case bandwidth of angular control loops is set to 3Hz.

### 9.3 Seismic noise

Ground motion dominates RMS of optical cavity length fluctuations. Feedforward seismic noise cancellation scheme can significantly reduce fringe velocity during the process of lock acquisition when interferometric signals are strongly non-linear.

Multiple low noise STS-2 seismometers are installed around the chambers to measure ground motion near the cavity optics. Transfer functions from seismometer signals to cavity length signal are estimated when cavity is locked. Afterwards seismometer signals are multiplied by these transfer functions to reduce fringe velocity for future lock acquisition processes.

Since seismometer signals are generally correlated between each other, cross couplings play a significant role in the process of feedforward noise cancellation. In particular, cross couplings make it insufficient to only measure transfer functions between seismometer signals and cavity length. Transfer functions between seismometer signals should be also measured and included in the process of noise subtraction.

Well known techniques that optimize feedforward subtraction are static Wiener filters [95] and adaptive filters [96]. First type of filters minimizes residual error in the mean-least-square sense by using data from witness and desired signals collected in advance. Then computed optimal filter can be applied for the future data. Second type of filters adapt their coefficients on the fly starting from initial guess.

### 9.3.1 Static filter

Wiener filter is of finite impulse response (FIR) type and is parameterized by  $N$  numbers known as filter coefficients  $w_i, i = 0, \dots, N-1$ . Given filter input  $u(k)$  at particular time moment  $k$ , output of the filter is computed according to equation:

$$s(k) = \mathbf{w}'\mathbf{u} \quad (9.5)$$

where  $\mathbf{w} = [w_0, w_1, \dots, w_{N-1}]$  is  $N \times 1$  vector of filter coefficients and  $\mathbf{u} = [u(k), u(k-1), u(k-N+1)]$  is an input vector.

Usually several witness channels are used and one FIR filter is introduced for each of them. If number of witness channels is  $P$ , then the total number of coefficients increases from  $N$  up to  $N \times P$ . In this case total filter output is given by equation

$$s(k) = \sum_{p=1}^P s_p(k) = \sum_{p=1}^P \mathbf{w}_p' \mathbf{u}_p \quad (9.6)$$

Coefficients  $\mathbf{w}_p$  are computed to minimize least-mean-square error of the feedforward subtraction. Optimal solution  $\mathbf{w}_{\text{opt}}$  minimizes quadratic cost function:

$$J(\mathbf{w}) = E(ee^*) = E(d-s)(d-s)^* = E\left(d - \sum_{p=1}^P \mathbf{w}_p' \mathbf{u}_p\right) \left(d - \sum_{p=1}^P \mathbf{w}_p' \mathbf{u}_p\right)^* \quad (9.7)$$

$$\nabla J(\mathbf{w})|_{\mathbf{w}=\mathbf{w}_{\text{opt}}} = 0$$

where symbol  $E$  denotes expectation value,  $e$  is residual error,  $d$  is desired or target signal.

Equation 9.7 can be simplified if all coefficient vectors and witness channel vectors are combined in two vectors  $\mathbf{v} = [\mathbf{w}_1, \mathbf{w}_2, \dots, \mathbf{w}_P]$  and  $\mathbf{y} = [\mathbf{u}_1, \mathbf{u}_2, \dots, \mathbf{u}_P]$ :

$$J(\mathbf{v}) = E(d - \mathbf{v}'\mathbf{y})(d - \mathbf{v}'\mathbf{y})^* \quad (9.8)$$

$$\nabla J(\mathbf{v}_{\text{opt}}) = -2E(d - \mathbf{v}_{\text{opt}}'\mathbf{y})\mathbf{y}' = -2(E(d\mathbf{y}) - \mathbf{v}'E(\mathbf{y}\mathbf{y}')) = 0$$

Solution of equation 9.8 determines optimal Wiener filter coefficients  $\mathbf{v}$ . In the matrix form they

can be written as:

$$\mathbf{w}_{\text{opt}} = R_u^{-1} R_{ud} \quad (9.9)$$

where  $R_u = E(\mathbf{y}\mathbf{y}')$  and  $R_{ud} = E(d\mathbf{y})$  are autocorrelation and crosscorrelation matrices of size  $N \cdot P \times N \cdot P$  and  $N \cdot P \times 1$ . Matrix  $R_u$  is of Toeplitz form since  $E(y(k)y(k-q)) = E(y(k-z)y(k-z-q))$  for arbitrary  $q$  and  $z$ . Inversion process of matrix  $R_u$  can be done with complexity of  $O(N^2)$  and allows time efficient solution of equation 9.9

In the case of seismic feedforward subtraction,  $d$  is cavity length signal,  $\mathbf{u}_p$  is buffered seismometer signal from channel  $p$ ,  $e$  is residual motion of the cavity after feedforward subtraction. Online feedforward subtraction scheme is implemented in three steps:

- Optimal Wiener filter coefficients are computed using equation 9.9. It takes about 3 minutes to solve this equation if 30 minutes of data is collected with sampling rate of 256Hz. Each filter has 10000 coefficients
- Optimal filters are converted from FIR to IIR type with less amount of coefficients using Vectfit utility [97]. First, frequency response of optimal FIR filters is computed and conditioned to avoid noise injections at high frequencies. Then this response is fitted using IIR filters. Resultant IIR filters had only 10 poles and zeros. This allows to save computational type and use feedforward subtraction filters online. Figure 9.7 shows fitting process of optimal FIR filter using Vectfit utility

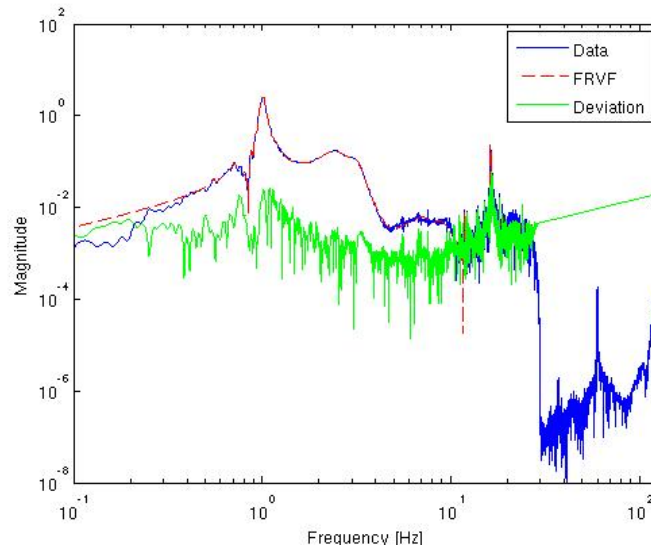


Figure 9.7: Fitting of FIR filter with 10000 coefficients using IIR filter with 10 poles and zeros using Vectfit utility.

- Invert actuator and plug in optimal IIR filters to online system for feedforward subtraction

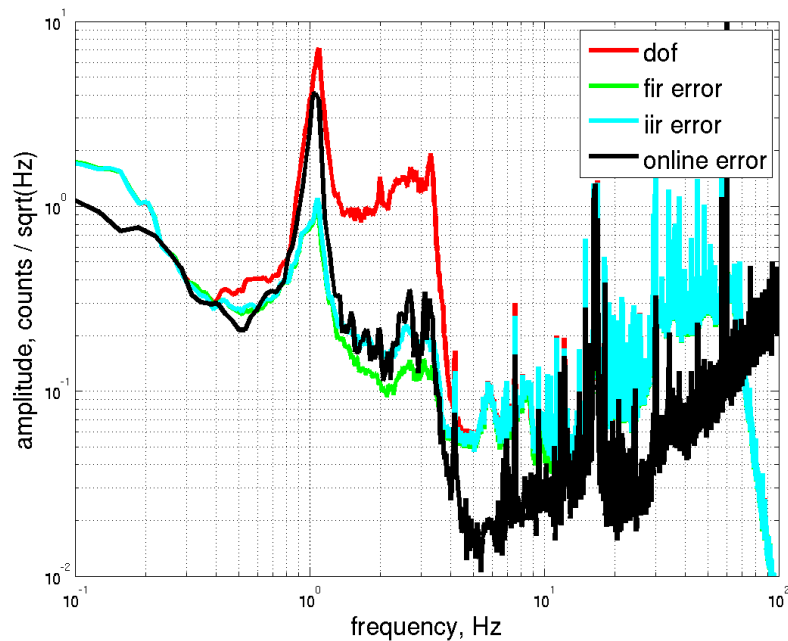


Figure 9.8: Result of static feedforward subtraction using static Wiener filtering technique. Red trace shows initial target signal before subtraction. Green curve is residual signal after applying FIR Wiener filter. Blue trace shows residual motion after applying IIR filter obtained by fitting optimal FIR filter. Black trace shows residual motion after installing IIR filter in the online system.

Figure 9.8 shows IMC length signal before and after feedforward subtraction. Online filtering requires accurate compensation for the actuator. Transfer function from ground motion to cavity length fluctuation changes on the time scale of few weeks, and subtraction performance slowly degrades. Adaptive filters can account for this problem and update their coefficients to track transfer functions from seismometers to the cavity length signal.

### 9.3.2 Adaptive filters

Gradient descent algorithms dynamically estimate Wiener filter coefficients by starting from an initial guess:

$$\mathbf{w}_{\mathbf{p},i+1} = \mathbf{w}_{\mathbf{p},i} - \mu \nabla J(\mathbf{w}_{\mathbf{p},i}), \quad \mathbf{w}_{\mathbf{p},0} = 0 \quad (9.10)$$

where step-size  $\mu$  determines the rate of coefficient update and should be smaller than some critical value  $\mu_c r$  for convergence.

In online filtering applications, matrices  $R_u$  and  $R_{ud}$  are not known and can be approximated using available data. LMS algorithm omits operator of expectation value  $E$  from equation 9.7 and

uses instantaneous values of error signal to estimate  $\nabla J(\mathbf{w}_p)_i$ :

$$\mathbf{w}_{p,i+1} = \mathbf{w}_{p,i} + \mu e \mathbf{u}_{p,i} \quad (9.11)$$

Step-size parameter  $\mu$  can be time dependent. Normalized LMS algorithm uses constant step-size parameter divided by the norm of the witness vector:  $\mu(i) = \frac{\mu_0}{\|\mathbf{u}_p\|^2}$ . Necessary condition for convergence of coefficient vector is  $\mu_0 < 2$ .

Leaky-LMS algorithm [98] tends to minimize cost function  $J(\mathbf{w})$  from equation 9.7 and norm of the coefficient vector  $\mathbf{w}_{\text{opt}}$ . New cost function sets a limit on the norm of the coefficient vector is can be written as  $\alpha \|\mathbf{w}\|^2 + J(\mathbf{w})$ .

Combined normalized and leaky LMS algorithms give equation for coefficient adaptation:

$$\mathbf{w}_{p,i+1} = (1 - \tau) \mathbf{w}_{p,i} + \frac{\mu_0}{\|\mathbf{u}_p\|^2} e \mathbf{u}_{p,i} \quad (9.12)$$

where parameter  $\tau \ll 1$ .

LMS algorithm was applied for feedforward subtraction of seismic noise from input mode cleaner and arm cavity length signals at the 40m prototype interferometer. Seismometers and accelerometers installed on the ground were used as witness signals as shown in figure 9.9. Cavity length signals were used as error signals.

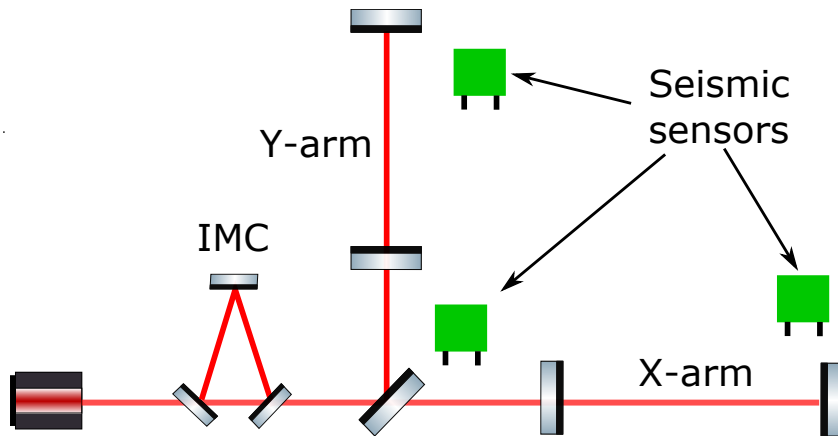


Figure 9.9: Test of LMS adaptive filters at the 40m prototype. Seismometers are located in the corner and end stations.

Key property of this problem is that not only seismometer signals are partially coherent between themselves but also target signals are coupled. Correlation occurs since laser is locked to the input mode cleaner and arm length is measured relative to the laser wavelength.

Front-end C1OAF model running at 2kHz was installed to perform adaptive filtering of the cavity length signals. Since coherence between witness and desired signals is seen only below 20Hz,

adaptive filters perform downsampling of witness and error signals by a factor of  $D_s = 8$ . Anti-aliasing (AA) and anti-imaging (AI) filters were installed in the input and output of the filter to account for downsampling.

Adaptive filters produce outputs that are sent to the models that run on other computers. Inevitable transmission delays in the actuation path cause degradation of feedforward cancellation performance.

Filtered-X LMS [99] algorithm accounts for the AI filters and delay in the compensation path by replacing vector  $\mathbf{u}_p$  in equation 9.12 with vector  $\mathbf{r}_p = F\mathbf{u}_p$ , where operator  $F$  is the product of all operators that are applied to the filter output before subtraction of this signal from the target signal. Figure 9.10 shows the scheme of adaptive feedforward cancellation of seismic noise from cavity length signals using Fx-LMS algorithm.

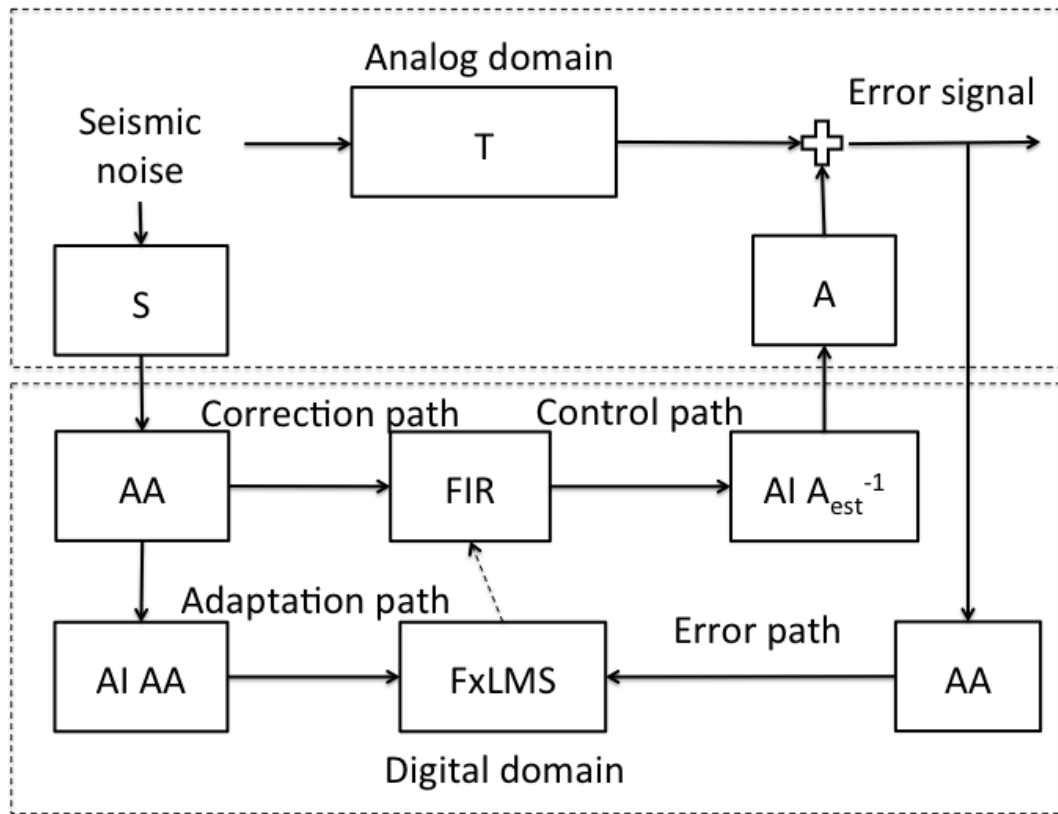


Figure 9.10: Online adaptive seismic noise cancellation scheme using FxLMS algorithm.

Running time of one cycle of the MIMO adaptive filter on a 3GHz Intel processor was experimentally found to satisfy the following equation:

$$T_0 = 24 \cdot \frac{N}{10000} \cdot \frac{1}{D_s} \cdot \frac{P}{1} \cdot \frac{M}{1} \text{usec} \quad (9.13)$$

where  $M$  is number of target signals. In case of filtering seismic noise from input mode cleaner

and arm cavities using seismometer and accelerometer signals  $M = 3$ ,  $P = 9$ . Since C1OAF model runs at 2048Hz,  $T_0$  should be smaller than 488usec. Table 9.2 summarizes values of parameters used during adaptive noise cancellation at the 40m prototype:

$M$	3	number of target signals
$P$	9	number of witness signals
$N$	4000	number of coefficients
$\mu_0$	0.03	step-size parameter
$\tau$	$10^{-5}$	leaky parameter
$Ds$	8	downsample ratio
delay	5	actuation path delay

Table 9.2: Adaptive filter parameters used during the seismic noise subtraction.

Convergence time of adaptive filter using parameters from the table 9.2 was 3 minutes. This convergence rate is sufficient to track slow variations of the transfer functions from ground motion to interferometric signals. Figure 9.11 shows norm of the filter coefficient vector during convergence process.

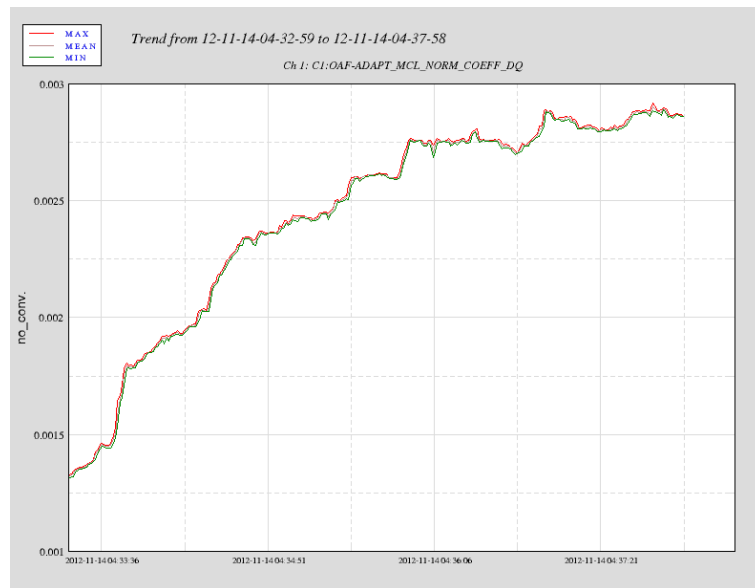


Figure 9.11: Norm of the filter coefficient vector during convergence process of FxLMS filter.

Figure 9.12 shows result of seismic noise subtraction from input mode cleaner, X- and Y-arm length signals using 3 seismometer signals that measure ground motion in X, Y, and Z directions. Seismometers were located in the corner and end stations as shown on the figure 9.9. Seismic noise was subtracted in the frequency range 0.7-10Hz near the stack resonances. Subtraction factor of 50 was measured at 3Hz.

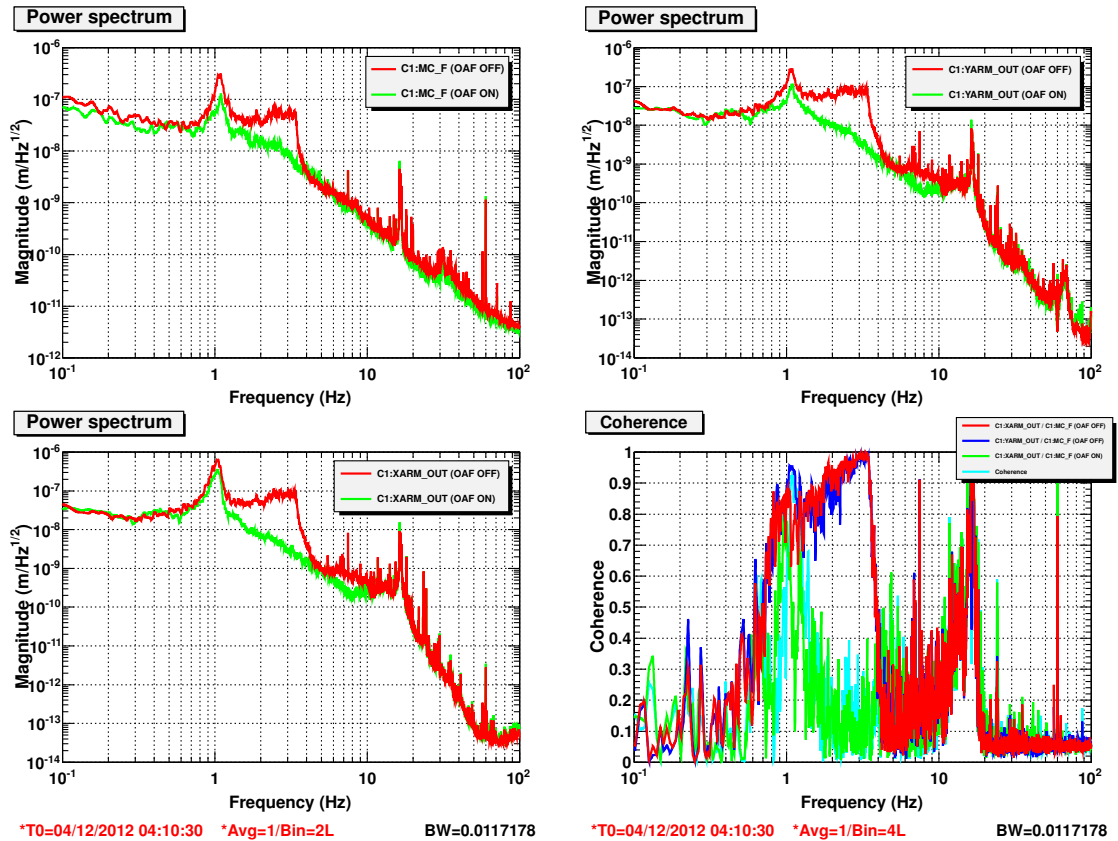


Figure 9.12: Feedforward subtraction of seismic noise from IMC and arms.

Adaptive filters use cavity length signal as online error. This signal is not available when lock is lost. For this reason, step-size parameter  $\mu$  is slowly reduced to zero after filter coefficients converge to optimal solution. If filter performance degrades, adaptation process is engaged again to account for changes in the transfer function from seismometers to cavity length.

## Chapter 10

# Optimal feedback control

Feedback control techniques are widely used in advanced LIGO to stabilize interferometer longitudinal and angular degrees of freedom, suppress motion of optical benches, and damp high-Q resonances using local sensors as discussed in chapters 3, 4, 5. Standard approach in designing control loops in LIGO is to measure or simulate actuator and sensor transfer functions and design a single input single output (SISO) control filter by looking at its frequency response.

Most of the control loops used in LIGO should have high gain at low frequencies in order to achieve strong suppression of the seismic motion and fast roll off at high frequencies to avoid sensing noise injection to gravitational wave channel. Design of control filters requires fine tuning for best performance and has to be updated based on the level of seismic and sensing noises.

An alternative approach in designing stable control loops is based on cost function minimization. A number of algorithms, like LQR, H-infinity, and  $\mu$ -synthesis, are successfully used in stabilizing suspensions, vibration systems and inverted pendulum [100, 101, 102]. Once cost function is defined based on the requirements, algorithms return stable controllers that minimize the cost function. Since stability is guaranteed, a new controller can be quickly designed in case of plant modification.

Modern control techniques can also be applied to generate multiple-input-multiple-output (MIMO) controllers. This is a significant advantage over standard frequency domain approach. MIMO controllers account for cross couplings between the loops that are neglected when SISO controllers are applied.

This chapter gives an overview of domain optimal control technique applied to aLIGO problems. Sections 1, 2, and 3 describe LQR, Kalman, and H-infinity optimal control techniques and state estimators. Section 4 is devoted to robust control of suspensions when the stabilizing controller is stable relative to small variations of the plant.

These methods use state-space approach to formulate control problem. Linear system is repre-

sented as:

$$\begin{aligned}\dot{x} &= Ax + Bu \\ y &= Cx + Du\end{aligned}\tag{10.1}$$

where  $x$  is system state vector,  $u$  are control inputs,  $y$  are measured outputs,  $A$  is matrix with internal dynamics,  $B$  input matrix,  $C$  is measurement matrix,  $D$  is feedthrough matrix.

## 10.1 Linear quadratic regulator

In LQR technique control  $u$  is selected to minimize quadratic cost function  $J$ . In aLIGO most systems are time invariant and only infinite time horizon case is of interest:

$$J = \int_{t_0}^{t_1} (x^T P x + u^T Q u) dt, \quad t_1 \rightarrow \infty\tag{10.2}$$

where  $P$  is a positive semidefinite and  $Q$  is a positive definite matrix. Matrices  $P$  and  $Q$  determine cost imposed on position and control. The optimal control law is linear [103]:

$$u^*(t) = Kx(t)\tag{10.3}$$

Control matrix  $K$  is obtained by minimizing cost function 10.2 under constraint 10.1. Solving via introducing Lagrangian multipliers, the following Riccati equation is achieved:

$$\begin{aligned}-A^T S - SA - P + SBQ^{-1}B^T S &= 0 \\ K &= -Q^{-1}B^T S\end{aligned}\tag{10.4}$$

### 10.1.1 State-space augmentation

Equation 10.3 implies that size of control matrix  $K$  equals to the product of control inputs and number of system states. In aLIGO applications it is required to introduce frequency shaping of the cost function 10.2. It can be done by introducing new states to the system using plant augmentation technique [104]. First, cost function 10.2 is written in the frequency domain using Parseval's theorem

and then frequency dependence of matrices  $P$  and  $Q$  is introduced:

$$\begin{aligned} J &= \frac{1}{2} \int_{-\infty}^{\infty} (x^T(i\omega)Px(i\omega) + u(i\omega)^TQu(i\omega))d\omega \rightarrow \\ J &= \frac{1}{2} \int_{-\infty}^{\infty} (x^T(i\omega)P(i\omega)x(i\omega) + u(i\omega)^TQ(i\omega)u(i\omega))d\omega \end{aligned} \quad (10.5)$$

If the weighting functions  $P(i\omega)$  and  $Q(i\omega)$  are chosen to be rational functions of  $\omega^2$  then it is possible to write  $P(i\omega) = P_1^*(i\omega)P_1(i\omega)$  and  $Q(i\omega) = Q_1^*(i\omega)Q_1(i\omega)$  where  $P_1$  and  $Q_1$  are rational matrices. Then new states are introduced according to the following equations:

$$x' = P_1(i\omega)x \quad u' = Q_1(i\omega)u \quad (10.6)$$

After converting equations 10.6 to state-space form using states  $z_1, z_2$  and matrices  $(A_1, B_1, C_1, D_1), (A_2, B_2, C_2, D_2)$  for position and control, it is possible to augment initial state-space vector  $x$ , and equations of motion 10.1 transform to equations:

$$\begin{pmatrix} \dot{x} \\ \dot{z}_1 \\ \dot{z}_2 \end{pmatrix} = \begin{pmatrix} A & 0 & 0 \\ B_1 & A_1 & 0 \\ 0 & 0 & A_2 \end{pmatrix} \begin{pmatrix} x \\ z_1 \\ z_2 \end{pmatrix} + \begin{pmatrix} B \\ 0 \\ B_2 \end{pmatrix} u \quad (10.7)$$

$$\begin{pmatrix} y \\ x' \\ u' \end{pmatrix} = \begin{pmatrix} C & 0 & 0 \\ D_1 & C_1 & 0 \\ 0 & 0 & C_2 \end{pmatrix} \begin{pmatrix} x \\ z_1 \\ z_2 \end{pmatrix} + \begin{pmatrix} D \\ 0 \\ D_2 \end{pmatrix} u \quad (10.8)$$

Equations 10.7 and 10.8 show that LQR problem with frequency shaped cost function 10.5 can be reformulated into another LQR problem with frequency independent matrices  $P$  and  $Q$  and augmented state space.

### 10.1.2 Applications to LIGO

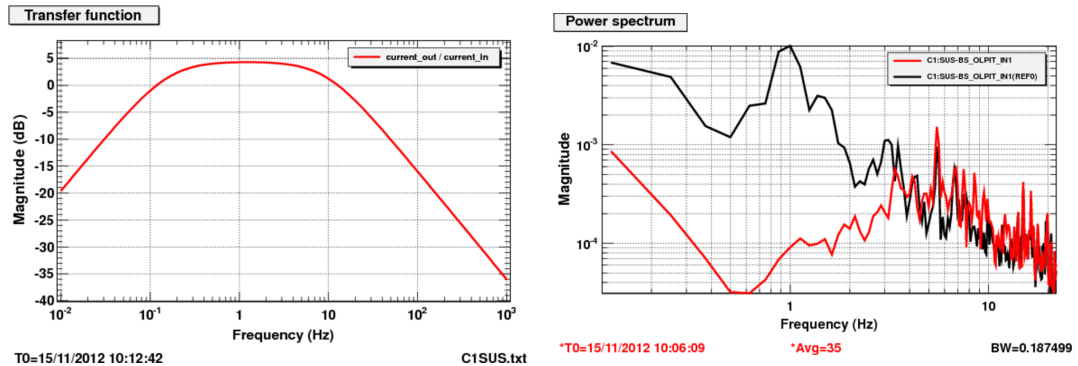
Linear quadratic regulator was applied to design an optical lever servo to control angular motion of BS suspension at the 40m prototype. Since BS is a single suspension, system dynamics is given using two state space variables:

$$\frac{d}{dt} \begin{pmatrix} \dot{\alpha} \\ \alpha \end{pmatrix} = \begin{pmatrix} -\gamma & -\omega_0^2 \\ 1 & 0 \end{pmatrix} \begin{pmatrix} \dot{\alpha} \\ \alpha \end{pmatrix} + \begin{pmatrix} 1/I \\ 0 \end{pmatrix} u \quad (10.9)$$

where  $\alpha$  and  $\dot{\alpha}$  are angle and angular velocity of the optic,  $\gamma$  is damping factor,  $\omega_0$  is eigen frequency of oscillator,  $I$  is BS moment of inertia,  $u$  is control torque applied to BS.

Control cost function is chosen to be frequency independent in this control problem. Position cost is shaped using two poles at 0.2Hz and 5Hz and one zero at 0Hz as shown in figure 10.1. Frequency shaped cost function augments state space  $\dot{\alpha}, \alpha$  by two states according to equation 10.7.

Solution of Riccati equation 10.4 is done using Matlab function *care* [105]. Figure 10.1 shows unsuppressed angular fluctuations of BS and error signal after engaging LQR controller.



(a) Position cost function developed for design of LQR controller.

(b) Suppression of BS angular motion using LQR controller.

Figure 10.1: Application of LQR technique to BS optical lever servo.

LQR control law 10.3 requires knowledge of all system states. In real applications, however, not all states are usually measured. BS optical lever only measures angle  $\alpha$  while angular velocity  $\dot{\alpha}$  is computed by differentiating  $\alpha$ . However, this state estimation technique is not optimal since sensing noise of  $\alpha$  is white at high frequencies and sensing noise of  $\dot{\alpha}$  grows with frequency as a result of differentiation.

Unmeasured states can be estimated optimally in least-mean-square sense using Kalman filter. LQR technique that uses Kalman filter as state estimator is known as Linear Quadratic Gaussian (LQG) control method. LQG controllers are also stable but phase margins can be very low and good robustness is not guaranteed.

## 10.2 Kalman filter

States of the system can be estimated optimally if covariances of the measurement and process noises are known. It is also assumed that these noises are white and Gaussian. If this is not the case but frequency shape of process and measurement noises is known, then system state-space can be augmented to include noise color. This approach is similar to state space augmentation for frequency shaping of LQR cost function 10.7

In LIGO control problems most systems are time independent and their dynamics is given by constant matrices  $A, B, C$ , and  $D$ . Then discrete time state space representation can be written in

the following way:

$$\begin{aligned}x_{k+1} &= Ax_k + Bu_k + w_k \\y_k &= Cx_k + Du_k + v_k\end{aligned}\tag{10.10}$$

where  $w_k$  is process noise that drives the system and  $v_k$  -measurement noise. Covariance matrices of noises  $w_k$  and  $v_k$  are assumed to be constant and equal to  $Q$  and  $R$ . Discrete time state space matrices  $A, B, C$ , and  $D$  with step size  $\tau$  are related to continuous time matrices via equations:

$$A_d \approx (I + \tau A_c), \quad B_d \approx \tau B_c, \quad C_d = C_c, \quad D_d = D_c\tag{10.11}$$

where subscript  $d$  means discrete time and  $c$  - continuous time model.

Kalman filter is a linear estimator and searches optimal solution as a linear sum of predicted state and current measurement. Predicted state  $\hat{x}_{k+1|k}$  is computed by propagating system state in the previous time step  $\hat{x}_{k|k}$  using dynamics matrices  $A$  and  $B$ .

$$\begin{aligned}\hat{x}_{k+1|k} &= A\hat{x}_{k|k} + Bu_k \\ \hat{x}_{k+1|k+1} &= \hat{x}_{k+1|k} + K_k(y - C\hat{x}_{k+1|k} - Du_k)\end{aligned}\tag{10.12}$$

where  $K_k$  is the optimal Kalman gain. Matrix  $K_k$  weighs contributions of state prediction using system dynamics and noisy measurement.  $K_k$  is computed to minimize estimation error  $E\|x_k - \hat{x}_{k|k}\|^2 = \text{trace}(\text{cov}(x_k - \hat{x}_{k|k}))$ . Since dynamics of the system is assumed to be time-invariant for LIGO applications, optimal Kalman gain  $K_k$  is also time-independent. Since in the general case it is difficult to explicitly solve matrix equation for  $K$ , Kalman gain is computed numerically using standard Kalman equations:

$$\begin{aligned}P_{k+1|k} &= AP_{k|k}A^T + Q \\ K_{k+1} &= P_{k+1|k}C^T(C^T P_{k+1|k}C + R)^{-1} \\ P_{k+1|k+1} &= (I - K_k C)P_{k+1|k}\end{aligned}\tag{10.13}$$

where  $P_{k|k} = \text{cov}(x_k - \hat{x}_{k|k})$  and  $P_{k+1|k} = \text{cov}(x_{k+1} - \hat{x}_{k+1|k})$ . First and third equation 10.13 follow from equations 10.12. Equation for Kalman gain is derived from condition  $\frac{\delta \text{trace}(P_{k|k})}{\delta K} = 0$ .

Kalman state estimation technique can be used together with LQR controllers or independently for sensor blending or estimating of test mass curvature and substrate lens, generated by optical heating and TCS ring heaters.

### 10.2.1 Test mass curvature estimation

Once interferometer is locked, carrier field resonates in the arm cavities and heats test masses due to absorption. Heating process is not uniform due to radial dependence of the beam intensity  $I(r) = I_0 \exp(-2\frac{r^2}{a_0^2})$ , where  $a_0$  is the size of the beam. Test mass gets more heat in the center compared to the sides. Temperature gradient changes substrate lens and curvature of the test mass surface according to equation:

$$\delta R = \beta(T(0) - T(r_0/2)) \quad (10.14)$$

where  $(T(r_0/2))$  is temperature at distance from the center equal to half optic radius,  $T(0)$  is temperature at the center of the optic,  $\beta > 0$  is constant coefficient in units of  $[m/W]$ .

Significant optical power resonating in the arm cavities ( $> 100kW$ ) changes ITM substrate lens by tens of micro-diopters and affects mode matching of power and signal recycling cavities to the arms. Ring heaters are installed on the sides of test masses and generate radial temperature gradient with opposite sign to the one created by optical heating. Ring heater power is tuned to compensate heating effect from optical power and improve mode matching between the optical cavities.

Substrate lens and radii of curvature can be measured using Hartmann wave front sensors [106] when interferometer is locked. Once the lock is lost, measurement data is not available. At the same time center of the optic cools down, and curvature increases since ring heater continues to operate.

The purpose of state space model and Kalman filtering is to estimate test mass radius of curvature or substrate lens from noisy Hartmann WFS measurements in lock and get approximate value of the lens strength after the lock is lost. Equation of heat transfer can be written as:

$$\frac{\delta T}{\delta t} = \alpha \nabla^2 T + f_{heat} - f_{loss} \quad (10.15)$$

where  $\alpha$  is thermal diffusivity, function  $f_{heat}$  includes test mass heating due to ring heater and optical power and  $f_{loss}$  includes heat transfer to environment via radiation and residual gas heat transfer through suspension.

This problem is addressed numerically using finite element analysis. Test mass is divided onto  $N$  rings, temperature inside each of them is assumed to be constant as shown in figure 10.2. Since the problem has radial symmetry, then  $\nabla^2 = \frac{d^2}{dr^2} + \frac{1}{r} \frac{d}{dr}$  and heat transfer equation 10.15 can be written in the form of the differential scheme which is first order in time and second order in coordinate:

$$\frac{T_k^{i+1} - T_k^i}{\tau} = \alpha \left( \frac{T_{k+1}^i + T_{k-1}^i - 2T_k^i}{dr^2} + \frac{T_{k+1}^i - T_{k-1}^i}{2r_k dr} \right) + f_{k,heat}^i - f_{k,loss}^i \quad (10.16)$$

where  $T_k$  is difference between the temperature of  $k$ -th test mass element and environment. Heat transfer from finite element to environment is proportional to  $T_k$ :  $f_{k,loss}^i = lT_k^i$ . Equation 10.16 is

valid for  $k = 2, \dots, N - 1$ . Boundary conditions for  $k = 1, N$  are set such that temperature of non-existing element 0 and  $N + 1$  is the same as temperature of element  $k = 1$  or  $k = N$ . Differential equation 10.16 is stable if time step  $\tau$  satisfies inequality  $\tau < \frac{dr^2}{2\alpha}$ .

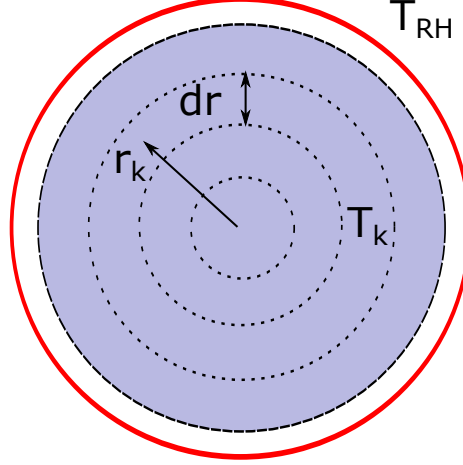


Figure 10.2: Test mass and ring heater.

Equation 10.16 determines state space model of the system with state space vector  $T = [T_1, T_2, \dots, T_N, T_{RH}]$  where  $T_{RH}$  is ring heater temperature determined by applied voltage:

$$\begin{aligned} T_k^{i+1} &= AT_k^i + B[P_{RH}, P_{cav}] \\ R^i &= \beta(T_1 - T_{N/2}) + v^i \end{aligned} \quad (10.17)$$

where  $P_{RH} = \bar{P}_{RH} + \delta P_{RH}$  is power on ring heater, covariance of noise  $\delta P_{RH}$  is  $Q_{RH}$ ,  $P_{cav} = \bar{P}_{cav} + \delta P_{cav}$  - optical power, covariance of noise term  $\delta P_{cav}$  is  $Q_{cav}$ ,  $R$  is change in test mass radius of curvature due to optical power and ring heater,  $v$  is measurement noise of covariance  $V$ . Since ring heater noise and fluctuations in the intracavity power are uncorrelated, total process covariance matrix  $Q$  is written as  $Q = B(\text{diag}(Q_{RH}, Q_{cav}))B^T$ .

System dynamics given by matrices  $A$  and  $B$  is determined by thermal diffusivity  $\alpha$ , loss parameter  $l$ , absorption  $\eta$ , test mass heat capacity  $C$ , and heat transfer from ring heater to test mass. These parameters are known with precision of few percents, and matrices  $A$  and  $B$  have uncertainties. In the process of simulating this problem it was found that good results can be achieved if Kalman gain is computed using slightly overestimated process covariance matrix  $Q$ .

The problem of curvature estimation is solved numerically in two steps. First, Kalman gain is computed by solving equations 10.13 in loop before stationary solution is achieved as shown in figure 10.3. Then state space vector  $T^i$  is computed using equations 10.12.

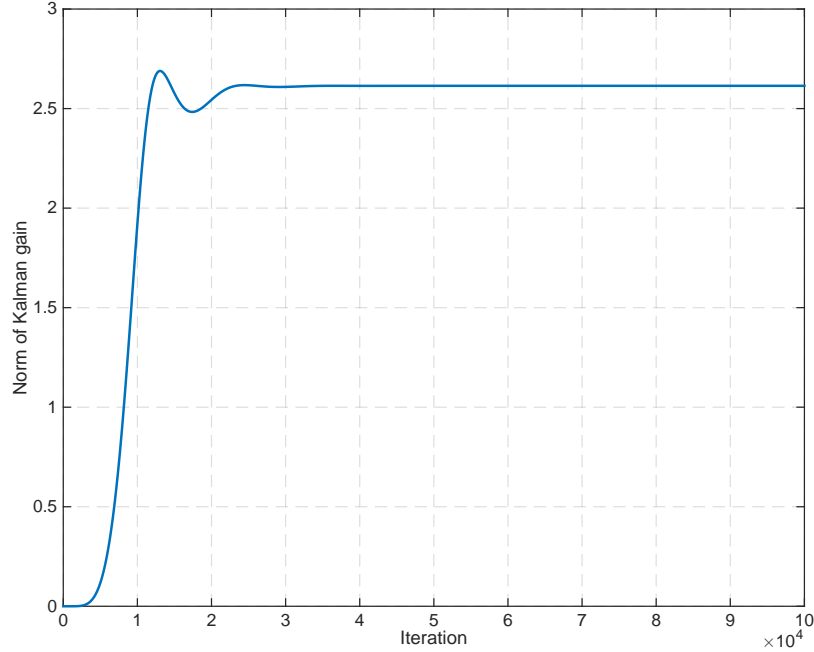


Figure 10.3: Norm of Kalman gain during the process of iterative solution of equations 10.13.

Figure 10.4 shows estimation of test mass radius of curvature. At time moment  $t = 0\text{sec}$  interferometer is locked, test mass is heated by the beam and radius of curvature increases. Hartmann WFS are used to measure change in radius of curvature. State-space model used for estimation is 3 percent different from the true model. At time moment  $t = 2000\text{sec}$  ring heater is engaged to compensate for the optical power and test mass radius of curvature is back to nominal. At time moment  $t = 4000\text{sec}$  cavity loses lock and test mass becomes more curved due to ring heater power. Hartmann WFS reading are not available at this time and Kalman gain is set to zero:  $K = 0$ . Curvature estimations rely on the model. At time moment  $t = 6000\text{sec}$  cavity is relocked, measurement is available again and radius of curvature increases towards its nominal value.

Figure 10.4 shows that Kalman filter reduces WFS noise and estimation of radius of curvature is close to the real value. If measurement is not available, estimation is based on the model, and ring heater power can be adjusted to keep radius of curvature at its nominal value. Such a set up can be used to control test mass curvature using feedback controller.

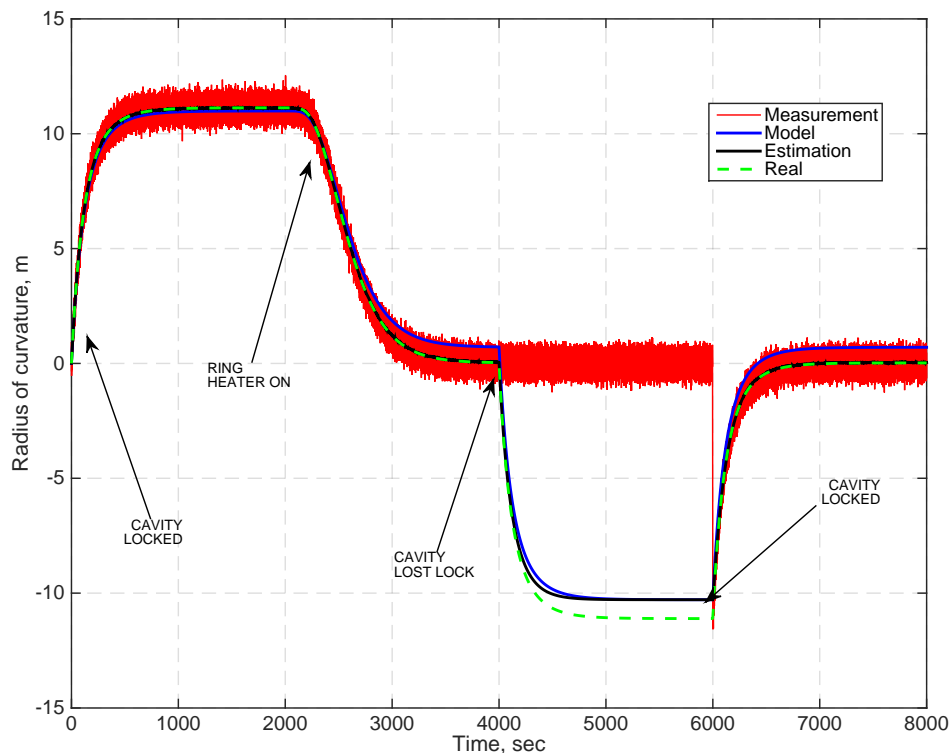


Figure 10.4: Estimation of test mass radius of curvature using model and measurement.

### 10.3 $H_\infty$ control technique

Similar to LQR,  $H_\infty$  control technique is based on cost function minimization and guarantees stabilization of dynamical system. Optimal solution minimizes closed loop transfer matrix from disturbance to the error signal.  $H_\infty$  norm of the stable transfer matrix  $T$  in the frequency domain is given by equation:

$$\|T\|_\infty = \sup_{\omega} \sigma_{\max} T(i\omega) \quad (10.18)$$

where  $\sigma$  are singular value of the matrix  $T(i\omega)$ .

System dynamics is determined by the state space model. It is convenient to introduce measure-

ment noise and error signals in the equations 10.1:

$$\begin{aligned} \dot{x} &= Ax + B_1w + B_2u \\ z &= C_1x + D_{12}u \\ y &= C_2x + D_{21}w \end{aligned} \tag{10.19}$$

where  $z$  is error signal,  $y$  - system output,  $w$  contains both process and measurement noises. Error  $z$  is an empirical signal that is not measured and determined by position and control cost functions. In general case not all states are being measured and similar to LQG, it is necessary to estimate state space vector from the measurement  $y$  and state space dynamics matrices  $A$ ,  $B_1$ , and  $B_2$ .

Optimal  $H_\infty$  controller that minimizes  $H_\infty$  norm  $\|T_{wz}\|_\infty$  of the transfer matrix from disturbance  $w$  to error signal  $z$  is hard to find in the general case. Suboptimal controllers stabilize system 10.19 such that  $\|T_{wz}\|_\infty < \gamma$ , where  $\gamma$  is an arbitrary number bigger than norm  $\|T_{wz}\|_\infty$  achieved by optimal controller. Solution to suboptimal  $H_\infty$  problem is given in [107]. This solution includes both controller design and optimal estimator of the system state-space vector. Once suboptimal controller is achieved,  $\gamma$  can be reduced if controller performance should be improved.

$H_\infty$  control technique was applied at LIGO Livingston Observatory to stabilize BS triple suspension. The first application is related to the angular control using optical lever servo. The second application deals with local damping of 6 degrees of freedom using shadow sensors.

Practical realization of  $H_\infty$  control technique relative to LIGO applications is shown in figure 10.5. Suspension moves under disturbance  $w$ , position is measured using noisy sensor. Controller uses measurement outcome  $y$  and produces controls signal  $u$ . Cost function is created by multiplying noise free position and control signals by function  $W_{err}$  and  $W_{ctrl}$ . Suspension model augmented with cost functions  $W_{err}$  and  $W_{ctrl}$  is known as generalized plant.

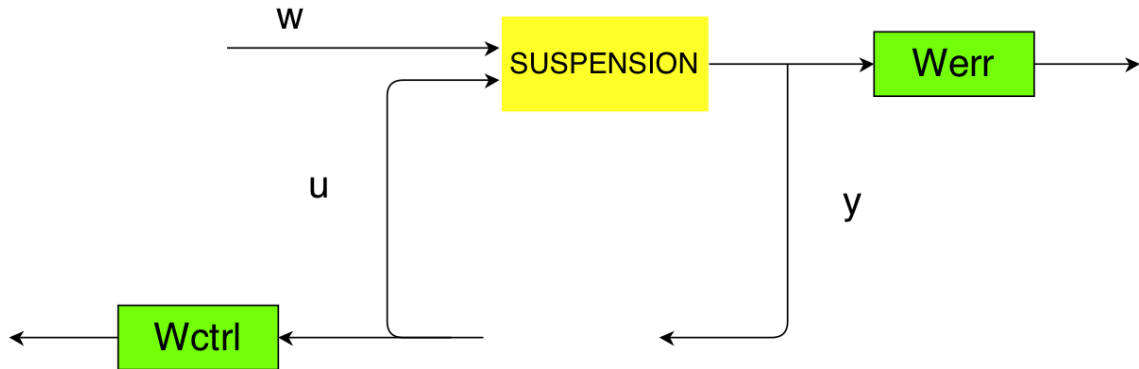


Figure 10.5: Application of  $H_\infty$  technique to LIGO suspension control problems.

### 10.3.1 Optical lever damping

Beam splitter is used to control simple Michelson length when interferometer is locked. During lock acquisition process, BS gets a controls transient when sideband power in DRMI flashes. Transients in control signal cause angular motion of BS due to length to angle couplings. Angular motion of BS due to lock acquisition transients is too high for DRMI to grab the lock.

Interferometric signals are still not available during lock acquisition and BS angular control is done using optical levers. Servos are supposed to damp main suspension resonances at 0.48Hz and 1.2Hz. At the same time control signal should be rolled off above 3Hz to avoid significant noise injections above 10Hz. Optical levers signals at low frequencies (below 0.1Hz) usually dominate by the motion of the laser and photodiode, and servo should avoid noise injection to suspension at these frequencies. These conditions determine the shape of position and control transfer functions. Control cost grows at high and low frequencies while position cost is high in the frequency range 0.3-2Hz.

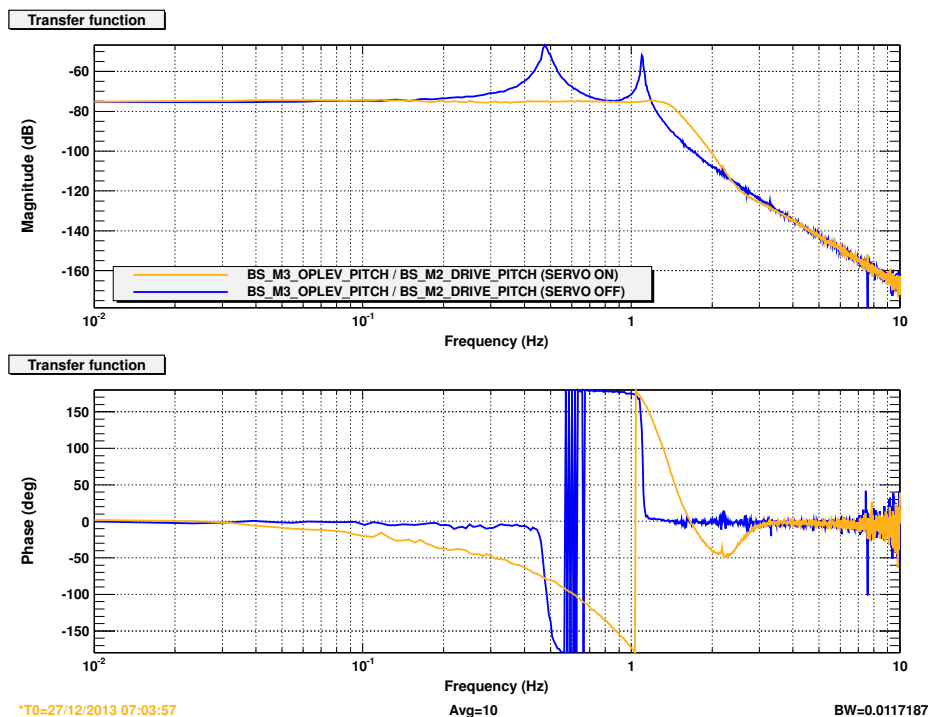


Figure 10.6: Application of  $H_\infty$  technique to BS optical lever damping. Blue trace shows BS pitch to pitch transfer function when loop is open, and orange trace shows the same transfer function when loop is closed.

Suspension angular transfer function was measured and fitted using Vectfit utility [97]. Then suspension state space model was connected with cost functions  $W_{err}$  and  $W_{ctrl}$  into generalized plant, and suboptimal  $H_\infty$  controller was synthesized using Matlab function *hinfsyn* [108].

Figure 10.6 shows the result of optical level damping of BS suspension using  $H_\infty$  control technique. Resultant controller stabilizes suspension according to requirements listed above and makes lock acquisition more robust.

### 10.3.2 Local damping

Suspension resonances have Q-factors of 100-1000 and are damped using shadow sensors. Servos should reduce Q-factor down to 10 and avoid noise injections to gravitational wave channel above 10Hz. Shadow sensors measure position of the mass, and their sensing noise is on the level of  $2 \cdot 10^{-11} \frac{m}{\sqrt{Hz}}$ . At the same time control noise at 10Hz should be less than  $10^{-17} \frac{m}{\sqrt{Hz}}$  for BS suspension in longitudinal direction.

Six degrees of freedom are damped from the top suspension stage. State-space model is derived from suspension dynamics that was simulated using Mathematica software by suspension group [109]. Position cost function is frequency independent and examples of control cost functions are shown in figure 10.7.

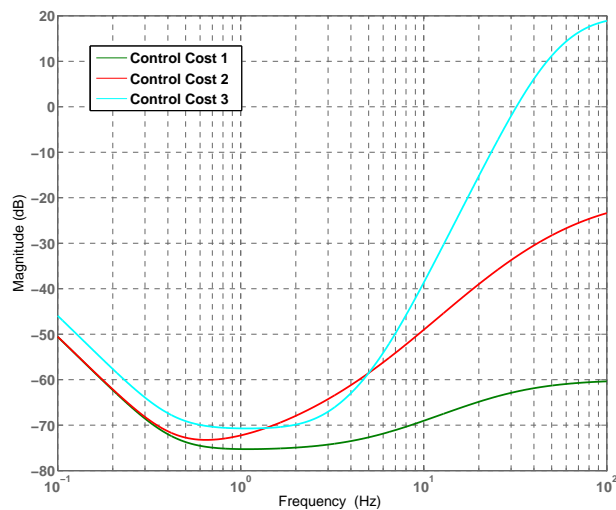


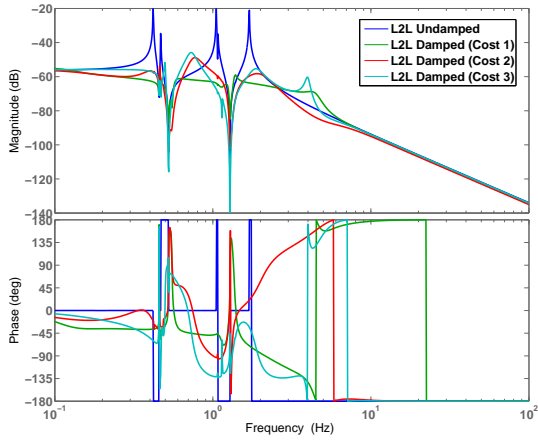
Figure 10.7: Magnitude of control cost functions developed for design of  $H_\infty$  controllers.

Three controllers were synthesized using  $H_\infty$  control technique for BS suspension in the longitudinal direction. If more control cost is applied at high frequencies then less noise is injected at frequencies higher than 10Hz. But at the same time damping of eigen modes is weaker.

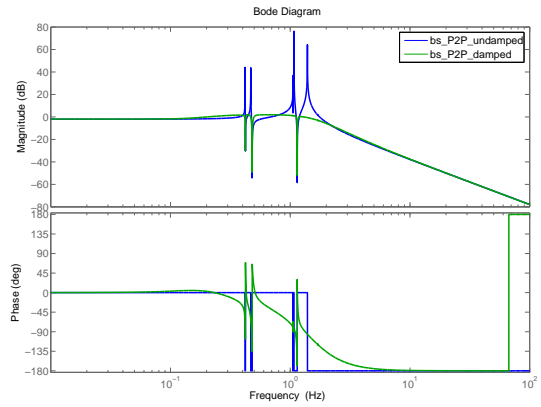
At low frequencies  $f < 0.3Hz$  control cost increases to make servos AC coupled. Functions are close to flat in the frequency range  $0.3Hz < f < 3Hz$  where all suspension resonances are. Starting from  $3Hz$  up to  $100Hz$  control cost function grows. The first control cost in figure 10.7 grows proportionally to frequency  $f$ , the second one as  $f^2$  and the third one as  $f^4$ .

First figure 10.8 shows comparison of longitudinal suspension transfer function when loop is open and closed using  $H - \infty$  controllers that minimize cost functions shown in figure 10.7. Other figures

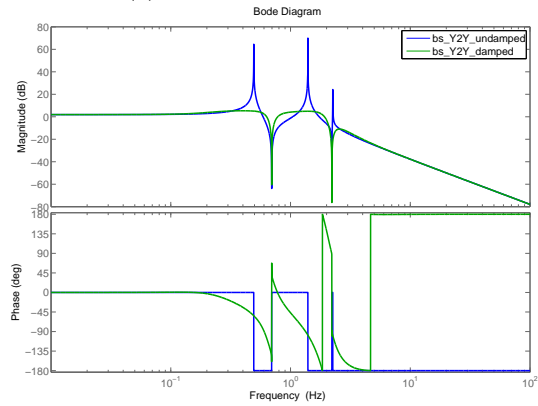
show damping of pitch, yaw, vertical, roll and translation degrees of freedom. Cost function is chosen to damp suspension modes and avoid gain peaking.



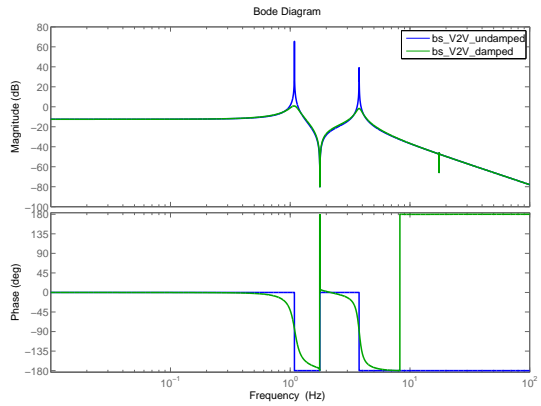
(a) Longitudinal damping.



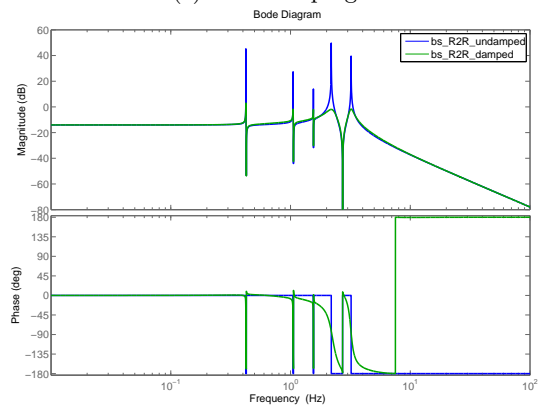
(b) Pitch damping.



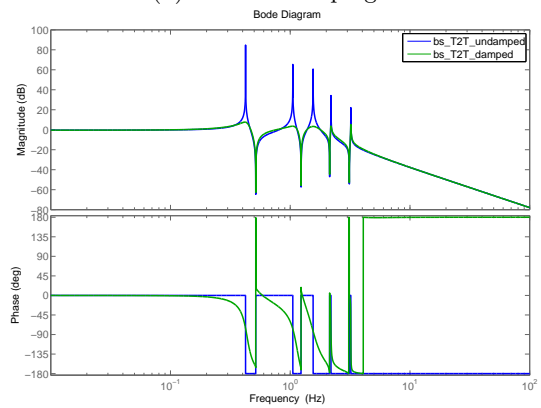
(c) Yaw damping.



(d) Vertical damping.



(e) Roll damping.



(f) Translation damping.

Figure 10.8: Simulation of damping BS suspension modes using  $H_\infty$  controller.

$H_\infty$  controller shows good performance with a simulated plant with no uncertainties. However, after installing synthesized controllers in the front end system, not all of them worked as in the simulation. In particular, longitudinal and pitch resonances around  $0.4 - 0.5\text{Hz}$  were poorly

damped by stabilizing controllers, as shown in figure 10.9.

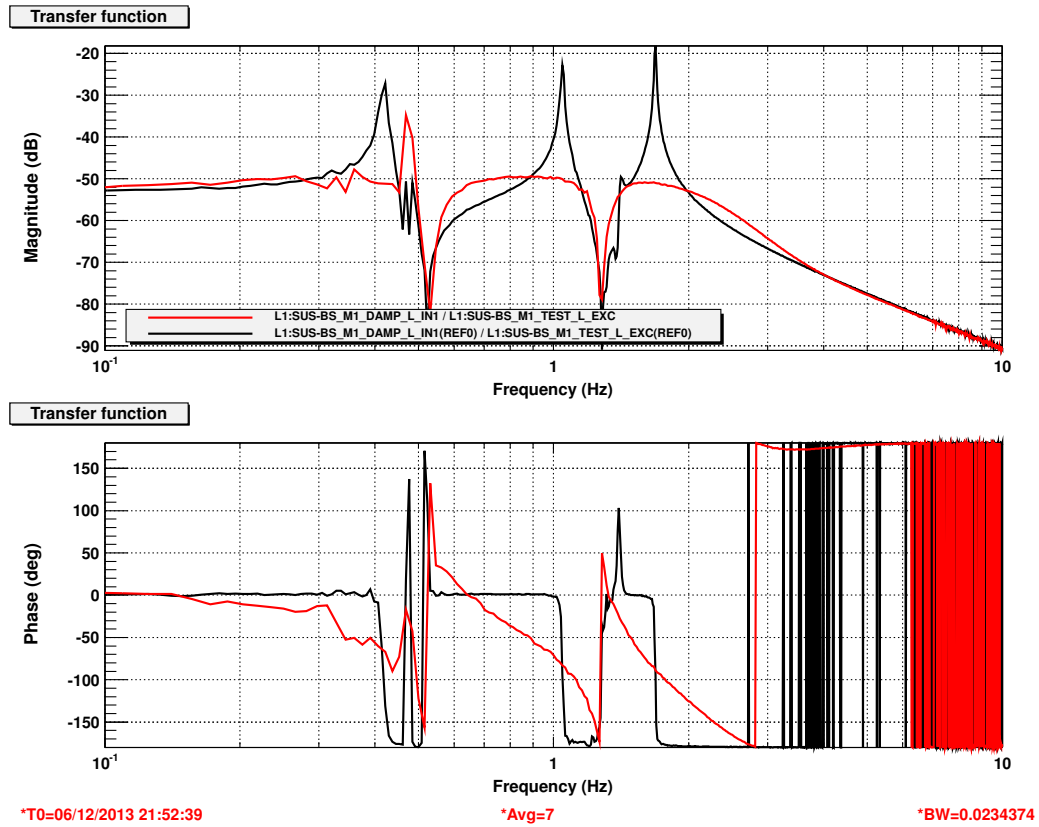


Figure 10.9: Transfer function of BS top stage in longitudinal degree of freedom. Black trace corresponds to the case when BS is undamped, red trace - damped using  $H_{\infty}$  controller.

Small errors in the simulated state space model of the suspension made  $H_{\infty}$  controller unstable. Another control algorithm based on  $H_{\infty}$  known as  $\mu$ -synthesis finds robust controller relative to uncertainties in the plant.

## 10.4 $\mu$ -synthesis

Robust controllers should guarantee stability of the closed loop under small uncertainties of the plant:

$$A = A_0 + \Delta A, B = B_0 + \Delta B \quad (10.20)$$

$$C = C_0 + \Delta C, D = D_0 + \Delta D \quad (10.21)$$

where matrices  $A_0, B_0, C_0, D_0$  represent known dynamics and  $\Delta A, \Delta B, \Delta C, \Delta D$  - uncertainties in the model.

Possible solution to robust control problem can be achieved using  $\mu$ -synthesis technique. In this approach controller robustness is measured using complex structure singular values [110] and uncertain systems are represented using linear fractional transformations.

Robust controller can be generated using Matlab function *dksyn* for models with uncertainties using D-K iteration process [111]. This function was used to generate robust controller for longitudinal damping of BS suspension.

### 10.4.1 Robust local damping

Uncertainties of 1% were introduced in resonant frequencies of BS suspension and feedback controller was generated to be stable under these uncertainties using  $\mu$ -synthesis technique.

Figure 10.10 shows frequency shaped position and control cost functions used to achieve robust and low noise damping of BS suspension. Position cost has a resonance around 0.5Hz to improve damping of the main BS longitudinal resonance at 0.45Hz. Control cost grows at high frequencies to avoid noise coupling of sensor noise to gravitational wave channel.

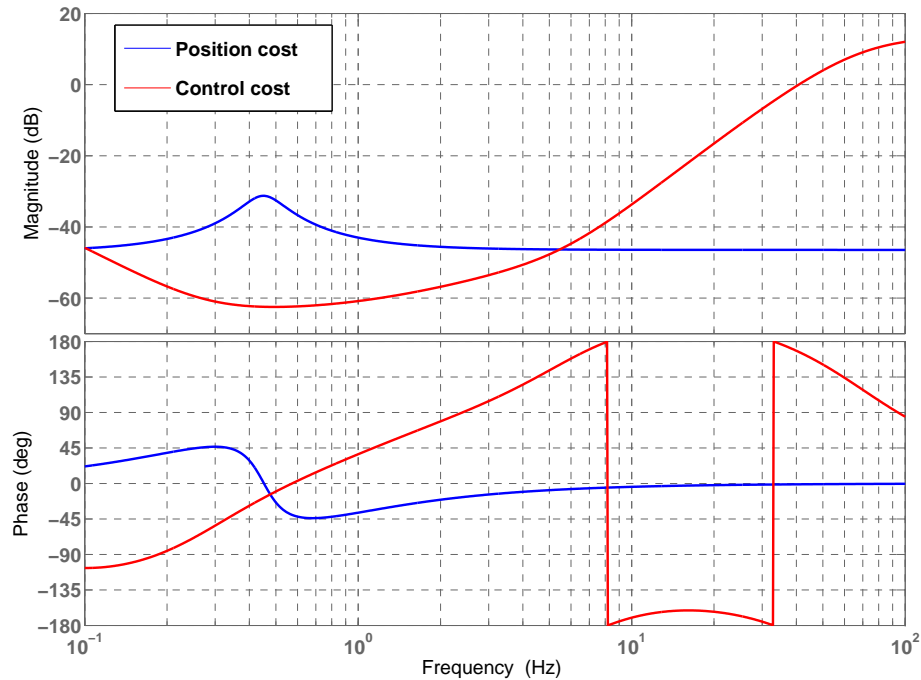


Figure 10.10: Frequency shape of position and control cost function generated for longitudinal damping of BS suspension.

Robust controller was converted to zpk form and installed in the front end system. Longitudinal BS transfer functions were measured with feedback loop open and closed as shown in figure 10.11. In contrast with  $H_\infty$  controller,  $\mu$  design damps all resonances including the one at 0.45Hz.

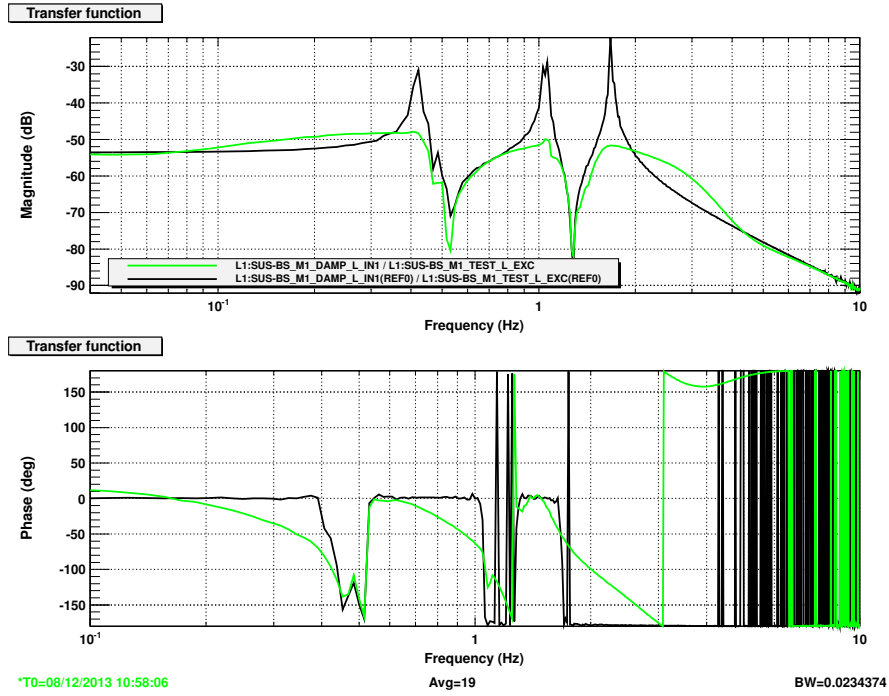


Figure 10.11: Damping of BS longitudinal resonances using robust controller.

Sensing noise injected by robust controller above 10Hz satisfies the requirement and is less than  $10^{-17} \frac{m}{\sqrt{Hz}}$ . Figure 10.12 shows noise injected by feedback loop compared to BS thermal noise.

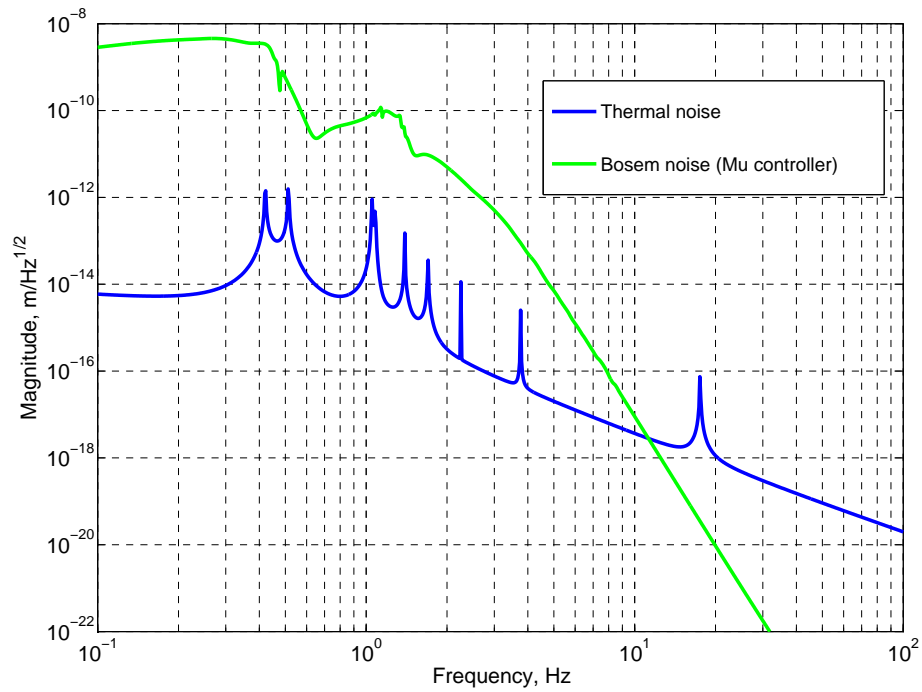


Figure 10.12: BS longitudinal displacement due to sensor noise.

## Chapter 11

# Future work

Commissioning of advanced interferometers is still in progress, and in the short term (0-2 years), LIGO scientists will be working on improving low frequency noise and instrument sensitivity towards its designed level, reducing lock acquisition time, and making the process more robust during winter times when microseismic activity is high.

Medium term (3-5 years) goals include upgrades of aLIGO interferometers to improve detector sensitivity by factor of 2-3. These upgrades [112] include increasing beam size and intracavity power to reduce coating Brownian noise and shot noise, make mirrors more massive to reduce quantum radiation pressure and suspension thermal noises. Other upgrades introduce squeezed states of light through the interferometer antisymmetric port to reduce quantum noise [113], and cancel or mitigate of gravity gradient noise [63].

Research and development team also works towards improving LIGO sensitivity by factor of 10 up to the infrastructure limit. This limit is determined by residual gas pressure in the arm cavities and Newtonian noise. Long term goals (5-10 years) include reducing suspension and coating Brownian thermal noises by introducing cryogenics systems [114, 115], higher quality optical coatings [116] and 1550nm laser beams [117]. It will be also possible to increase input power and squeezing factor to reduce shot noise level down to phase noise of residual gas in the arm cavities. New optical configurations are also considered such as Sagnac speed meter [118, 119], unstable optomechanical filters, and white light cavities [120].

Orthogonal approach towards better strain sensitivity is to increase length of the arm cavities by order of magnitude [121]. Research and development on optical design of 40km interferometer are now in progress.

This chapter describes ideas on how to improve LIGO sensitivity and control in the short, medium and long terms based on the lessons learned during commissioning process. Minor changes to aLIGO configuration and ideas concerning design of the future instruments are discussed as well.

## 11.1 Short term upgrades

This section describes problems encountered during commission of aLIGO interferometers and possible solutions:

- Offsets of beam position from geometrical center of beam splitter in horizontal direction lead to significant power drop in the power recycling cavity. Optic diameter is 37 cm and since angle of incidence is  $45^\circ$ , horizontal size of the mirror projection on the plane perpendicular to the beam is 26cm.

Thickness of the optic is 6cm, and consequently distance between X- and Y- arm beams on the back BS surface is 6cm. At the same time sizes of the carrier and sideband beams on the mirror are 5.3cm and 5.9cm. Simulations show that horizontal beam off-centering by 1cm leads to 10% power drop for sidebands.

Possible solution to the problem is to increase horizontal size of the mirror and coating in such way that their projections on the surface perpendicular to the beam have circular shape.

- Penultimate stage of beam splitter suspension is used for longitudinal control of Michelson interferometer. Coil-magnet pairs on the bottom stage are not installed. This leads to a slower lock acquisition process since Michelson unity gain frequency is limited to 10Hz.

Installing actuators on the bottom stage with range of  $\sim 1\mu\text{m}$  would increase MICH UGF and reduce lock acquisition time. Bottom stage actuators can also be used in full lock for high MICH bandwidth since they should not excite suspension bounce and roll modes.

- Coupling of electrostatic driver noise of end test masses to gravitational wave channel is still above aLIGO best sensitivity curve, and ITM drivers are used for high frequency DARM control. Low noise electrostatic drivers are now being designed.
- Alignment of power recycling cavity is not controlled during CARM offset reduction. In full lock, alignment signals in reflected port are dominated by common arm modes, and two signals for input beam and power recycling cavity alignment are still derived from REFL WFS. Sensing matrix depends on beam position on BS, contrast defect and mode matching between the cavities. This leads to instabilities in the angular control system if one of the parameters is changed.

Alignment controls can be improved by adding a pair of WFS in pick-of-port. RF signal should be demodulated at 36MHz to provide alignment signals only for power recycling cavity and input beam. Sensitivity of these photodetectors for carrier alignment is small, and alignment loops can be engaged during CARM offset reduction.

- aLIGO intensity stabilization servo sees backscattering noise when power recycling mirror is aligned. Scattered light adds amplitude noise seen in gravitational wave channel. This problem can be addressed by relocating ISS photodiodes or changing optical path on HAM2 bench.
- Bounce and roll modes of quadruple suspensions have ring down time of  $\approx 2$  hours and get excited every lock loss up to the level of  $\sim 10^{-9} - 10^{-10}m$  in vertical direction. Coupling to longitudinal direction is  $\sim 10^{-3}m/m$  and height of the modes seen in DARM is  $\sim 10^{-12} - 10^{-13}m$ .

Bounce and roll modes are damped in full lock using DARM or WFS angular signals since local sensors installed on suspensions are not sensitive enough to vertical motion of these amplitudes. Damping process takes 5-10 minutes before interferometer is transitioned to low noise regime and another 5 minutes after transition.

Installing additional shadow sensors on penultimate mass with broadband noise of  $3 \cdot 10^{-11} - 10^{-10}m/\sqrt{Hz}$  would help to damp bounce and roll modes down to the level of  $\sim 10^{-12}m$  in the vertical direction during lock acquisition before DARM signal is available.

- Lock acquisition sequence and interferometer control should be adjusted depending on seismic activities. If ground motion is high, engagement of ALS DIFF loop becomes problematic since VCO in the corner and end stations saturate on the output and error signal gets a transient, suspensions are excited, and lock is lost. Angular fluctuations of the test masses also make ALS DIFF beat note fluctuate, and PFD produces a glitch once beat note signal is reduced below the threshold level of  $\approx -35dBm$  with the current noise floor.

This problem is addressed by increasing range of ALS DIFF VCO by factor of 10. ALS DIFF noise is also increased below 0.1Hz due to coupling of ADC noise. Suspension optical levers are engaged to suppress angular motion of test masses in the frequency range 0.04Hz - 0.5Hz. There is no reason to do these additional steps during summertime when microseismic activity is low and lock acquisition time can be reduced.

Time required for DRMI lock acquisition can be significantly reduced during windy days by feeding forward differential CPS signals of BS and ITM ISI tables to BS suspension to slow down fringe velocity of Michelson interferometer. At the same time this feedforward technique is not required when wind velocity is low.

Bandwidth of angular loops should also depend on the level of seismic noise. Coupling of angular control noise above 10Hz depends on the loop bandwidth and can be reduced during summertime.

Blending of position and inertial seismic sensors should also depend on the ground motion. During windy days it is necessary to shift up blending frequencies of CPS and T240.

- Scattering noise from HAM6 chamber is one of the main noise sources limiting current interferometer sensitivity in the frequency range 20Hz - 150Hz. OMC cover is now being manufactured and will be installed later to reduce light scattering from OMC to the chamber walls. It could happen that scattering occurs from other optical components as well and additional covers will be required.

Orthogonal approach is to cover HAM6 and adjacent tube sections with insulation. It will reduce tube motion due to background acoustic motion by factor of  $\approx 3$  in the frequency range 50Hz - 1kHz.

- Bottom reaction mass on quadruple suspensions is used for actuation on the test mass. At the same time small gap between reaction and test masses leads to squeezed damping noise and makes a less efficient discharging of the back mirror surface compared to the front one.

One possible solution investigated by LIGO suspension group is to make a hole in the reaction mass. Electrostatic blades are installed close to the edges of the reaction mass, and circular hole of the diameter of 10cm should not change the actuation if total mass is conserved.

- Residual gas pressure is still more than order of magnitude away from the design value of  $10^{-9} Torr$ . Ion pumps at the end stations are now turned off to avoid charging of the test masses. Ion pumps will be relocated or different type of pumps will be used to reduce gas pressure in the arm tubes and avoid charging of the test masses.
- Parametric instabilities in the arm cavities were first seen when input power was 12W. After using TCS ring heater, it was possible to shift resonant frequencies of HOMs and increase input power up to 25W. Interferometer stayed locked for up to 30 hours in this configuration. For the power of 125W it will be necessary to actively damp body modes using electrostatic actuators.

## 11.2 Medium term improvements

This section describes ideas on how to improve control system of aLIGO interferometers and tune instrument sensitivity towards a particular gravitational wave detector.

### 11.2.1 Interferometer control

Current aLIGO feedback control systems are designed and analyzed using frequency domain approach. Loop parameters are chosen manually and sometimes not optimally. Frequency domain approach also does not account for cross couplings between suspension and interferometric degrees of freedom that can cause instabilities. Time domain approach can be used to generate optimal

multiple-input-multiple-output stable controllers based on the state-space model of dynamic system:

- Adaptive sensor blending using Kalman filtering can significantly improve performance of seismic isolation at low frequencies. Currently blending frequencies between position and inertial sensors are chosen based on the average seismic level. Tuning blending filters depending on seismic motion can help to reduce low frequency motion during windy days or microseismic activity when winds are low.
- Stable multiple-input-multiple-output controllers can also improve low frequency motion of ISI tables. Longitudinal degrees of freedom use T-240 signals at frequencies higher than 40mHz. However, seismometer signal is also sensitive to the tilt of the table. Building an accurate model of the table with cross couplings on the actuation and sensing side will make it possible to apply optimal time domain controllers, like LQR or  $H_\infty$ , for stabilization of optical tables.
- MIMO controllers should be applied to local damping of suspensions. Current design uses shadow sensors on the top mass and six SISO controllers damp suspension resonances. Some modes are left not perfectly damped like 0.41Hz and 3Hz pitch modes of test masses or 2.1Hz yaw mode of beam splitter. These modes do not couple strong enough to the top stage motion or arise from cross coupling between the loops. Distributed control system can use lower stages for resonances below 1Hz to avoid noise injections in gravitational wave band. Control system should also be of MIMO type and be able to damp cross couplings in the suspensions.
- Kalman state estimation should be used to control radius of curvature and ITM substrate lens during lock stretches and after lock losses when readings from Hartmann sensors are not available as discussed in chapter 10.2.
- Feedforward noise cancellation algorithms can be applied for subtraction of acoustic noise coupling through scattered light. Since beam spot position of chamber walls move, transfer function from acoustic noise to gravitational wave channel also changes with time. For this reason, subtraction of acoustic noise might require adaptive filters.

### 11.2.2 OMC backscattering

Phase noise due to scattered light at the output of inteferometer can be reduced by stabilizing the distance between signal recycling mirror and output mode cleaner. This can be done by improving seismic isolation system of HAM ISI optical benches. Improvement can be achieved at microseismic frequencies 0.1-0.3Hz by putting T-240 seismometer on the tables and using these sensors in the frequency range 50mHz - 1Hz.

Reduction of HAM ISI motion at microseismic frequencies by factor of 2-3 will also significantly reduce DRMI lock acquisition time and improve power fluctuation due to angular motion in the power and signal recycling cavities during winter time.

An orthogonal approach to reduce OMC backscattering noise is to remove DARM offset and inject carrier light through the separate path. Balanced homodyne detection scheme is studied in [122]. Reference carrier light is picked off from power recycling cavity, is filtered and beats against DARM sidebands. Research on phase control of reference beam is now ongoing.

### 11.2.3 Data analysis and detector performance

Advanced LIGO sensitivity can be optimized for a particular gravitational wave source. It is possible to shape quantum noise of interferometer to improve sensitivity to continuous gravitational waves by a factor of 3 to 6 in the frequency range 500Hz - 3kHz.

In order to improve sensitivity to binary objects, online detection algorithms should be developed. Gravitational wave signal can be detected in the frequency range 10Hz to 40Hz and tracked towards higher frequencies. One aLIGO interferometer can be in broadband configuration while the other one can be optimized for the narrow band search.

Gravitational waves from binary neutron star coalescence can be detected in the frequency range 1kHz - 4kHz. Signal parameters can be used for better understanding of physics of neutron stars, like equation of state as well as matter at subnuclear densities and bulk properties of neutron-rich matter [123]. For this reason, gravitational wave detectors should be able to optimize their sensitivity at these frequencies by changing optical configuration on the time scale of msec.

Quantum noise of gravitational wave detectors can be controlled by tuning following parameters:

- Input power determines the level of shot noise and quantum radiation pressure noise in the arm cavities. Reduction of input power increases shot noise level and instrument sensitivity at frequencies higher than 50Hz but improves at lower frequencies. In order to improve sensitivity to final moments of binary neutron star coalescence, input power should be increased. Currently input power is limited by excitation of parametric instabilities in the arm cavities but they usually ring up on the time scale from tens of minutes to few hours, and power can be increased for short periods of time.
- Configuration of the signal recycling cavity can be set to optimize interferometer sensitivity to gravitational waves at particular frequencies. First SRC parameter that can be modified is the round trip phase accumulation in the cavity  $\varphi_{SRC}$  [124]. This parameter can be quickly tuned in aLIGO configuration by introducing offsets to the error point of SRCL servo. Second parameter is finesse of signal recycling cavity. Since transmission of signal recycling mirror is

fixed, it is not possible to quickly change finesse of the cavity in aLIGO configuration. Next section 11.3 describes ideas on how to make finesse variable.

Figure 11.1 shows aLIGO quantum noise when SRM transmission is set to 1, 0.36 and 0.2 and input power to interferometer is 125W. Effect from SRC detuning by 30nm is also shown in figure. In the current configuration with SRM power transmission of 0.36 DARM pole equals to 385Hz. In case of no signal recycling cavity, quantum noise level improves around 80Hz but DARM pole is reduced down to 40Hz. If transmission of SRM is reduced to 0.2, then DARM pole increases up to 850Hz and interferometer sensitivity improves at high frequencies and gets worse in the frequency range 80Hz - 600Hz.

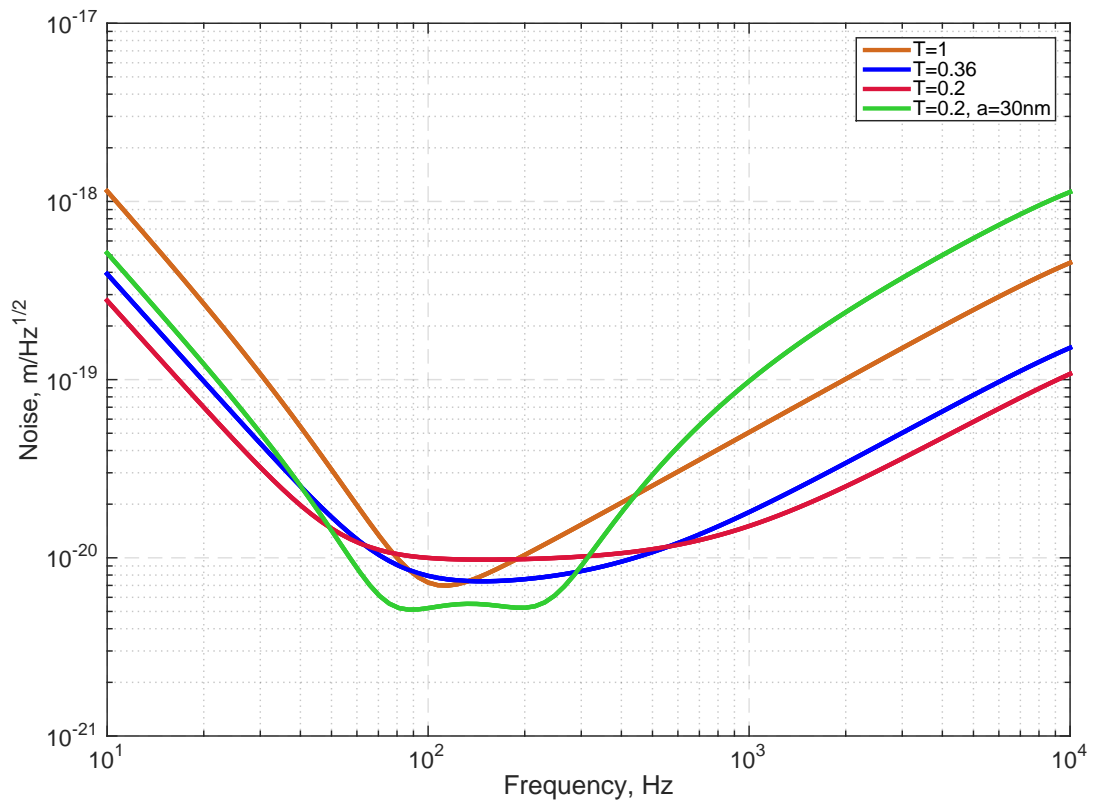


Figure 11.1: Interferometer quantum noise depending SRM transmission  $T$  and detuning of signal recycling cavity  $a$ .

- Injection of squeezed states of light through the antisymmetric port will improve noise in one quadrature and make it worse in the other. Since radiation pressure noise is the dominant quantum noise below 40Hz and shot noise above 40Hz with input power of 125W, frequency dependent squeezing [125] can improve noise coming from each quadrature in particular frequency band. However, due to optical losses in the filter cavities [126] it will be possible to

reduce noise in one quadrature in a particular frequency band and avoid amplification of noise in the other frequency band. Rotation of the squeezing angle can be done fast and improve interferometer sensitivity at low or high frequencies depending on the gravitational wave signal.

### 11.3 Variable finesse of the signal recycling cavity

This section discusses ideas on how LIGO configuration can change in the next 10 years. Quantum noise will limit interferometer sensitivity of both proposed future designs involving cryogenic systems and building new facility with longer arms. For this reason, configuration of the signal recycling cavity should be able to optimize quantum noise in particular frequency band.

If SR2 folding mirror is replaced with a triangular cavity as shown in figure 11.2, then transmission of SR2 compound mirror can be changed by introducing offsets in the cavity length. In this case transmission of SRM is set to zero and gravitational wave signal is extracted from transmission of compound SR2 mirror. Cavity length can be tuned to reject sidebands and get only carrier in transmission.

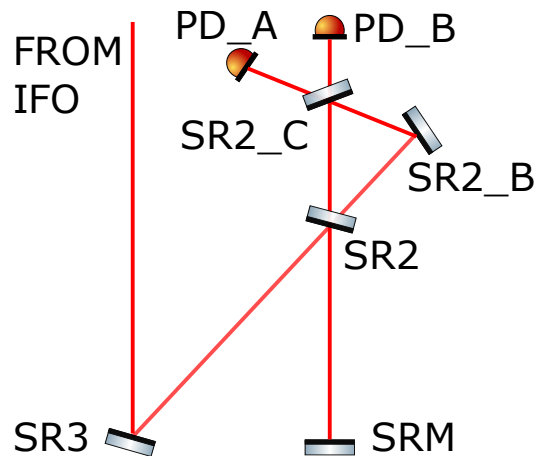


Figure 11.2: Compound SR2 mirror inside the signal recycling cavity.

Major difficulty in this design is to control signal recycling and auxiliary SR2 cavities. Since detuning of SR2 cavity changes not only amplitude of field reflectivity but also phase as shown in figure 11.3, SRM should be moved in longitudinal direction to compensate for this shift. For this reason, changing of SRC finesse as well as detuning phase is limited by the SRCL loop bandwidth of  $\approx 30 - 100Hz$ .

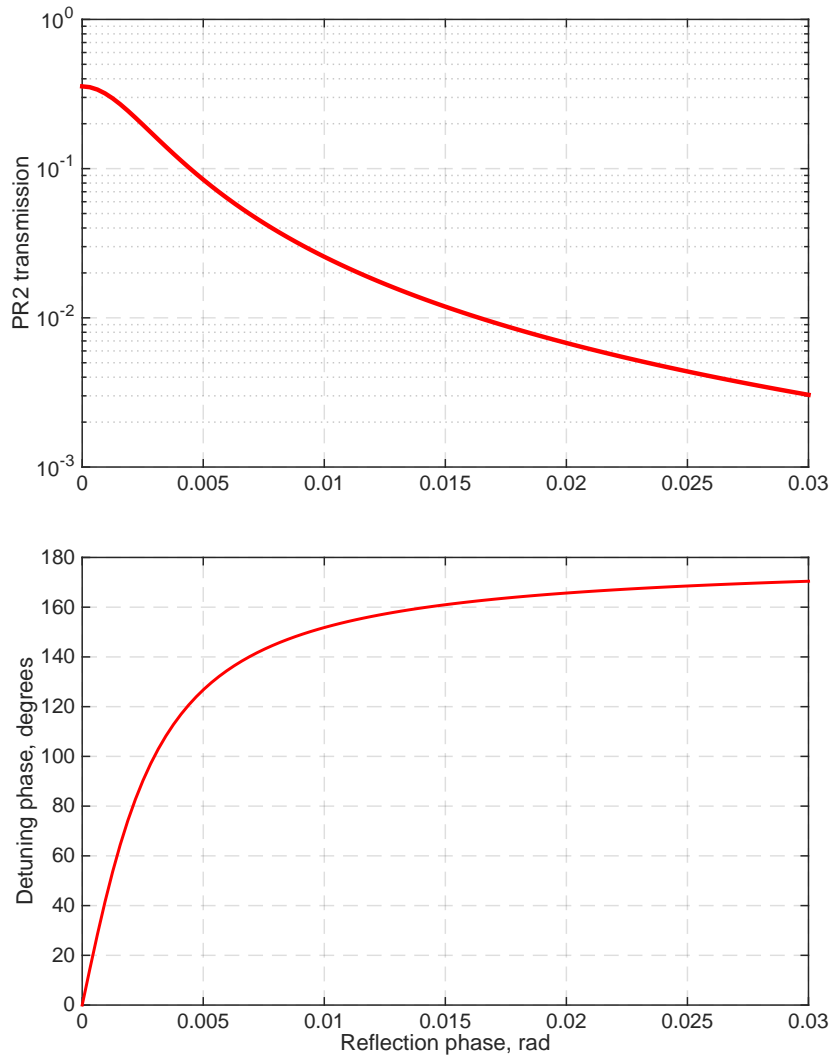


Figure 11.3: Power transmission and reflection phase from compound SR2 mirror based on cavity detuning.

Transmission of SR2 mirrors are  $T_{SR2} = 10^{-2}$ ,  $T_{SR2.B} = 0$ ,  $T_{SR2.C} = 10^{-3}$ . These values were used to simulate transmission and phase of reflected light shown in figure 11.3. When cavity is not detuned, power transmission of the compound cavity is similar to the transmission of aLIGO signal recycling mirror  $T_{SRM} = 0.36$ .

Residual motion of SR2 cavity should be suppressed down to 1pm to achieve stable DARM optical transfer function. Figure 11.4 shows interferometer quantum noise with compound SR2 mirror. If cavity is not detuned, then quantum noise is similar to aLIGO one. If SR2.B mirror is detuned by 4nm and SRM by 51nm, then quantum noise above 2kHz is factor of 3-4 better compared to aLIGO

noise. This configuration can be used for detection of bursts during binary neutron star coalescence.

Quantum noise at low frequencies depends on the mass of SR2 mirrors. Red curve in figure 11.4 shows quantum noise when mass of SR2 mirrors is very large. Black curve is simulated under assumption that mass of all three SR2 mirrors is 0.03kg. In this regime optomechanics coupling inside SR2 cavity becomes important.

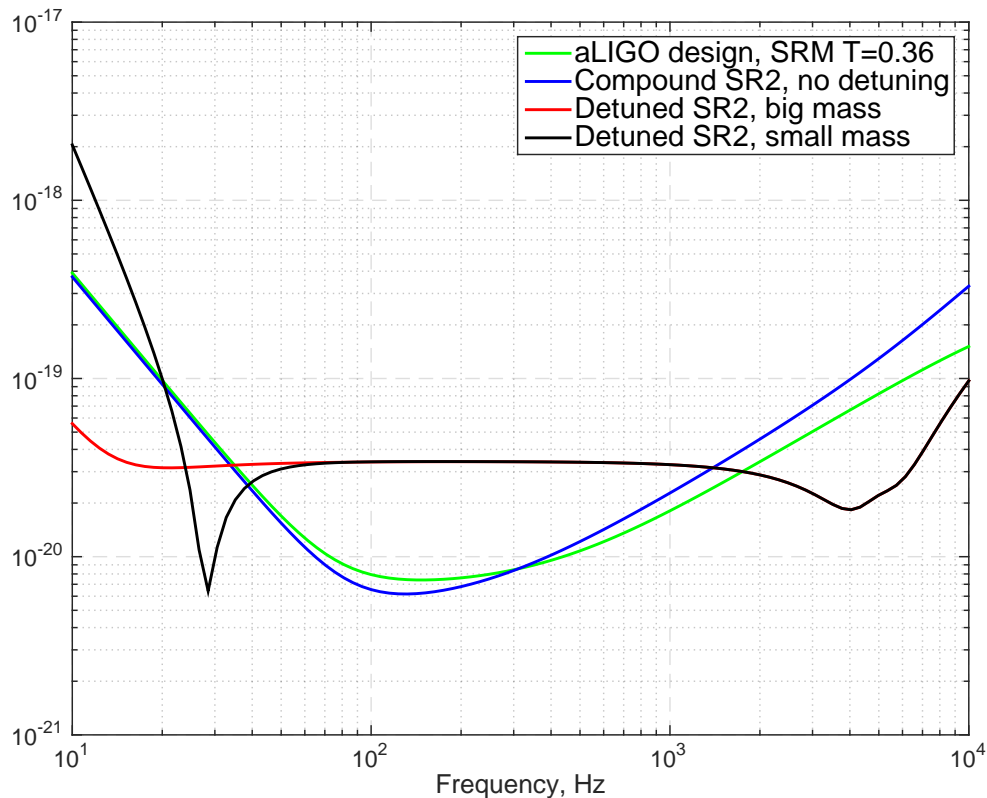


Figure 11.4: Interferometer quantum noise with SR2 cavity depending on cavity detuning and mass of the mirrors.

Compound SR2 mirror also works as a mode cleaner for the 00 carrier light. Higher order modes leaving interferometer will be rejected from the SR2 cavity and leave interferometer through reflected port if finesse of SR2 cavity is significantly higher compared to power recycling cavity finesse.

Finesse of signal recycling cavity in this optical configuration is significantly higher for sidebands compared to carrier since sidebands are anti resonant in the SR2 cavity. This leads to higher SRCL optical gain compared to aLIGO configuration. Given SR2 cavity parameters  $T_{SR2} = 10^{-2}$ ,  $T_{SR2-B} = 0$ ,  $T_{SR2-C} = 10^{-3}$ , shot noise level of SRCL converted to meters is reduced by factor of 3 in case of zero DARM and SRCL detuning as shown in figure 11.5. Mass of all SR2 mirrors is assumed to be 2.9kg.

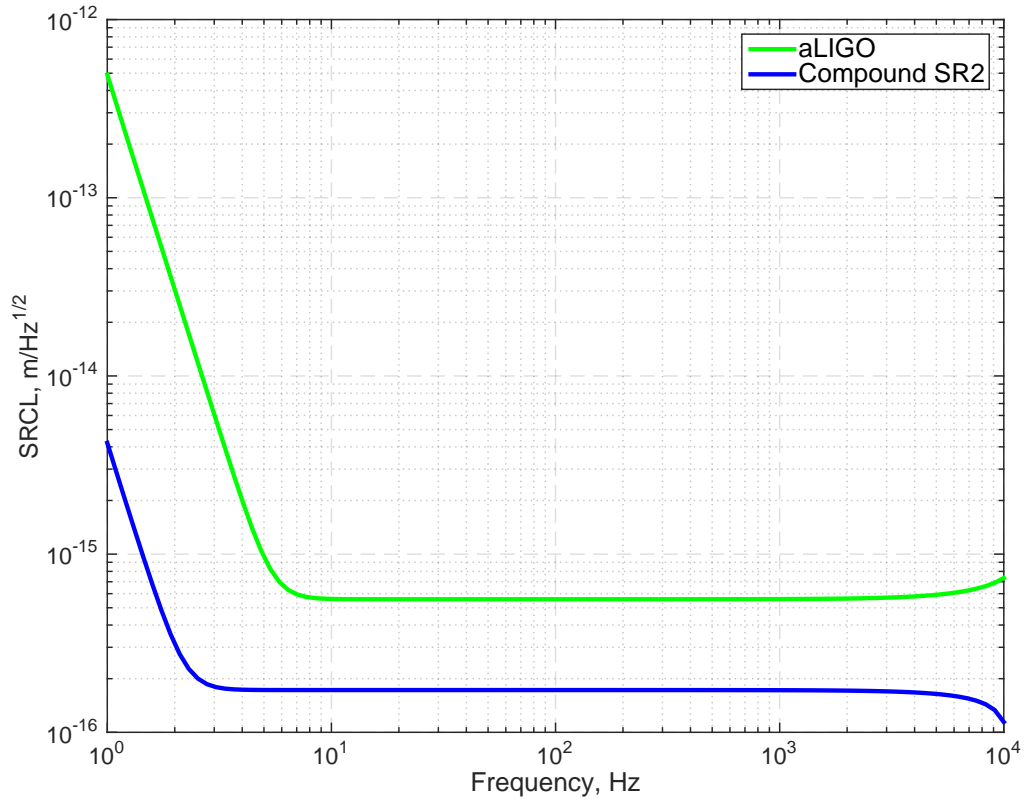


Figure 11.5: Comparison of SRCL quantum noise in aLIGO configuration and with compound SR2 cavity. SRC finesse for carrier is the same in both cases.

# Summary and conclusions

Advanced LIGO interferometers have been successfully brought into linear regime in 2014 after initial LIGO shut down in 2010. First part of this thesis is devoted to longitudinal and angular controls of the arm cavities and auxiliary degrees of freedom. Servos are tuned to keep interferometer in its operating point with small residual motion. Full sequence of lock acquisition takes about 10 minutes, and another few minutes are required to transition the instrument to low noise regime. Control system was proven to be robust, and interferometer stayed in low noise regime for many hours. Longest lock in low noise regime lasted for 30 hours.

The sensitivity of the advanced LIGO interferometers to binary neutron stars is already a factor of 3 higher compared to initial LIGO instruments and continues to improve on a monthly basis. Data from gravitational wave channel is calibrated using online procedure described in the second part of this thesis. Achieved precision of DARM calibration should be better than 10%. Displacement and sensing noise couplings were investigated to understand aLIGO sensitivity curve. Problems of residual gas and scattered light will be addressed before O1 run to improve sensitivity curve at low frequencies.

Feedforward cancellation systems are used to reduce coupling coefficient of auxiliary degrees of freedom and angular controls to gravitational wave channel. This thesis describes optical coupling and setup of online feedforward correction system. Cancellation factors of 10-30 are achieved in the frequency range 10-70Hz. Online MIMO adaptive feedforward filters were tested at the 40m prototype using input mode cleaner, arm cavities and seismometer signals. Subtraction factors of 10-30 are achieved in the frequency range 1-4Hz.

State-space approach to feedback control design promises to improve performance of aLIGO control system. In the third part of this thesis several optimal time domain control techniques, like LQR, Kalman filter,  $H_\infty$ , and  $\mu$ -synthesis, are discussed and possible applications to advanced LIGO interferometers are considered.  $H_\infty$  control technique was successfully applied to the problem of beam splitter local damping and angular stabilization. Simulations show that optimal Kalman filter can be used to control curvature of test masses. LQR technique with frequency shaping of the cost function was tested at the 40m prototype on single stage beam splitter suspension. Robust controllers generate using  $\mu$ -synthesis technique were applied to BS local damping. All suspension

modes were damped and sensor noise injection above 10Hz was less compared to suspension thermal noise.

The last chapter of this thesis contains ideas for future research and improvements of LIGO interferometers. The first science run will take place in the Fall of 2015 and will last for 3 months. Some of the new systems discussed in this thesis can be installed after O1 in the beginning of 2016. Other ideas will be implemented in the future towards direct detection of gravitational waves and important research of astrophysical sources.

# Appendix A

## Acronyms

This appendix gives a list of abbreviations frequently used in this thesis:

ADC	Analog to digital converter
ALS	Auxiliary length stabilization
AO	Additive offset
AS	Antisymmetric port
ASC	Alignment sensing and control
BNS	Binary neutron star
BS	Beam splitter
BSC	Beam splitter chamber
CARM	Common arm
DAC	Digital to analog converter
DARM	Differential arm
DRMI	Dual recycled Michelson interferometer
EOM	Electro-optical modulator
ESD	Electrostatic driver
ETM	End test mass
HAM	Horizontal axis module
IMC	Input mode cleaner
ITM	Input test mass
ISI	Internal seismic isolation
MICH	Michelson interferometer
OMC	Output mode cleaner
PFD	Phase frequency discriminator
PLL	Phase locked loop
POP	Pick off power recycling

PRC	Power recycling cavity
PRCL	Power recycling cavity length
PRM	Power recycling mirror
PSL	Pre-stabilized laser
QUAD	Quadruple suspension
REFL	Reflected port
SRC	Signal recycling cavity
SRCL	Signal recycling cavity length
SRM	Signal recycling mirror
UGF	Unity gain frequency
WFS	Wave front sensor

## Appendix B

# Quantization noise

A significant fraction of aLIGO analog signals is acquired using ADC and processed in the digital domain. After being conditioned, signals are converted to analog domain for actuation or saved using data acquisition system for future analysis.

Poles and zeros of aLIGO filters are most commonly tuned in continuous representation and then filter is converted to digital domain using bilinear transformation. During the process of digital filtering, quantization noise arises from finite precision of number representation inside CPU. Output noise of the digital filter can be written as:

$$e(t) = x_d(t) - x_a(t) \tag{B.1}$$

where  $x_a$  is filter output if numbers with infinite precision or analog signals are used for calculations and  $x_d$  - filter output if finite precision arithmetic is applied.

In floating point arithmetic noise  $e$  depends on the input signal and particular way of digital filter realization. Input signals depend on interferometer configuration and cannot be changed but it is necessary to optimize computational form of digital filter to reduce noise  $e$ .

First step in minimizing quantization noise applied in LIGO digital system is to split the filter in a set of second order sections. Each SOS is determined by five parameters: gain  $g$ , zero coefficients  $b_1, b_2$ , and pole coefficients  $a_1, a_2$ . Output of SOS at particular time step  $t$  in dependence of input signal  $s$  is given by equation:

$$x_d(t) = g \cdot (s(t) + b_1 s(t-1) + b_2 s(t-2)) - a_1 x_d(t-1) - a_2 x_d(t-2) \tag{B.2}$$

Second step in minimizing digital noise is to optimize signal flow inside second order sections. Equation B.2 can be computed using infinite amount of forms. This can be most clearly seen if the

filter is presented in the discrete time-invariant state-space form using  $(A, B, C, D)$  matrices:

$$\begin{aligned} z(t+1) &= Az(t) + Bx(t) \\ y(t) &= Cz(t) + Dx(t) \end{aligned} \tag{B.3}$$

where  $z(t)$  is state-space vector of the model. State space representation B.3 is not unique since for any non-singular matrix  $T$  it is possible to introduce another state space vector  $z_T = Tz$  and matrices  $A_T = TAT^{-1}$ ,  $B_T = TB$ ,  $C_T = CT^{-1}$ ,  $D_T = D$  such that state space model  $(A_T, B_T, C_T, D_T)$  represents digital filter B.2.

Optimal state-space realization of digital filter in terms of minimum quantization noise is described in [127, 128]. In order to compute output of digital filter,  $(N+1)^2$  multiplications and  $N(N+1)$  additions are required, where  $N$  is order of the filter. Other algorithms suggest lower computational cost and processing time with higher level of quantization noise [129].

Direct form 2 has minimum possible amount of additions, delays and multiplications. This form is the fastest way to compute filter output and was used in initial LIGO CDS system. Signal flow is shown in figure B.1a. Most significant disadvantage of using this form is high quantization noise since signal is first propagated through filter poles and only then through zeros. This way of signal flow leads to large internal numbers and quantization errors.

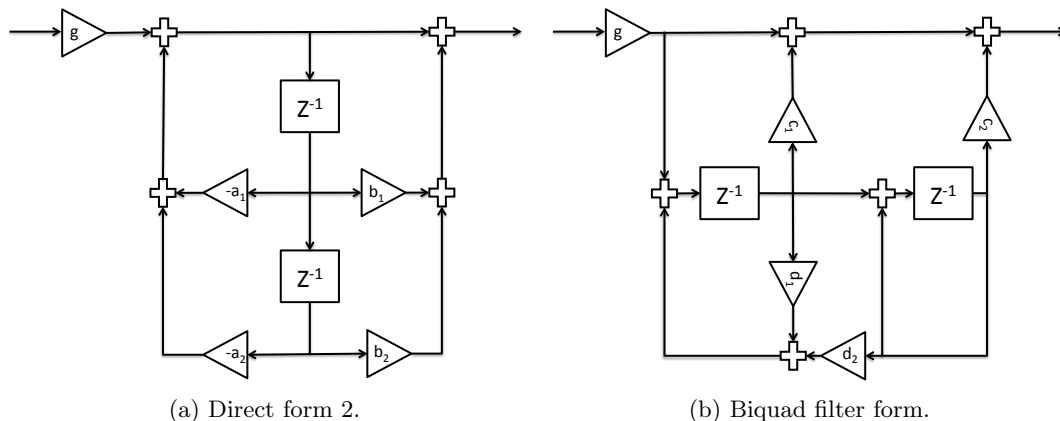


Figure B.1: Filter forms used in initial and advanced LIGO to compute output of SOS.

Advanced LIGO uses another form of computing SOS known as "biquad" form [130]. This form requires one additional summation but avoids large internal numbers, and minimizes number of flops, and is similar to realization of analog second order sections. Figure B.1b shows computational process of SOS using biquad form. Biquad form gains are related to coefficients B.2 using following equations:  $c_1 = b_1 - a_1$ ,  $c_2 = b_2 - a_2 + b_1 - a_1$ ,  $d_1 = -a_1 - 1$ ,  $d_2 = -a_2 - a_1 - 1$ .

This appendix describes software developed to estimate quantization noise of digital filters used in

initial and advanced LIGO signal processing systems. This system was tested at the 40m prototype. Section 1 describes the algorithm for the estimation of digital noise. Section 2 is devoted to the system that is design to check all digital filters running at the 40m prototype.

## B.1 Estimation algorithm

Since quantization noise of a digital filter depends on the filter input signal and biquadratic form used to compute filter output, noise is checked for specified filter bank using online input signal. Main idea of the estimation algorithm is to compute and compare filter outputs using two types of variables with different mantissa size. In more details:



Figure B.2: DARM filter bank. Algorithm downloads input signal and computes output using two types of variables to estimate quantization noise of digital filters that are engaged.

- 32 seconds of filter input signal is downloaded using data acquisition system. This data is used to estimate quantization noise of digital filters. Since data in most LIGO channels is stationary, it is sufficient to download filter input signal once per week.
- SOS representation of all digital filters that are currently engaged in the specified filter bank is obtained from the filter configuration file. If later in time state of the filter bank changes or coefficients of the filters are replaced then quantization noise should be checked again. Figure B.2 shows example of the signal flow in the filter bank with 8 active filters out of 10.
- Calculations are done using two types of variables with different numbers of bits. As a result quantization noise in filter outputs  $x_{d,1}$  and  $x_{d,2}$  is also different. Second type of variables is chosen to have much more bits compared to the first one.
- Quantization noise of digital filter is computed by subtracting filter outputs  $x_{d,1}$  and  $x_{d,2}$ . Second signal contains much less digital noise compared to the first one and difference  $x_{d,1} - x_{d,2}$  determines noise of filter output when first type of variables is used. Since aLIGO CDS system uses double precision format, quantization noise is extrapolated assuming that it scales with mantissa length.

Precision of digital filtering at the 40m prototype and LIGO Livingston Observatory was tested using single and double precision numbers. Extrapolation factor of  $2^{D-S} \sim 10^8$  was used to scale

quantization noise from single to double precision.  $D$  is number of bits used in double precision mantissa,  $S$  in single precision.

Script is written in Matlab using C blocks. Outputs of digital filters is computed in C-functions that are similar to the ones used in online system. Matlab is used to download data, get SOS-representation of the filter and plot spectrum of quantization noise. Figure B.3 shows application of the digital filter checking code to the HAM ISI vertical damping loop.

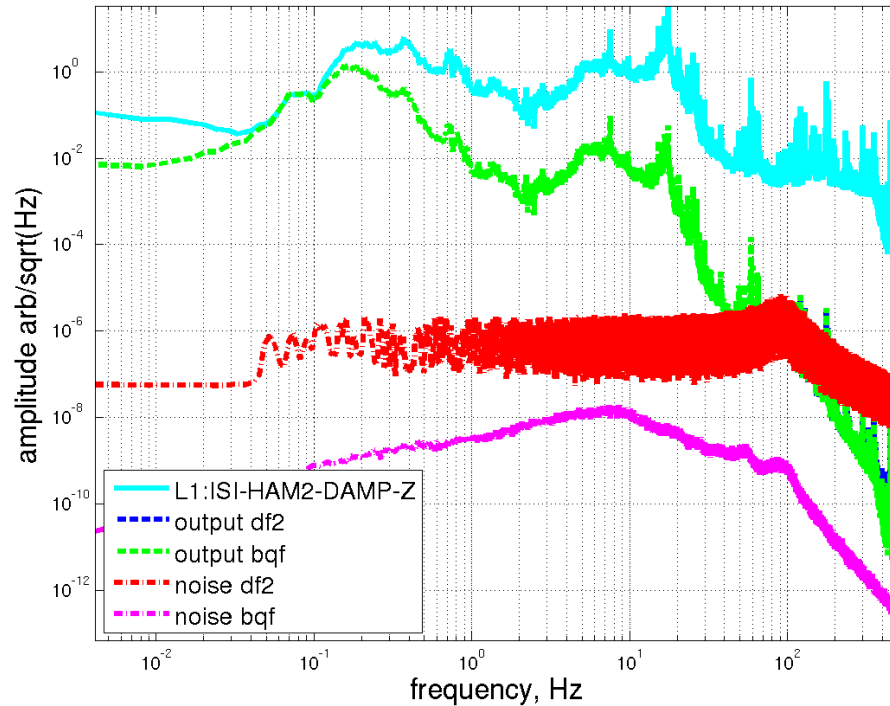


Figure B.3: Quantization noise of HAM ISI vertical damping loop. Noise is lower if "biquad" form is used instead of direct form 2.

## B.2 Monitor of the full system

All digital filters at the 40m prototype were checked for high quantization noise by applying algorithm discussed in the previous section to the full system [131]. Script reads model names from the input list and for each model finds all filter banks, downloads input data for a group of 64 digital filters. Quantization noise is estimated for this group of filters and then input data for next group is downloaded for noise estimation. When all digital filters are checked, script creates a warning if signal to noise ratio for the filter bank is less than  $10^4$ . If the limit is set in the filter bank, the script also checks for saturation of the output signal.

## Appendix C

# Suspension wire heating

During aLIGO commissioning it was noticed that alignment drift of power recycling cavity depends on intracavity power. This optomechanical effect misaligned completely PRC axis relative to the input beam in less than 5 minutes if resonating optical power was as low as 60W. If optical power in PRC cavity was increased up to 100W, instability occurred and power started to oscillate at 0.7Hz before lock was lost.

Looking at local suspension sensors and optical levers it was discovered that PR3 and BS are responsible for power fluctuations in PRC. Drift in pitch was a factor of 10-30 larger compared to yaw. After lock was lost, suspensions drifted by  $4\mu\text{rad}$  to its initial position on the time scale of 10 minutes, as shown in figure C.1.

Since beam size on PR3 and BS is  $\approx 5.5\text{cm}$ , effect of pitch drift was explained by assuming that front wires of suspensions were heated by optical power resonating in the cavity. Length of the front wires slightly increased and optic moved in pitch. Back suspension wires were heated much less compared to the front ones since optical power could not get to that part of suspension.

Optical power increases temperature of PR3 and BS wires by  $\sim 0.3\text{mK/Watt}$ . Since Young's modulus depends on temperature of the material, violin mode frequency should also shift. This was indeed observed on PR3 and BS suspensions. Violin mode frequencies were measured when input power was 3W and 10W as shown in figure C.2. Frequency of the mode shifted by  $\approx 10\text{mHz}$  and confirmed that wires are heated by the optical power resonating in the cavity.

Problem of PR3 and BS suspension wire heating was solved by installing additional baffles on the mirrors that block optical power from getting to the wires. Baffles have reduced angular drift by factor of  $\sim 30$  and wire heating problem became much less significant to aLIGO interferometers.

PRM and PR2 did not drift since beam size is much smaller on these mirrors. In this configuration only small optical power gets on the wires and thermal drift is negligible. Test masses also did not drift since they are suspended using fused silica fibers instead of metal wires. Fibers are well baffled and also transparent to 1064nm laser light. Absorption of light in fibers is small enough to avoid misalignment of test masses.

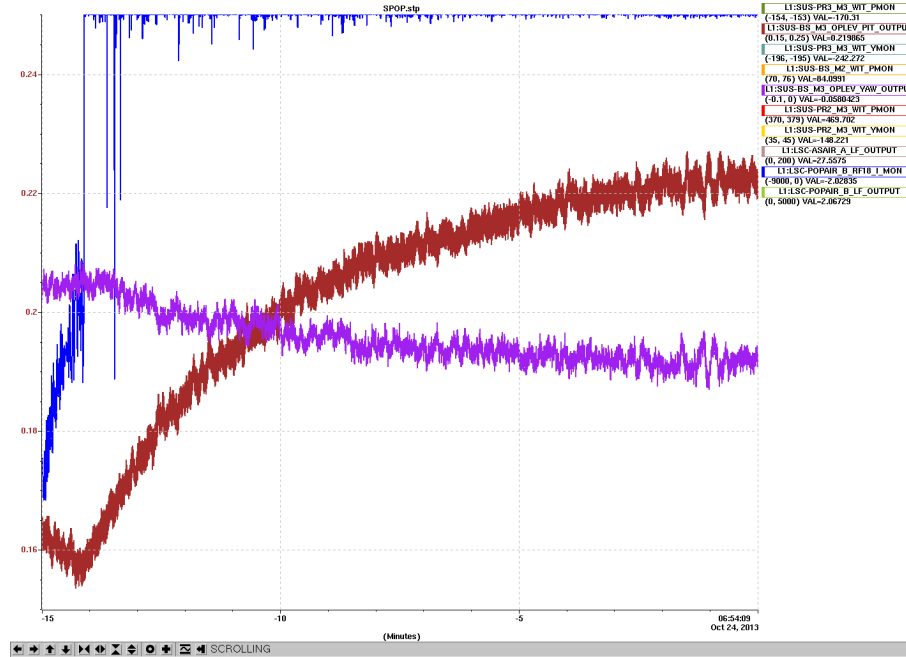


Figure C.1: Drift of BS pitch after lock is lost. Blue trace shows intracavity power measured by POP18 signal, red - BS pitch, magenta - BS yaw angle measured by optical lever. POP18 signal is negative when PRC is locked on carrier. This signal goes to zero when lock is lost. When PRC was locked, intracavity power was 60W.

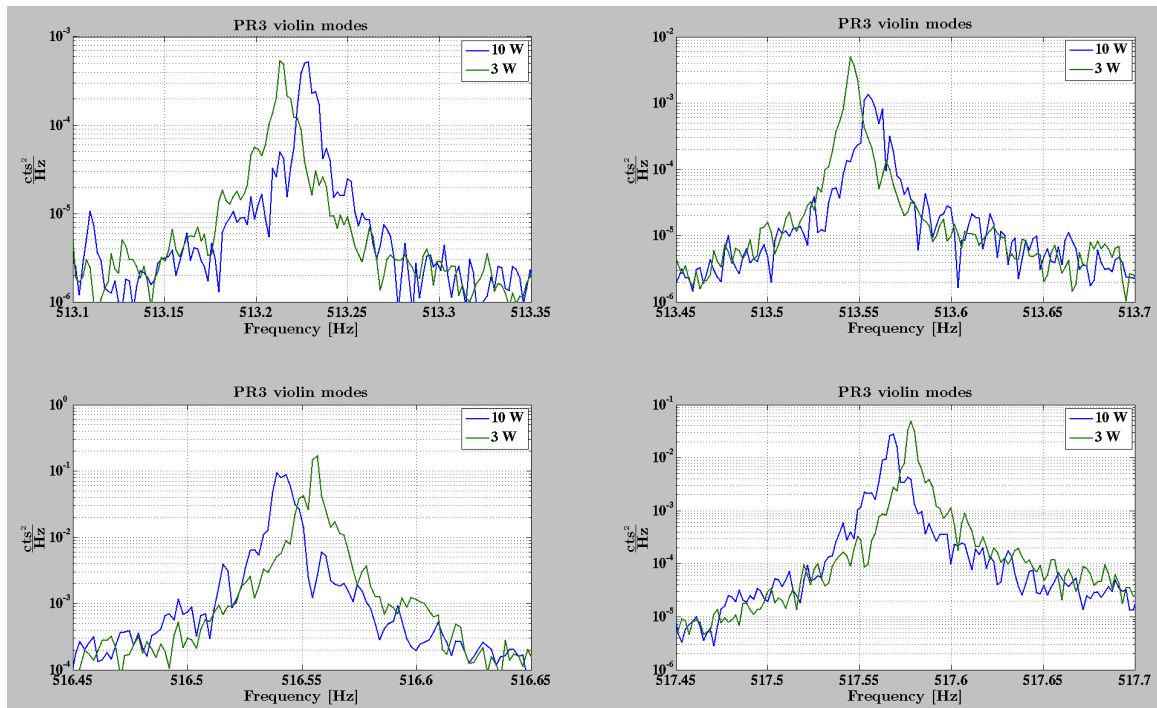


Figure C.2: Frequency shift of PR3 violin modes when input power was increased from 3W up to 10W. This shift confirmed that wires are heated by optical power resonating in the power recycling cavity.

## Appendix D

# Beam clipping in Michelson interferometer

When power recycling gain was first locked and properly aligned, optical build up was only 20 instead of 55 computed based on transmission of HR mirror surfaces  $T_{prm} = 0.03, T_{itm} = 0.0148$  and reflection of AR surfaces  $R^{ar} \approx 50ppm$ .

Recycling gain was increased up to 30 after optimizing beam position on the beam splitter by moving PRC mirrors that were not controlled by angular servos. Next two effects were considered to explain low power recycling gain:

- Mismatch of ITM radii of curvature by  $\approx 34m$  is responsible for Michelson contrast defect of  $\approx 10^{-2}$ . Power leaks to interferometer antisymmetric port and power recycling gain is reduced.
- When ETMs are misaligned and power recycling is locked, size of the beam on beam splitter is  $\approx 6cm$  and optical losses on the back surface of BS and ITMs are responsible for low power recycling gain.

These two ideas were tested using TCS ring heaters and CO2 laser beams. Both technique can improve contrast defect of Michelson interferometer by a factor of  $\sim 30$  but change beam size on BS in a different ways. TCS ring heaters increase g-factor of PRC cavity and beam size on BS. Opposite effect is achieved while applying CO2 laser beams. Angular WFS loops were running during the measurement to avoid changing of power build up due to alignment effects.

First ITMs were matched to improve contrast defect of Michelson interferometer by applying power to ITMX ring heater. Figure D.1 shows 4 hours of data of power recycling gain, contrast defect and ring heater power applied to ITMs. Heating of the mirror substrate has delay of  $\approx 30 - 40minutes$  due to heat capacity of ring heater and conductivity of the test masses. For this reason effects from changing ring heater power on PRC build up and contrast defect are delayed.

Minimal contrast defect of  $\approx 8 \cdot 10^{-4}$  was achieved when power of 0.55W was applied to ITMX ring heater. At the same time power build up in PRC increased from 27 up to 37 due to lower

contrast defect. When both ITM ring heaters were engaged to keep contrast defect constant but increase beam size on BS, recycling gain has significantly reduced. When ITMX was heated with 1W and ITMY - with 0.5W, power build up reduced to 15.

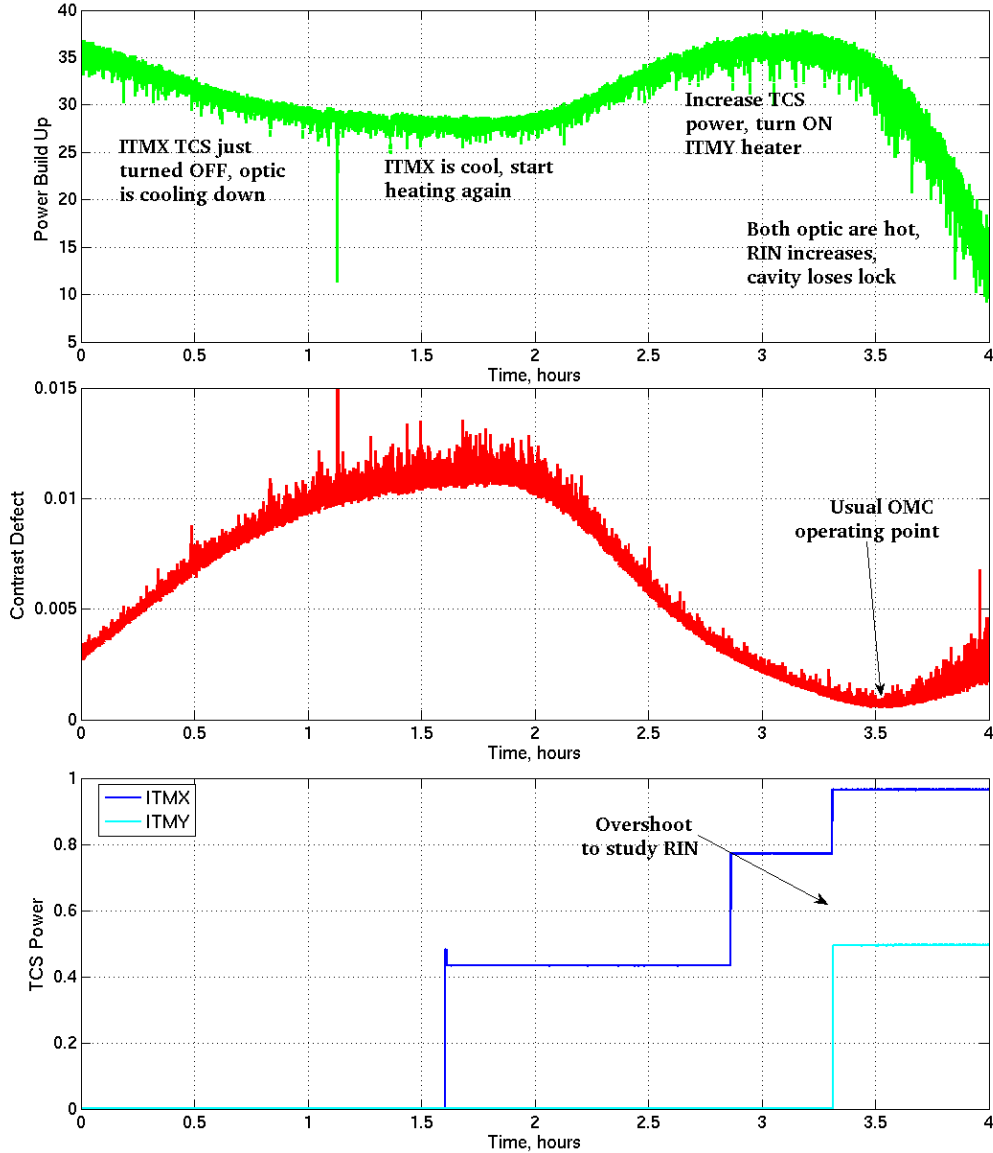


Figure D.1: Power recycling gain, Michelson contrast defect and ring heater power during TCS test. Power on ring heaters was increased in steps to monitor effects in recycling gain and contrast defect.

Power fluctuations also increased since cavity g-factor shifted closed to 1. It was monitored by dithering PR3 optic at  $f_0 = 4Hz$  and demodulating resonating power at the second harmonic of the drive. As discussed in section 2.1.2.3 relative power fluctuation at the second harmonic of the drive

is proportional to:

$$\frac{\Delta P}{P^0}(2f_0) \approx \frac{\theta_{exc}^2}{2\theta_0^2} \quad (D.1)$$

where  $\theta_0$  - divergence angle of power recycling cavity and  $\theta_{exc} = K\theta_{pr3}$  - waist tilt due to excitation  $\theta_{pr3}$ ,  $K$  is coupling from PR3 angular motion to waist tilt. ABCDEF of power recycling cavity discussed in section 4.2.1 gives the number  $K = 478$ . Figure D.2 shows demodulated intracavity power at the second harmonic of the drive frequency. After two hours when both ITMs were heated and recycling gain dropped to 15, relative power fluctuations demodulated at the second harmonic of the drive frequencies increased by factor of 3 and  $K$  increased by  $\approx 1.7$ . This means that coupling of mirror angular motion to waist tilt has increased by 1.7 during TCS test.

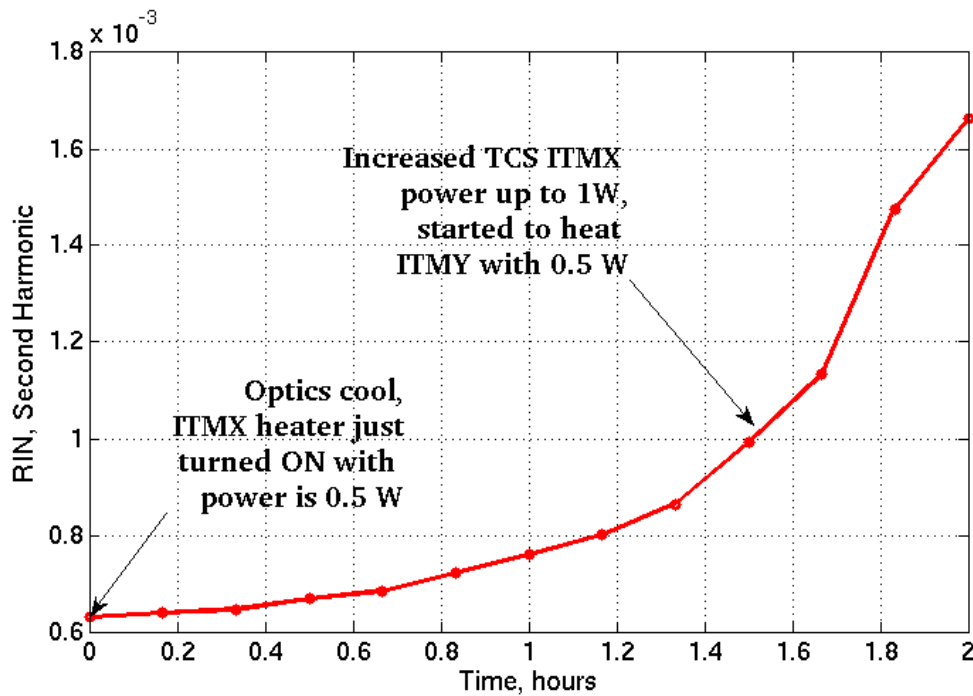


Figure D.2: Measurement of PRC g-factor during TCS test.

Then CO2 laser beam was applied to ITMY to optimize contrast defect. Minimal value of  $4 \cdot 10^{-4}$  was achieved when CO2 laser power was 175mW. At the same time power build up in PRC increased from 33 up to 45. Cavity visibility has also reduced towards its nominal value of 0.85.

Figure D.3 shows 6 hours of power recycling gain, Michelson contrast defect and cavity visibility. During this time power of ITMY CO2 laser beam was slowly increasing to optimize contrast defect. When power of CO2 laser beam was increased up to 185mW Michelson contrast defect started to degrade.

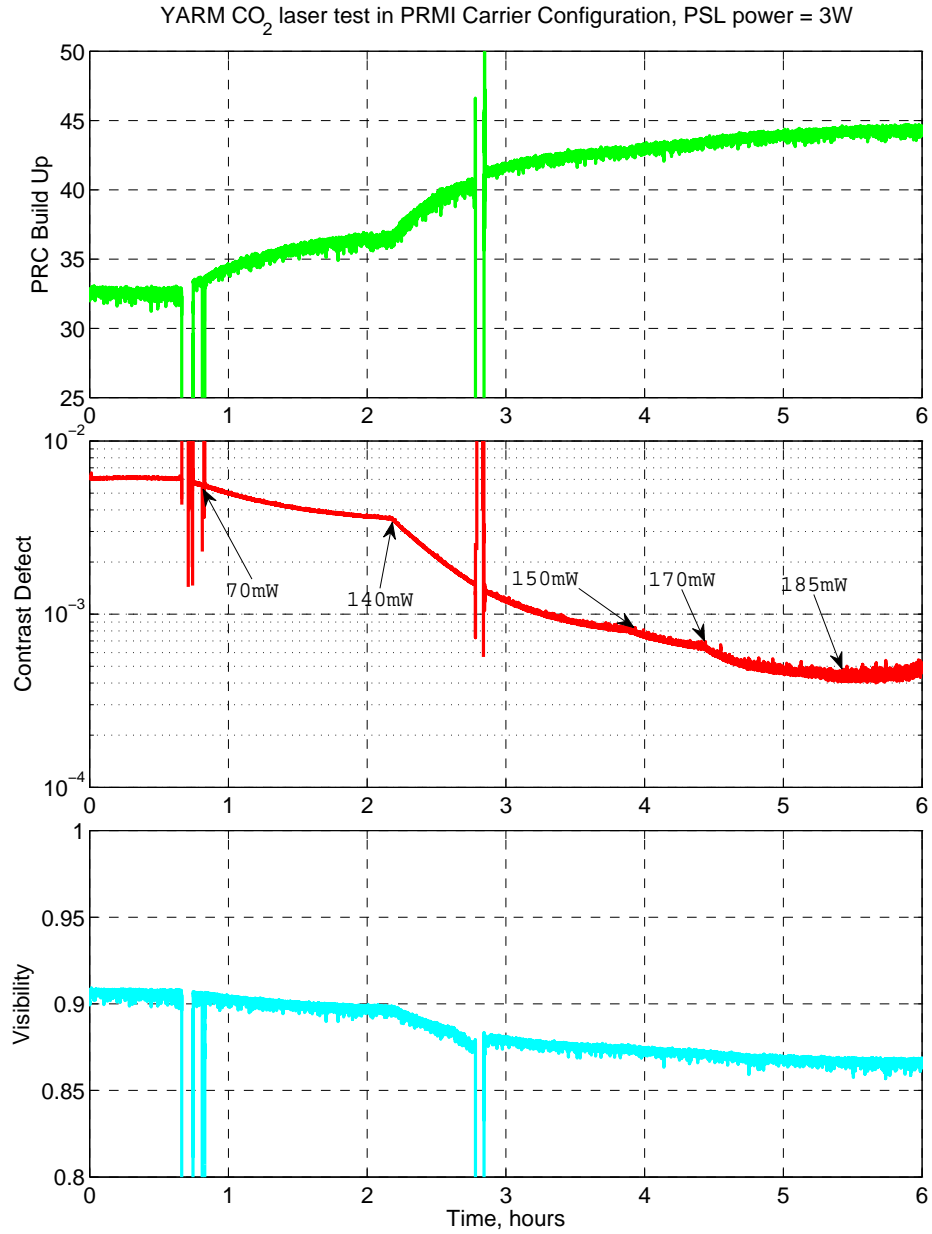


Figure D.3: Power recycling gain, Michelson contrast defect and cavity visibility during CO<sub>2</sub> laser test. Power of CO<sub>2</sub> beam power was slowly increased from 0 up to 175mW.

This measurement confirms that beam size is crucial for the power recycling build up due to clipping inside Michelson interferometer. Power recycling gain of 54 was achieved when both CO<sub>2</sub> laser beam were used in common to keep optimal Michelson contrast defect and reduce beam size on the beam splitter.

## Appendix E

# Seismometer isolation kit

Seismometers installed at the 40m lab to monitor ground motion in the frequency range from 10mHz up to 50Hz. A network of Trillium T-240, Guralp CMG-40T and Streckeisen STS-2 seismometers is also used for feedforward noise cancellation from interferometric degrees of freedom at low frequencies.

In order to achieve maximum sensitivity of seismometers to ground motion, instrument should be isolated from the ambient temperature, pressure and magnetic fluctuations. For this reason seismometer isolation kits were designed to reduce coupling of environmental noises to seismometer signal. Isolation kit also protects expensive seismometers from being accidentally broken by human activity.

Assembly of the isolation kit designed using Solidworks software [132] is shown in figure E.1. Seismometer stands on the  $18 \times 18''$  granite block with surface tolerance of  $0.01''$ . Stainless steel pot is attached to granite block using clamps and o-ring and covers seismometer on the top.

Seismometer cable comes through a hole in the granite block. Isolation kit has its own short cable going from connector plate to seismometer. This is done to improve interior isolation from ambient pressure and temperature fluctuations and to avoid seismometer noise coming from motion of the long cable from readout box. Inner cable also protects seismometer in case of accidental pull of the long outer cable.

Common granite blocks, pots and clamps are used for isolation of all seismometer types at the 40m prototype. At the same time connection plates are custom since Guralp uses different connectors from STS-2 and T-240. Connection plates are attached to the granite block using screws and o-ring to improve filtering of ambient temperature and pressure fluctuations. Pole frequency is controlled using small feed through connectors. Diameter of the hole can be adjusted using proper filters. Auxiliary cable for temperature and pressure sensors go inside the kits with T240 seismometers.

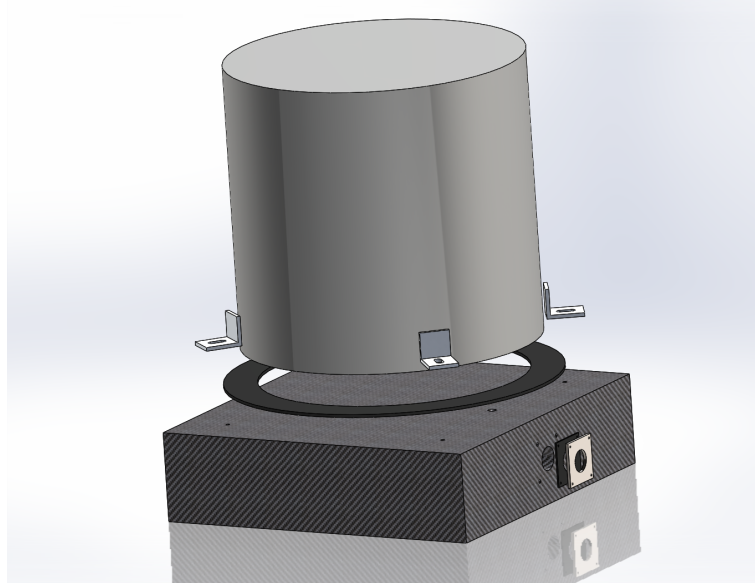


Figure E.1: Assembly of the seismometer isolation kit.

Figures E.2 show pictures of isolation kit installed at the Y-end of the 40m lab. Length of the interior cable is  $\approx 1m$ .



Figure E.2: Guralp seismometer installed in the seismic isolation kit with internal cabling.

Figures E.3, E.4 and E.5 show drawings of granite block and connection plates for Guralp and T-240/STS-2 seismometers.

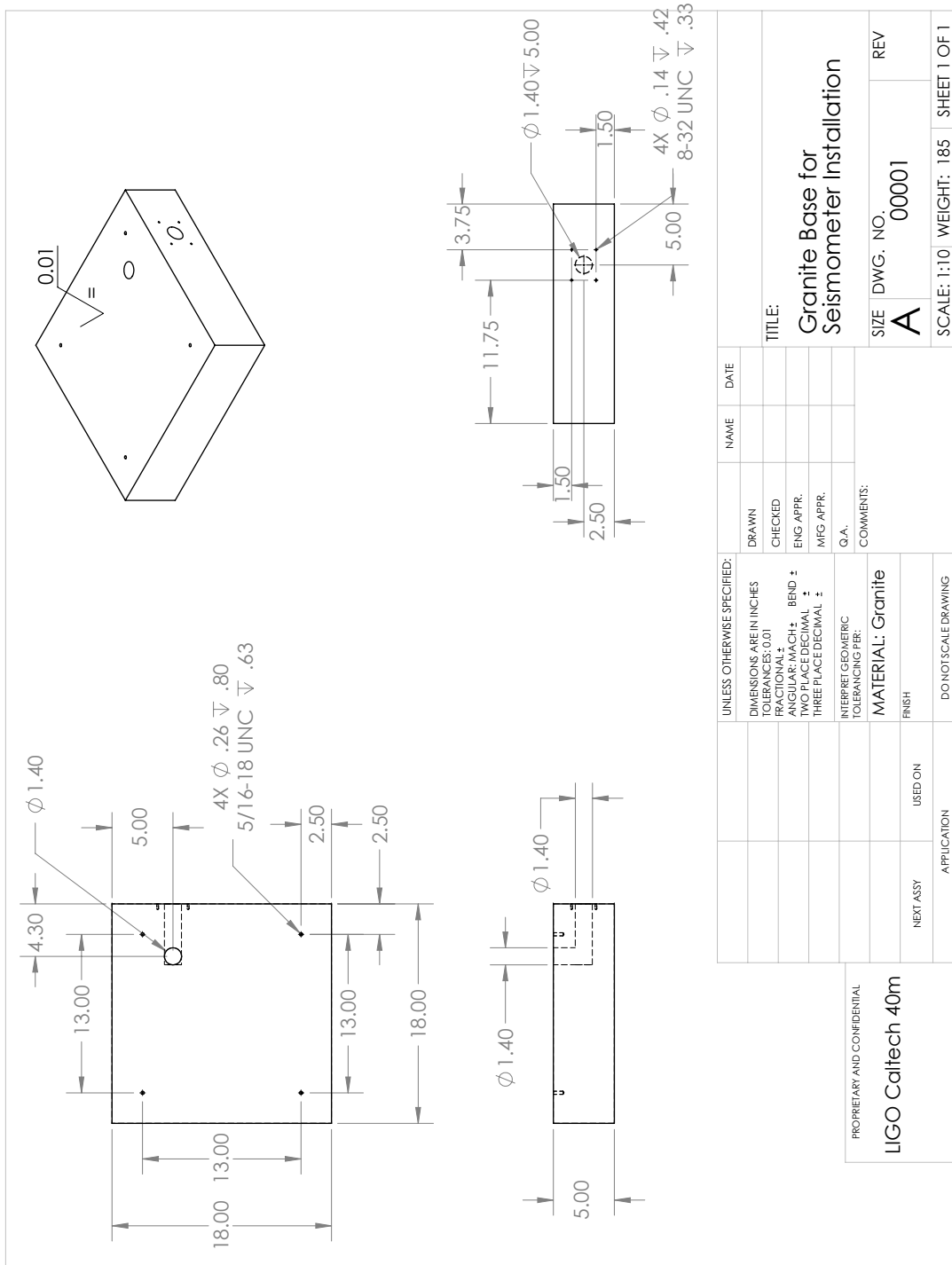


Figure E.3: Drawing of granite block.

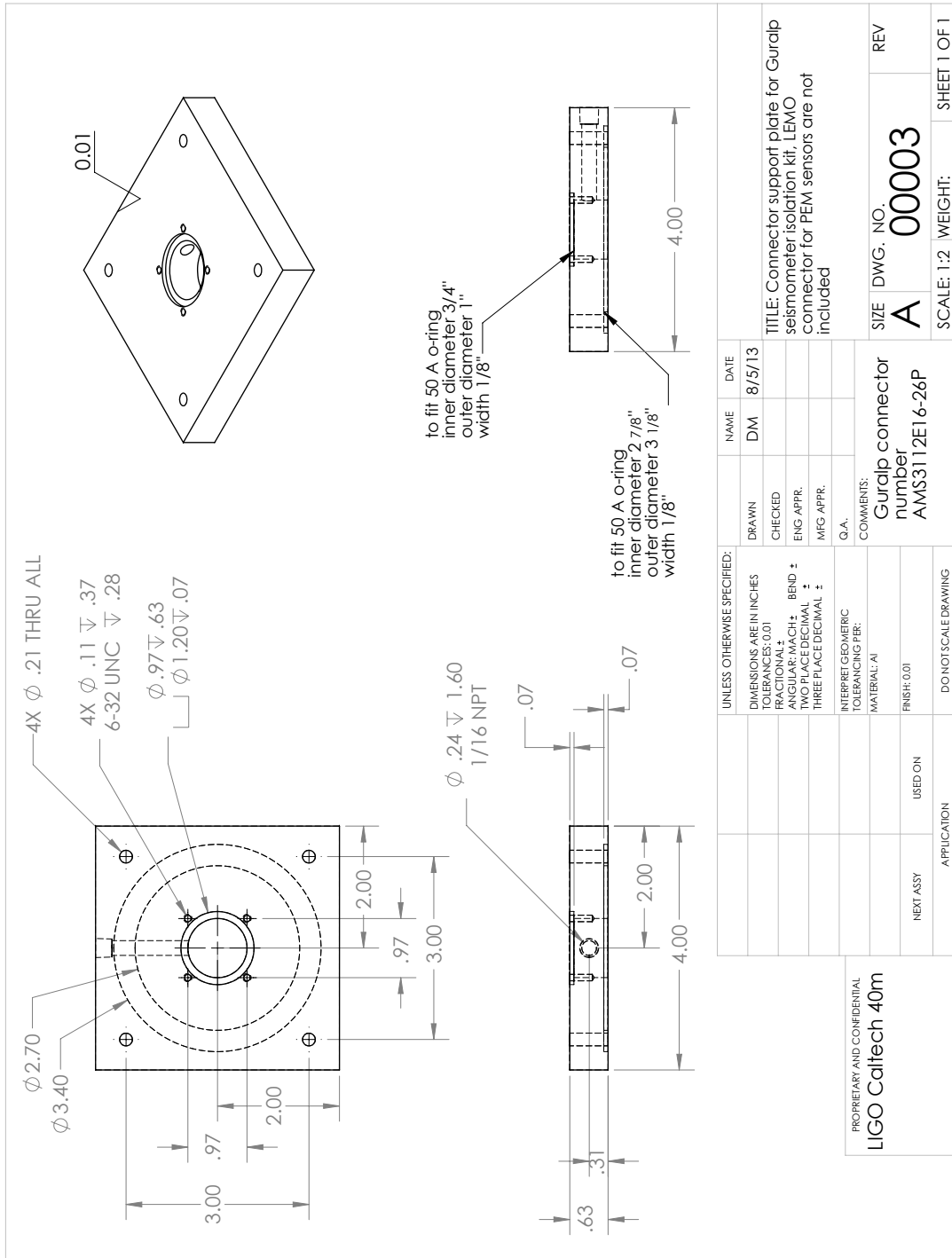


Figure E.4: Drawing of connector plate for Guralp seismometer kit.



# Bibliography

- [1] A. Einstein. *The Meaning of Relativity: Including the Relativistic Theory of the Non-Symmetric Field*. Princeton University Press, fifth edition, 2014.
- [2] R. Hulse and J. Taylor. Discovery of a pulsar in a binary system. *The Astrophysical Journal*, 195, 1975. <http://adsabs.harvard.edu/abs/1975ApJ...195L..51H>.
- [3] A. Abramovici et al. Ligo: The laser interferometer gravitational-wave observatory. *Science*, 256(5055):325–333, 1992. [http://pages.uoregon.edu/rayfrey/intro/Science\\_1992.pdf](http://pages.uoregon.edu/rayfrey/intro/Science_1992.pdf).
- [4] LIGO scientific collaboration. Ligo: the laser interferometer gravitational-wave observatory. *Rep. Prog. Phys.*, 72(7), 2009. <http://arxiv.org/pdf/0711.3041v2.pdf>.
- [5] LIGO scientific collaboration. Advanced ligo. *Class. Quant. Grav.*, 32(7), 2015. <http://iopscience.iop.org/0264-9381/32/7/074001/>.
- [6] VIRGO Collaboration. The virgo project: A wide band antenna for gravitational wave detection. *Nuclear Instruments and Methods in Physics Research Section A: Accelerators, Spectrometers, Detectors and Associated Equipment*, 289(3):518–525, 1990. <http://www.sciencedirect.com/science/article/pii/016890029091525G>.
- [7] T. Uchiyama et al. Present status of large-scale cryogenic gravitational wave telescope. *Class. Quant. Grav.*, 21:11611172, 2004. <http://www.astro.umd.edu/~miller/Compact/lcgt.pdf>.
- [8] Ligo india project. <http://www.gw-indigo.org/tiki-index.php>.
- [9] V. Fafone. Resonant-mass detectors: status and perspectives. *Class. Quant. Grav.*, 21(5):377–383, 2004. <http://iopscience.iop.org/0264-9381/21/5/001/>.
- [10] S. Bagaev. A high frequency resonance gravity gradiometer. *Rev. Sci. Instrum.*, 85, 2014. <http://scitation.aip.org/content/aip/journal/rsi/85/6/10.1063/1.4883901>.
- [11] J. Harms et al. Low-frequency terrestrial gravitational-wave detectors. *Phys. Rev. D*, 88, 2013. <http://arxiv.org/abs/1308.2074>.

- [12] M. Ando. Torsion-bar antenna for low-frequency gravitational-wave observations. *Phys. Rev. Lett.*, 105, 2010. <http://journals.aps.org/prl/abstract/10.1103/PhysRevLett.105.161101>.
- [13] P. Amaro-Seoane et al. elisa: Astrophysics and cosmology in the millihertz regime. Arxiv. <http://arxiv.org/abs/1201.3621>.
- [14] Seiji Kawamura et al. The japanese space gravitational wave antenna: Decigo. *Class. Quant. Grav.*, 28(9), 2011. <http://iopscience.iop.org/0264-9381/28/9/094011>.
- [15] L. D. Landau and E. M. Lifshitz. *The Classical Theory of Fields*. Pergamon Press, 1951.
- [16] S Weinberg. *Gravitation and Cosmology. Principles and applications of the general theory of relativity*. John Wiley and Sons, Inc, 1972.
- [17] R. Kerr. Gravitational field of a spinning mass as an example of algebraically special metrics. *Phys. Rev. Lett.*, 11(5):237–238, 1963. <http://journals.aps.org/prl/abstract/10.1103/PhysRevLett.11.237>.
- [18] K. Schwarzschild. On the gravitational field of a mass point according to einstein’s theory. *Sitzungsber.Preuss.Akad.Wiss.Berlin*, 7:189–196, 1916. Translation - <http://arxiv.org/abs/physics/9905030>.
- [19] S Shapiro and S. Teukolsky. *Black Holes, White Dwarfs and Neutron Stars: The Physics of Compact Objects*. Wiley-VCH, 1983.
- [20] P. Hajicek. *An Introduction to the Relativistic Theory of Gravitation (Lecture Notes in Physics)*. Springer, 2010.
- [21] C. Misner, K. Thorne, and J. Wheeler. *Gravitation*. W. H. Freeman and Co., 1970.
- [22] P. Saulson. *Fundamentals of Interferometric Gravitational Wave Detectors*. World Scientific Pub Co Inc, 1994.
- [23] C. D. Ott, A. Burrows, E. Livne, and R. Walder. Gravitational waves from axisymmetric, rotating stellar core collapse. *The Astrophysical Journal*, 600(2), 2004. <http://iopscience.iop.org/0004-637X/600/2/834>.
- [24] LIGO Scientific Collaboration. Implications for the origin of grb 070201 from ligo observations. *The Astrophysical Journal*, 681:1419 – 1430, 2008. <http://iopscience.iop.org/0004-637X/681/2/1419/pdf/73666.web.pdf>.

- [25] LIGO Scientific Collaboration. Search for high frequency gravitational-wave bursts in the first calendar year of ligo's fifth science run. *Physical Review D*, 80(10), 2009. <http://arxiv.org/abs/0904.4910>.
- [26] M. Hereld. *A Search for Gravitational Radiation from PSR 1937+214*. PhD thesis, Caltech, 1983. <http://adsabs.harvard.edu/abs/1984PhDT.....16H>.
- [27] LIGO Scientific Collaboration. Einstein@home search for periodic gravitational waves in early s5 ligo data. *Physical Review D*, 80(4), 2009. <http://arxiv.org/abs/0905.1705>.
- [28] L. Bildsten. Gravitational radiation and rotation of accreting neutron stars. *The Astrophysical Journal*, 501, 1998. <http://arxiv.org/abs/astro-ph/9804325>.
- [29] L. Blanchet. Gravitational radiation from post-newtonian sources and inspiralling compact binaries. *Living Reviews in Relativity*, 9(4), 2006. <http://arxiv.org/abs/1310.1528>.
- [30] LIGO Scientific Collaboration. Search for gravitational waves from low mass compact binary coalescence in 186 days of ligo's fifth science run. *Physical Review D*, 80(4), 2009. <http://arxiv.org/abs/0905.3710>.
- [31] LIGO Scientific Collaboration. Analysis of first ligo science data for stochastic gravitational waves. *Physical Review D*, 69(12), 2004. <http://arxiv.org/abs/gr-qc/0312088>.
- [32] N. Christensen. Measuring the stochastic gravitational-radiation background with laser-interferometric antennas. *Physical Review D*, 46(12):52505266, 1992. <http://journals.aps.org/prd/abstract/10.1103/PhysRevD.46.5250>.
- [33] B. Carr B. Bertotti. The prospects of detecting gravitational background radiation by doppler tracking interplanetary spacecraft. *The Astrophysical Journal*, 236:1000 – 1011, 1980. <http://adsabs.harvard.edu/abs/1980ApJ...236.1000B>.
- [34] R. Drever et al. Laser phase and frequency stabilization using an optical resonator. *Appl. Phys. B*, 31(2), 1983.
- [35] A. Siegman. *Laser*. University Science Books, Sausalito, California, 1986.
- [36] M. Evans. Optickle. <https://github.com/Optickle/Optickle>.
- [37] Finesse 2. <http://www.gwoptics.org/finesse>.
- [38] G. Vajente. Mist. <http://sourceforge.net/projects/optics-mist>.
- [39] L. Schnupp. Talk at a european collaboration meeting on interferometric detection of gravitational waves, sorrento, 1988. <http://sourceforge.net/projects/optics-mist>.

- [40] G. Muellerl. Beam jitter coupling in advanced ligo. *Optics Express*, 13(18):7118–7132, 2005. <https://www.osapublishing.org/ao/abstract.cfm?uri=ao-23-17-2944>.
- [41] D. Anderson. Alignment of resonant optical cavities. *Applied Optics*, 23(17):2944–2949, 1984. <http://authors.library.caltech.edu/2871/1/ANDao84a.pdf>.
- [42] N. Mavalvala et al. Experimental test of an alignment-sensing scheme for a gravitational-wave interferometer. *Applied Optics*, 37(33), 1998. <http://authors.library.caltech.edu/6066/1/MAVao98.pdf>.
- [43] N. Smith. A la mode: mode matching and beam propagation solutions for matlab. <https://github.com/nicolassmith/alm>.
- [44] P. Fritschel. Second generation instruments for the laser interferometer gravitational wave observatory (ligo). Arxiv document. <http://arxiv.org/pdf/gr-qc/0308090.pdf>.
- [45] C. Caves. Quantum-mechanical noise in an interferometer. *Phys. Rev. D*, 23(8), 1981. [http://cua.mit.edu/8.422\\_S05/caves\\_PRD.pdf](http://cua.mit.edu/8.422_S05/caves_PRD.pdf).
- [46] P. Fritschel. *Techniques for laser interferometer gravitational wave detectors*. PhD thesis, MIT, 1992. <http://dspace.mit.edu/handle/1721.1/77753>.
- [47] M. Evans. *Lock Acquisition in Resonant Optical Interferometers*. PhD thesis, Caltech, 2002. <http://www.ligo.caltech.edu/~mevans/lockAcq/thesis.pdf>.
- [48] M. Evans et al. Lock acquisition of a gravitational wave interferometer. *Optics Letters*, 27(8):598–600, 2002. <https://www.osapublishing.org/ol/abstract.cfm?uri=ol-27-8-598>.
- [49] K. Arai. *Robust extraction of control signals for power-recycled interferometric gravitational-wave detectors*. PhD thesis, U Tokyo, 2001. <http://citeseerx.ist.psu.edu/viewdoc/download?doi=10.1.1.121.8460&rep=rep1&type=pdf>.
- [50] K. Arai et al. Lock acquisition of a gravitational wave interferometer. *Class. Quantum Grav*, 19(7), 2002. <http://iopscience.iop.org/0264-9381/19/7/383>.
- [51] L. Barsotti. *The control of the Virgo interferometer for gravitational wave detection*. PhD thesis, U Pisa, 2006. <http://wwwcascina.virgo.infn.it/locking/Training/Barsotti.pdf>.
- [52] F. Acernese et al. The variable finesse locking technique. *Class. Quantum Grav*, 23(8), 2006. <http://iopscience.iop.org/0264-9381/23/8/S12>.

- [53] A. Mullavey et al. Arm-length stabilisation for interferometric gravitational-wave detectors using frequency doubled auxiliary lasers. *Optics Express*, 20(1):81–89, 2012. <http://arxiv.org/abs/1112.3118>.
- [54] K. Izumi et al. Multi-color cavity metrology. *Josa A*, 29(10):2092–2103, 2012. <http://arxiv.org/abs/1205.1257>.
- [55] A. Staley and D. Martynov et al. Achieving resonance in the advanced ligo gravitational-wave interferometer. *Classical and Quantum Gravity*, 31(24), 2014. <http://iopscience.iop.org/0264-9381/31/24/245010>.
- [56] L Barsotti, M Evans, and P Fritschel. Alignment sensing and control in advanced ligo. *Classical and Quantum Gravity*, 27(8), 2010. <http://iopscience.iop.org/0264-9381/27/8/084026>.
- [57] R. Weiss. Collection of reports on barkhausen noise. LIGO report. <https://dcc.ligo.org/LIGO-T0900061/public>.
- [58] K. strom and R. Murray. Feedback systems: An introduction for scientists and engineers. Online book. [http://www.cds.caltech.edu/~murray/amwiki/index.php/Main\\_Page](http://www.cds.caltech.edu/~murray/amwiki/index.php/Main_Page).
- [59] LIGO Scientific Collaboration. Calibration of the ligo gravitational wave detectors in the fifth science run. *Nuclear Instruments and Methods*, 624(1):223–240, 2010. <http://arxiv.org/abs/1007.3973>.
- [60] E. Goetz et al. Precise calibration of ligo test mass actuators using photon radiation pressure. *Classical and Quantum Gravity*, 26(24), 2009. <http://iopscience.iop.org/0264-9381/26/24/245011>.
- [61] R. Adhikari. *Sensitivity and Noise Analysis of 4 km Laser Interferometric Gravitational Wave Antennae*. PhD thesis, MIT, 2004. <http://dspace.mit.edu/bitstream/handle/1721.1/28646/58964895-MIT.pdf?sequence=2>.
- [62] S. Rampone et al. Neural network aided glitch-burst discrimination and glitch classification. *Int.J.Mod.Phys*, 24(arXiv:1401.5941), 2014. <http://arxiv.org/abs/1401.5941>.
- [63] J. Driggers, J. Harms, and R. Adhikari. Subtraction of newtonian noise using optimized sensor arrays. *Phys. Rev. D*, 86, 2012. <http://arxiv.org/abs/1207.0275>.
- [64] B. Schumaker and C. Caves. New formalism for two-photon quantum optics. ii. mathematical foundation and compact notation. *Phys. Rev. A*, 31, 1985. <http://journals.aps.org/pr/abstract/10.1103/PhysRevA.31.3093>.

- [65] T. Corbitt. *Quantum Noise and Radiation Pressure Effects in High Power Optical Interferometers*. PhD thesis, MIT, 2008. [https://gwic.ligo.org/thesisprize/2008/Corbitt\\_Thesis.pdf](https://gwic.ligo.org/thesisprize/2008/Corbitt_Thesis.pdf).
- [66] A. Buonanno and Y. Chen. Quantum noise in second generation, signal-recycled laser interferometric gravitational-wave detectors. *Phys. Rev. D*, 64, 2001. <http://arxiv.org/pdf/gr-qc/0102012v2.pdf>.
- [67] Yu. Levin. Internal thermal noise in the ligo test masses: a direct approach. *Phys. Rev. D*, 57, 1998. <http://arxiv.org/abs/gr-qc/9707013>.
- [68] K. Yamamoto. *Study of the thermal noise caused by inhomogeneously distributed loss*. PhD thesis, U Tokyo, 2000. [http://t-munu.phys.s.u-tokyo.ac.jp/theses/yamamoto\\_d.pdf](http://t-munu.phys.s.u-tokyo.ac.jp/theses/yamamoto_d.pdf).
- [69] H. Grote. Estimation of test mass damping from esd / hv drive impedance. aLIGO log book. <https://alog.ligo-la.caltech.edu/aLOG/index.php?callRep=14541>.
- [70] G. Harry. Thermal noise in interferometric gravitational wave detectors due to dielectric optical coatings. *Class. Quant. Grav.*, 19(5):897917, 2002. <http://arxiv.org/pdf/gr-qc/0109073v3.pdf>.
- [71] G. Harry. Titania-doped tantala/silica coatings for gravitational-wave detection. *Class. Quant. Grav.*, 24:405–415, 2007. <http://iopscience.iop.org/0264-9381/23/15/014/>.
- [72] LIGO collaboration. Gwinc. <https://awiki.ligo-wa.caltech.edu/aLIGO/GWINC>.
- [73] V. Braginsky, M. Gorodetsky, and S. Vyatchanin. Thermodynamical fluctuations and photo-thermal shot noise in gravitational wave antennae. *Phys. Lett. A*, 264(1):1–10, 1999. <http://www.sciencedirect.com/science/article/pii/S0375960199007859>.
- [74] Y. Liu and K. Thorne. Thermoelastic noise and homogeneous thermal noise in finite sized gravitational-wave test masses. *Phys. Rev. D*, 62(12), 2000. <http://arxiv.org/pdf/gr-qc/0002055.pdf>.
- [75] S Wen. Hydraulic external pre-isolator system for ligo. *Class. Quantum Grav*, 31(23), 2014. <http://arxiv.org/abs/1309.5685>.
- [76] F. Matichard et al. Prototyping, testing, and performance of the two-stage seismic isolation system for advanced ligo gravitational wave detectors. In *Proc. ASPE Conf. on Control of Precision Systems*, 2010. [http://aspe.net/publications/Spring\\_2010/Spr10Ab/2996Matichard.pdf](http://aspe.net/publications/Spring_2010/Spr10Ab/2996Matichard.pdf).

- [77] S Aston et al. Update on quadruple suspension design for advanced ligo. *Class. Quantum Grav*, 29(23), 2012. <http://iopscience.iop.org/0264-9381/29/23/235004>.
- [78] D Ugolini et al. Discharging fused silica optics occluded by an electrostatic drive. *Rev Sci Instrum*, 85(3), 2014. <http://scitation.aip.org/content/aip/journal/rsi/85/3/10.1063/1.4867248>.
- [79] P Campsie et al. Charge mitigation techniques using glow and corona discharges for advanced gravitational wave detectors. *Class. Quantum Grav*, 28(21), 2011. [http://iopscience.iop.org/0264-9381/28/21/215016/pdf/cqg11\\_21\\_215016.pdf](http://iopscience.iop.org/0264-9381/28/21/215016/pdf/cqg11_21_215016.pdf).
- [80] S. Margulies. Force on a dielectric slab inserted into a parallel-plate capacitor. *Am. J. Physics*, 52(6), 1984. <http://adsabs.harvard.edu/abs/1984AmJPh..52..515M>.
- [81] L. Garbone et al. Sensors and actuators for the advanced ligo mirror suspensions. *Class. Quantum Grav*, 29(11), 2012. <http://iopscience.iop.org/0264-9381/29/11/115005>.
- [82] M. Suijlen et al. Squeeze film damping in the free molecular flow regime with full thermal accommodation. *Sensors and Actuators A: Physical*, 156(1):171–179, 2009. <http://www.sciencedirect.com/science/article/pii/S0924424709001691>.
- [83] R. Weiss. Gas damping of the final stage in the advanced ligo suspensions. LIGO technical note T0900509. [https://dcc.ligo.org/DocDB/0006/T0900509/001/Weiss%20gas\\_damping%2009-10-19.pdf](https://dcc.ligo.org/DocDB/0006/T0900509/001/Weiss%20gas_damping%2009-10-19.pdf).
- [84] M. Evans, P. Fritschel, and R. Weiss. Gas damping monte carlo. LIGO technical note T0900582-. <https://dcc.ligo.org/DocDB/0007/T0900582/007/GasDampingMonteCarlo.pdf>.
- [85] A. Cavalleri et al. Gas damping force noise on a macroscopic test body in an infinite gas reservoir. *Physics Letters A*, 374(34):33653369, 2010. <http://arxiv.org/pdf/0907.5375.pdf>.
- [86] M. Zucker and S. Whitcomb. Measurement of optical path fluctuations due to residual gas in the ligo 40 meter interferometer. In *Proceedings of the Seventh Marcel Grossman Meeting on recent developments in theoretical and experimental general relativity, gravitation, and relativistic field theories*, pages 1434–1436, 1996.
- [87] V. Braginsky, S. Strigin, and S. Vyatchanin. Analysis of parametric oscillatory instability in power recycled ligo interferometer. *Phys. Lett. A*, 305(3-4):111–124, 2002. <http://arxiv.org/abs/gr-qc/0209064>.

- [88] M. Evans et al. Observation of parametric instability in advanced ligo. *Phys. Rev. Lett.*, 114, 2015. <http://arxiv.org/abs/1502.06058>.
- [89] T. Isogai et al. Loss in long-storage-time optical cavities. *Optics Express*, 21(24), 2014. <http://arxiv.org/abs/1310.1820>.
- [90] H. Grote et al. First long-term application of squeezed states of light in a gravitational-wave observatory. *Phys. Rev. Lett.*, 110, 2013. <http://arxiv.org/abs/1302.2188>.
- [91] D. Ottaway et al. The impact of upconverted scattered light on advanced interferometric gravitational wave detectors. *Optics Express*, 20(8):8329–8336, 2012. <https://www.osapublishing.org/oe/abstract.cfm?uri=oe-20-8-8329>.
- [92] G. Meadors et al. Increasing ligo sensitivity by feedforward subtraction of auxiliary length control noise. *Class. Quantum Grav*, 31(10), 2014. <http://arxiv.org/abs/1311.6835>.
- [93] R. DeRosa et al. Global feed-forward vibration isolation in a km scale interferometer. *Class. Quantum Grav*, 29(21), 2012. <http://arxiv.org/abs/1204.5504>.
- [94] J. Driggers et al. Active noise cancellation in a suspended interferometer. *Rev. Sci. Instrum*, 81, 2012. <http://arxiv.org/abs/1112.2224>.
- [95] S. Haykin. *Adaptive Filter Theory*. Prentice Hall, 2001.
- [96] A. Sayed. *Fundamentals of Adaptive Filtering*. Wiley-IEEE Press, 2003.
- [97] B. Gustavsen and A. Semlyenl. Rational approximation of frequency domain responses by vector fitting. *IEEE Trans. Power Delivery*, 14(3):1052–1061, 1999. [http://www.ligo.caltech.edu/~rana/mat/vectfit/VF\\_paper.pdf](http://www.ligo.caltech.edu/~rana/mat/vectfit/VF_paper.pdf).
- [98] V. Nascimento and A. Sayed. Unbiased and stable leakage-based adaptive filters. *IEEE Trans. on Signal Processing*, 47(12), 1999. <http://www.lps.usp.br/vitor/artigos/tsp99.pdf>.
- [99] B. Widrow et al. On adaptive inverse control. In *Proc. 15th Asilomar Conf*, pages 185–189, 1981. <http://www-isl.stanford.edu/~widrow/papers/c1981onadaptive.pdf>.
- [100] A. Shirdel, E. Gatavi, and Z. Hashemiyan. Comparison of  $h-\infty$  and optimized-lqr controller in active suspension system. In *Second International Conference on Computational Intelligence, Modelling and Simulation*, pages 241–246, 2010. <http://ieeexplore.ieee.org.clsproxy.library.caltech.edu/stamp/stamp.jsp?tp=&arnumber=5701851>.
- [101] I. Tijani, R. Akmeliawati, and A. Abdullateef. Control of an inverted pendulum using mode-based optimized lqr controller. In *Industrial Electronics and Applications (ICIEA)*, pages

- 1759 – 1764, 2013. <http://ieeexplore.ieee.org.clsproxy.library.caltech.edu/stamp/stamp.jsp?tp=&arnumber=6566653>.
- [102] C. Logan. A comparison between h-infinity/mu-synthesis control and sliding-mode control for robust control of a small autonomous underwater vehicle. In *Autonomous Underwater Vehicle Technology*, pages 399 – 416, 1994. <http://ieeexplore.ieee.org.clsproxy.library.caltech.edu/stamp/stamp.jsp?tp=&arnumber=518653>.
- [103] A. Bryson and Y. Ho. *Applied Optimal Control*. CRC Press, 1975.
- [104] N. Gupta. Frequency-shaped cost functionals: Extension of linear-quadratic-gaussian design methods. *J. Guidance, control and dynamics*, 3(6):529–535, 1980. <http://adsabs.harvard.edu/abs/1980JGCD....3..529G>.
- [105] Matlab function. <http://www.mathworks.com/help/control/ref/care.html?refresh=true>.
- [106] A. Brooks et al. Ultra-sensitive wavefront measurement using a hartmann sensor. *Optics Express*, 15(16):10370–10375, 2007. <https://www.osapublishing.org/oe/abstract.cfm?uri=oe-15-16-10370>.
- [107] J. Doyle et al. State-space solutions to standard  $h_2$  and  $h_\infty$  control problems. *IEEE Trans. on Automatic Control*, 34(8), 1989. <http://authors.library.caltech.edu/3087/1/D0Yieetac89.pdf>.
- [108] Matlab function. <http://www.mathworks.com/help/robust/ref/hinfsyn.html>.
- [109] Ligo suspension modeling website. <http://www.ligo.caltech.edu/~e2e/SUSmodels/>.
- [110] A. Packard and J. Doyle. The complex structured singular value. *Automatica*, 29(1):71–109, 1993. [http://control.ee.ethz.ch/~ifaatic/2014/references/Packard\\_Automatica\\_1993.pdf](http://control.ee.ethz.ch/~ifaatic/2014/references/Packard_Automatica_1993.pdf).
- [111] Matlab function. <http://www.mathworks.com/help/robust/ref/dksyn.html>.
- [112] B. Barr et al. Ligo 3 strawman design, team red. LIGO technical note. <https://dcc.ligo.org/public/0086/T1200046/001/LIGO-T1200042-v1.pdf>.
- [113] LIGO scientific collaboration. Enhanced sensitivity of the ligo gravitational wave detector by using squeezed states of light. *Nature Photonics*, 7:613619, 2013. <http://www.phys.ufl.edu/~tanner/PDFS/Aasi13natphot-squeezing.pdf>.
- [114] T. Uchiyama et al. Reduction of thermal fluctuations in a cryogenic laser interferometric gravitational wave detector. *Phys. Rev. Lett.*, 108, 2012. <http://arxiv.org/abs/1202.3558>.

- [115] E. Hirose et al. Update on the development of cryogenic sapphire mirrors and their seismic attenuation system for kagra. *Class. Quant. Grav.*, 31(22), 2014. [http://iopscience.iop.org/0264-9381/31/22/224004/pdf/CQG\\_31\\_22\\_224004.pdf](http://iopscience.iop.org/0264-9381/31/22/224004/pdf/CQG_31_22_224004.pdf).
- [116] G. Cole et al. Tenfold reduction of brownian noise in high-reflectivity optical coatings. *Nature Photonics*, 7:644650, 2013. <http://arxiv.org/pdf/1302.6489.pdf>.
- [117] J. Steinlechner et al. Optical absorption measurement at 1550 nm on a highly-reflective si/sio2 coating stack. *Class. Quant. Grav.*, 31(10), 2014. <http://iopscience.iop.org/0264-9381/31/10/105005>.
- [118] Y. Chen. Sagnac interferometer as a speed-meter-type, quantum-nondemolition gravitational-wave detector. *Phys. Rev. D*, 67, 2003. <http://arxiv.org/abs/gr-qc/0208051>.
- [119] S. Danilishin et al. Quantum noise of non-ideal sagnac speed meter interferometer with asymmetries. *New Journal of Physics*, 17, 2015. <http://arxiv.org/pdf/1412.0931v2.pdf>.
- [120] A. Wicht et al. White-light cavities, atomic phase coherence and gravitational wave detectors. *Optics Communications*, 134:431–439, 1997. <http://pubman.mpg.de/pubman/item/escidoc:153016/component/escidoc:153015/372445.pdf>.
- [121] S. Dwyer et al. A gravitational wave detector with cosmological reach. *Phys. Rev. D*, 91, 2015. <http://arxiv.org/pdf/1410.0612.pdf>.
- [122] P. Fritschel, M. Evans, and V. Frolov. Balanced homodyne readout for quantum limited gravitational wave detectors. *Opt. Express*, 22(4):4224–34, 2014. <http://adsabs.harvard.edu/abs/2014OExpr..22.4224F>.
- [123] C. Pethick and D. Ravenhall. Matter at large neutron excess and the physics of neutron-star crusts. *Annual Review of Nuclear and Particle Sciences*, 45(45):429–484, 1995. <http://adsabs.harvard.edu/abs/1995ARNPS..45..429P>.
- [124] S. Hild et al. Demonstration and comparison of tuned and detuned signal recycling in a large-scale gravitational wave detector. *Class. Quant. Grav.*, 24(6), 2007. <http://iopscience.iop.org/0264-9381/24/6/009>.
- [125] S. Chelkowski. Experimental characterization of frequency-dependent squeezed light. *Phys. Rev. A*, 71, 2005. <http://arxiv.org/abs/0706.4479>.
- [126] M. Evans et al. Realistic filter cavities for advanced gravitational wave detectors. *Phys. Rev. D*, 88, 2013. <http://arxiv.org/abs/1305.1599>.

- [127] C.T. Mullis and R.A. Roberts. Synthesis of minimum roundoff noise fixed-point digital filters. *IEEE Trans. Circuits Syst.*, 23(9):551–562, 1976.
- [128] S.Y. Hwang. Minimum uncorrelated unit noise in state-space digital filtering. *IEEE Trans. Acoust. Speech Signal Process*, 25(4):273–281, 1977.
- [129] Gang Li et al. A novel digital filter structure with minimum roundoff noise. *Digital Signal Processing*, 20:1000–1009, 2010. <http://www.sciencedirect.com/science/article/pii/S1051200409001961>.
- [130] M. Evans. Digital filter noise. LIGO technical note. <https://dcc.ligo.org/DocDB/0006/G0900928/001/G0900928-v1.pdf>.
- [131] D. Martynov. Filter checker: set of scripts to estimate quantization noise of ligo digital filters. <https://github.com/denismartynov/quantization>.
- [132] Solidworks software. <https://www.solidworks.com/>.